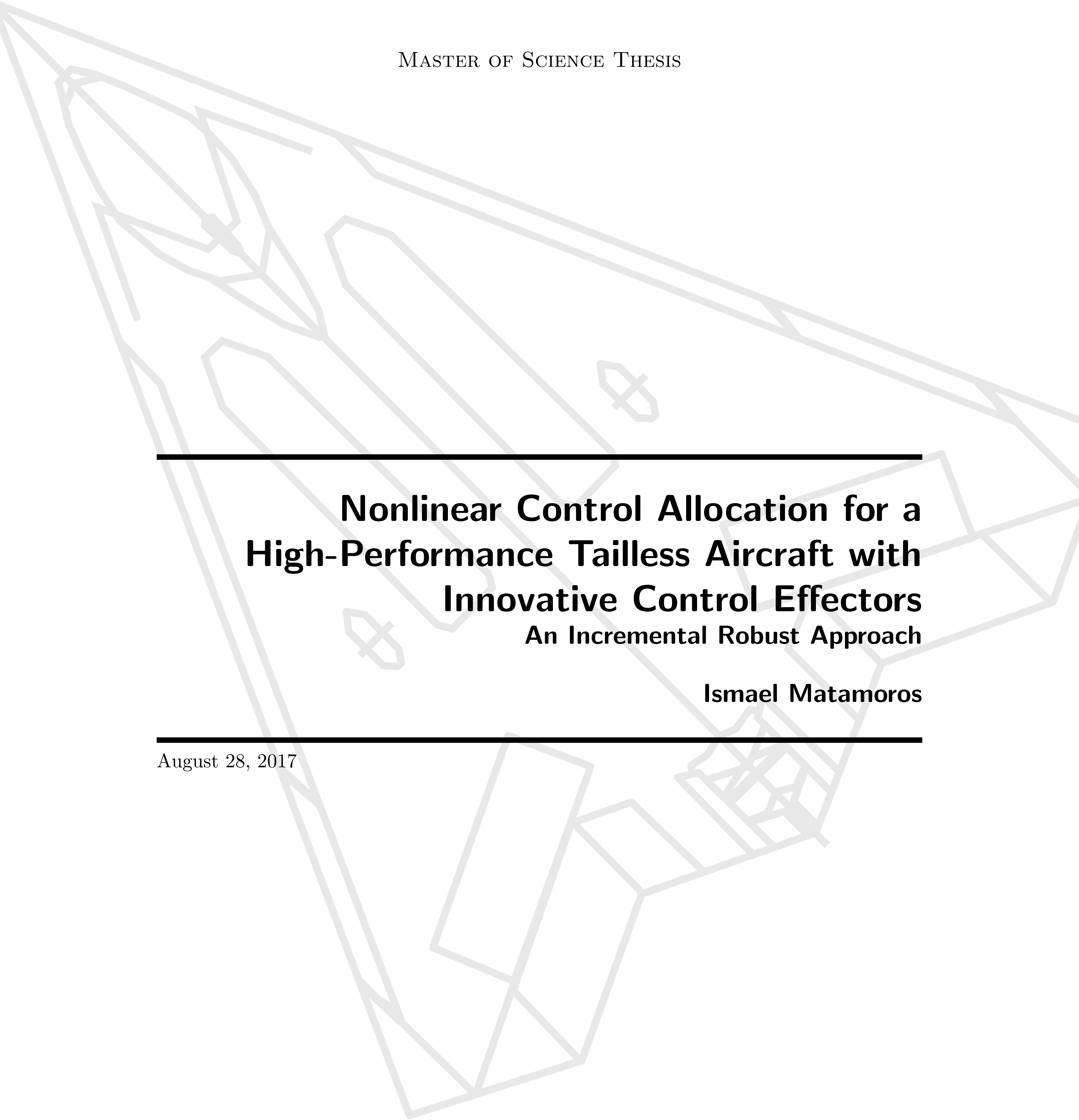

MASTER OF SCIENCE THESIS

Nonlinear Control Allocation for a High-Performance Tailless Aircraft with Innovative Control Effectors

An Incremental Robust Approach

Ismael Matamoros

August 28, 2017

Faculty of Aerospace Engineering · Delft University of Technology

Nonlinear Control Allocation for a High-Performance Tailless Aircraft with Innovative Control Effectors

An Incremental Robust Approach

MASTER OF SCIENCE THESIS

For obtaining the degree of Master of Science in Aerospace
Engineering at Delft University of Technology

Ismael Matamoros

August 28, 2017

Faculty of Aerospace Engineering · Delft University of Technology

TU Delft
Delft
University of
Technology

DELFT UNIVERSITY OF TECHNOLOGY
DEPARTMENT OF
CONTROL & SIMULATION

The undersigned hereby certify that they have read and recommend to the Faculty of Aerospace Engineering for acceptance a thesis entitled **"Nonlinear Control Allocation for a High-Performance Tailless Aircraft with Innovative Control Effectors"** by **Ismael Matamoros** in partial fulfillment of the requirements for the degree of **Master of Science**.

Dated: August 28, 2017

Head of department: Dr.ir. Q.P. Chu

Supervisor: Dr.ir. C.C. de Visser

Reader: Dr.ir. E. van Kampen

Reader: Dr. S.J. Hulshoff

Summary

Conventional linear control allocation (LCA) methods fail to provide satisfactory performance in flight control systems (FCS) for aircraft with highly nonlinear and coupled control effector suites, especially for tailless aircraft configurations. This is due to the inability of linear models to capture non-negligible nonlinearities and interactions of innovative control effectors. Nonlinear control allocation methods developed to date prove potential benefits of nonlinear control allocation in such cases, but are too computationally complex for real-time implementation in flight control computers (FCC).

This thesis implements and tests through real-time simulation an incremental nonlinar control allocation (INCA) approach that captures nonlinear control moments and control effector interactions, while being solvable with simple and computationally efficient linear solvers. This makes INCA suitable for real-time, robust nonlinear control allocation in FCS with advanced control effector suites. This incremental approach only relies on a Jacobian model of the control moments and an angular acceleration feedback, which reduces model dependency and provides strong robustness against model mismatch. In addition, a control effector position feedback mitigates negative effects of actuator dynamics.

In this thesis an LCA- and an INCA-based FCS were designed for Lockheed Martin's Innovative Control Effectors (ICE) aircraft, a highly manoeuvrable tailless aircraft with a redundant suite of 13 unconventional control effectors. These FCS were tested in a real-time simulation framework set up with a high-fidelity aerodynamic model of the ICE aircraft including actuator dynamics. The flight control systems were implemented with two typical control allocation solvers and include inner angular rate loops and outer loops to track reference trajectories. Actuator saturation and partial flight envelope protection are handled through pseudo-control hedging (PCH).

The performance of INCA was tested through real-time simulation of aggressive air combat maneuvers given as references to the outermost control loops of the FCS. These maneuvers included loopings, aileron rolls, barrel rolls, high-angle-of-attack commands and more. The obtained results showed the ability of INCA to perform maneuvers which could not be achieved with LCA. Important improvements of INCA with respect to LCA were observed in terms tracking performance by a factor of 3.0, and in terms of control allocation performance by a factor of 4.5. Generally, the overall control performance obtained with INCA was remarkably superior than the performance obtained with LCA. No significant increase of computational load or control effort was observed with INCA with respect to LCA.

A robustness analysis of the INCA system against Jacobian model mismatch demonstrated very small sensitivity to model error in the form of model offset and scaling. Only small degradations in control allocation performance up to 10% for model offsets of ±30% and scaling factors between 0.6 and 0.8 were observed. In addition, it was observed that underestimation of the magnitude of the Jacobian model is beneficial for the control performance of INCA.

The suggested lines of research for future work mainly concern the implementation of INCA in fault-tolerant flight control systems with online system identification, the refinement of the on-board spline-based Jacobian model to higher orders of continuity, extension of the control system with translational control modules, inclusion of sensor dynamics, delays, noise and state estimation algorithms, and eventually practical validation of the INCA concept through flight testing.

Acknowledgements

I wish to thank my daily supervisor Dr. C.C. de Visser for his implication and enthusiasm for this project. Important outcomes of this thesis are a reality thanks to his important contributions and voluntary work. I would also like to express my gratitude to Dr. Q.P. Chu for giving me the chance to undertake this beautiful project. Long discussions with him have shaped this work from beginning to end.

I am deeply grateful to Ariana for being an essential pillar in these years, for being on my side along this journey and for always listening to me. I owe my deepest gratitude to my parents Susi and Joaquin for their hard work and unconditional support and to Denise, for her love and strength as a sister and as a friend.

Delft, The Netherlands
August 28, 2017

Ismael Matamoros

Contents

List of Figures

List of Tables

Nomenclature

Latin Symbols

$\mathbb{A}$	Attainable moments set.	[-]
A_x, A_y, A_z	Body frame accelerations.	[ft/sec]
$\mathbf{a}$	Auxiliary variable.	[-]
B	Control effectiveness matrix.	[-]
b	Wing span.	[ft]
C_l	Dimensionless rolling moment coefficient.	[-]
C_m	Dimensionless pitching moment coefficient.	[-]
C_n	Dimensionless yawing moment coefficient.	[-]
C_X	Dimensionless axial force coefficient.	[-]
C_Y	Dimensionless lateral force coefficient.	[-]
C_Z	Dimensionless vertical force coefficient.	[-]
Ceff	Control effort.	[deg]
$\mathbf{c}$	Intercept correction term in affine effector models.	[-]
$\bar{c}$	Mean aerodynamic chord.	[ft]
D	Diagonal matrix.	[-]
$\mathbf{d}$	Pseudo-control input.	[-]
d_n	Moment arm of the thrust force.	[ft]
E	Auxiliary matrix.	[-]
$\mathbf{e}$	Column vector of ones.	[-]
$\mathcal{F}$	Reference frame.	[-]
$\mathcal{H}$	Hamiltonian function.	[-]

I	Identity matrix.	[-]
$\mathcal{J}$	Cost function.	[-]
J	Inertia matrix.	[lb·ft^2]
L, M, N	Rolling, pitching and yawing moments.	[lbf·ft]
$\mathcal{L}$	Lagrangian function.	[-]
M	Mach number.	[-]
m	Dimension of the pseudo-control input vector.	[-]
n	Dimension of the state vector.	[-]
n_i	Number of iterations.	[-]
p	Dimension of the actuator positions vector.	[-]
p, q, r	Rolling, pitching and yawing rates.	[deg/sec]
$\mathbb{R}$	Set of real numbers.	[-]
S	Total wing area.	[ft^2]
$\mathbf{T}$	Thrust vector.	[lbf]
t	Time.	[sec]
$\mathbf{u}$	Pseudo-control input vector.	[-]
u, v, w	Airspeed components.	[ft/sec]
$\mathcal{V}$	Lyapunov function.	[-]
V	True airspeed.	[ft/sec]
$\mathcal{W}$	Working/active set.	[-]
W	Aircraft total weight.	[lb]
W_δ	Weighting matrix for control minimization.	[-]
W_τ	Weighting matrix for error minimization.	[-]
X, Y, Z	Axial, lateral and normal aerodynamic forces in body frame.	[lbf]
$\mathbf{x}$	State vector.	[-]
$\mathbf{y}$	Output vector.	[-]
z	Auxiliary variable.	[-]

Greek Symbols

α	Angle of attack.	[deg]
β	Angle of sideslip.	[deg]
γ	Auxiliary function.	[-]
Δ	Increment.	[-]
$\boldsymbol{\delta}$	Control effector positions.	[deg]
ϵ	Weighting factor for the mixed optimization problem.	[-]
ε	Error.	[-]
$\boldsymbol{\kappa}$	Barrier function.	[-]

$\boldsymbol{\lambda}$	Lagrange multiplier.	[-]
$\boldsymbol{\nu}$	Virtual control.	[-]
ξ	Parameter.	[-]
$\boldsymbol{\Phi}$	Control effectiveness function.	[-]
ρ	Air density.	[lbf/ft^3]
ϕ, θ, ψ	Roll, pitch and yaw angles.	[deg]
$\boldsymbol{\tau}$	Vector of body-axis aerodynamic moments.	[lbf·ft]
$\boldsymbol{\omega}$	Vector of angular body rates.	[rad/sec]

Subscripts

$_{\delta}$	Referent to control input.
$_{\text{sat}}$	Saturated effectors.
$_{a}$	Referent to airframe.
$_{b}$	Body frame.
$_{c}$	Command.
$_{p}$	Preferred value.
$_{s}$	Slack variable.

Superscripts

$^{+}$	Moore-Penrose pseudo-inverse matrix.
$^{\sharp}$	Generalized weighted pseudo-inverse.
$^{\text{rm}}$	Reference model.
^{h}	Hedge.
^{s}	Spline function.
^{T}	Transpose matrix.

Abbreviations

A/T	Auto throttle.
AC	Aerodynamic center.
ADF	Aerodynamic Development Facility.
AMS	Attainable moments set.
AMT	All moving wing tips.
AoA	Angle of attack.

CA	Control allocation.
DA	Direct allocation.
DoF	Degrees of freedom.
FCC	Flight control computer.
FCS	Flight control system.
FTFC	Fault-tolerant flight control.
ICE	Innovative control effectors.
INCA	Incremental nonlinear control allocation.
INDI	Incremental nonlinear dynamic inversion.
LCA	Linear control allocation.
LEF	Leading edge flaps.
LEU	Leading edge up.
LMTAS	Lockheed Martin Tactical Aircraft Systems.
LM	Levenberg-Marquardt.
LP	Linear programming.
MAC	Mean aerodynamic chord.
MILP	Mixed-integer linear program.
MPC	Model predictive control.
MTV	Multi-axis thrust vectoring.
NAWCAD	Naval Air Warfare Center.
NDI	Nonlinear dynamic inversion.
NP	Nonlinear programming.
PCH	Pseudo-Control Hedging.
PF	Pitch flaps.
PWL	Piecewise linear functions.
QP	Quadratic programming.
RCS	Radar cross section.
RMS	Root mean square.
RM	Reference model.
RWPI	Redistributed weighted pseudo-inverse.
SAS	Stability augmentation system.
SQP	Sequential quadratic programming.
SSD	Slpoiler-slot deflectors.
TED	Trailing edge down.
TEU	Trailing edge up.
USA	United States of America.
WL	Wright Laboratory.

Chapter 1

Introduction

In the last decades, the need for low signature characteristics and reduced structural weight has encouraged the development of tailless aircraft configurations. Due to the resultant loss of directional stability and control authority, typically provided by the vertical stabilizer and the rudder, such configurations require unconventional control effector suites with multiple, highly redundant and axis-coupled control effectors. Redundant actuation systems have additional benefits, such as improved recoverability capabilities after structural damage or actuator faults in fault-tolerant flight control (FTFC) systems.

Given the inherent benefits of highly redundant control effector suites, aircraft over-actuation is an increasingly common practice in aerospace design. Over-actuated systems have more control inputs than controlled variables, and therefore an attainable control command may be achievable through multiple combinations of actuator positions. Consequently, the problem of allocating control commands to actuator deflections is underdetermined. In flight control systems (FCS), control allocation (CA) algorithms distribute control commands over the available set of control effectors, aiming to maximally exploit the maneuverability and handling qualities of the aircraft while accounting for the physical limitations of the actuators.

Most conventional CA methods operate under the assumption that a linear relationship exists between actuator positions and control-induced forces and moments. This simplification yields a very tractable affine formulation of the control allocation problem, which can be solved with efficient linear algorithms suitable for real-time implementation in FCS. However, previous research has shown that the assumption of linearity of the control effectors has important shortcomings for aircraft with large numbers of highly nonlinear and interacting control effectors (Buffington, 1997, 1999; Davidson, Lallman, & Bundick, 2001b; Bolender & Doman, 2004b; Poonamallee, Yurkovich, Serrani, Doman, & Oppenheimer, 2004).

First, linear models are unable to capture interactions between control effectors. Although such couplings are usually negligible in conventional actuator suites, more innovative configurations feature actuators positioned downstream of others, resulting in important nonlinear interactions. In some cases, such interactions can be positively exploited such as in the case of slots, which can be used to recover control effectiveness of trailing-edge control surfaces at high angles of attack (AoA). In other cases, these interactions can have negative effects on control effectiveness, such as in the case of leading-edge actuators that disturb the downstream airflow when deflected.

Second, independently-moving control surfaces produce secondary-axis yawing moments by generating drag through a lever arm with respect to the aircraft longitudinal axis. Although conventional aircraft use a rudder for directional control, tailless configurations exploit these secondary-axis moments as a principal source of directional control power. These moments can also be used in conventional actuator suites to regain directional controllability after rudder failure. Common actuators using this principle are all-moving wing tips, ailerons and elevons (Doman & Sparks, 2002; Bolender & Doman, 2004b). Whereas they produce locally linear rolling moments, they have highly nonlinear contributions to yawing moment, especially at low AoA, where parasitic drag dominates induced drag effects. Secondary-axis yawing moments are generally asymmetric parabolic functions of the actuator deflections, which cannot be captured with linear effector models. This shortcoming has two negative effects concerning control allocation. First, the yawing moments not included in the on-board aerodynamic model are seen as external disturbances by the control system, and need to be mitigated with other sources of directional control power. Second, the ability to positively exploit these sources of yawing moment is lost, which is particularly critical in tailless configurations.

Finally, although the control moment curves of conventional actuators are locally linear for small deflections, nonlinearities exist in extreme regions of their operational range. Failing to capture such nonlinearities results in model mismatch causing control allocation error, which needs to be mitigated by the robustness of the flight control laws (Doman & Oppenheimer, 2002). This is detrimental to the overall performance of the system, especially in faulty conditions where the non-faulty actuators are forced to operate within extreme regions of their moment curves.

In most conventional aircraft configurations the inaccuracies introduced by the assumption of linearity are relatively small and can be acceptably absorbed by robust control systems. However, linear control allocation fails to provide adequate performance in more advanced and innovative designs, especially in tailless aircraft, which produce directional control power mainly through secondary-axis parabolic yawing moments. A very representative example is Lockheed Martin's Innovative Control Effectors (ICE) research aircraft concept, a tailless flying wing with a highly redundant control effectors suite of 13 actuators, which produce highly nonlinear and cross-axis coupled moments and exhibit strong interactions. Nonlinear control allocation methods have been explored as a solution with a number of different approaches. Although the methods proposed to date clearly demonstrate important improvements over conventional linear approaches, nonlinear optimization algorithms are highly computationally complex and not suitable for implementation in real time.

This thesis implements and tests on a simulation framework an incremental nonlinear control allocation (INCA) method for the tailless ICE aircraft. This approach is based on a reformulation of the control allocation problem in incremental form that exploits the time scale separation principle between slow and fast dynamics. It is based on a nonlinear Jacobian model of the control effectors, which can capture actuator nonlinearities, including interactions between control effectors. An angular acceleration feedback loop reduces the model dependency of the nonlinear control system and makes it highly robust against model mismatch. The crux of this method is that it operates in an incremental scheme, which allows the nonlinear CA problem to be solved with simple and efficient linear control allocation algorithms that are well-suited for real-time implementation in FCS. Unlike most typical CA algorithms, INCA uses information of the current position of the actuators, which are dynamically driven towards their optimal positions through small increments. This mitigates the negative impact of actuator dynamics in control allocation, which has been focus of extensive research (Harkegard, 2004; Luo, Serrani, Yurkovich, Doman, & Oppenheimer, 2004; Luo, Serrani, Yurkovich, Oppenheimer, & Doman, 2007; Hanger, 2011; Johansen, 2004).

This thesis demonstrates substantial benefits of INCA in terms of tracking and control allocation performance for innovative aircraft designs with respect to linear control allocation (LCA) methods. For this, an LCA-based and an INCA-based nonlinear FCS were designed for the ICE aircraft, and their performance was evaluated through real-time simulation using the high-fidelity simulation model of the ICE aircraft described by Niestroy, Dorsett, and Markstein (2017). The simulation model includes actuator dynamics, in addition to position and rate constraints. Both LCA- and INCA-based FCS were implemented with two typical linear control allocation solvers to compare their performance.

The research objective of this thesis was to develop and implement a control allocation system that can handle aerodynamic nonlinearities and control effector interactions in unconventional control suites such as the ICE aircraft, and whose computational complexity is in the order of conventional methods well-suited for real-time implementation in FCS.

In order to pursue the research objective, the next research questions were formulated:

1. How can control commands be allocated to control effectors in an over-actuated aircraft to minimize the allocation error while taking into account the nonlinearities and interactions of the actuators?
2. Is the performance of an INCA-based FCS better than that of an LCA-based FCS for the ICE aircraft?
    - Is the tracking error over aggressive maneuvers smaller?
    - Is the allocation error over aggressive maneuvers smaller?
    - Is the control effort over aggressive maneuvers similar or smaller?
    - Can aggressive maneuvers which cannot be performed by an LCA-based FCS be performed with an INCA-based FCS?
3. Is the computational complexity of INCA higher than that of LCA-based systems with typical solvers such as the redistributed weighted pseudo-inverse and active-set based quadratic programming?
4. Is the performance of INCA influenced by the CA solver in a similar way as LCA?
    - Are the tracking and control allocation errors and the control effort significantly different when using a redistributed weighted pseudo-inverse solver or an active set-based quadratic programming solver?
    - If so, is this influence consistent with that observed for LCA?

5. How robust is INCA against control effectiveness Jacobian model mismatch?
    - How does Jacobian model offset affect tracking and allocation performance and control effort?
    - How does Jacobian model scaling affect tracking and allocation performance and control effort?

The remainder of this thesis is structured as follows. Chapter 2 provides a detailed literature review on the state-of-the-art of existing control allocation methods. In Chapter 3 the ICE aircraft and the high-fidelity model used in this thesis are described and analysed in detail, including a linear analysis of the aircraft controllability and stability. Chapter 4 provides the theoretical development and discussion of the proposed INCA method. In Chapter 5 the design of the LCA- and INCA-based FCS is discussed, including the on-board models derived for real-time use in each system. The simulations and results are presented and discussed in Chapter 6, and conclusions and final remarks are given in Chapter 7.

A scientific paper was submitted and accepted for presentation at the 2018 AIAA Guidance, Navigation, and Control Conference. It was also nominated for presentation at the Best Student Paper Award Competition. The paper will be presented the 8th-12th of January 2018 at Kissimmee, Florida. The conference paper is included in Appendix A. Additionally, a journal paper will be submitted shortly after the defence of this thesis for publication on the AIAA Journal of Guidance, Control, and Dynamics. A draft version of the journal paper is included in Appendix B[1].

---

[1] The double-spaced draft will be shortened to 35-40 pages in upcoming revisions, which corresponds to approximately 20 pages in the edited journal format for publication.

Chapter 2

Control Allocation Background

Control allocation is the process of distributing control commands over the available set of actuators given an over-actuated controlled system. A wide range of control allocation methods are available in the literature. One of the first surveys on CA algorithms is given in (Enns, 1998), which reviews the control allocation methods developed during the last century, mostly based on generalized inverses and geometric approaches. Johansen and Fossen (2013) provide a more up-to-date and complete survey, which covers more sophisticated methods, including handling nonlinearities and dynamic control allocation. Other relevant surveys such as (Oppenheimer, Doman, & Bolender, 2006, 2010), which are equally complete and up-to-date, focus on CA methods for aerospace applications.

The choice of a suitable control allocation approach is strongly application-dependent. Most real-time CA applications in aerospace control require reliable and computationally efficient algorithms that guarantee convergence and can be run on-board in digital computers with sampling frequencies in the order of 100 Hz. Bodson (2002) provides a comparative evaluation of optimization methods for CA, emphasizing on their performance in terms of computational efficiency. Page and Steinberg (2000) also compare the performance of different control allocation methods, but focus in their ability to attain commanded moments and their behaviour in closed-loop with a flight control system. Existing CA methods are reviewed and discussed in this chapter.

2.1 The Control Allocation Problem

Let the dynamics of a nonlinear system be described in the generic input-affine form

$$\dot{\mathbf{x}}(t) = \mathbf{f}(\mathbf{x}, t) + \mathbf{g}(\mathbf{x}, t)\,\mathbf{u}(t) \tag{2.1}$$

where t is time, $\mathbf{x} \in \mathbb{R}^n$ the state vector and $\mathbf{u} \in \mathbb{R}^m$ a vector of pseudo-control inputs. Here, the system dynamics are externally influenced only by the pseudo-control input $\mathbf{u}$, which usually corresponds to the control-induced forces and moments generated by the control effectors, generally given by

$$\mathbf{u}(t) = \mathbf{h}(\mathbf{x}, \boldsymbol{\delta}, t) \tag{2.2}$$

where $\boldsymbol{\delta} \in \mathbb{R}^p$ is the vector of actuator positions and $\mathbf{h}$ a generally nonlinear function. The control effectors are subject to rate and position constraints

$$\begin{aligned} \boldsymbol{\delta}_{\min} \leq \boldsymbol{\delta} \leq \boldsymbol{\delta}_{\max} \\ |\dot{\boldsymbol{\delta}}| \leq \dot{\boldsymbol{\delta}}_{\max} \end{aligned} \tag{2.3}$$

Due to computational constraints of real-time control systems, it is common to assume that actuator dynamics are much faster than the dynamics of the controlled system, such that the dynamic nonlinear function in Eq. (2.2) can be approximated at a given time step as the static mapping

$$\mathbf{u} = \mathbf{h}(\mathbf{x}, \boldsymbol{\delta}) \tag{2.4}$$

This simplification implies the assumption that actuators respond instantaneously to commands (Oppenheimer et al., 2010), which usually results in undesirable coupling effects between control allocators and actuator dynamics (Oppenheimer & Doman, 2004). Dynamic control allocation methods that account for actuator dynamics are discussed at the end of this chapter.

Static control allocation algorithms run in discrete-time computers, computing the control distribution at each time step for the current state $\mathbf{x}_0$. Thus, given a measured or estimated $\mathbf{x}_0$ at a given time step, the control effectiveness function $\mathbf{h}(\mathbf{x}, \boldsymbol{\delta})$ becomes a generally nonlinear static mapping $\mathbf{h}(\mathbf{x}_0) : \mathbb{R}^p \to \mathbb{R}^m$.

In a discrete-time system the actuator rate limits can be translated into local position limits for the current time step as

$$\Delta \boldsymbol{\delta}_{\max} = \dot{\boldsymbol{\delta}}_{\max} \Delta t \tag{2.5}$$

The effective local position limits at a given time step are

$$\underline{\boldsymbol{\delta}} \leq \boldsymbol{\delta} \leq \overline{\boldsymbol{\delta}} \tag{2.6}$$

with

$$\begin{aligned} \overline{\boldsymbol{\delta}} &= \min\left(\boldsymbol{\delta}_{\max}, \boldsymbol{\delta} + \dot{\boldsymbol{\delta}}_{\max} \Delta t\right) \\ \underline{\boldsymbol{\delta}} &= \max\left(\boldsymbol{\delta}_{\min}, \boldsymbol{\delta} - \dot{\boldsymbol{\delta}}_{\max} \Delta t\right) \end{aligned} \tag{2.7}$$

where $\overline{\boldsymbol{\delta}}$ and $\underline{\boldsymbol{\delta}}$ are the most restrictive upper and lower bounds of the position and rate constraints of the actuators at a given time step, respectively (Oppenheimer et al., 2006).

Usually, and especially in vehicle control applications, the pseudo-control inputs of the system dynamics $\mathbf{u}$ are the moments about the three main body axes, denoted $\boldsymbol{\tau} \in \mathbb{R}^3$:

$$\boldsymbol{\tau} = \mathbf{h}(\mathbf{x}, \boldsymbol{\delta}) \tag{2.8}$$

This problem is usually referred to as the three-moment problem (Durham, 1994b). The control allocation problem consists of determining the control effector positions $\boldsymbol{\delta}$ that

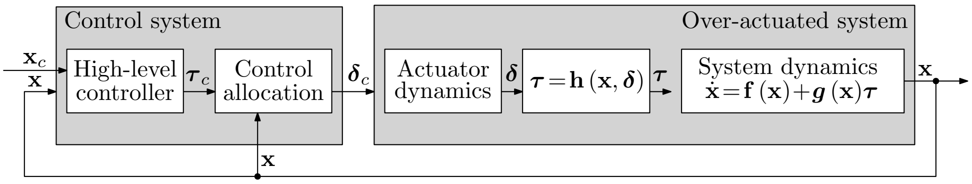

Figure 2.1: Classical control scheme for over-actuated systems.

produce a commanded moment $\boldsymbol{\tau}_c$. Over-actuated systems have more control effectors than controlled variables, i.e. $p>m$ and therefore the system of equations in Eq. (2.8) is underdetermined with $p-m$ degrees of freedom. As shown in the classical control scheme for over-actuated systems in Figure 2.1, the moment commands are typically provided by a high-level control system. Then, the CA algorithm allocates the commanded pseudo-control inputs into individual actuator positions such that the total generated moments amount to the desired $\boldsymbol{\tau}_c$.

For a given time step, the static control allocation problem is formulated as: given the current state $\mathbf{x}_0$, the control effector model $\boldsymbol{\tau} = \mathbf{h}(\mathbf{x}_0, \boldsymbol{\delta})$ and a pseudo-control command $\boldsymbol{\tau}_c$, determine a control vector $\boldsymbol{\delta}$ such that

$$\begin{aligned} \mathbf{h}(\mathbf{x}_0, \boldsymbol{\delta}) &= \boldsymbol{\tau}_c \\ \text{subject to} \quad \underline{\boldsymbol{\delta}} \leq \boldsymbol{\delta} &\leq \overline{\boldsymbol{\delta}} \end{aligned} \tag{2.9}$$

Note that the inverse problem of computing $\boldsymbol{\delta}$ given $\boldsymbol{\tau}_c$ is ill-posed and generally its solution is not unique. A wide variety of approaches are available to solve the CA problem, depending on the assumptions made. Figure 2.2 provides a broad classification of existing methods. These methods are discussed in detail in the following sections.

2.2 Linear Control Allocation

Most commonly used CA methods are based on the assumption that a linear relationship exists between control effector positions and control-induced moments, i.e. that $\mathbf{h}(\mathbf{x}, \boldsymbol{\delta})$ is linear in the control inputs. Thus, the control-induced moments can be expressed using a control effectiveness matrix $B(\mathbf{x}) \in \mathbb{R}^{m \times p}$ in the form

$$\boldsymbol{\tau} = \mathbf{h}(\mathbf{x}, \boldsymbol{\delta}) = B(\mathbf{x})\,\boldsymbol{\delta} \tag{2.10}$$

Since the control allocation problem is solved statically at every time step, the control effectiveness matrix is scheduled for the current state $\mathbf{x}_0$ without regard as how it will change over time (Johansen & Fossen, 2013). For simplicity, the instantaneous control effectiveness matrix $B(\mathbf{x}_0)$ will be referred to as simply B in the remainder. The effects of scheduling the control effectiveness matrix are discussed in (Hodel, 2000).

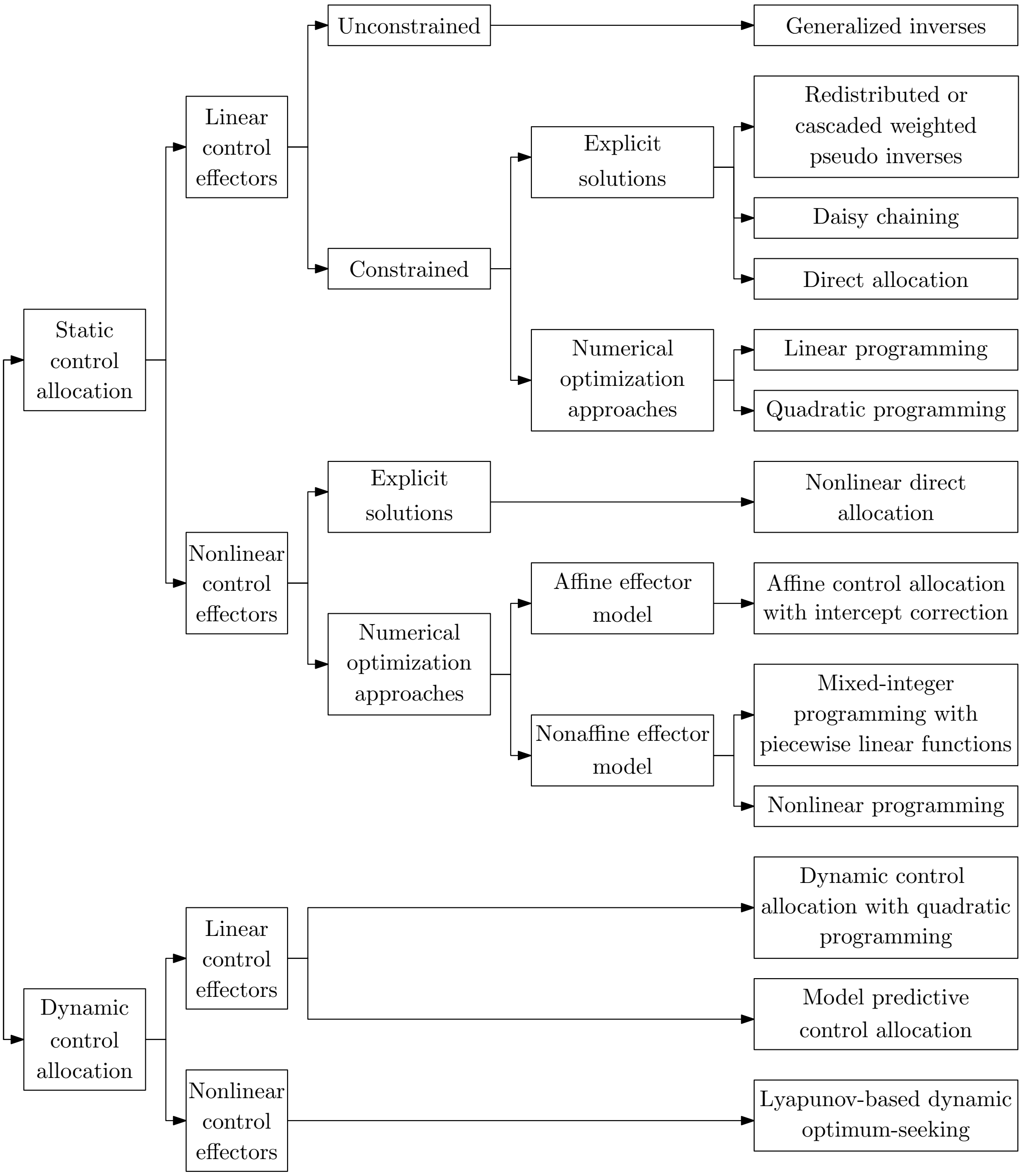

Figure 2.2: General classification of control allocation methods.

The assumption of linearity is valid when the control effectors are placed separate enough such that interactions are negligible, and as long as the actuators operate within the linear region of their operational range, i.e. far from their position limits. Although this assumption neglects nonlinearities and interactions of the control effectors, it greatly facilitates the manipulation of the control effector equations either to find explicit solutions to the unconstrained LCA problem or to apply efficient numerical optimization-based solution methods with explicit constraints. The applicability of computationally efficient linear solvers makes LCA approaches highly suitable for real-time CA systems.

2.2.1 Generalized Pseudo-Inverses

An explicit solution can be found by solving the unconstrained LCA problem. When the actuator position and rate limits are removed, the LCA problem can be posed as the ℓ_2-norm minimization problem

$$\begin{aligned} \min_{\boldsymbol{\delta}} \quad & \mathcal{J} = \frac{1}{2}(\boldsymbol{\delta} - \boldsymbol{\delta}_p)^T W_{\boldsymbol{\delta}} (\boldsymbol{\delta} - \boldsymbol{\delta}_p) \\ \text{subject to} \quad & B\boldsymbol{\delta} = \boldsymbol{\tau}_c \end{aligned} \tag{2.11}$$

where $\boldsymbol{\delta}_p \in \mathbb{R}^p$ is a vector of preferred actuator positions (usually $\boldsymbol{\delta}_p = 0$ to minimize control effort), and $W_{\boldsymbol{\delta}}$ is nonsingular weighting matrix that establishes preferences on using some control effectors over others. If BB^T is full-rank, the unconstrained problem has the explicit solution

$$\boldsymbol{\delta} = \boldsymbol{\delta}_p + B^{\sharp}\left(\boldsymbol{\tau}_c - B\boldsymbol{\delta}_p\right) \tag{2.12}$$

with

$$B^{\sharp} = W_{\boldsymbol{\delta}}^{-1} B^T \left(B W_{\boldsymbol{\delta}}^{-1} B^T\right)^{-1} \tag{2.13}$$

a generalized weighted pseudo-inverse. This solution is derived in (Enns, 1998) and (Oppenheimer et al., 2006) by applying Lagrange multipliers to the minimization problem with equality constraints in (2.11).

Note that when no preferences are assigned to control effectors ($W_{\boldsymbol{\delta}} = I$), and the preferred actuator deflections are zero ($\boldsymbol{\delta}_p = 0$), the solution is given by the Moore-Penrose pseudo-inverse:

$$\boldsymbol{\delta} = B^{+}\boldsymbol{\tau}_c = B^T(BB^T)^{-1}\boldsymbol{\tau}_c \tag{2.14}$$

This method provides a solution to the unconstrained problem as long as it exists and BB^T is not rank-deficient[1].

The main drawbacks of the pseudo-inverse method are that it does not guarantee that the actuator position and rate constraints are met, and does not take into account secondary objectives. The most straightforward solution to the constrained problem is simple saturation (or clipping) of the unconstrained solution. However, if each actuator command is clipped individually to its corresponding limit, the direction of the desired moment is not kept. If all commands are scaled down by a common factor, then the direction of the moment command is preserved. The performances of different command clipping strategies for the pseudo-inverse method are evaluated in (Page & Steinberg, 2000). Despite the simplicity of the method, Durham (1993) concluded that no generalized inverse can yield exact allocation whenever possible using simple saturation (Johansen & Fossen, 2013).

2.2.2 Redistributed Weighted Pseudo-Inverse

The redistributed weighted pseudo-inverse (RWPI), also called cascaded generalized inverse, is an iterative method that uses the generalized weighted pseudo-inverse method to find a solution that meets actuator constraints, if it exists. First, the unconstrained explicit solution is computed with the weighted pseudo-inverse in Eq. (2.12). If the found

---

[1] Control suites for mechanical systems usually avoid control effector deficiencies by design.

control distribution $\boldsymbol{\delta}$ is within the local actuator limits, the solution is kept. Otherwise, if one or more effectors violate constraints, the next steps are followed. First, the columns in B corresponding to the saturated actuators are zeroed, forming an auxiliary matrix B_{sat}. Second, the values of the saturated effectors are placed in the preference vector $\boldsymbol{\delta}_p$, forming an auxiliary preference vector $\boldsymbol{\delta}_{p,\text{sat}}$. Then, the RWPI solution is re-computed as follows:

$$\boldsymbol{\delta} = \boldsymbol{\delta}_{p,\text{sat}} + B_{\text{sat}}^{\sharp} \left(\boldsymbol{\tau}_c - B\boldsymbol{\delta}_{p,\text{sat}}\right) \tag{2.15}$$

This process is repeated until all effectors are saturated or a solution within the local actuator limits is found.

Bodson (2002) and Ducard (2009) reported results showing that the RWPI method can yield suboptimal solutions. Additionally, Johansen and Fossen (2013) claim that the method does not guarantee convergence to a feasible solution, even if it exists. These conclusions were also reached by Harkegard (2002). In spite of its shortcomings, the RWPI method is very efficient and reliable, so it is a very popular solution for real-time control allocation in safety-critical systems, see (Eberhardt & Ward, 1999; Davidson, Lallman, & Bundick, 2001a; Davidson et al., 2001b; Shtessel, Buffington, & Banda, 2002; Alwi & Edwards, 2006; T. J. J. Lombaerts, Looye, Chu, & Mulder, 2012).

2.2.3 Daisy Chaining

The daisy chaining method was first presented and evaluated by Buffington and Enns (1996). It establishes a hierarchy for the use of control effectors over certain axes. In order to achieve a certain command, the first effector in the hierarchy is deflected until the desired moment is attained or the actuator saturates. If saturation occurs before the command is achieved, then the error between the allocated and the required moments is allocated to the next effector in the hierarchy. The process is repeated until a feasible solution is found or all actuators are saturated. For more extensive discussion on this method, see (Buffington & Enns, 1996; Oppenheimer et al., 2010).

Due to the existence of a hierarchy, the solutions produced by daisy chaining may not exploit the full control power of certain effectors to reduce the allocation error. This leads to suboptimal solutions in comparison with RWPI (Johansen & Fossen, 2013).

2.2.4 Direct Allocation

Direct allocation (DA) is a control allocation method based on geometric principles, and has the property of preserving the direction of the commanded moments (Page & Steinberg, 2000). The original DA algorithm was developed by Durham (1993, 1994b).

Let the attainable moments set (AMS) be the subset $\mathbb{A} \subset \boldsymbol{\tau}_c \in \mathbb{R}^m$ of commanded moments for which the constrained CA problem has at least one feasible solution. For linear control effectors with control effectiveness function in the form of Eq. (2.10), the AMS is a convex hull with planar surfaces (Oppenheimer et al., 2006). The direct allocation algorithm operates as follows. First, the pseudo-inverse solution is computed. If $\boldsymbol{\delta}$ satisfies the position and rate constraints, the solution is kept. Otherwise, the solution is projected into the boundary of $\mathbb{A}$ by preserving the direction of the desired moment. This is achieved by finding a scaling factor $\rho \in [0,\ 1]$ that satisfies

$$\begin{aligned} &\max_{\rho \leq 1} \quad \rho \\ &\text{subject to} \quad B\boldsymbol{\delta} = \rho\boldsymbol{\tau}_c, \quad \rho\boldsymbol{\tau}_c \in \mathbb{A} \end{aligned} \tag{2.16}$$

Solving Eq. (2.16) is not trivial, especially in problems with a large number of actuators. Durham (1994a) proposed a method to compute the AMS for the three-moment problem. Numerical algorithms with different complexities have been proposed to solve the DA problem (Johansen & Fossen, 2013).

This approach has been extensively addressed and improved by Durham and other authors, see (Durham, 1999, 2001; Bordignon, 1996; Bodson, 2002). Moreover, the method is generalizable to problems with nonlinear constraints, provided that the AMS can be computed. Nonlinear direct allocation will be discussed later in this chapter.

As stated by Durham (2001), the AMS changes with the state of the aircraft and therefore must be re-computed at every time step, which is too computationally complex to be suitable for real-time applications when the number of control effectors is large.

2.2.5 Numerical Optimization-Based Approaches

Three types of outcomes can be expected from a CA problem: either the solution does not exist (the command is unattainable), exactly one solution exists, or there are infinite solutions. In the first case, it is desirable to obtain the solution that provides the minimum error between the commanded and allocated moments. In the latter case, a solution may be chosen according to the fulfillment of a secondary objective. Given this situation, control allocation can be formulated as an optimization problem with primary and secondary objectives.

The primary objective of the CA problem is to minimize the control allocation error, i.e. the difference between the required and the allocated moments. This is generally referred to as the *error minimization problem*, and can be posed as follows: given a command $\boldsymbol{\tau}_c$ and a control effectiveness matrix B, find $\boldsymbol{\delta}$ such that

$$\begin{aligned} &\min_{\boldsymbol{\delta}} \quad \mathcal{J} = ||B\boldsymbol{\delta} - \boldsymbol{\tau}_c|| \\ &\text{subject to} \quad \underline{\boldsymbol{\delta}} \leq \boldsymbol{\delta} \leq \overline{\boldsymbol{\delta}} \end{aligned} \tag{2.17}$$

Where $||\cdot||$ is some norm that will determine the numerical optimization algorithm required to solve the problem.

When there is sufficient control authority to attain the command, i.e. $\mathcal{J} = 0$, one or infinite solutions exist. In the latter case, a secondary objective may be minimized to select a preferred solution. The most common approach is to minimize the actuator deflections with respect to a preferred position $\boldsymbol{\delta}_p$. This is often referred to as the *control minimization problem* (Bodson, 2002; Harkegard, 2002; Oppenheimer et al., 2006), and is posed as follows: given a command $\boldsymbol{\tau}_c$ and an effectiveness matrix B, find $\boldsymbol{\delta}$ such that

$$\begin{aligned} &\min_{\boldsymbol{\delta}} \quad \mathcal{J} = ||\boldsymbol{\delta} - \boldsymbol{\delta}_p|| \\ &\text{subject to} \quad B\boldsymbol{\delta} = \boldsymbol{\tau}_c \end{aligned} \tag{2.18}$$

The objective achieved depends on the choice of $\boldsymbol{\delta}_p$. Typical secondary objectives are minimum control deflection, minimum wing loading, minimum drag or minimum actuator power (Oppenheimer et al., 2010). For further discussion on secondary objectives, see (Buffington, 1999). A popular secondary objective is minimizing the control effort, which is achieved by setting $\boldsymbol{\delta}_p = 0$. It guarantees that, whenever a command has multiple solutions, the actuators will remain as close to their neutral positions as possible. This mitigates counterbalancing effects, i.e. diverging deflections of effectors that produce opposite moments of equal magnitude.

It is also possible to combine primary and secondary objectives in a single cost function to formulate a *mixed optimization problem* (Bodson, 2002). It is posed as: given a command $\boldsymbol{\tau}_c$ and an effectiveness matrix B, find $\boldsymbol{\delta}$ such that

$$\begin{aligned} \min_{\boldsymbol{\delta}} \ \ & \mathcal{J} = W_{\boldsymbol{\tau}} \left|\left| B\boldsymbol{\delta} - \boldsymbol{\tau}_c \right|\right| + \epsilon W_{\boldsymbol{\delta}} \left|\left| \boldsymbol{\delta} - \boldsymbol{\delta}_p \right|\right| \\ \text{subject to} \ \ & \underline{\boldsymbol{\delta}} \leq \boldsymbol{\delta} \leq \overline{\boldsymbol{\delta}} \end{aligned} \tag{2.19}$$

where $W_{\boldsymbol{\tau}}$ and $W_{\boldsymbol{\delta}}$ are nonsingular weighting matrices and ϵ is a scalar, selected sufficiently small to prioritize error minimization over the secondary objective.

The minimization problems described above can be solved with linear numerical optimization algorithms. The kind of suitable algorithms depends on the norm used to define the cost function of the problem. Below the most common numerical optimization algorithms used in optimization-based CA are discussed.

Linear Programming

If an ℓ_1 norm is chosen, the optimization problem can be formulated as a linear program. The linear programming (LP) approach was used for multi-branch control allocation in (Enns, 1998; Buffington, 1999). The first publications on LP-based control allocators are (Paradiso, 1989, 1991). The linear program is posed as:

$$\begin{aligned} \min_{\boldsymbol{\delta}} \ \ & \mathcal{J} = W_{\boldsymbol{\tau}} \boldsymbol{\delta}_s \\ \text{subject to} \ \ & \begin{bmatrix} \boldsymbol{\delta}_s \\ -\boldsymbol{\delta} \\ \boldsymbol{\delta} \\ -B\boldsymbol{\delta} + \boldsymbol{\delta}_s \\ B\boldsymbol{\delta} + \boldsymbol{\delta}_s \end{bmatrix} \geq \begin{bmatrix} 0 \\ -\overline{\boldsymbol{\delta}} \\ \underline{\boldsymbol{\delta}} \\ -\boldsymbol{\tau}_c \\ \boldsymbol{\tau}_c \end{bmatrix} \end{aligned} \tag{2.20}$$

where $\boldsymbol{\delta}_s \in \mathbb{R}^p$ is a vector of slack variables. If $\mathcal{J} > 0$ the required moment is unattainable, and the solution found is that which minimizes the weighted ℓ_1 norm distance between the allocated and the commanded moments (Page & Steinberg, 2000). When $\mathcal{J} = 0$, the secondary objective is minimized as the linear program:

$$\begin{aligned} \min_{\boldsymbol{\delta}} \ \ & \mathcal{J} = W_{\boldsymbol{\delta}} \boldsymbol{\delta}_s \\ \text{subject to} \ \ & \begin{bmatrix} \boldsymbol{\delta}_s \\ -\boldsymbol{\delta} \\ \boldsymbol{\delta} \\ -\boldsymbol{\delta} + \boldsymbol{\delta}_s \\ \boldsymbol{\delta} + \boldsymbol{\delta}_s \end{bmatrix} \geq \begin{bmatrix} 0 \\ -\overline{\boldsymbol{\delta}} \\ \underline{\boldsymbol{\delta}} \\ -\boldsymbol{\delta}_p \\ \boldsymbol{\delta}_p \end{bmatrix}, \quad B\boldsymbol{\delta} = \boldsymbol{\tau}_c \end{aligned} \tag{2.21}$$

Note that other control allocation formulations can also be solved with LP. For instance, Bodson (2002) reformulated the direct allocation and the mixed optimization problems into linear programs.

Several numerical methods are available to solve the LP problem. The most common are the simplex method (Bodson, 2002), active set methods (Harkegard, 2002) and interior-point methods (Petersen & Bodson, 2005, 2006). Although the simplex method tends to converge to the optimal solution within a number of iterations not bigger than the number of variables and constraints, a maximum number of iterations is hard to guarantee (Johansen & Fossen, 2013). Thus, since in real-time applications a limit for iterations must be set, some degree of suboptimality needs to be assumed. Possible degeneracies of the simplex algorithm for control allocation are addressed in (Bodson, 2002).

Interior-point algorithms were proposed in (Petersen & Bodson, 2005) for ℓ_1-norm mixed optimization problems and direct allocation, both formulated as linear programs. The authors concluded that, despite being slower than the simplex method, interior-point methods progress uniformly toward the optimum, which makes them more suitable in real-time applications where the number of iterations per time step is limited.

As discussed in (Bodson, 2002), LP-based solutions with the ℓ_1 norm tend to exploit a smaller number of effectors. On the other hand, solutions found with ℓ_2 norm and ℓ_∞ norm tend to allocate the control demand to a larger number of effectors, distributing the control effort. This is one of the reasons why quadratic programming approaches are more popular (Johansen & Fossen, 2013).

Quadratic Programming

When the optimization problem is defined with an ℓ_2 norm, several possibilities arise. Enns (1998) proposes some approaches with different complexities. First of all, note that when the problem is formulated with an ℓ_2 norm and the position and rate constraints are removed, the explicit pseudo-inverse solution in Eqs. (2.11)-(2.14) is obtained.

One of the simplest approaches for the error minimization problem with ℓ_2 norm is as follows. First, find the explicit solution of the unconstrained problem

$$\min_{\boldsymbol{\delta}} \ \mathcal{J} = ||B\boldsymbol{\delta} - \boldsymbol{\tau}_c||_2 \tag{2.22}$$

with the pseudo-inverse method. If $\boldsymbol{\delta}$ does not satisfy the position and rate limits, then find the optimal solution by adding the equality constraint

$$||\boldsymbol{\delta}||_2 = p \tag{2.23}$$

with $p \in \mathbb{R}^p$. To determine the equality constraint in Eq. (2.23), first an affine transformation of the inequality constraints $\underline{\boldsymbol{\delta}} \leq \boldsymbol{\delta} \leq \overline{\boldsymbol{\delta}}$ into a single equality constraint $||\boldsymbol{\delta}||_\infty = 1$ is required. The latter is an ℓ_∞ box constraint that can be approximated with the ℓ_2 equality constraint $||\boldsymbol{\delta}||_2 = p$ (Bodson, 2002). In the 2-dimensional case, $||\boldsymbol{\delta}||_2 = p$ can be seen as an elliptical constraint, whose p is selected such that it adjusts to the rectangular region enclosed by the equality constraints, see Figure 3 in (Enns, 1998).

The explicit solution to the problem with equality constraint, as derived in (Enns, 1998) with Lagrange multipliers, is given by

$$\boldsymbol{\delta} = B^T \left(BB^T + \lambda I\right)^{-1} \boldsymbol{\tau}_c \tag{2.24}$$

which is similar to the Moore-Penrose pseudo-inverse solution except for the Lagrange multiplier λ, which can be found by solving the equation

$$\gamma(\lambda) = \left|\left|B^T \left(BB^T + \lambda I\right)^{-1} \boldsymbol{\tau}_c\right|\right|_2 = p \tag{2.25}$$

Bodson (2002) proposes the bisection method as a suitable and efficient solver for Eq. (2.25), given the fact that $\gamma(\lambda)$ turns out to be a monotonically decreasing function. According to the analysis given in (Bodson, 2002), despite being computationally simple, this method may yield not exact solutions as a consequence of the approximation of the ℓ_∞ by an ℓ_2 constraint. Therefore command clipping needs to be applied to meet the actual constraints, which usually yields suboptimal solutions.

A more common approach when using the ℓ_2 norm is to formulate the constrained mixed optimization problem (2.19) as a quadratic program (Petersen & Bodson, 2006). The ℓ_2 formulation of the problem is

$$\begin{aligned} \min_{\boldsymbol{\delta}} \;\; & \mathcal{J} = \left|\left|B\boldsymbol{\delta} - \boldsymbol{\tau}_c\right|\right|_2 + \epsilon \left|\left|\boldsymbol{\delta} - \boldsymbol{\delta}_p\right|\right|_2 \\ \text{subject to} \;\; & \underline{\boldsymbol{\delta}} \leq \boldsymbol{\delta} \leq \overline{\boldsymbol{\delta}} \end{aligned} \tag{2.26}$$

As developed in (Petersen & Bodson, 2006), this problem can be rewritten as a standard quadratic program as follows. Let the constraints be rewritten as

$$\mathbf{z} = \boldsymbol{\delta} - \underline{\boldsymbol{\delta}}, \qquad \mathbf{z}_p = \boldsymbol{\delta}_p - \underline{\boldsymbol{\delta}} \tag{2.27}$$

$$\mathbf{z}_{\max} = \overline{\boldsymbol{\delta}} - \underline{\boldsymbol{\delta}}, \qquad \boldsymbol{\tau}_0 = \boldsymbol{\tau}_c - B\underline{\boldsymbol{\delta}} \tag{2.28}$$

Then, the resulting constraints set is

$$\mathbf{z} + \mathbf{z}_s = \mathbf{z}_{\max}, \quad \mathbf{z} \geq 0, \quad \mathbf{z}_s \geq 0 \tag{2.29}$$

where $\mathbf{z}_s$ is a slack variable that guarantees the upper bound of $\mathbf{z}$. The quadratic programming (QP) problem is then formulated as

$$\begin{aligned} \min_{\boldsymbol{\delta}} \;\; & \mathcal{J} = \frac{1}{2}\mathbf{z}^T Q_1 \mathbf{z} + Q_2^T \mathbf{z} \\ \text{subject to} \;\; & \mathbf{z} + \mathbf{z}_s = \mathbf{z}_{\max}, \quad \mathbf{z} \geq 0, \quad \mathbf{z}_s \geq 0 \end{aligned} \tag{2.30}$$

with

$$Q_1 = 2\left(B^T B + \epsilon I\right) \tag{2.31}$$

$$Q_2^T = -2\left(\boldsymbol{\tau}_0^T B + \epsilon \mathbf{z}_p^T\right) \tag{2.32}$$

Many numerical algorithms are available to solve the QP problem. The most common are fixed-point methods, active set methods and interior-point methods.

The fixed-point method is an iterative algorithm, which was used in (Burken, Lu, & Wu, 1999; Burken, Lu, Wu, & Bahm, 2001) to solve the mixed optimization problem in Eq. (2.30). This algorithm was assessed by Lu (1996), who proved its global convergence. However, as claimed by Petersen and Bodson (2006), its convergence tends to be slow for large commands, and therefore it is usually implemented with limited iterations (Harkegard, 2002; Bodson, 2002).

Active set methods were proposed by Harkegard (2002) to solve both LP and QP control allocation problems in aircraft control. The optimal active set is defined as the set of constraints that are active (i.e. the equality relation holds) at the optimal solution. Active set methods are iterative algorithms which improve their guess of the optimal active set at each iteration.

In addition to LP, interior-point algorithms were proposed to solve QP problems in (Petersen & Bodson, 2005, 2006). In the latter publication, the authors concluded that the active set algorithm converges exactly to the solution in a finite number of steps and is computationally efficient for control allocation problems of small size, whereas interior-point algorithms perform better in control allocation problems with a larger number of control effectors, despite requiring more computations.

2.3 Nonlinear Control Allocation

As already seen, most existing control allocation methods work under the assumption that a linear relationship exists between control-induced moments and control effector positions. Although the expression derived from this assumption results very tractable for the inverse problem of control allocation, forces and moments produced by aircraft control surfaces are almost always nonlinear functions of their displacements (Bolender & Doman, 2004b). This is particularly true for large displacements, when the effectors operate at extreme regions of the control effectiveness curve. When the linearity assumption fails, the resulting control allocation errors need to be mitigated by the robustness of the feedback control laws (Poonamallee et al., 2004).

Although linear effector models are usually valid for aircraft with conventional actuator suites under nominal flight conditions, there are situations when the error due to nonlinearities in the control moment curves becomes especially relevant. For instance, in case of failure events the operative actuators are forced to operate in highly nonlinear regions of the control effectiveness curve, close to their position limits. In such situations, the linear approximation may not be sufficiently accurate for the vehicle to be safely recovered (Bolender & Doman, 2004b).

In conventional configurations of control effectors, where the actuators are placed far enough from each other to avoid interactions, the control effector model can be assumed affine in the actuator displacements. However, when more control effectors are placed on a vehicle, the probability of interactions between control effectors increases (Oppenheimer & Doman, 2007). In certain situations interaction effects become particularly relevant, especially in configurations where some actuators are placed downstream of others. This was noticed by Oppenheimer and Doman (2007), who proposed a method to correct for control effector interactions. This method only applies to interactions between two control effectors when they can be described by a bilinear function.

Certain control effectors have nonlinear moment contributions that cannot be captured with an affine relationship. Common examples given in (Doman & Sparks, 2002; Bolender & Doman, 2004b) are the contributions to yawing moment of right-left pairs of effectors such as all-moving wing tips, ailerons and elevons with asymmetric deflections. While such effectors produce locally linear rolling moments, they have highly nonlinear contributions to yawing moment, especially at low angles of attack where parasitic drag dominates induced drag effects (Doman & Sparks, 2002). Such contributions are usually quadratic, and have the same direction for positive and negative deflections. Although these effects are relatively small compared to their primary-axis contributions, they become important in order to attain directional control under rudder failure or when the aircraft operates at high AoA and the flow over the rudder is interrupted by the airframe body (Doman & Sparks, 2002).

Finally, the linear effector assumption can yield suboptimal control allocation solutions in situations where beneficial use can be made of the nonlinear effects of the actuators. This possibility was noticed by Oppenheimer et al. (2010), who state that fully exploiting the effector suite of the aircraft to further improve control allocation accuracy requires benefiting from its nonlinearities. Bolender and Doman (2004a) give some examples. The latter authors also suggested other interesting applications of nonlinear control allocation, such as the determination of constraints for use with trajectory reshaping algorithms (Schierman, Hull, & Ward, 2003).

All these reasons have encouraged research effort in the last decade to emphasize on the development of suitable nonlinear control allocation algorithms that can be utilized in real-time applications. Below the most relevant developments are discussed.

2.3.1 Nonlinear Direct Allocation

One of the first attempts to develop algorithms for nonlinear control allocation was presented by Doman and Sparks (2002) as an extension for the direct allocation algorithm proposed by Durham (1993). The method proposed consists on the computation of nonlinear AMS such that the direct allocation algorithm can be implemented. However, as stated by Oppenheimer et al. (2006), the construction of the AMS for a nonlinear problem can become extremely difficult. Since the AMS needs to be re-computed in each time step, this solution is too computationally complex to be suitable for real-time applications.

2.3.2 Affine Control Allocation with Intercept Correction

Since most control allocation algorithms assume an affine relationship between control effectors and control-induced moments, keeping this structure can be beneficial. Doman and Oppenheimer (2002) suggest using an additional intercept term in the affine effector model to correct for local errors in the slope of the control moment curve. Figure 2.3 shows a typical control moment curve. In a linear control allocation scheme, at every time step one may find a B matrix at the current opreating point such that $\mathbf{h}(\mathbf{x}_0, \boldsymbol{\delta}) = B\boldsymbol{\delta}$. However, the individual control effectiveness terms, i.e. the slopes of $\mathbf{h}(\mathbf{x}_0, \boldsymbol{\delta})$ in the directions of $\boldsymbol{\delta}$ will be inaccurate due to nonlinearities. This is due to the fact that, given the linear formulation, global slopes are used. In order to enforce the condition $\mathbf{h}(\mathbf{x}_0, \boldsymbol{\delta}) = B\boldsymbol{\delta}$,

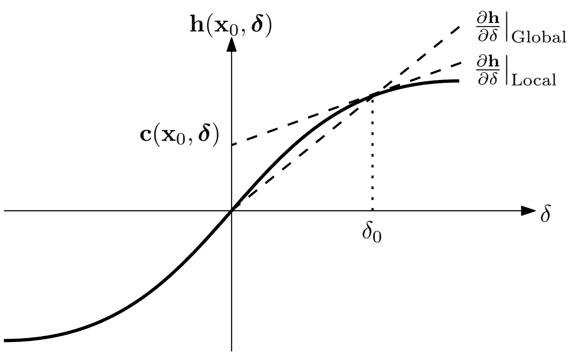

Figure 2.3: One-dimensional representation of a typical control moment curve.

an error is assumed between global and local slopes, depicted by the difference in the slopes of the dashed lines in Figure 2.3. This mismatch in control effectiveness terms often results in control allocation error when linear control effectors are assumed.

Doman and Oppenheimer (2002) proposed adding an intercept term $\mathbf{c}(\mathbf{x}, \boldsymbol{\delta})$ in the definition of the pseudo-control commands $\boldsymbol{\tau}_c$ to adjust to the local slope. The linear control effector model can be reformulated as an affine model with intercept correction as

$$\boldsymbol{\tau}_c = \mathbf{h}(\mathbf{x}, \boldsymbol{\delta}) = B\boldsymbol{\delta} + \mathbf{c}(\mathbf{x}, \boldsymbol{\delta}) \tag{2.33}$$

The addition of the intercept term corrects the error in effectiveness resulting from approximating local slopes as global slopes. Aerodynamic databases can be used to compute the slopes and intercepts of the affine control effector model. Then, the control allocation problem can be reformulated for a new pseudo-control command

$$\boldsymbol{\tau}'_c = \boldsymbol{\tau}_c - \mathbf{c}(\mathbf{x}, \boldsymbol{\delta}) = B\boldsymbol{\delta} \tag{2.34}$$

Now, any linear control allocation method can be applied to solve the problem for $\boldsymbol{\tau}'_c$.

As shown in (Bolender & Doman, 2004b) and (Poonamallee et al., 2004), the method performs well in regions where the linear behavior is dominant with monotonic moment deflection relationships, but performs poorly when nonlinearities become significant. Moreover, the affine control effector model may not be applicable in cases where the control-induced moments are quadratic, have non-monotonic behaviour, or when the effectiveness of the control surfaces becomes small, i.e. the slope approaches to zero. It also does not consider interactions between control effectors. Despite these limitations, the results presented in (Doman & Oppenheimer, 2002) show significant improvements in body rate tracking performance with respect to linear effector models. This demonstrates the potential benefits of nonlinear control allocation.

2.3.3 Mixed-Integer Programming with Piecewise Linear Functions

Typically, aerodynamic databases are discrete-valued multidimensional lookup tables. The method proposed in (Bolender & Doman, 2004b) takes advantage of this structure and connects the data points in the aerodynamic database with piecewise linear (PWL) functions. The resulting control effectors model is a set of PWL. Then, the control allocation problem can be posed as a piecewise linear program, a type of formulation that approximates nonlinear programming problems that are comprised by separable functions. This formulation of the problem can account for nonlinearities in the control moment curves, but it assumes that the PWL are separable, i.e. interactions between control effectors are neglected.

The control allocation problem is solved by formulating PWL programs for the ℓ_1 norm error minimization and control minimization problems in Eqs. (2.17) and (2.18), each of which can be considered an approximation of a nonlinear programming problem. These PWL programs are then transformed and solved as a mixed-integer linear program (MILP) with a branch-and-bound algorithm. The resulting MILP is substantially more complex and difficult to solve than a regular LP problem.

Bolender and Doman (2004b) compared the performance of an affine control allocator with intercept correction proposed in (Doman & Oppenheimer, 2002) to a PWL-based control allocator under a failure event, where secondary nonlinear effects must be used to control the vehicle and the actuators are forced to operate in the extreme region of the control moment curves. Poor performance was observed for the affine control allocator with intercept correction, which did not manage to recover the aircraft. The PWL-based control allocator, however, managed to maintain control and land the aircraft after actuator failure.

Despite the proven benefits of the proposed method, Bolender and Doman (2004b) point out that this algorithm is extremely slow due to its computational complexity, which makes it not suitable for real-time applications. Therefore, this work is a proof of the potential benefits of nonlinear control allocation, rather than a suitable proposal for real-time implementation with nowadays digital computers.

2.3.4 Nonlinear Programming

The existing solution that yields the most direct consideration of nonlinearities of the control effectors is the formulation of the CA problem as a nonlinear program. The ℓ_2 norm mixed optimization CA problem can be generally formulated as a nonlinear programming (NP) problem as follows: given a command $\boldsymbol{\tau}_c$ and an operating point $\mathbf{x}_0$, find $\boldsymbol{\delta}$ such that

$$\begin{aligned} \min_{\boldsymbol{\delta}} \quad & \mathcal{J} = ||\mathbf{h}(\mathbf{x}_0, \boldsymbol{\delta}) - \boldsymbol{\tau}_c||_2 + \epsilon \, ||\boldsymbol{\delta} - \boldsymbol{\delta}_p||_2 \\ \text{subject to} \quad & \underline{\boldsymbol{\delta}} \leq \boldsymbol{\delta} \leq \overline{\boldsymbol{\delta}} \end{aligned} \tag{2.35}$$

with $\mathbf{h}(\mathbf{x}_0, \boldsymbol{\delta})$ a generally nonlinear nonconvex control effector model. Different possibilities have been explored in the literature to solve the nonlinear program, such as sequential quadratic programming (SQP), the Gauss-Newton algorithm and the Levenberg-Marquardt (LM) algorithm.

SQP is a popular approach, which has been used in (Poonamallee et al., 2004; Johansen, Fossen, & Berge, 2004; Luo et al., 2007). Since nonconvex optimization requires a large number of iterations at each time step, Johansen et al. (2004) suggested a reformulation of the nonlinear program as a locally convex quadratic program. This is achieved by local first-order linearization of the effector model at each time step:

$$\mathbf{h}(\mathbf{x},\boldsymbol{\delta}) = \mathbf{h}(\mathbf{x}_0,\boldsymbol{\delta}_0) + \left.\frac{\partial \mathbf{h}(\mathbf{x},\boldsymbol{\delta})}{\partial \boldsymbol{\delta}}\right|_{\substack{\boldsymbol{\delta}=\boldsymbol{\delta}_0\\ \mathbf{x}=\mathbf{x}_0}} (\boldsymbol{\delta}-\boldsymbol{\delta}_0) \tag{2.36}$$

which yields the convex nonlinear quadratic program

$$\begin{aligned} \min_{\boldsymbol{\delta}} \ \mathcal{J} = \left|\left| \mathbf{h}(\mathbf{x}_0,\boldsymbol{\delta}_0) + \left.\frac{\partial \mathbf{h}(\mathbf{x},\boldsymbol{\delta})}{\partial \boldsymbol{\delta}}\right|_{\substack{\boldsymbol{\delta}=\boldsymbol{\delta}_0\\ \mathbf{x}=\mathbf{x}_0}} (\boldsymbol{\delta}-\boldsymbol{\delta}_0) - \boldsymbol{\tau}_c \right|\right|_2 + \epsilon\,||\boldsymbol{\delta}-\boldsymbol{\delta}_p||_2 \\ \text{subject to} \quad \underline{\boldsymbol{\delta}} \leq \boldsymbol{\delta} \leq \overline{\boldsymbol{\delta}} \end{aligned} \tag{2.37}$$

Note that SQP may converge to local minima of $\mathcal{J}$. However, as long as the optimal control allocation solutions are within the neighbourhood of the current state, this is not regarded as a significant problem.

The applicability of the Gauss-Newton algorithm to solve the NP problem was discussed in (Tol, De Visser, Van Kampen, & Chu, 2014). Although it shows good convergence when the initial solution is in the neighbourhood of the optimal solution, its convergence performance is poor otherwise.

The Levenberg-Marquardt algorithm (Marquardt, 1963) was applied to solve the NP problem in (Tol et al., 2014). This method overcomes the problem of global convergence and increases robustness by adaptively varying between the Gauss-Newton search direction and the steepest descent search direction. However, a remarkable drawback of the LM algorithm is that it does not take into account actuator limits during the optimization process. A possible solution for this issue is to impose a barrier function in the objective function (Johansen, 2004). In the case of flight control, optimal solutions are usually close to the boundaries of the solution space, especially in the event of actuator failures. For this reason, adding a barrier function can be detrimental to the performance of the algorithm. A possible workaround is simple clipping of the controls that exceed their position limits.

All the methods presented above are considered not suitable for real-time applications in safety-critical systems. First, their computational complexity is too high to render acceptable solutions when running in rates typical of on-board computers (i.e. in the order of 100 Hz). Second, their convergence is not always guaranteed. However, in all cases nonlinear control allocation demonstrated a dramatic improvement of the control performance and recoverability in case of failure events with respect to linear solutions.

2.4 Dynamic Control Allocation

Oppenheimer and Doman (2004) noticed that neglecting actuator dynamics may result in negative coupling effects between control allocators and actuator dynamics. Dynamic control allocation methods deal with cases where the assumption that actuator dynamics are much faster than the dynamics of the controlled system does not hold. In such cases, the dynamic behaviour of the actuators must be accounted for. Actuator dynamics are generally described in state-space form as

$$\begin{aligned}\dot{\boldsymbol{\delta}}(t) &= A_{\boldsymbol{\delta}}\boldsymbol{\delta}(t) + B_{\boldsymbol{\delta}}\boldsymbol{\delta}_c(t) \\ \underline{\boldsymbol{\delta}} \leq &\boldsymbol{\delta} \leq \overline{\boldsymbol{\delta}} \quad \forall t\end{aligned} \tag{2.38}$$

where $\boldsymbol{\delta}_c \in \mathbb{R}^p$ is the input command for the actuators, $\boldsymbol{\delta} \in \mathbb{R}^p$ the actual actuator deflections, $A_{\boldsymbol{\delta}}$ the state matrix, and $B_{\boldsymbol{\delta}}$ the input matrix. Thus, the relationship between control-induced moments and actuator deflections must be generally described as a dynamic mapping in the form

$$\boldsymbol{\tau}(t) = \mathbf{h}(\mathbf{x}, \boldsymbol{\delta}, t) \tag{2.39}$$

In such cases computational complexity of the algorithms can be relaxed since an optimal solution is not required at each time step, but rather a solution that dynamically converges to the optimum with time. The most relevant methods for dynamic control allocation proposed in the literature are described below.

2.4.1 Dynamic Control Allocation with Quadratic Programming

The approach presented by Harkegard (2004) poses the dynamic control allocation problem as a constrained quadratic program, in which the control distribution not only depends on current state, but also on the control distribution of the previous sampling instant, subject to actuator rate constraints. The method extends the QP control allocation scheme, which uses linear control effectors, by penalizing actuator rates through an additional term in the cost function.

A linear control effector model is assumed in the dynamic form

$$\boldsymbol{\tau}(t) = B(t)\boldsymbol{\delta}(t) \tag{2.40}$$

The extended QP problem is then posed as: given a time-varying command $\boldsymbol{\tau}_c(t)$ and a control effectiveness matrix $B(t)$, find $\boldsymbol{\delta}(t)$ such that

$$\begin{aligned}\min_{\boldsymbol{\delta}} \;\; \mathcal{J} = \left|\left|B(t)\boldsymbol{\delta}(t) - \boldsymbol{\tau}_c(t)\right|\right|_2 + \epsilon_1 \left|\left|\boldsymbol{\delta}(t) - \boldsymbol{\delta}_p(t)\right|\right|_2 + \epsilon_2 \left|\left|\boldsymbol{\delta}(t) - \boldsymbol{\delta}_p(t-\Delta t)\right|\right|_2 \\ \text{subject to} \quad \underline{\boldsymbol{\delta}} \leq \boldsymbol{\delta} \leq \overline{\boldsymbol{\delta}}\end{aligned} \tag{2.41}$$

To solve the CA problem the two last terms of $\mathcal{J}$ in Eq. (2.41) can be merged without affecting the solution. Then, the problem can be solved with any QP solver suitable for real-time implementation. The resulting control command will be some mapping in the form

$$\boldsymbol{\delta}(t) = g(\boldsymbol{\tau}_c(t), \boldsymbol{\delta}(t-\Delta t)) \tag{2.42}$$

Hence, the control allocator becomes a dynamic system. This results in a CA scheme whose control distribution is frequency-dependent, and therefore accounts for different actuator bandwidths. Thus, advantage can be taken of actuator redundancy to allocate control effort to different actuators over different frequency ranges (Luo et al., 2007). Harkegard (2004) concluded that, for the nonsaturated case, the control allocator becomes a stable linear filter. Moreover, the method considers actuator position and rate constraints to redistribute the control effort in case of actuator saturation.

2.4.2 Model Predictive Control Allocation

Model predictive control (MPC) was applied to the dynamic control allocation problem in (Luo et al., 2004, 2007; Hanger, 2011). The control effector model is considered in affine form with intercept correction (Doman & Oppenheimer, 2002) as a time-varying mapping

$$\boldsymbol{\tau}(t) = B(t)\boldsymbol{\delta}(t) + \mathbf{c}(\mathbf{x}, \boldsymbol{\delta}) \tag{2.43}$$

As a model-based approach, MPC relies on an on-board dynamic model of the controlled system in the form

$$\dot{\mathbf{x}}(t) = \mathbf{f}\left(\mathbf{x}, t\right) + B\boldsymbol{\delta}(t) + \mathbf{c}(\mathbf{x}, \boldsymbol{\delta}) \tag{2.44}$$

where $\mathbf{f}$ includes the forces and moments that are not produced by the control effectors.

Then, a virtual control $\boldsymbol{\nu}(t)$ is defined as

$$\boldsymbol{\nu}(t) = \dot{\mathbf{x}}(t) - \mathbf{f}\left(\mathbf{x}, t\right) - \mathbf{c}(\mathbf{x}, \boldsymbol{\delta}) = B\boldsymbol{\delta}(t) \tag{2.45}$$

The MPC control allocation problem is then posed as follows: for the constrained system

$$\begin{aligned} \dot{\boldsymbol{\delta}}(t) &= A_\delta\boldsymbol{\delta}(t) + B_\delta\boldsymbol{\delta}_c(t) \\ \mathbf{y}(t) &= B\boldsymbol{\delta}(t) \\ \underline{\boldsymbol{\delta}} \leq \boldsymbol{\delta} &\leq \overline{\boldsymbol{\delta}} \quad \forall t \end{aligned} \tag{2.46}$$

find $\boldsymbol{\delta}_c$(t) such that $\mathbf{y}(t)$ tracks $\boldsymbol{\nu}_c(t)$ as closely as possible, $\boldsymbol{\nu}_c(t)$ being the predicted value of the virtual control $\boldsymbol{\nu}(t)$ obtained from the on-board model (2.44). In addition, a dynamic model of the actuators in the form of Eq. (2.38) is used to predict $\mathbf{y}(t)$ in future time steps. The MPC problem is solved by reformulating it into a linear complementary problem, which is solved with Lemke's algorithm.

The algorithm was proven in (Luo et al., 2004, 2007) to provide better tracking performance than typical linear static control allocation schemes in problems where actuator dynamics were slow enough to be comparable to the dynamics of the system.

2.4.3 Lyapunov-Based Dynamic Optimum-Seeking

Johansen et al. (2004) proposed a reformulation of the static control allocation problem as a control-Lyapunov function, and developed an optimizing control allocation algorithm in the form of a dynamic update law with constructive Lyapunov-design methods. The dynamic control allocation laws derived with this method are generally applicable to both nonlinear and linear control effector models.

A general nonlinear representation of the system and control effectors are considered in the form

$$\begin{aligned} \dot{\mathbf{x}} &= \mathbf{f}(\mathbf{x}, \boldsymbol{\tau}, t) \\ \boldsymbol{\tau} &= \mathbf{h}(\mathbf{x}, \boldsymbol{\delta}, t) \end{aligned} \tag{2.47}$$

A generic instantaneous cost function $\mathcal{J}(\mathbf{x}, \boldsymbol{\delta}, t)$ is defined, which may incorporate power consumption or control effort. In order to account for actuator position constraints, the cost function is augmented with a barrier function $\boldsymbol{\kappa}(\boldsymbol{\delta})$:

$$\mathcal{J}'(\mathbf{x}, \boldsymbol{\delta}, t) = \mathcal{J}(\mathbf{x}, \boldsymbol{\delta}, t) + \boldsymbol{\kappa}(\boldsymbol{\delta}) \tag{2.48}$$

such that the fulfilment of actuator position constraints is guaranteed. Then, the control allocation problem is posed as

$$\begin{aligned} \min_{\boldsymbol{\delta}} \quad & \mathcal{J}'(\mathbf{x}, \boldsymbol{\delta}, t) \\ \text{subject to} \quad & \boldsymbol{\tau}_c = \mathbf{h}(\mathbf{x}, \boldsymbol{\delta}, t) \end{aligned} \tag{2.49}$$

The optimization problem is reformulated with Lagrange multipliers $\boldsymbol{\lambda} \in \mathbb{R}^p$ and the Lagrangian

$$\mathcal{L}\left(\boldsymbol{\lambda}, \mathbf{x}, \boldsymbol{\delta}, t\right) = \mathcal{J}'\left(\mathbf{x}, \boldsymbol{\delta}, t\right) + \left(\boldsymbol{\tau}_c - \mathbf{h}(\mathbf{x}, \boldsymbol{\delta}, t)\right)^T \boldsymbol{\lambda} \tag{2.50}$$

It is assumed that a Lyapunov function $\mathcal{V}_0\left(\mathbf{x}, t\right)$ exists for the high-level control system. Then, the following Lyapunov function is defined for the design of the control allocation law:

$$\mathcal{V}\left(\boldsymbol{\lambda}, \mathbf{x}, \boldsymbol{\delta}, t\right) = \sigma \mathcal{V}_0\left(\mathbf{x}, t\right) + \frac{1}{2}\left(\frac{\partial L^T}{\partial \boldsymbol{\delta}}\frac{\partial L}{\partial \boldsymbol{\delta}} + \frac{\partial L^T}{\partial \boldsymbol{\lambda}}\frac{\partial L}{\partial \boldsymbol{\lambda}}\right) \tag{2.51}$$

with $\sigma > 0$ some constant specified in the design. By assuming $\dot{\mathcal{V}} < 0$ along the trajectories of the system, the control allocator can be derived as a dynamic update law in the form

$$\begin{bmatrix} \dot{\boldsymbol{\delta}} \\ \dot{\boldsymbol{\lambda}} \end{bmatrix} = \begin{bmatrix} -\Gamma \alpha \\ -W \beta \end{bmatrix} + \begin{bmatrix} \zeta \\ \phi \end{bmatrix} \tag{2.52}$$

where Γ and K are positive symmetric matrices containing gains, and α, β, ζ and ϕ are terms derived from Lyapunov-design methods, whose expressions can be found in (Johansen et al., 2004).

The dynamic control allocation update law guarantees asymptotic optimality, which implies that an optimal solution does not need to be found at each sample step. This substantially reduces the computational complexity compared to nonlinear programming approaches to control allocation. It also guarantees not to destabilize the closed-loop system (Johansen & Fossen, 2013).

Note, however, that the dynamic control allocation law is only asymptotically optimal, and may deviate from the instantaneous optimal control distribution at a given time step. Tavasoli and Naraghi (2011) showed that this can lead to some loss of performance. The control allocator can also run into convergence problems in the case of nonconvex cost functions and constraints (Johansen, 2004).

Chapter 3

The Innovative Control Effectors Aircraft

Back in the 1990's, after the fall of the Soviet Union, the office of the Deputy Director of Research and Engineering at the Department of Defense of the United States of America faced the challenge of leading a national program to produce substantial improvements in aerospace technology with a dramatic reduction of spending in aerospace. Amongst other strategic objectives, effort was focused on reducing overall costs, reducing airframe weight, and improving aircraft lift to drag ratio and manoeuvrability (Bowlus, Multhopp, & Banda, 1997). In parallel, low radar cross section (RCS) design practices introduced more restrictive signature-related design constraints, enforcing requirements in external shaping, reduction or elimination of vertical control surfaces and alignment of control surface edges with external airframe edges (Dorsett & Mehl, 1996).

One of the most promising solutions to meet new standards in terms of weight and cost reduction and low RCS are tailless aircraft configurations. In this context, the Innovative Control Effectors (ICE) program was conceived in 1993 by the Flight Control Division of the Flight Dynamics Directorate with the objective of developing and validating innovative aerodynamic flight control effector suites for tailless aircraft (Bowlus et al., 1997). The main objectives of this thesis are motivated by the challenges and opportunities implied by the ICE configuration, and therefore the nonlinear control allocation scheme hereby developed is implemented and tested with a high-fidelity simulation model of the ICE aircraft.

This chapter discusses the ICE aircraft configuration, the high-fidelity aerodynamic model and its challenges in terms of control, and presents an analysis of the dynamic characteristics, stability and controllability of the aircraft. Section 3.1 provides an overview of the ICE program. Section 3.2 describes the ICE control suite, whereas the challenges posed by this design are discussed in Section 3.3. A detailed description of the high-fidelity ICE aerodynamic model used in this thesis is provided in Section 3.4. A linear analysis on the dynamics, stability and controllability of the aircraft is made in Section 3.5. Finally, Section 3.6 discusses the state-of-the-art of control allocation research for the ICE aircraft.

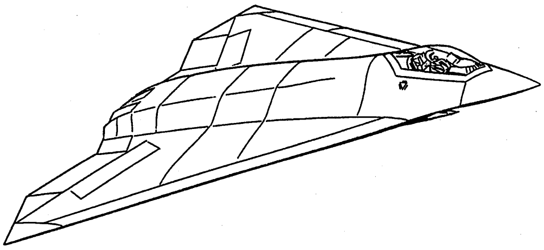

Figure 3.1: Land-based ICE concept.

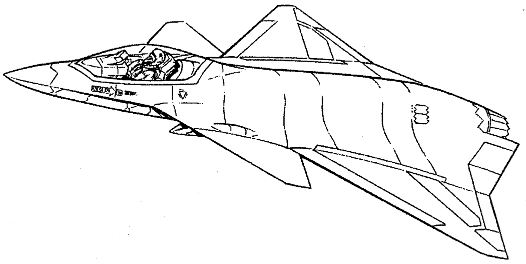

Figure 3.2: Carrier-based ICE concept.

3.1 The Innovative Control Effectors Program

The ICE program was divided into two phases. Phase I (Dorsett & Mehl, 1996) was sponsored by the Wright Laboratory (WL/FIGC) and the Naval Air Warfare Center (NAWCAD), and focused on the conceptual design and analytical study of two baseline aircraft configurations with innovative control effector suites. The baseline concepts under study were the land-based configuration for the Air Force in Figure 3.1 and the carrier-based configuration for the Navy in Figure 3.2. In the analytical study, various types of control effectors and combinations were assessed on the two baseline vehicles.

In Phase II (Dorsett, Fears, & Houlden, 1997) the concepts with greatest potential were subject to wind tunnel tests at the Lockheed Martin Tactical Aircraft Systems (LMTAS) Aerodynamic Development Facility (ADF). The main objectives were gathering empirical data to develop accurate aerodynamic models at high Reynolds numbers, develop control effector models and identify control effector interactions.

3.2 The ICE Control Suite

The simulation model used in this thesis corresponds to the land-based baseline configuration in Figure 3.1 or ICE 101-TV, which will be referred to as the ICE aircraft in the remainder. The ICE aircraft is a 65 deg sweep delta flying wing, single engine, multi-role supersonic fighter with internal weapons carriage (Buffington, 1997) in the class of 38,000 lb takeoff gross weight (Eberhardt & Ward, 1999). The control suite, shown in the plant view in Figure 3.3, includes a number of innovative control concepts, whose main design goals were improved low RCS characteristics, high AoA effectiveness, applicability to tailless configurations, weight and lift-to-drag ratio reduction with respect to conventional controls, reduced hinge moment and reduced susceptibility to aeroelastic effects (Dorsett & Mehl, 1996). The control effectors included in the ICE configuration are:

- **Leading edge flaps (LEF):** The ICE configuration has four LEF in total, two inboard and two outboard. Differential deflections provide lateral-directional control power at high AoA. Leading edge up (LEU) deflections increase drag in the deflected side, causing adverse yaw. LEF are most useful for stability augmentation and roll coordination at low speed and high AoA. Their control effectiveness is nonlinear with AoA in both roll and yaw, and significant interactions between inboard and outboard LEF were reported in (Dorsett & Mehl, 1996; Dorsett et al., 1997).

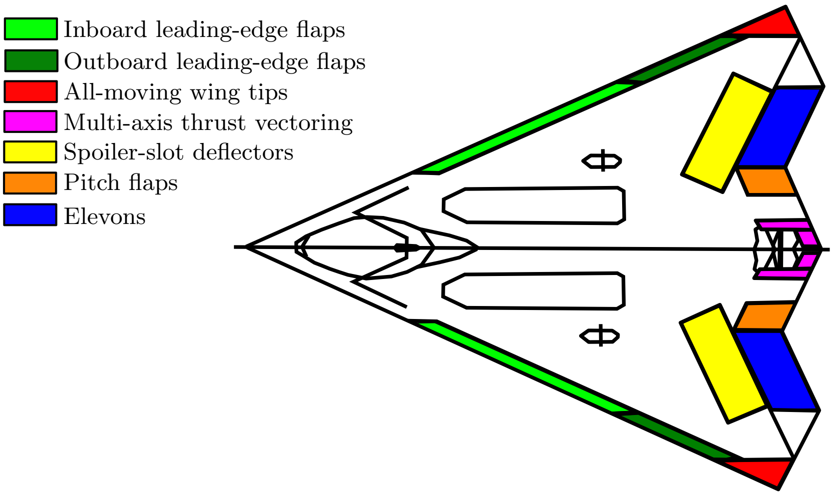

Figure 3.3: ICE control effectors suite.

- **All moving wing tips (AMT):** Trailing edge down (TED) deflections provide yaw control power by increasing profile and induced drag through a moment arm. TED deflections also produce coupled rolling moments. AMTs are an excellent source of yaw control power at very high AoA (Gillard & Dorsett, 1997), producing yaw control moments at large deflections in the order of those produced by an F-16 rudder (Dorsett & Mehl, 1996). Although trailing edge up (TEU) deflections can provide good roll effectiveness up to high AoA, the AMT deflections are constrained to TED in order to allow hingeline sealing for RCS reduction purposes. Further details about integration, configuration and testing of AMTs can be found in (Gillard & Dorsett, 1997).

- **Multi-axis thrust vectoring (MTV):** The thrust vector can be directed in both pitch and yaw axes. MTV serves the purpose of meeting the high-AoA roll performance and agility requirements, since aerodynamic control power alone was not sufficient (Bowlus et al., 1997). Originally traditional nozzle-based thrust vectoring was considered, but more recent designs use fluidic thrust vectoring. The thrust vector is limited by an omnidirectional deflection constraint of 15 deg.

- **Spoiler-slot deflectors (SSD):** Unlike conventional spoilers, SSD open a slot between the lower and upper wing skins when deflected. SSDs provide improved lateral-directional control effectiveness at high AoA and transonic flight with respect to conventional spoilers. Furthermore, SSDs are less affected by high-speed flexibility effects compared to conventional ailerons (Dorsett & Mehl, 1996). Their main drawback is the strong influence over the control effectiveness of pitch and roll control surfaces placed downstream of the SSDs.

- **Pitch flaps (PF):** Pitch flaps are linked to deflect simultaneously and symmetrically, and therefore constitute a unique control effector with control authority in pitch. In addition to providing longitudinal control power, they contribute to longitudinal trim at high AoA and when other control surfaces with pitch authority become ineffective.

- **Elevons:** The control suite has two elevons that can deflect independently in two directions, and therefore constitute two separate control effectors. They provide control power in both pitch and roll by deflecting symmetrically and asymmetrically, respectively. Independent elevon deflections also cause secondary-axis yawing moments due to the increment of parasitic and induced drag.

3.3 Flight Control Challenges

Several control issues appear when considering tailless aircraft configurations. Important challenges are the problems of generating yaw control power and ensuring lateral-directional stability. Of more relevance are, however, the challenges faced in control allocation, which are addressed in this thesis.

3.3.1 Lateral-Directional Control and Stability

In conventional control suites, lateral-directional stability is mainly provided by the vertical stabilizer, and quasi-uncoupled yaw control power is generated by the rudder. The elimination of vertical tails, therefore, relaxes directional stability and reduces directional control power (Buffington, 1997). These control and stability challenges are overcome by using redundant control suites with control effectors producing multi-axis forces and moments, and by designing suitable control laws for stability and control augmentation.

Control and stability challenges have been extensively addressed for the ICE aircraft. Bowlus et al. (1997) presented the stability and control challenges of tailless aircraft configurations. The problem of generating directional control with all moving wing tips was addressed in (Gillard & Dorsett, 1997). A manual flight control system based on dynamic inversion was presented in (Ngo, Reigelsperger, Banda, & Bessolo, 1996), which addressed issues regarding stability, performance and plant uncertainties. A more sophisticated modular control system for the ICE aircraft, which included basic control allocation with the pseudo-inverse method, was developed in (Buffington, 1999). More work has been done in flight control and stability, such as the adaptive flight control system in (Eberhardt & Ward, 1999) and the continuous sliding mode controller in (Shtessel et al., 2002).

3.3.2 The Control Allocation Problem

A more challenging problem presented by the ICE configuration is control allocation. The ICE aircraft has 13 highly redundant, multi-axis control effectors. Since the aircraft is strongly over-actuated, a control allocator is required to distribute the control demands among the available control effectors in an optimal way. Currently, the only control allocation methods tested with the ICE configuration that are suitable for real-time implementation are linear approaches, especially methods based on generalized pseudo-inverses. These CA methods assume, on the one hand, that the contributions of the individual control effectors to control-induced forces and moments are separable (i.e. that there are no interactions between control effectors) and, on the other hand, that a linear relationship exists between control-induced moments and actuator deflections.

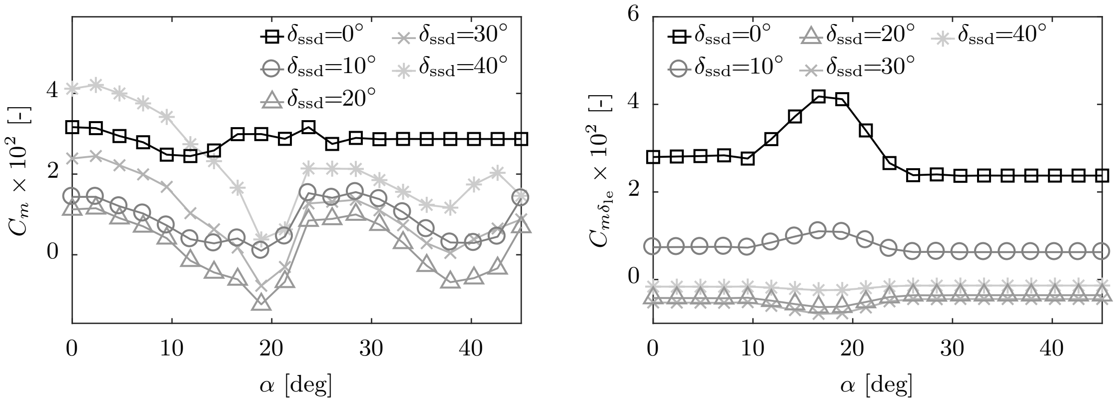

(a) Total C_m for $\delta_{\text{e}} = -30$ including airframe and control effector contributions influenced by δ_{ssd}.

(b) Isolated C_m contribution of $\delta_{\text{e}} = -30$ deg influenced by δ_{ssd}.

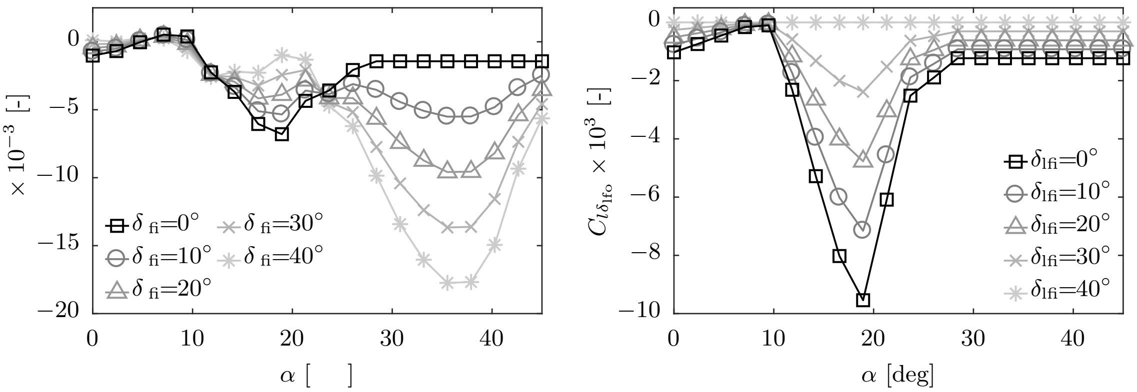

(c) Total C_l for $\delta_{\text{lfo}} = 30$ including airframe and control effector contributions influenced by δ_{lfi}.

(d) Isolated C_l contribution of $\delta_{\text{lfo}} = 30$ deg influenced by δ_{lfi}.

Figure 3.4: Dimensionless aerodynamic coefficients from the high-fidelity ICE aerodynamic database showing substantial nonlinear interactions between control effectors. The values shown correspond to $M = 0.6$ and $\alpha = \beta = 0$ deg.

However, as has been emphasized in (Buffington, 1997; Eberhardt & Ward, 1999; Davidson et al., 2001a), these assumptions are especially not valid in the case of the ICE aircraft. Due to the high number of control effectors, the mechanisms used to produce control moments and the proximity between some control surfaces, the control effectiveness of the ICE actuators is highly nonlinear and coupled. Some examples obtained from the aerodynamic database of the ICE aircraft are presented here.

Figures 3.4a-3.4b show the dimensionless pitching moment C_m produced by a deflection of the left elevon $\delta_{\text{e}} = -30$ deg for different positions of the left SSD, δ_{ssd}. In Figure 3.4a it can be observed that the total pitching moment produced by both the elevon and the SSD is a highly nonlinear and nonconvex function of α. Figure 3.4b shows the isolated contribution of the elevon, exhibiting a highly nonlinear influence of the SSD position. A similar example is given in Figures 3.4c-3.4d for the dimensionless pitching moment C_l produced by a deflection of the left outboard LEF $\delta_{\text{lfo}} = 30$ deg, for different deflections

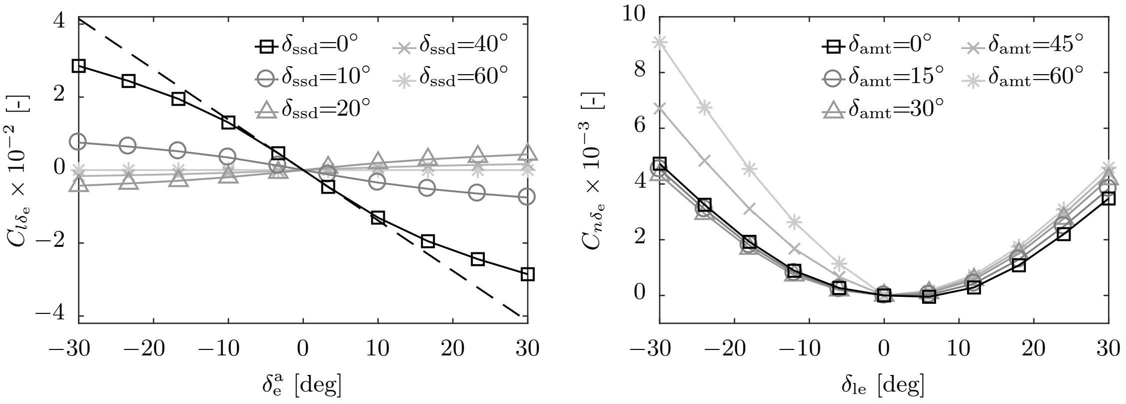

(a) Rolling moment curves of asymmetric elevon deflections influenced by δ_{ssd}.

(b) Yawing moment curves of the left elevon influenced by δ_{amt}.

Figure 3.5: Control moment curves showing nonlinear behaviour and control effector interactions. The values shown correspond to $M = 0.6$, $\alpha = 0$ deg and $\beta = 0$ deg. The dashed line represents a linear approximation of the rolling moment curve for $\delta_{ssd} = 0$ deg.

of the left inboard LEF, δ_{lfi}. Figure 3.4d shows that the control effectiveness of δ_{lfo} in the roll axis is significantly degraded when the inboard LEF is deflected. Note that, for a full deflection of the inboard LEF, the outboard LEF does not produce any control moment in the roll axis. This has a substantial effect in the total roll contribution of the LEF pair, as can be observed in 3.4c: the degeneration of the effectiveness of the outboard LEF as a consequence of the deflection of the inboard LEF causes a change of sign in the slope of C_l with α, which can have dramatic consequences for control allocation purposes if such effects are not taken into account.

Examples of control moment curves of effectors exhibiting nonlinear behaviour and interactions are shown in Figure 3.5. Figure 3.5a shows an example of a control moment curve that is close to linear around the neutral position and becomes nonlinear for extreme deflections close to the position limits. The dashed line in Figure 3.5a represents a linear approximation of the rolling moment curve for $\delta_{ssd} = 0$ deg, which demonstrates the inaccuracy of linear effector models at big deflections. The observed influence of δ_{ssd} on the rolling moment curve is remarkable: for a deflection of the SSDs to less than 15% of their position limits, the control effectiveness of the elevons is reduced to less than 30%. Also, for SSD deflections of 20 deg and higher the slope of the control effectiveness curve of the elevons shifts from negative to positive, which can have dramatic effects on the control allocation strategy. Finally, the elevons completely lose their control effectiveness for full deflection of the SSDs (note that the curves shown correspond to $\alpha = 0$ deg).

Figure 3.5b shows the quadratic yawing moment contribution of the left elevon, influenced by δ_{amt}. Besides the asymmetric influence of AMT deflections, the quadratic nature of this yawing moment curve is particularly worth being taken into consideration. As previously mentioned, in tailless configurations all aerodynamic contributions to yawing moment are originated by the generation of profile and induced drag with horizontal control surfaces, which leads to quadratic moment curves that cannot be captured with linear control effector models.

An extensive study of the control effectiveness of the control effectors of the ICE aircraft can be found in (Addington & Myatt, 2000). The results thereby shown were obtained from wind tunnel tests at the Airforce Research Laboratory's Vertical Wind Tunnel, and show the nonlinearities and control effector interactions of the ICE control effectors suite.

To summarise, three main challenges arise for the ICE aircraft regarding control allocation. First, the control effectiveness of the actuators is strongly nonlinear. Second, highly nonlinear interactions between control effectors exist. Third, directional control power is mainly achieved with horizontal control surfaces, whose contributions to yaw are quadratic and asymmetrical, and therefore cannot be captured with linear effector models.

3.4 High-Fidelity Aerodynamic Model

A high-fidelity aerodynamic database of the ICE aircraft mainly obtained from wind tunnel tests was released by Lockheed Martin for academic use. This aerodynamic model, which is described in detail in (Niestroy et al., 2017), is used in this thesis to simulate the ICE dynamics. Its structure and characteristics are described in this section.

3.4.1 Reference Frames

The aircraft dimensionless aerodynamic coefficients are expressed in body frame $\mathcal{F}^b$, which is defined as the standard aerospace right-hand axis system:

- Origin: aircraft center of gravity.
- X-axis: pointing forward through the vehicle's nose.
- Y-axis: pointing to the right.
- Z-axis: pointing downwards, completing the right-hand axis system.

The coefficients provided in the lookup tables are defined in the aerodynamic model body frame $\mathcal{F}^m$, which is a right-hand axis system with:

- Origin: aircraft center of gravity.
- X-axis: pointing backwards through the vehicle's tail.
- Y-axis: pointing to the right.
- Z-axis: pointing upwards, completing the right-hand axis system.

3.4.2 Control Effectors

The control input vector $\boldsymbol{\delta} \in \mathbb{R}^{14}$ is composed by the deflections of the 11 aerodynamic control surfaces, 2 MTV deflections in pitch and yaw, and 1 throttle input. The control surfaces and throttle are limited by absolute position constraints implemented as saturations, whereas the MTV deflection vector is subject to a circular constraint in the form

$$\sqrt{\delta_{\mathrm{ptv}}^2 + \delta_{\mathrm{ytv}}^2} \leq \delta_{\mathrm{tv}_{\max}} \tag{3.1}$$

Table 3.1: Dynamic properties of the ICE control effectors.

Control effector	Notation	Positive deflection	Position limits [deg]	Rate limit [deg]	Dynamics
Inboard LEF	$\delta_{\text{lfi}}, \delta_{\text{rfi}}$	LED	[0, 40]	40	$H_l(s)$
Outboard LEF	$\delta_{\text{lfo}}, \delta_{\text{rfo}}$	LED	[-40, 40]	40	$H_l(s)$
AMT	$\delta_{\text{lamt}}, \delta_{\text{ramt}}$	TED	[0, 60]	150	$H_h(s)$
Elevons	$\delta_{\text{lele}}, \delta_{\text{rele}}$	TED	[-30, 30]	150	$H_h(s)$
SSD	$\delta_{\text{lssd}}, \delta_{\text{rssd}}$	TEU	[0, 60]	150	$H_h(s)$
PF	δ_{pf}	TED	[-30, 30]	150	$H_h(s)$
MTV	$\delta_{\text{ptv}}, \delta_{\text{ytv}}$	$\dot{\boldsymbol{\omega}} > 0$	[-15, 15]	150	$H_h(s)$

Actuator dynamics are considered in the form of no-load rate limits and second-order transfer functions. A low-bandwidth or high-bandwidth transfer function is used depending on the control effector:

$$H_l(s) = \frac{(18)(100)}{(s+18)(s+100)} \quad (3.2) \qquad H_h(s) = \frac{(40)(100)}{(s+40)(s+100)} \quad (3.3)$$

The position limits, no-load rate limits and dynamics of the ICE control effectors are listed in Table 3.1.

3.4.3 Multi-Axis Thrust Vectoring Model

The MTV model provided by Lockheed Martin in the current release of the ICE model did not consider the 3D projection of the thrust vector $\mathbf{T}$. In order to improve accuracy, the MTV model was extended in this thesis to account for thrust vector projections. This extended model has been reviewed by Lockheed Martin and will be included in the next release of the ICE model.

The model considers the direction of the pitch δ_{ptv} and yaw δ_{ytv} deflection angles such that positive deflections produce negative pitching and yawing moments, respectively. Using this convention, the projections of the thrust vector $\mathbf{T}$ onto the body frame $\mathcal{F}^b$ for arbitrary deflections δ_{ptv} and δ_{ytv} are represented in the diagram in Figure 3.6. Thus, the vectored thrust force $\mathbf{T}$ and moment $\boldsymbol{\tau}_{\text{T}}$ vectors are given by Eqs. (3.4) and (3.5), where $d_n = 18.75$ ft is the moment arm of the thrust force.

$$\mathbf{T} = \text{T}\begin{bmatrix}\cos(\delta_{\text{ptv}})/\cos(\delta_{\text{ytv}}) \\ \cos(\delta_{\text{ptv}})\tan(\delta_{\text{ytv}}) \\ \sin(\delta_{\text{ptv}})\end{bmatrix} \quad (3.4) \qquad \boldsymbol{\tau}_{\text{T}} = -\text{T}d_n\begin{bmatrix}0 \\ \sin(\delta_{\text{ptv}}) \\ \cos(\delta_{\text{ptv}})\tan(\delta_{\text{ytv}})\end{bmatrix} \quad (3.5)$$

3.4.4 Aerodynamic Model

The ICE aerodynamic model is a six degrees-of-freedom (6-DoF) model developed mainly from wind tunnel data, and includes nonlinear control effector interaction effects, dynamic derivatives, aeroelastic effects and hinge moment derivatives. It provides dimensionless coefficients for the aerodynamic forces and moments as a summation of nonlinear terms stored in lookup tables.

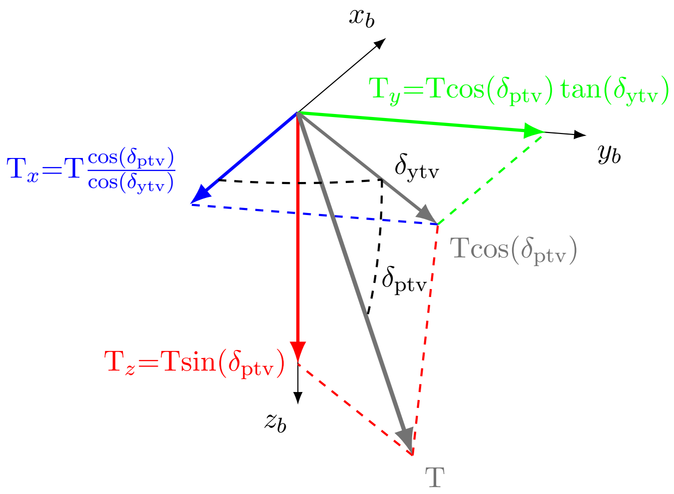

Figure 3.6: Projections of the thrust vector in body frame.

The aerodynamic forces in body frame $[X\ Y\ Z]^T$ are obtained from the dimensionless force coefficients, which are normalized as follows:

$$C_X = \frac{X}{\frac{1}{2}\rho V^2 S}; \qquad C_Y = \frac{Y}{\frac{1}{2}\rho V^2 S}; \qquad C_Z = \frac{Z}{\frac{1}{2}\rho V^2 S} \tag{3.6}$$

where ρ is the air density in slug/ft^3, V the true airspeed in ft/sec and S the total wing area in ft^2. These dimensionless coefficients are computed as a summation of nonlinear terms stored in lookup tables as a function of the operating point (α, β, M) and control effector positions $\boldsymbol{\delta}$:

$$\begin{aligned}
-C_X = \; & + C_{X_1}(\alpha, M) + C_{X_2}(\alpha, \beta, M) + C_{X_3}(\alpha, \delta_{\mathrm{ls}}, \delta_{\mathrm{le}}, M) + C_{X_4}(\alpha, \delta_{\mathrm{rs}}, \delta_{\mathrm{re}}, M) \\
& + C_{X_5}(\alpha, \beta, \delta_{\mathrm{lfi}}) + C_{X_6}(\alpha, \beta, \delta_{\mathrm{rfi}}) + C_{X_7}(\alpha, \beta, \delta_{\mathrm{lfi}}, \delta_{\mathrm{lfo}}, M) + C_{X_8}(\alpha, \beta, \delta_{\mathrm{rfi}}, \delta_{\mathrm{rfo}}, M) \\
& + C_{X_9}(\alpha, \delta_{\mathrm{lfo}}, \delta_{\mathrm{la}}) + C_{X_{10}}(\alpha, \delta_{\mathrm{rfo}}, \delta_{\mathrm{ra}}) + C_{X_{11}}(\alpha, \delta_{\mathrm{la}}, \delta_{\mathrm{le}}) + C_{X_{12}}(\alpha, \delta_{\mathrm{ra}}, \delta_{\mathrm{re}}) \\
& + C_{X_{13}}(\alpha, \delta_{\mathrm{rs}}, \delta_{\mathrm{ls}}, \delta_{\mathrm{pf}}, M) + C_{X_{14}}(\alpha, \beta, \delta_{\mathrm{la}}) + C_{X_{15}}(\alpha, \beta, \delta_{\mathrm{ra}}) + C_{X_{16}}(\alpha, \beta, \delta_{\mathrm{ls}}) \\
& + C_{X_{17}}(\alpha, \beta, \delta_{\mathrm{rs}})
\end{aligned} \tag{3.7}$$

$$\begin{aligned}
C_Y = \; & + C_{Y_1}(\alpha, M) + C_{Y_2}(\alpha, \beta, M) + C_{Y_3}(\alpha, \delta_{\mathrm{ls}}, \delta_{\mathrm{le}}, M) - C_{Y_4}(\alpha, \delta_{\mathrm{rs}}, \delta_{\mathrm{re}}, M) \\
& - C_{Y_5}(\alpha, \beta, \delta_{\mathrm{lfi}}) + C_{Y_6}(\alpha, \beta, \delta_{\mathrm{rfi}}) - C_{Y_7}(\alpha, \beta, \delta_{\mathrm{lfi}}, \delta_{\mathrm{lfo}}, M) + C_{Y_8}(\alpha, \beta, \delta_{\mathrm{rfi}}, \delta_{\mathrm{rfo}}, M) \\
& + C_{Y_9}(\alpha, \delta_{\mathrm{lfo}}, \delta_{\mathrm{la}}) - C_{Y_{10}}(\alpha, \delta_{\mathrm{rfo}}, \delta_{\mathrm{ra}}) + C_{Y_{11}}(\alpha, \delta_{\mathrm{la}}, \delta_{\mathrm{le}}) - C_{Y_{12}}(\alpha, \delta_{\mathrm{ra}}, \delta_{\mathrm{re}}) \\
& + C_{Y_{13}}(\alpha, \delta_{\mathrm{rs}}, \delta_{\mathrm{ls}}, \delta_{\mathrm{pf}}, M) + C_{Y_{14}}(\alpha, \beta, \delta_{\mathrm{la}}) - C_{Y_{15}}(\alpha, \beta, \delta_{\mathrm{ra}}) + C_{Y_{16}}(\alpha, \beta, \delta_{\mathrm{ls}}) \\
& - C_{Y_{17}}(\alpha, \beta, \delta_{\mathrm{rs}})
\end{aligned} \tag{3.8}$$

$$\begin{aligned}
-C_Z = {} & + C_{Z_1}\left(\alpha, M\right) + C_{Z_2}\left(\alpha, \beta, M\right) + C_{Z_3}\left(\alpha, \delta_{\mathrm{ls}}, \delta_{\mathrm{le}}, M\right) + C_{Z_4}\left(\alpha, \delta_{\mathrm{rs}}, \delta_{\mathrm{re}}, M\right) \\
& + C_{Z_5}\left(\alpha, \beta, \delta_{\mathrm{lfi}}\right) + C_{Z_6}\left(\alpha, \beta, \delta_{\mathrm{rfi}}\right) + C_{Z_7}\left(\alpha, \beta, \delta_{\mathrm{lfi}}, \delta_{\mathrm{lfo}}, M\right) + C_{Z_8}\left(\alpha, \beta, \delta_{\mathrm{rfi}}, \delta_{\mathrm{rfo}}, M\right) \\
& + C_{Z_9}\left(\alpha, \delta_{\mathrm{lfo}}, \delta_{\mathrm{la}}\right) + C_{Z_{10}}\left(\alpha, \delta_{\mathrm{rfo}}, \delta_{\mathrm{ra}}\right) + C_{Z_{11}}\left(\alpha, \delta_{\mathrm{la}}, \delta_{\mathrm{le}}\right) + C_{Z_{12}}\left(\alpha, \delta_{\mathrm{ra}}, \delta_{\mathrm{re}}\right) \\
& + C_{Z_{13}}\left(\alpha, \delta_{\mathrm{rs}}, \delta_{\mathrm{ls}}, \delta_{\mathrm{pf}}, M\right) + C_{Z_{14}}\left(\alpha, \beta, \delta_{\mathrm{la}}\right) + C_{Z_{15}}\left(\alpha, \beta, \delta_{\mathrm{ra}}\right) + C_{Z_{16}}\left(\alpha, \beta, \delta_{\mathrm{ls}}\right) \\
& + C_{Z_{17}}\left(\alpha, \beta, \delta_{\mathrm{rs}}\right) + \frac{q\bar{c}}{2V} C_{Z_{18}}\left(\alpha, M\right)
\end{aligned} \tag{3.9}$$

The aerodynamic moments in body frame $\boldsymbol{\tau} = [L \ M \ N]^T$ are obtained from the dimensionless moment coefficients, which are normalized as follows:

$$C_l = \frac{L}{\frac{1}{2}\rho V^2 S b}; \qquad C_m = \frac{M}{\frac{1}{2}\rho V^2 S \bar{c}}; \qquad C_n = \frac{N}{\frac{1}{2}\rho V^2 S b} \tag{3.10}$$

where b is the wing span in ft and $\bar{c}$ the mean aerodynamic chord (MAC) in ft. These dimensionless coefficients are computed as a summation of nonlinear terms stored in lookup tables as a function of the operating point (α, β, M) and actuator deflections $\boldsymbol{\delta}$:

$$\begin{aligned}
C_l = {} & + C_{l_1}\left(\alpha, M\right) + C_{l_2}\left(\alpha, \beta, M\right) + C_{l_3}\left(\alpha, \delta_{\mathrm{ls}}, \delta_{\mathrm{le}}, M\right) - C_{l_4}\left(\alpha, \delta_{\mathrm{rs}}, \delta_{\mathrm{re}}, M\right) \\
& - C_{l_5}\left(\alpha, \beta, \delta_{\mathrm{lfi}}\right) + C_{l_6}\left(\alpha, \beta, \delta_{\mathrm{rfi}}\right) - C_{l_7}\left(\alpha, \beta, \delta_{\mathrm{lfi}}, \delta_{\mathrm{lfo}}, M\right) + C_{l_8}\left(\alpha, \beta, \delta_{\mathrm{rfi}}, \delta_{\mathrm{rfo}}, M\right) \\
& + C_{l_9}\left(\alpha, \delta_{\mathrm{lfo}}, \delta_{\mathrm{la}}\right) - C_{l_{10}}\left(\alpha, \delta_{\mathrm{rfo}}, \delta_{\mathrm{ra}}\right) + C_{l_{11}}\left(\alpha, \delta_{\mathrm{la}}, \delta_{\mathrm{le}}\right) - C_{l_{12}}\left(\alpha, \delta_{\mathrm{ra}}, \delta_{\mathrm{re}}\right) \\
& + C_{l_{13}}\left(\alpha, \delta_{\mathrm{rs}}, \delta_{\mathrm{ls}}, \delta_{\mathrm{pf}}, M\right) + C_{l_{14}}\left(\alpha, \beta, \delta_{\mathrm{la}}\right) - C_{l_{15}}\left(\alpha, \beta, \delta_{\mathrm{ra}}\right) + C_{l_{16}}\left(\alpha, \beta, \delta_{\mathrm{ls}}\right) \\
& - C_{l_{17}}\left(\alpha, \beta, \delta_{\mathrm{rs}}\right) + \frac{pb}{2V} C_{l_{18}}\left(\alpha, M\right) + \frac{rb}{2V} C_{l_{19}}\left(\alpha, M\right)
\end{aligned} \tag{3.11}$$

$$\begin{aligned}
C_m = {} & + C_{m_1}\left(\alpha, M\right) + C_{m_2}\left(\alpha, \beta, M\right) + C_{m_3}\left(\alpha, \delta_{\mathrm{ls}}, \delta_{\mathrm{le}}, M\right) + C_{m_4}\left(\alpha, \delta_{\mathrm{rs}}, \delta_{\mathrm{re}}, M\right) \\
& + C_{m_5}\left(\alpha, \beta, \delta_{\mathrm{lfi}}\right) + C_{m_6}\left(\alpha, \beta, \delta_{\mathrm{rfi}}\right) + C_{m_7}\left(\alpha, \beta, \delta_{\mathrm{lfi}}, \delta_{\mathrm{lfo}}, M\right) + C_{m_8}\left(\alpha, \beta, \delta_{\mathrm{rfi}}, \delta_{\mathrm{rfo}}, M\right) \\
& + C_{m_9}\left(\alpha, \delta_{\mathrm{lfo}}, \delta_{\mathrm{la}}\right) + C_{m_{10}}\left(\alpha, \delta_{\mathrm{rfo}}, \delta_{\mathrm{ra}}\right) + C_{m_{11}}\left(\alpha, \delta_{\mathrm{la}}, \delta_{\mathrm{le}}\right) + C_{m_{12}}\left(\alpha, \delta_{\mathrm{ra}}, \delta_{\mathrm{re}}\right) \\
& + C_{m_{13}}\left(\alpha, \delta_{\mathrm{rs}}, \delta_{\mathrm{ls}}, \delta_{\mathrm{pf}}, M\right) + C_{m_{14}}\left(\alpha, \beta, \delta_{\mathrm{la}}\right) + C_{m_{15}}\left(\alpha, \beta, \delta_{\mathrm{ra}}\right) + C_{m_{16}}\left(\alpha, \beta, \delta_{\mathrm{ls}}\right) \\
& + C_{m_{17}}\left(\alpha, \beta, \delta_{\mathrm{rs}}\right) + \frac{q\bar{c}}{2V} C_{m_{18}}\left(\alpha, M\right)
\end{aligned} \tag{3.12}$$

$$\begin{aligned}
C_n = {} & + C_{n_1}\left(\alpha, M\right) + C_{n_2}\left(\alpha, \beta, M\right) + C_{n_3}\left(\alpha, \delta_{\mathrm{ls}}, \delta_{\mathrm{le}}, M\right) - C_{n_4}\left(\alpha, \delta_{\mathrm{rs}}, \delta_{\mathrm{re}}, M\right) \\
& - C_{n_5}\left(\alpha, \beta, \delta_{\mathrm{lfi}}\right) + C_{n_6}\left(\alpha, \beta, \delta_{\mathrm{rfi}}\right) - C_{n_7}\left(\alpha, \beta, \delta_{\mathrm{lfi}}, \delta_{\mathrm{lfo}}, M\right) + C_{n_8}\left(\alpha, \beta, \delta_{\mathrm{rfi}}, \delta_{\mathrm{rfo}}, M\right) \\
& + C_{n_9}\left(\alpha, \delta_{\mathrm{lfo}}, \delta_{\mathrm{la}}\right) - C_{n_{10}}\left(\alpha, \delta_{\mathrm{rfo}}, \delta_{\mathrm{ra}}\right) + C_{n_{11}}\left(\alpha, \delta_{\mathrm{la}}, \delta_{\mathrm{le}}\right) - C_{n_{12}}\left(\alpha, \delta_{\mathrm{ra}}, \delta_{\mathrm{re}}\right) \\
& + C_{n_{13}}\left(\alpha, \delta_{\mathrm{rs}}, \delta_{\mathrm{ls}}, \delta_{\mathrm{pf}}, M\right) + C_{n_{14}}\left(\alpha, \beta, \delta_{\mathrm{la}}\right) - C_{n_{15}}\left(\alpha, \beta, \delta_{\mathrm{ra}}\right) + C_{n_{16}}\left(\alpha, \beta, \delta_{\mathrm{ls}}\right) \\
& - C_{n_{17}}\left(\alpha, \beta, \delta_{\mathrm{rs}}\right) + \frac{pb}{2V} C_{n_{18}}\left(\alpha, M\right) + \frac{rb}{2V} C_{n_{19}}\left(\alpha, M\right)
\end{aligned} \tag{3.13}$$

A classification of the different aerodynamic terms, their dependencies and physical interpretations are listed in Table 3.2. Detailed information about the model including trim maps is provided in (Niestroy et al., 2017).

Table 3.2: ICE aerodynamic model terms and their physical interpretation.

Coefficient		Dependencies	Physical interpretation
$C_{i\text{a}}$	C_{i_1}	(α, M)	Aerodynamic contribution of airframe.
	C_{i_2}	(α, β, M)	
$C_{i\delta_j}$	C_{i_5}	$(\alpha, \beta, \delta_{\text{lfi}})$	Isolated contributions of inboard LEFs.
	C_{i_6}	$(\alpha, \beta, \delta_{\text{rfi}})$	
	$C_{i_{14}}$	$(\alpha, \beta, \delta_{\text{la}})$	Isolated contributions of AMTs.
	$C_{i_{15}}$	$(\alpha, \beta, \delta_{\text{ra}})$	
	$C_{i_{16}}$	$(\alpha, \beta, \delta_{\text{ls}})$	Isolated contributions of SSDs.
	$C_{i_{17}}$	$(\alpha, \beta, \delta_{\text{rs}})$	
$C_{i\delta_j,\delta_k}$	C_{i_3}	$(\alpha, \delta_{\text{ls}}, \delta_{\text{le}}, M)$	Contribution of elevons, influenced by SSDs.
	C_{i_4}	$(\alpha, \delta_{\text{rs}}, \delta_{\text{re}}, M)$	
	C_{i_7}	$(\alpha, \beta, \delta_{\text{lfi}}, \delta_{\text{lfo}}, M)$	Contribution of outboard LEFs, influenced by inboard LEFs.
	C_{i_8}	$(\alpha, \beta, \delta_{\text{rfi}}, \delta_{\text{rfo}}, M)$	
	$C_{i_{13}}$	$(\alpha, \delta_{\text{rs}}, \delta_{\text{ls}}, \delta_{\text{pf}}, M)$	Contribution of PF, influenced by SSDs.
	C_{i_9}	$(\alpha, \delta_{\text{lfo}}, \delta_{\text{la}})$	Interaction effects between all-moving wingtips and outboard trailing-edge flaps.
	$C_{i_{10}}$	$(\alpha, \delta_{\text{rfo}}, \delta_{\text{ra}})$	
	$C_{i_{11}}$	$(\alpha, \delta_{\text{la}}, \delta_{\text{le}})$	Interaction effects between all-moving wingtips and elevons.
	$C_{i_{12}}$	$(\alpha, \delta_{\text{ra}}, \delta_{\text{re}})$	
$C_{i\omega_j}$	$\frac{pb}{2V}C_{i_{18}}$	(α, M)	Unsteady effects of the airframe.
	$\frac{q\bar{c}}{2V}C_{i_{19}}$	(α, M)	
	$\frac{rb}{2V}C_{i_{20}}$	(α, M)	

3.5 Controllability and Stability Analysis

Prior to the design of a flight control system, the controllability, inherent stability and dynamic modes of the ICE aircraft were studied for a representative set of trimmed flight conditions within its flight envelope. Besides general controllability and stability characteristics, it was also of interest to extract information about the dependency of the aircraft controllability on the use of multi-axis thrust vectoring, and therefore the controllability analysis was performed both with and without MTV. Of particular interest were low speed and high AoA conditions in the range of Mach 0.3 - 0.5, since nonlinearities and cross-axis control effector interactions become particularly significant in this region of the flight envelope. Additionally, it was important to study stability and controllability in both subsonic and supersonic regions, and with different mass configurations.

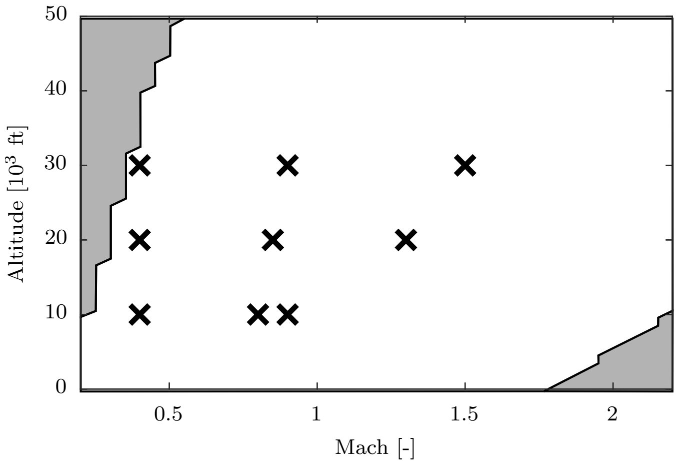

Figure 3.7: Flight envelope of the ICE aircraft and trim points used for the controllability and stability analysis. The flight envelope was taken from (Niestroy et al., 2017).

3.5.1 Trim Conditions

In order to address all the aforementioned aspects of the aircraft dynamic characteristics, the ICE model was trimmed and linearized around a representative set of operational points for different altitudes, Mach numbers, mass configurations, and with/without using MTV. Trimming was performed by minimizing the square of control surface deflections at zero state derivatives with the active set algorithm with tolerances of 10^{-4}. Model linearization at the trim points was performed with the Matlab built-in function `linmod`.

The altitudes and speeds of the trim operating points were chosen across a representative region of the flight envelope, as shown in Figure 3.7 and listed in Table 3.3. The system was trimmed and linearized at every operating point for three different mass configurations taken from (Niestroy et al., 2017), see Tables 3.4-3.6. The sets of active control effectors used for the trim modes with and without MTV are listed in Table 3.7. Note that for the no-MTV mode the two thrust vectoring inputs were replaced by the pitch flap. As specified in (Niestroy et al., 2017), the aerodynamic center (AC) was placed at $\sim 40\%\bar{c}$ for subsonic flight and shifted backwards to $\sim 50\%\bar{c}$ for supersonic regimes. The combinations of 9 operating points, 3 mass configurations and 2 trim modes (with and without MTV) resulted in a representative set of 46 trim points (trimming was not achievable for 8 of the 54 flight conditions).

3.5.2 System Linearization

The system was linearized around the 46 trim points, resulting in a state-space representation of the aircraft equations of motion in the form:

$$\begin{aligned} \dot{\mathbf{x}} &= A\mathbf{x} + C\boldsymbol{\delta} \\ \mathbf{y} &= C\mathbf{x} + D\boldsymbol{\delta} \end{aligned} \tag{3.14}$$

with $\mathbf{x} \in \mathbb{R}^{12}$ the state vector, $\mathbf{y} \in \mathbb{R}^{25}$ the output vector and $\boldsymbol{\delta} \in \mathbb{R}^{13}$ the input vector.

Table 3.3: Trim altitudes and airspeeds.

Altitude	Trim airspeed		
10000 ft	$V = 430$ ft/sec $M = 0.40$	$V = 862$ ft/sec $M = 0.80$	$V = 970$ ft/sec $M = 0.90$
20000 ft	$V = 415$ ft/sec $M = 0.40$	$V = 880$ ft/sec $M = 0.85$	$V = 1350$ ft/sec $M = 1.30$
30000 ft	$V = 400$ ft/sec $M = 0.40$	$V = 895$ ft/sec $M = 0.90$	$V = 1500$ ft/sec $M = 1.50$

Table 3.4: Nominal mass configuration at 50% internal fuel.

Weight and CG		Inertias [slug-ft^2]	
W	32750 lb	$\mathrm{I_{xx}}$	35479
x_{cg}	38.84% $\bar{c}$	$\mathrm{I_{yy}}$	78451
y_{cg}	0	$\mathrm{I_{zz}}$	110627
z_{cg}	88.97 ft	$\mathrm{I_{xz}}$	-525

Table 3.5: Lightweight mass configuration.

Weight and CG		Inertias [slug-ft^2]	
W	25989 lb	$\mathrm{I_{xx}}$	35479
x_{cg}	40% $\bar{c}$	$\mathrm{I_{yy}}$	67500
y_{cg}	0	$\mathrm{I_{zz}}$	83800
z_{cg}	88.97 ft	$\mathrm{I_{xz}}$	-250

Table 3.6: Heavyweight mass configuration.

Weight and CG		Inertias [slug-ft^2]	
W	37084 lbf	$\mathrm{I_{xx}}$	42576
x_{cg}	36% $\bar{c}$	$\mathrm{I_{yy}}$	81903
y_{cg}	0	$\mathrm{I_{zz}}$	118379
z_{cg}	88.97 ft	$\mathrm{I_{xz}}$	-525

Table 3.7: Sets of active control effectors for the trim modes with and without MTV.

Trim mode	Set of active effectors
MTV	$\delta_{\mathrm{T}}\ \delta_{\mathrm{lamt}}\ \delta_{\mathrm{lele}}\ \delta_{\mathrm{ramt}}\ \delta_{\mathrm{rele}}\ \delta_{\mathrm{ptv}}\ \delta_{\mathrm{ytv}}$
No MTV	$\delta_{\mathrm{T}}\ \delta_{\mathrm{lamt}}\ \delta_{\mathrm{lele}}\ \delta_{\mathrm{pf}}\ \delta_{\mathrm{ramt}}\ \delta_{\mathrm{rele}}$

The state and output vectors contain:

$$\boldsymbol{x} = [x_e\ y_e\ z_e\ u_b\ v_b\ w_b\ \varphi\ \theta\ \psi\ p\ q\ r\ ] \tag{3.15}$$

$$\boldsymbol{y} = [x_e\ y_e\ z_e\ u_b\ v_b\ w_b\ A_x\ A_y\ A_z\ \varphi\ \theta\ \psi\ p\ q\ r\ \dot{p}\ \dot{q}\ \dot{r}\ u_e\ v_e\ w_e\ M\ \alpha\ \beta\ ] \tag{3.16}$$

An example linearization of the system at 20000 ft, $M = 0.85$ with nominal mass configuration and MTV is given in Eq. (3.17). A linearization about the same operating point but without MTV is given in Eq. (3.18). These representations of the model have been simplified to improve readability by removing x_e, y_e, z_e, φ, θ and ψ from the state vector.

$$\begin{bmatrix}\dot{u}_b\\ \dot{v}_b\\ \dot{w}_b\\ \dot{p}\\ \dot{q}\\ \dot{r}\end{bmatrix}=\begin{bmatrix}-0.008 & -0.003 & 0.06 & 0 & -31 & 0 & 0 & -42 & 0\\ 0 & -0.01 & -0.002 & 31 & 0.01 & 0 & 42 & 0 & -878\\ -0.03 & 0.01 & -1.0 & 0.32 & -1.5 & 0 & 0 & 866 & 0\\ 0 & -0.01 & 0.004 & 0 & 0 & 0 & -1.5 & 0 & 0.11\\ 0 & 0 & -0.01 & 0 & 0 & 0 & 0 & -0.98 & 0\\ 0 & -0.002 & 0 & 0 & 0 & 0 & -0.06 & 0 & -0.02\end{bmatrix}\begin{bmatrix}u_b\\ v_b\\ w_b\\ p\\ q\\ r\end{bmatrix}$$

$$+\begin{bmatrix}-0.01 & -0.01 & -0.04 & 0.02 & -0.25 & 0.01 & -0.01 & -0.01 & -0.04 & 0.01 & -0.25 & 0 & 0\\ 0.03 & 0.01 & 0.01 & 0.02 & 0.11 & 0 & -0.03 & -0.01 & -0.01 & -0.01 & -0.11 & 0 & 0.07\\ 0 & 0.02 & -0.83 & -1.7 & 0.73 & -0.65 & 0 & 0.02 & -0.83 & -1.7 & 0.81 & 0.07 & 0\\ 0 & -0.004 & 0.24 & 0.30 & -0.15 & 0 & 0 & 0.004 & -0.24 & -0.30 & 0.16 & 0 & 0\\ -0.004 & 0 & 0.10 & -0.24 & 0.03 & 0.08 & -0.004 & 0 & -0.10 & -0.24 & 0.04 & -0.01 & 0\\ 0 & -0.001 & -0.006 & 0.005 & -0.03 & 0 & 0 & 0.001 & 0.006 & -0.005 & 0.03 & 0 & -0.01\end{bmatrix}\begin{bmatrix}\delta_{\mathrm{lfi}}\\ \delta_{\mathrm{lfo}}\\ \delta_{\mathrm{la}}\\ \delta_{\mathrm{le}}\\ \delta_{\mathrm{ls}}\\ \delta_{\mathrm{pf}}\\ \delta_{\mathrm{rfi}}\\ \delta_{\mathrm{rfo}}\\ \delta_{\mathrm{ra}}\\ \delta_{\mathrm{re}}\\ \delta_{\mathrm{rs}}\\ \delta_{\mathrm{ptv}}\\ \delta_{\mathrm{ytv}}\end{bmatrix} \tag{3.17}$$

$$\begin{bmatrix}\dot{u}_b\\ \dot{v}_b\\ \dot{w}_b\\ \dot{p}\\ \dot{q}\\ \dot{r}\end{bmatrix}=\begin{bmatrix}-0.009 & -0.003 & 0.06 & 0 & -31 & 0 & 0 & -42 & 0\\ 0 & -0.01 & -0.003 & 31 & 0.013 & 0 & 42 & 0 & -878\\ -0.03 & 0.01 & -1.0 & 0.28 & -1.5 & 0 & 0 & 866 & 0\\ 0 & -0.01 & 0.003 & 0 & 0 & 0 & -1.5 & 0 & 0.111\\ 0 & 0 & -0.01 & 0 & 0 & 0 & 0 & -0.98 & 0\\ 0 & -0.002 & 0 & 0 & 0 & 0 & -0.06 & 0 & -0.02\end{bmatrix}\begin{bmatrix}u_b\\ v_b\\ w_b\\ p\\ q\\ r\end{bmatrix}$$

$$+\begin{bmatrix}-0.01 & -0.02 & -0.04 & 0.03 & -0.25 & -0.08 & -0.01 & -0.02 & -0.04 & 0.01 & -0.25\\ 0.03 & 0.03 & 0.009 & 0.02 & 0.11 & 0 & -0.03 & -0.03 & -0.01 & -0.01 & -0.11\\ 0 & 0.05 & -0.84 & -1.7 & 0.67 & -0.65 & 0 & 0.05 & -0.83 & -1.7 & 0.83\\ 0 & -0.009 & 0.24 & 0.30 & -0.10 & 0 & 0 & 0.008 & -0.24 & -0.31 & 0.16\\ -0.004 & -0.001 & -0.10 & -0.23 & 0.02 & -0.08 & -0.004 & 0 & -0.10 & -0.24 & 0.04\\ 0 & -0.003 & -0.005 & 0.006 & -0.03 & 0 & 0 & 0.003 & 0.006 & -0.005 & 0.03\end{bmatrix}\begin{bmatrix}\delta_{\mathrm{lfi}}\\ \delta_{\mathrm{lfo}}\\ \delta_{\mathrm{la}}\\ \delta_{\mathrm{le}}\\ \delta_{\mathrm{ls}}\\ \delta_{\mathrm{pf}}\\ \delta_{\mathrm{rfi}}\\ \delta_{\mathrm{rfo}}\\ \delta_{\mathrm{ra}}\\ \delta_{\mathrm{re}}\\ \delta_{\mathrm{rs}}\end{bmatrix} \tag{3.18}$$

3.5.3 Dynamics and Stability Analysis

The eigenvalues of the 49 linearized systems were extracted in order to find unstable eigenmodes in the open-loop aircraft dynamics. At least one unstable eigenmode was found for every condition, hence it was concluded that the ICE aircraft is inherently unstable for all the considered flight conditions. This is an expected result for two reasons. First, highly maneuverable aircraft are typically designed with inherent instablity in order to maximize maneuverability when operated with stability augmentation systems (SAS) in closed-loop. Second, the absence of a vertical stabilizer in tailless configurations generally implies inherent lateral-directional instability. Although unstable eigenmodes were mostly lateral-directional, also longitudinal unstable modes were found for some flight conditions.

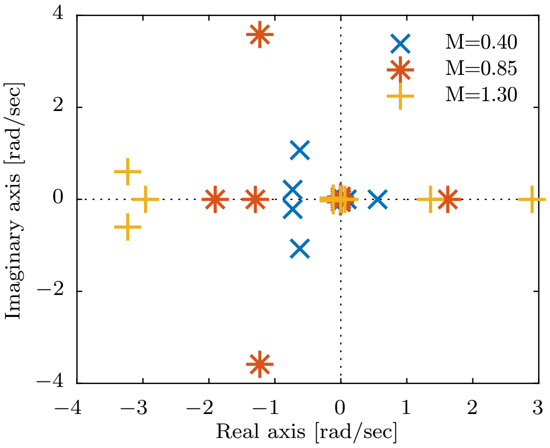

Figure 3.8: ICE eigenmodes on the imaginary plane for different Mach regimes at 20000 ft and nominal mass configuration at 50% internal fuel.

Table 3.8: ICE eigenvalues for different Mach regimes at 20000 ft and nominal mass configuration at 50% internal fuel.

State	Trim condition		
	M=0.40	M=0.85	M=1.3
u_b	$-0.622+1.07i$	$-1.23+3.58i$	2.90
v_b	$-0.622-1.07i$	$-1.23-3.58i$	-2.96
w_b	0.557	-1.904	$-3.23+0.602i$
ϕ	$-0.730+0.212i$	1.62	$-3.23-0.602i$
θ	$-0.730-0.212i$	-1.30	1.36
ψ	0.090	-0.0009	0.061
p	$0.001+0.060i$	$-0.005+0.05i$	$-0.116+0.030i$
q	$0.001-0.060i$	$-0.005-0.05i$	$-0.116-0.030i$
r	0.003	0.006	-0.002

The eigenmodes of the ICE aircraft dynamics for three different Mach regimes at 20000 ft and nominal mass configuration at 50% internal fuel are given as examples in Figure 3.8 and Table 3.8. Note that directional eigenmodes are always unstable, and that at least two damped oscillatory modes appear in all cases. Similar scenarios were found for the rest of flight conditions.

3.5.4 Controllability Analysis

Prior to undertaking the design of adequate flight control systems, analyzing the controllability of the system is essential. Controllability matrices of the linearized systems around the 49 flight conditions considered in this analysis were constructed as

$$C_o = \begin{bmatrix} B & AB & A^2B & \dots & A^{n-1}B \end{bmatrix} \tag{3.19}$$

For all the flight conditions under study, including the modes with and without MTV usage, the controllability matrix C_o was full rank. Therefore it was concluded that the ICE aircraft with the considered control effectors suite is fully controllable for all the flight conditions under study, hence an asymptotically stable flight control system exists for this configuration.

3.6 State of the Art of Control Allocation with ICE

Given the large redundancy of the ICE effectors suite and its innovative configuration, the ICE aircraft has been used in past research to implement and evaluate control allocation systems. The first published control system design for the ICE aircraft was (Ngo et al., 1996), which developed a dynamic inversion control system for subsonic flight with neither LEFs nor SSDs. Ngo et al. (1996) used a control selector based on simple ganging of the control effectors to reduce the number of degrees of freedom to three. The control derivatives were updated from a database storing values for various trim flight conditions.

Buffington (1997) developed a control allocator that considered the full ICE actuator suite. The CA problem was stated as a constrained parameter optimization problem with linear control effectors, solved with sequential linear programming. A control command and axis prioritization scheme was also implemented to maintain decoupled axis responses for unachievable control commands. This is an advantage with respect to direction-preserving command clipping strategies, which were found to exhibit unacceptable cross-axis coupling. Simulations were run with a state-space model of the aircraft linearized around a nominal trim point. Despite the use of a linear effector model, Buffington (1997) stresses the relevance of the highly nonlinear and coupled actuators in the ICE configuration, and suggests the development of nonlinear CA strategies as future work.

Buffington (1999) proposed a control allocation scheme with linear programming using linear control effectors. One of the major improvements of this work with respect to previous implementations was the development of multi-branch control allocation, consisting of two independent linear programs: the error minimization problem in Eq. (2.17) and the control minimization problem in Eq. (2.18). In this scheme, the error minimization problem is solved first. If the commands are attainable, then the best solution according to secondary criteria is chosen by solving the control minimization problem. Buffington (1999) reported problems encountered due to the linear effectors assumption, which did not allow to account for nonlinearities, especially control effector interactions. Such problems were solved by limiting the deflections of the SSD, which underexploits the available control power and the capabilities of the control suite.

The development of reconfigurable control allocation systems in (Davidson et al., 2001a) and (Davidson et al., 2001b) utilized the RWPI method for the ICE model. In the former, the algorithm was extended to account for actuator rate limits, leading to an extended method referred to as frequency-apportioned control allocation. In the latter publication, the limitations of assuming linear control effectiveness were reported. It was suggested that, since the linearity assumption fails in the case of the ICE aircraft, future research effort needs to focus on developing methods that include key control interaction effects and can be solved in real time on flight control computers. For the first time, Davidson et al. (2001b) proposed a cost function for the CA problem that included a term accounting for control effector interactions. However, no method for solving the nonlinear CA problem in real time was proposed, and the simulations in the remainder of the work assumed linear effector models with no interactions. Nevertheless, a very simple static allocation case was solved for comparison between linear and nonlinear control effectiveness models with a nonlinear constrained optimization routine. The results showed that including control interaction effects results in a better tracking of the commanded moments. At this point, the potential benefits of nonlinear control allocation were demonstrated for a very simple case. Future work shall then focus on developing nonlinear CA methods that can be implemented in real-time and safety-critical applications.

The most recently published works on control allocation for the ICE aircraft are (Shtessel et al., 2002; Li, Qin, & Zheng, 2009), both implementing sliding mode control systems. In both cases, control allocation is not a main focus and is addressed with linear control effector models. In the former work, for example, the most coupled and nonlinear effectors (the SSDs and LEFs) were removed from the model to overcome inaccuracies due to control effector interactions.

As discussed earlier, the non negligible presence of strong nonlinearities and interactions in the ICE control effectors has been a known issue since the first studies in control allocation for the ICE aircraft were conducted. However, no suitable solution has been proposed to date.

Chapter 4

Incremental Nonlinear Control Allocation

Most common techniques for nonlinear flight control, such as nonlinear dynamic inversion (NDI) (Snell, Garrard, & Enns, 1990; Enns, Bugajski, Hendrick, & Stein, 1994), operate by computing absolute actuator deflections at each time step. An alternative approach, commonly named incremental nonlinear dynamic inversion (INDI) (Ostroff & Bacon, 2002; Sieberling, Chu, & Mulder, 2010; Simplício, Pavel, van Kampen, & Chu, 2013; Smeur, Chu, & de Croon, 2016) reformulates the nonlinear control problem in incremental form, and operates by computing increments in actuator deflections with respect to the current actuator positions. This incremental control technique has been successfully implemented in aerospace applications (Ostroff & Bacon, 2002; Sieberling et al., 2010; Simplício et al., 2013; Smeur et al., 2016).

This thesis presents an incremental nonlinear control allocation (INCA) approach that operates under the incremental scheme typical of incremental flight control systems. The INCA scheme relies upon angular acceleration feedback, actuator position feedback and a Jacobian model of the control effectors. Besides providing a methodology to perform nonlinear control allocation in real time, this scheme has other inherent benefits such as reduction of aerodynamic model dependency, robustness against model mismatch and mitigation of the negative effects of actuator dynamics. The method presented is based on a generalization of the spline-based CA method proposed by Tol et al. (2014). The generic INCA formulation based on the INDI control scheme provides insight into control-related aspects such as real-time performance, robustness, model dependency and actuator dynamics and saturation handling.

This chapter provides a general description of the INCA method. Section 4.1 derives the incremental formulation of the nonlinear control problem, which is extended to the INCA problem formulation in Section 4.2. Translation of actuator constraints and preferences into incremental form is discussed in Section 4.3. In Section 4.4 a typical LCA solver is reformulated in incremental form. Finally, robustness and mitigation of the negative effects of actuator dynamics are discussed in Section 4.5.

4.1 The Nonlinear Control Problem in Incremental Form

Consider the aircraft dynamics expressed in the general form

$$\dot{\mathbf{x}}(t) = \mathbf{f}(\mathbf{x}) + \mathbf{g}(\mathbf{x})\,\boldsymbol{\tau} \tag{4.1}$$

where $\mathbf{x} \in \mathbb{R}^n$ is the state vector and $\boldsymbol{\tau} \in \mathbb{R}^m$ the aerodynamic inputs to the equations of motion. Control allocation in aerospace applications typically concerns attitude control, with $\boldsymbol{\tau} \in \mathbb{R}^3$ being the aerodynamic moments in body frame. The aerodynamic moment inputs can be separated into an exclusively state-dependent part and an input-dependent part

$$\boldsymbol{\tau} = \boldsymbol{\tau}_a + \boldsymbol{\tau}_\delta \tag{4.2}$$

where $\boldsymbol{\tau}_a$ contains the aerodynamic moments generated by the airframe, and $\boldsymbol{\tau}_\delta$ is the control effector model, providing the control-induced moments produced by the actuators. The control effector model can be generally expressed as the nonlinear mapping

$$\boldsymbol{\tau}_\delta = \boldsymbol{\Phi}(\mathbf{x}, \boldsymbol{\delta}) \tag{4.3}$$

Thus, the system dynamics can be rewritten as

$$\dot{\mathbf{x}} = [\mathbf{f}(\mathbf{x}) + \mathbf{g}(\mathbf{x})\,\boldsymbol{\tau}_a] + \mathbf{g}(\mathbf{x})\,\boldsymbol{\Phi}(\mathbf{x}, \boldsymbol{\delta}) = \mathbf{F}(\mathbf{x}) + \mathbf{g}(\mathbf{x})\,\boldsymbol{\Phi}(\mathbf{x}, \boldsymbol{\delta}) \tag{4.4}$$

where $\mathbf{F}(\mathbf{x})$ contains all the effects not produced by the control effectors.

When the control system works in a discrete-time scheme, the dynamic equations of the system can be locally linearized at every time step around the current state $\mathbf{x}_0$ and actuator positions $\boldsymbol{\delta}_0$ as a first-order Taylor expansion:

$$\dot{\mathbf{x}} \approx \dot{\mathbf{x}}_0 + \frac{\partial}{\partial \mathbf{x}} \left[\mathbf{F}(\mathbf{x}) + \mathbf{g}(\mathbf{x})\,\boldsymbol{\Phi}(\mathbf{x}, \boldsymbol{\delta})\right]\Bigg|_{\substack{\boldsymbol{\delta}=\boldsymbol{\delta}_0 \\ \mathbf{x}=\mathbf{x}_0}} (\mathbf{x} - \mathbf{x}_0) + \frac{\partial}{\partial \boldsymbol{\delta}} \left[\mathbf{F}(\mathbf{x}) + \mathbf{g}(\mathbf{x})\,\boldsymbol{\Phi}(\mathbf{x}, \boldsymbol{\delta})\right]\Bigg|_{\substack{\boldsymbol{\delta}=\boldsymbol{\delta}_0 \\ \mathbf{x}=\mathbf{x}_0}} (\boldsymbol{\delta} - \boldsymbol{\delta}_0) \tag{4.5}$$

The time scale separation principle states that, for systems where the derivatives of the states have significantly faster dynamics than the states themselves, the term $(\mathbf{x}-\mathbf{x}_0)$ is small enough to be neglected at high sampling rates. This principle commonly applies to systems where $\boldsymbol{\delta}$ can change significantly faster than $\mathbf{x}$ over a time step, which is the case when the influence of $\boldsymbol{\delta}$ on the derivatives of the states is significantly higher than the influence of the states. This has been proven to be true for aerial vehicles such as aircraft (Sieberling et al., 2010), helicopters (Simplício et al., 2013) and quadrotors (Smeur et al., 2016) at common sampling frequencies of 100 Hz.

Applying the time scale separation principle and setting the virtual control input $\boldsymbol{\nu}(\mathbf{x}) = \dot{\mathbf{x}}$, Eq. (4.5) can be simplified to

$$\boldsymbol{\nu}(\mathbf{x}) = \dot{\mathbf{x}} \approx \dot{\mathbf{x}}_0 + \mathbf{g}(\mathbf{x}_0)\,\frac{\partial \boldsymbol{\Phi}(\mathbf{x}_0, \boldsymbol{\delta}_0)}{\partial \boldsymbol{\delta}} \Delta\boldsymbol{\delta} \tag{4.6}$$

where $\mathbf{g}(\mathbf{x}_0)\,\partial\boldsymbol{\Phi}(\mathbf{x}_0, \boldsymbol{\delta}_0)\,/\partial\boldsymbol{\delta}$ is a control effectiveness Jacobian function that can be nonlinear in $\boldsymbol{\delta}$ and include interactions between input variables. In the three-moment problem, the time derivative of the state vector $\dot{\mathbf{x}}_0$ corresponds to body angular accelerations.

These can be obtained either by direct measurement or state estimation methods as will be discussed later.

At this point the system dynamics can be linearized with an incremental nonlinear dynamic inversion loop by inverting the incremental dynamics in Eq. (4.6):

$$\Delta\boldsymbol{\delta}_c = \left[\frac{\partial\boldsymbol{\Phi}(\mathbf{x}_0,\boldsymbol{\delta}_0)}{\partial\boldsymbol{\delta}}\right]^{-1} \mathbf{g}(\mathbf{x})^{-1}\left[\boldsymbol{\nu}(\mathbf{x}) - \dot{\mathbf{x}}_0\right] \tag{4.7}$$

This incremental control law provides increments of the actuator positions with respect to the current position vector $\boldsymbol{\delta}_0$, such that the absolute actuator position command is computed as

$$\boldsymbol{\delta}_c = \boldsymbol{\delta}_0 + \Delta\boldsymbol{\delta}_c \tag{4.8}$$

This control law linearizes the response between the virtual control input $\boldsymbol{\nu}(\mathbf{x})$ and $\mathbf{x}$. Moreover, model dependency is significantly reduced with respect to typical NDI control laws, since the incremental control law is independent of the aerodynamic terms in $\boldsymbol{\tau}_a$. This reduction in model dependency is due to the acceleration feedback, which provides an estimate of the forces and moments acting on the system at a given time step.

In over-actuated systems the Jacobian $\partial\boldsymbol{\Phi}(\mathbf{x},\boldsymbol{\delta})/\partial\boldsymbol{\delta}$ is a non-square $m\times p$ matrix, and therefore it cannot be inverted to implement the incremental control law in Eq. (4.7). However, a control allocation scheme can be implemented by reformulating the control allocation problem in incremental form with Eq. (4.6).

4.2 The Control Allocation Problem in Incremental Form

Note that Eq. (4.6) establishes an affine relationship between the virtual control input $\boldsymbol{\nu}(\mathbf{x})$ and increments in actuator positions $\Delta\boldsymbol{\delta}$. The nonlinearities and interactions of the control effectors are captured by the Jacobian matrix $\partial\boldsymbol{\Phi}(\mathbf{x}_0,\boldsymbol{\delta}_0)/\partial\boldsymbol{\delta}$, which can be updated for the current state and actuator positions at every time step. To simplify notation, let the Jacobian matrix of $\boldsymbol{\Phi}(\mathbf{x},\boldsymbol{\delta})$ with respect to $\boldsymbol{\delta}$ be denoted as

$$\nabla_{\boldsymbol{\delta}}\boldsymbol{\Phi}(\mathbf{x},\boldsymbol{\delta}) = \frac{\partial\boldsymbol{\Phi}(\mathbf{x},\boldsymbol{\delta})}{\partial\boldsymbol{\delta}} \tag{4.9}$$

and define the pseudo-control input $\mathbf{d}_c \in \mathbb{R}^n$

$$\mathbf{d}_c = \mathbf{g}(\mathbf{x})^{-1}\left[\boldsymbol{\nu}(\mathbf{x}) - \dot{\mathbf{x}}_0\right] \tag{4.10}$$

The INCA problem is formulated as: given the current state $\mathbf{x}_0$, the current control effector positions $\boldsymbol{\delta}_0$, acceleration measurements $\dot{\mathbf{x}}_0$ and a pseudo-control input command $\mathbf{d}_c = \mathbf{g}(\mathbf{x})^{-1}\left[\boldsymbol{\nu}(\mathbf{x}) - \dot{\mathbf{x}}_0\right]$, determine an increment in the control input vector $\Delta\boldsymbol{\delta}$ such that

$$\begin{gathered}\nabla_{\boldsymbol{\delta}}\boldsymbol{\Phi}(\mathbf{x}_0,\boldsymbol{\delta}_0)\,\Delta\boldsymbol{\delta} = \mathbf{d}_c \\ \text{subject to} \quad \underline{\boldsymbol{\Delta\delta}} \leq \boldsymbol{\Delta\delta} \leq \overline{\boldsymbol{\Delta\delta}}\end{gathered} \tag{4.11}$$

where $\underline{\boldsymbol{\Delta\delta}}$ and $\overline{\boldsymbol{\Delta\delta}}$ are the most restrictive upper and lower bounds of the local position and rate constraints of the actuators, translated into local incremental constraints. Note that the INCA control allocator provides required increments of the actuator positions,

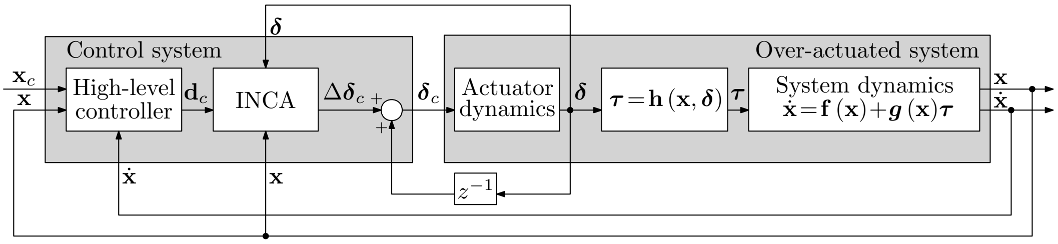

Figure 4.1: Incremental nonlinear control allocation scheme for over-actuated systems.

which must be added to the current actuator positions to obtain the absolute actuator position command. The top-level INCA-based control scheme is depicted in Figure 4.1.

The main advantage of INCA is that the incremental problem formulated in Eq. (4.11) is linear in the increments of actuator positions, and therefore can be solved with simple and efficient linear methods, such as RWPI or QP. The fact that only local increments $\Delta\boldsymbol{\delta}$ are determined at each time step implies that the Jacobian $\nabla_{\boldsymbol{\delta}}\boldsymbol{\Phi}(\mathbf{x},\boldsymbol{\delta})$, which captures nonlinearities and control effector interactions, can be updated for the new state and actuator positions at every time step while the actuators are dynamically driven towards their optimal positions. Thus, the direction of the increments of the control vector may change at every time step, in contrast to conventional LCA methods, which compute absolute positions at each time step. Additionally, actual actuator positions $\boldsymbol{\delta}_0$ are fed back into the system, and therefore the allocation is always performed based on actual actuator position measurements, which mitigates the negative impact of actuator dynamics. In contrast, most conventional CA methods assume $\boldsymbol{\delta}_c = \boldsymbol{\delta}_0$, resulting in coupling effects between control allocators and actuator dynamics (Oppenheimer & Doman, 2004).

Note that an incremental formulation of the control allocation problem was derived for the particular case of multivariate spline-based control systems in (Tol et al., 2014). In this thesis, the method is generalized to incremental flight control systems based on any kind of on-board aerodynamic model with angular acceleration feedback, and focuses on controller-related aspects such as real-time performance, robustness, model dependency and actuator dynamics and saturation handling.

4.3 Incremental Actuator Constraints and Preferences

The incremental formulation of the control allocation problem requires the absolute position and rate constraints of the actuators to be translated into equivalent local constraints in incremental form. Under a discrete-time scheme, rate limits are directly mapped into position limits over a time step Δt as

$$\begin{aligned}\Delta\boldsymbol{\delta}^r_{\max} &= \ \ \dot{\boldsymbol{\delta}}_{\max}\Delta t\\ \Delta\boldsymbol{\delta}^r_{\min} &= -\dot{\boldsymbol{\delta}}_{\max}\Delta t\end{aligned} \tag{4.12}$$

Similarly, absolute position limits can be translated into local constraints imposed over a time step as

$$\begin{aligned}\Delta\boldsymbol{\delta}^p_{\max} &= \boldsymbol{\delta}_{\max} - \boldsymbol{\delta}_0\\ \Delta\boldsymbol{\delta}^p_{\min} &= \boldsymbol{\delta}_{\min} - \boldsymbol{\delta}_0\end{aligned} \tag{4.13}$$

The local upper and lower bounds of the actuator position increments at a given time step are the most restrictive of the local rate and position limits:

$$\begin{aligned} \overline{\Delta\boldsymbol{\delta}} &= \min\left(\dot{\boldsymbol{\delta}}_{\max}\Delta t_s,\ \boldsymbol{\delta}_{\max} - \boldsymbol{\delta}_0\right) \\ \underline{\Delta\boldsymbol{\delta}} &= \max\left(-\dot{\boldsymbol{\delta}}_{\max}\Delta t_s,\ \boldsymbol{\delta}_{\min} - \boldsymbol{\delta}_0\right) \end{aligned} \tag{4.14}$$

Similarly, a reformulation of the preference vector used in typical CA algorithms is required when operating in incremental form. Note that in the INCA problem the preference vector refers to a preferred actuator position increment $\Delta\boldsymbol{\delta}_p$. If the preferred increment is set to $\Delta\boldsymbol{\delta}_p = 0$, the actuators are forced to remain at a constant, possibly nonzero position whenever it is possible. It has been observed that this can lead to complementary actuators (those producing moments of equal magnitude but opposite sign) diverging to asymmetric nonzero deflections while still producing a resultant moment of zero. To avoid this situation and minimize the control effort, the control effectors must be driven to their preferred positions whenever it is possible. Thus, the preferred position increment at each time step must correspond to the increment that brings the actuators closest to their preferred absolute positions $\boldsymbol{\delta}_p$. This is achieved by calculating the incremental preference vector $\Delta\boldsymbol{\delta}_p$ at each time step as

$$\Delta\boldsymbol{\delta}_p = \min\left(\left|\boldsymbol{\delta}_p - \boldsymbol{\delta}_0\right|,\ \left|\overline{\Delta\boldsymbol{\delta}}\right|,\ \left|\underline{\Delta\boldsymbol{\delta}}\right|\right) \cdot \operatorname{sign}\left(\boldsymbol{\delta}_p - \boldsymbol{\delta}_0\right) \tag{4.15}$$

4.4 Solving INCA with Conventional LCA Methods

As previously mentioned, one of the most relevant advantages of INCA is that it allows to solve the nonlinear control allocation problem with simple and efficient linear control allocation methods. With the purpose of demonstrating how typical linear CA methods can be adapted to the INCA scheme, a typical RWPI solver is reformulated in incremental form in this section. Note that this is exposed as an illustrative example, and the same principles apply to solve the INCA problem with other linear CA methods.

To solve the INCA problem with the RWPI method, an explicit solution to the incremental problem in Eq. (4.11) can be found by first solving analytically the unconstrained problem. This problem consists on finding an incremental control vector $\Delta\boldsymbol{\delta}$ that satisfies the control demand $\nabla_{\boldsymbol{\delta}}\boldsymbol{\Phi}(\mathbf{x}_0, \boldsymbol{\delta}_0)\,\Delta\boldsymbol{\delta} = \mathbf{d}_c$, while minimizing a quadratic cost function that penalizes displacement from a preferred increment $\Delta\boldsymbol{\delta}_p$.

The minimization problem is formulated using an ℓ_2-norm cost function as: given an operating point $\mathbf{x}_0$, the current control effector positions $\boldsymbol{\delta}_0$, acceleration measurements $\dot{\mathbf{x}}_0$ and a pseudo-control input command $\mathbf{d}_c = \mathbf{g}(\mathbf{x})^{-1}\left[\boldsymbol{\nu}(\mathbf{x}) - \dot{\mathbf{x}}_0\right]$, determine an increment in the control input vector $\Delta\boldsymbol{\delta}$ such that

$$\begin{aligned} \min_{\Delta\boldsymbol{\delta}}\ \ \mathcal{J} &= \frac{1}{2}\left(\Delta\boldsymbol{\delta} - \Delta\boldsymbol{\delta}_p\right)^T W_{\boldsymbol{\delta}}\left(\Delta\boldsymbol{\delta} - \Delta\boldsymbol{\delta}_p\right) \\ \text{subject to}\quad & \nabla_{\boldsymbol{\delta}}\boldsymbol{\Phi}(\mathbf{x}_0, \boldsymbol{\delta}_0)\,\Delta\boldsymbol{\delta} = \mathbf{d}_c \end{aligned} \tag{4.16}$$

To analytically derive a solution to the unconstrained problem, consider the Hamiltonian

$$\mathcal{H}(\Delta\boldsymbol{\delta}, \boldsymbol{\lambda}) = \frac{1}{2}\left(\Delta\boldsymbol{\delta} - \Delta\boldsymbol{\delta}_p\right)^T W_{\boldsymbol{\delta}}\left(\Delta\boldsymbol{\delta} - \Delta\boldsymbol{\delta}_p\right) + \boldsymbol{\lambda}\left(\nabla_{\boldsymbol{\delta}}\boldsymbol{\Phi}(\mathbf{x}_0, \boldsymbol{\delta}_0)\,\Delta\boldsymbol{\delta} - \mathbf{d}_c\right) \tag{4.17}$$

$$\mathcal{H}(\Delta\boldsymbol{\delta},\boldsymbol{\lambda}) = \frac{1}{2}\left(\Delta\boldsymbol{\delta}^T W_{\boldsymbol{\delta}}\Delta\boldsymbol{\delta} - \Delta\boldsymbol{\delta}_p^T W_{\boldsymbol{\delta}}\Delta\boldsymbol{\delta} - \Delta\boldsymbol{\delta}^T W_{\boldsymbol{\delta}}\Delta\boldsymbol{\delta}_p + \Delta\boldsymbol{\delta}_p^T W_{\boldsymbol{\delta}}\Delta\boldsymbol{\delta}_p\right) + \boldsymbol{\lambda}\left(\nabla_{\boldsymbol{\delta}}\boldsymbol{\Phi}(\mathbf{x}_0,\boldsymbol{\delta}_0)\,\Delta\boldsymbol{\delta} - \mathbf{d}_c\right) \quad (4.18)$$

where $\boldsymbol{\lambda} \in \mathbb{R}^p$ is a Lagrange multiplier. Then, minimize $\mathcal{H}(\Delta\boldsymbol{\delta},\boldsymbol{\lambda})$ by solving

$$\frac{\partial\mathcal{H}}{\partial\Delta\boldsymbol{\delta}} = 0; \qquad \frac{\partial\mathcal{H}}{\partial\boldsymbol{\lambda}} = 0 \quad (4.19)$$

Operating the partial derivatives and solving for $\Delta\boldsymbol{\delta}$ (Lewis & Syrmos, 1995), the biased weighted pseudo-inverse solution is found:

$$\Delta\boldsymbol{\delta} = \Delta\boldsymbol{\delta}_p + \nabla_{\boldsymbol{\delta}}\boldsymbol{\Phi}(\mathbf{x}_0,\boldsymbol{\delta}_0)^{\sharp}\left(\mathbf{d}_c - \nabla_{\boldsymbol{\delta}}\boldsymbol{\Phi}(\mathbf{x}_0,\boldsymbol{\delta}_0)\,\Delta\boldsymbol{\delta}_p\right) \quad (4.20)$$

with

$$\nabla_{\boldsymbol{\delta}}\boldsymbol{\Phi}(\mathbf{x}_0,\boldsymbol{\delta}_0)^{\sharp} = W_{\boldsymbol{\delta}}^{-1}\nabla_{\boldsymbol{\delta}}\boldsymbol{\Phi}(\mathbf{x}_0,\boldsymbol{\delta}_0)^T\left(\nabla_{\boldsymbol{\delta}}\boldsymbol{\Phi}(\mathbf{x}_0,\boldsymbol{\delta}_0)\,W_{\boldsymbol{\delta}}^{-1}\nabla_{\boldsymbol{\delta}}\boldsymbol{\Phi}(\mathbf{x}_0,\boldsymbol{\delta}_0)^T\right)^{-1} \quad (4.21)$$

the generalized weighted pseudo-inverse of $\nabla_{\boldsymbol{\delta}}\boldsymbol{\Phi}(\mathbf{x}_0,\boldsymbol{\delta}_0)$.

Note that the weighted pseudo-inverse solution in Eq. (4.25) does not consider local position and rate constraints, and hence requires further processing. At this point, a feasible solution to the constrained problem can be found with the RWPI method. First, the weighted pseudo-inverse solution is computed with Eq. (4.25). If the found $\Delta\boldsymbol{\delta}$ is within the local incremental limits, the solution is kept. Otherwise, if one or more control effectors violate the incremental limits, the next steps are followed. First, the columns in $\nabla_{\boldsymbol{\delta}}\boldsymbol{\Phi}(\mathbf{x}_0,\boldsymbol{\delta}_0)$ corresponding to the actuators that violate the limits are zeroed, forming an auxiliary matrix $\nabla_{\boldsymbol{\delta}}\boldsymbol{\Phi}(\mathbf{x}_0,\boldsymbol{\delta}_0)_{\text{sat}}$. Second, the saturated[1] values of the effectors that violate local constraints are placed in the preference vector $\Delta\boldsymbol{\delta}_p$, forming an auxiliary preference vector $\Delta\boldsymbol{\delta}_{p,\text{sat}}$. Then, the redistributed weighted pseudo-inverse solution to the auxiliary problem is computed again with $\nabla_{\boldsymbol{\delta}}\boldsymbol{\Phi}(\mathbf{x}_0,\boldsymbol{\delta}_0)_{\text{sat}}$ and $\Delta\boldsymbol{\delta}_{p,\text{sat}}$ as follows:

$$\Delta\boldsymbol{\delta} = \Delta\boldsymbol{\delta}_{p,\text{sat}} + \nabla_{\boldsymbol{\delta}}\boldsymbol{\Phi}(\mathbf{x}_0,\boldsymbol{\delta}_0)^{\sharp}_{\text{sat}}\left(\mathbf{d}_c - \nabla_{\boldsymbol{\delta}}\boldsymbol{\Phi}(\mathbf{x}_0,\boldsymbol{\delta}_0)\,\Delta\boldsymbol{\delta}_{p,\text{sat}}\right) \quad (4.22)$$

Note that two different Jacobian matrices are used in Eq. (4.22): the auxiliary Jacobian matrix to compute the weighted pseudo-inverse $\nabla_{\boldsymbol{\delta}}\boldsymbol{\Phi}(\mathbf{x}_0,\boldsymbol{\delta}_0)^{\sharp}_{\text{sat}}$, and the original Jacobian matrix for the auxiliary preference vector contribution $\nabla_{\boldsymbol{\delta}}\boldsymbol{\Phi}(\mathbf{x}_0,\boldsymbol{\delta}_0)\,\Delta\boldsymbol{\delta}_{p,\text{sat}}$. This process is repeated until all effectors are saturated or a solution within the incremental limits is found. The incremental RWPI algorithm is given in pseudocode in Algorithm 1.

This incremental reformulation of the RWPI method shows how typical and relatively simple CA solvers can be used to perform nonlinear control allocation under the INCA scheme. The same principles used here can be applied to reformulate other linear solvers in incremental form such as the active set algorithm-based QP, as will be shown later in this thesis.

---

[1] In the INCA scheme, the term saturation refers to overcoming the maximum local increments over the current time step, which does not necessarily imply reaching absolute position limits.

Algorithm 1 Redistributed weighted pseudo-inverse in incremental form.

```
Given a pseudo-control input command $\mathbf{d}_c \in \mathbb{R}^m$, an operating point $\mathbf{x}_0 \in \mathbb{R}^n$, the current control effector positions $\boldsymbol{\delta}_0 \in \mathbb{R}^p$ and a control effectiveness Jacobian $\boldsymbol{\Phi}(\mathbf{x}, \boldsymbol{\delta}) \in \mathbb{R}^{m \times p}$:
Compute the local incremental constraints
    $\overline{\Delta\boldsymbol{\delta}} \leftarrow \min\left(\dot{\boldsymbol{\delta}}_{\max}\Delta t_s,\ \boldsymbol{\delta}_{\max} - \boldsymbol{\delta}_0\right)$
    $\underline{\Delta\boldsymbol{\delta}} \leftarrow \max\left(-\dot{\boldsymbol{\delta}}_{\max}\Delta t_s,\ \boldsymbol{\delta}_{\min} - \boldsymbol{\delta}_0\right)$    (4.23)
Translate the absolute preference vector into incremental form
    $\Delta\boldsymbol{\delta}_p \leftarrow \min\left(|\boldsymbol{\delta}_p - \boldsymbol{\delta}_0|,\ |\overline{\Delta\boldsymbol{\delta}}|,\ |\underline{\Delta\boldsymbol{\delta}}|\right) \cdot \mathrm{sign}\left(\boldsymbol{\delta}_p - \boldsymbol{\delta}_0\right)$    (4.24)
Compute the optimal solution to the unconstrained problem
    $\Delta\boldsymbol{\delta} \leftarrow \Delta\boldsymbol{\delta}_p + \nabla_{\boldsymbol{\delta}}\boldsymbol{\Phi}(\mathbf{x}_0, \boldsymbol{\delta}_0)^{\sharp}\left(\mathbf{d}_c - \nabla_{\boldsymbol{\delta}}\boldsymbol{\Phi}(\mathbf{x}_0, \boldsymbol{\delta}_0)\,\Delta\boldsymbol{\delta}_p\right)$    (4.25)
with
    $\nabla_{\boldsymbol{\delta}}\boldsymbol{\Phi}(\mathbf{x}_0, \boldsymbol{\delta}_0)^{\sharp} = W_{\boldsymbol{\delta}}^{-1}\nabla_{\boldsymbol{\delta}}\boldsymbol{\Phi}(\mathbf{x}_0, \boldsymbol{\delta}_0)^T\left(\nabla_{\boldsymbol{\delta}}\boldsymbol{\Phi}(\mathbf{x}_0, \boldsymbol{\delta}_0)\,W_{\boldsymbol{\delta}}^{-1}\nabla_{\boldsymbol{\delta}}\boldsymbol{\Phi}(\mathbf{x}_0, \boldsymbol{\delta}_0)^T\right)^{-1}$    (4.26)
if (ANY $\Delta\boldsymbol{\delta} > \overline{\Delta\boldsymbol{\delta}}$) OR (ANY $\Delta\boldsymbol{\delta} < \underline{\Delta\boldsymbol{\delta}}$) then
    $n_{\mathrm{sat}} \leftarrow$ Number of saturated actuators
    while ((ANY $\Delta\boldsymbol{\delta} > \overline{\Delta\boldsymbol{\delta}}$) OR (ANY $\Delta\boldsymbol{\delta} < \underline{\Delta\boldsymbol{\delta}}$)) AND ($n_{\mathrm{sat}} < p$) do
        $\nabla_{\boldsymbol{\delta}}\boldsymbol{\Phi}(\mathbf{x}_0, \boldsymbol{\delta}_0)_{\mathrm{sat}} \leftarrow \nabla_{\boldsymbol{\delta}}\boldsymbol{\Phi}(\mathbf{x}_0, \boldsymbol{\delta}_0)$ with zeroed columns for saturated actuators.
        $\Delta\boldsymbol{\delta}_{p,\mathrm{sat}} \leftarrow \Delta\boldsymbol{\delta}$ with saturated increments for saturated actuators.
        $\Delta\boldsymbol{\delta} \leftarrow \Delta\boldsymbol{\delta}_{p,\mathrm{sat}} + \nabla_{\boldsymbol{\delta}}\boldsymbol{\Phi}(\mathbf{x}_0, \boldsymbol{\delta}_0)^{\sharp}_{\mathrm{sat}}\left(\mathbf{d}_c - \nabla_{\boldsymbol{\delta}}\boldsymbol{\Phi}(\mathbf{x}_0, \boldsymbol{\delta}_0)\,\Delta\boldsymbol{\delta}_{p,\mathrm{sat}}\right)$
        $n_{\mathrm{sat}} \leftarrow$ Number of saturated actuators
    end while
end if
```

4.5 Robustness and Implementation Particularities

Two important advantages of INCA are its robustness against aerodynamic model mismatch and its ability to deal with actuator dynamics in real time. These features are provided by two feedback loops present in the INCA control scheme: an acceleration feedback loop and an actuator position feedback loop.

Unlike typical NDI-based flight control systems, the INCA control law in Eq. (4.6) depends only on the control effectiveness Jacobian of the system, and is independent from the state-dependent part of the system dynamics $\mathbf{F}(\mathbf{x}) = \mathbf{f}(\mathbf{x}) + \mathbf{g}(\mathbf{x})\,\boldsymbol{\tau}_a$. This fact alone improves robustness against aerodynamic model mismatch with respect to conventional control systems. Note, however, that the incremental linearization law in Eq. (4.10) depends on a Jacobian model of the control effectiveness function with respect to $\boldsymbol{\delta}$, and thus one may be concerned about the sensitivity of the INCA performance to Jacobian model mismatch. As will be shown in the next chapter, in aircraft attitude control the acceleration feedback $\dot{\mathbf{x}}_0$ corresponds to the angular acceleration $\dot{\boldsymbol{\omega}}_0$, the virtual control input $\boldsymbol{\nu}(\mathbf{x})$ to an angular acceleration command $\dot{\boldsymbol{\omega}}_c$ and $\mathbf{g}(\mathbf{x})^{-1}$ to the matrix of inertia of the aircraft J. Consequently, the pseudo-control input $\mathbf{d}_c$ is equivalent to a commanded increment in control-induced moments $\Delta\boldsymbol{\tau}_c = J\left[\dot{\boldsymbol{\omega}}_c - \dot{\boldsymbol{\omega}}_0\right]$. The pseudo-control command can be rewritten as

$$\Delta\boldsymbol{\tau}_c = J\dot{\boldsymbol{\omega}}_c - J\dot{\boldsymbol{\omega}}_0 = \boldsymbol{\tau}_c - \boldsymbol{\tau}_0 \tag{4.27}$$

where the angular acceleration command $\dot{\boldsymbol{\omega}}_c$ is provided by an outer control loop and the current angular accelerations $\dot{\boldsymbol{\omega}}_0$ are provided by a feedback loop through state estimation or angular acceleration measurement. This acceleration feedback provides real-time information about the actual moments acting upon the system at each time step, providing added robustness against Jacobian model mismatch. A sensitivity analysis that will be discussed later in this thesis revealed that a rough estimation of the sign and magnitude of the Jacobian terms suffices to obtain satisfactory performance, and that large errors in the model can be handled by the robustness of the acceleration feedback loop.

Another point to address is whether an accurate measurement/estimate of the angular accelerations can be obtained in real time with acceptable sampling rates and delays. Incremental control with acceleration feedback has been satisfactorily implemented in previous research, see (Bacon & Ostroff, 2000; Sieberling et al., 2010; Simplício et al., 2013; Smeur et al., 2016). Smeur et al. (2016) implemented an INDI control system based on angular accelerometers for a quadrotor with fast dynamics, showing high performance, disturbance rejection and adaptiveness properties through flight testing. Implementation issues regarding delays occurring when deriving angular accelerations from angular rate measurements were successfully addressed. The most relevant point of this work for the questions hereby regarded is the demonstration of the feasibility of implementing incremental flight control systems relying on angular acceleration feedback. This has been also proven in further not yet published work at Delft University of Technology.

The second advantage of INCA discussed here is the minimization of negative effects of control effector dynamics on the control allocation performance. Most conventional control allocation methods (except for the explicitly dynamic control allocation methods discussed in Section 2.4) operate in open loop with regard to actuator positions, i.e. position commands $\boldsymbol{\delta}_c$ are sent to the actuators assuming $\boldsymbol{\delta}_0 = \boldsymbol{\delta}_c$. Under the INCA scheme, however, only increments with respect to the current actuator positions are computed at each time step, and therefore every incremental command is computed over the actual actuator positions, regardless of previous commands. This actuator position feedback loop eliminates the inaccuracies implied by the assumption $\boldsymbol{\delta}_0 = \boldsymbol{\delta}_c$. Thus, the actuators are dynamically driven towards the desired positions through small increments using updated information about their control effectiveness and actual positions at every time step. In practical implementation, the actuator position feedback may be achieved either through a companion model of the actuator dynamics or through measurements from actuator position sensors, which are relatively simple to obtain.

Chapter 5

Flight Control System Design

In order to test the INCA concept and assess its performance with respect to conventional LCA methods, an LCA-based and an INCA-based flight control systems were designed for the ICE aircraft. INCA and LCA were implemented with the RWPI and the active set-based QP control allocation solvers in order to extract performance metrics with different typical CA methods. The control allocation systems were applied to angular body rate control, the innermost loop of the FCS. The body rate loop was augmented with a pseudo-control hedging loop as a partial flight envelope protection and anti-windup system. Different kinds of outer loops were implemented, ranging from manual input loops to flight path guidance modes.

This chapter presents and discusses the design of both the LCA-based and the INCA-based flight control systems. The design of the innermost control loops where LCA and INCA are implemented for body rate control is discussed in Sections 5.1 and 5.2 respectively. These sections also include descriptions of the on-board models used for each type of controller and their derivation. The implementation of pseudo-control hedging as a method to handle actuator saturation is discussed in Section 5.4. Finally, Section 5.5 presents the design of the different outer loops implemented to complete the flight control system.

5.1 LCA-Based Flight Control System Design

The conventional LCA-based flight control system designed for the ICE aircraft is based on aerodynamic model inversion and includes a linear control effector model. This section discusses the identification of the linear control effector model, its adaptation to mitigate issues regarding nonlinearities of the ICE aerodynamics and the design of the LCA-based angular rate control law.

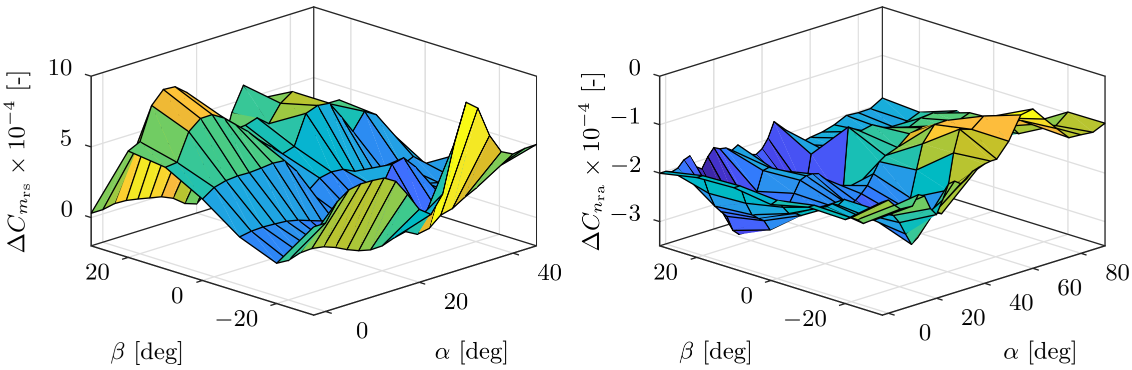

(a) Pitching moment control derivative of the right SSD.

(b) Yawing moment control derivative of the right AMT.

Figure 5.1: Examples of control derivatives scheduled for α and β.

5.1.1 Linear Control Effectors Model

As discussed in previous chapters, LCA methods require an on-board aerodynamic model in which the control-induced moments are affine in the actuator positions $\boldsymbol{\delta}$. Note, however that the aerodynamic terms and control derivatives can remain nonlinear functions of α, β and M. A linear control effector model was derived by using linear regressors to identify aerodynamic coefficients and control derivatives as functions of α, β and M at the data points available in the ICE aerodynamic database. In order to decouple the inputs, the interaction effects between control effectors were eliminated from the original database. The obtained coefficients and derivatives were stored in lookup tables. The structure of the affine aerodynamic model is

$$\begin{aligned} C_l &= C_{l_a}(\alpha,\beta,M) + \sum_{i=1}^{13} \Delta C_{l,\delta_i}(\alpha,\beta,M)\,\delta_i \\ C_m &= C_{m_a}(\alpha,\beta,M) + \sum_{i=1}^{13} \Delta C_{m,\delta_i}(\alpha,\beta,M)\,\delta_i \\ C_n &= C_{n_a}(\alpha,\beta,M) + \sum_{i=1}^{13} \Delta C_{n,\delta_i}(\alpha,\beta,M)\,\delta_i \end{aligned} \tag{5.1}$$

with $\Delta C_{j,\delta_i}$ the control derivative of $j = \{l, m, n\}$ with respect to δ_i, and

$$\begin{aligned} C_{l_a}(\alpha,\beta,M) &= C_{l,\alpha}(\alpha,M) + C_{l,\beta}(\alpha,\beta,M) + \frac{pb}{2V}C_{l,p}(\alpha,M) + \frac{rb}{2V}C_{l,r}(\alpha,M) \\ C_{m_a}(\alpha,\beta,M) &= C_{m,\alpha}(\alpha,M) + C_{m,\beta}(\alpha,\beta,M) + \frac{q\bar{c}}{2V}C_{m,q}(\alpha,M) \\ C_{n_a}(\alpha,\beta,M) &= C_{n,\alpha}(\alpha,M) + C_{n,\beta}(\alpha,\beta,M) + \frac{pb}{2V}C_{n,p}(\alpha,M) + \frac{rb}{2V}C_{n,r}(\alpha,M) \end{aligned} \tag{5.2}$$

the dimensionless nonlinear moments generated by the airframe. Examples of identified control derivatives scheduled for α and β are shown in Figure 5.1.

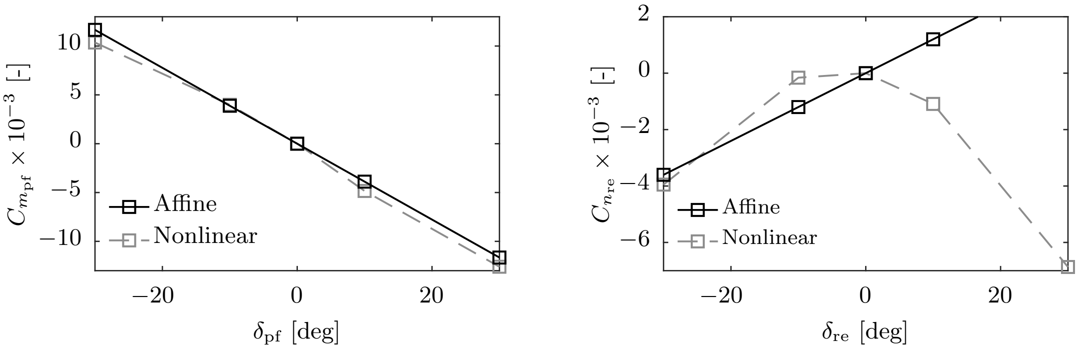

(a) Pitching moment of pitch flaps.

(b) Yawing moment of right elevon.

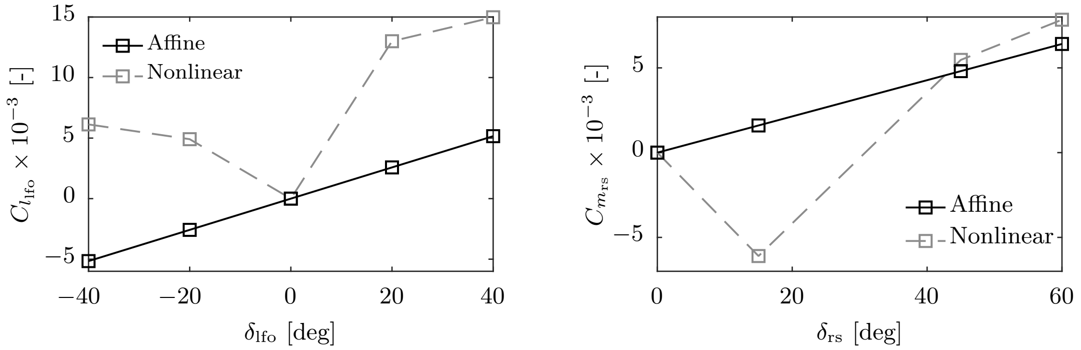

(c) Rolling moment of outboard LEF.

(d) Pitching moment of right SSD.

Figure 5.2: Linear control effectors model compared to original aerodynamic data.

As discussed earlier, the assumption of linearity in control-induced moments is accurate enough in some cases (see the pitching moment characteristic of the pitch flap in Figure 5.2a), but in other cases it fails to capture important effects. The parabolic yawing moment curve of the right elevon shown in Figure 5.2b is an example of the impossibility of linear models to capture parabolic yawing moment curves of horizontal control surfaces. Other examples of bad fitting are the rolling moment curve of the outboard LEF in Figure 5.2c and the pitching moment curve of the right SSD in Figure 5.2d. It can be observed that, due to these inaccuracies, the moments predicted by the linear model can have opposite sign than the actually produced moments, which can lead to instability of the closed-loop system. In order to achieve a stable LCA-based controller, the affine model requires certain adaptations, which will be discussed later in this section.

The nonlinear MTV model in Eq. (3.5) also requires linearization to be used in LCA. The pitching moment from the MTV can be derived from the first-order Taylor expansion of the pitching moment term $\boldsymbol{\tau}_{y_{\mathrm{T}}}$ around δ_{ptv}

$$\boldsymbol{\tau}_{y_{\mathrm{T}}} = -\mathrm{T}d_n \sin(\delta_{\mathrm{ptv}}) \approx \boldsymbol{\tau}_{y_{\mathrm{T}}}\bigg|_{\delta_{\mathrm{ptv}}=0} + \frac{\partial\left(\boldsymbol{\tau}_{y_{\mathrm{T}}}\right)}{\partial\delta_{\mathrm{ptv}}}\bigg|_{\delta_{\mathrm{ptv}}=0} \delta_{\mathrm{ptv}} = -\mathrm{T}d_n \cos(\delta_{\mathrm{ptv}})\bigg|_{\delta_{\mathrm{ptv}}=0} \delta_{\mathrm{ptv}} \tag{5.3}$$

which yields the linear approximation

$$\boldsymbol{\tau}_{y_{\mathrm{T}}} \approx -\mathrm{T}d_n\delta_{\mathrm{ptv}} \tag{5.4}$$

Similarly, using the first-order Taylor expansion of the yawing moment term $\boldsymbol{\tau}_{z_\mathrm{T}}$

$$\begin{aligned}\boldsymbol{\tau}_{z_\mathrm{T}} = -\mathrm{T}d_n\cos(\delta_\mathrm{ptv})\tan(\delta_\mathrm{ytv}) &\approx \boldsymbol{\tau}_{z_\mathrm{T}}\Big|_{\substack{\delta_\mathrm{ptv}\,=\,0\\ \delta_\mathrm{ytv}\,=\,0}} + \frac{\partial\left(\boldsymbol{\tau}_{z_\mathrm{T}}\right)}{\partial\delta_\mathrm{ptv}}\Big|_{\substack{\delta_\mathrm{ptv}\,=\,0\\ \delta_\mathrm{ytv}\,=\,0}}\delta_\mathrm{ptv} + \frac{\partial\left(\boldsymbol{\tau}_{z_\mathrm{T}}\right)}{\partial\delta_\mathrm{ytv}}\Big|_{\substack{\delta_\mathrm{ptv}\,=\,0\\ \delta_\mathrm{ytv}\,=\,0}}\delta_\mathrm{ytv}\\ &= \mathrm{T}d_n\sin(\delta_\mathrm{ptv})\tan(\delta_\mathrm{ytv})\Big|_{\substack{\delta_\mathrm{ptv}\,=\,0\\ \delta_\mathrm{ytv}\,=\,0}}\delta_\mathrm{ptv} - \frac{Td_n\cos(\delta_\mathrm{ptv})}{\cos^2(\delta_\mathrm{ytv})}\Big|_{\substack{\delta_\mathrm{ptv}\,=\,0\\ \delta_\mathrm{ytv}\,=\,0}}\delta_\mathrm{ytv}\end{aligned} \tag{5.5}$$

the next affine aproximation is found:

$$\boldsymbol{\tau}_{z_\mathrm{T}} \approx -\mathrm{T}d_n\delta_\mathrm{ytv} \tag{5.6}$$

Thus, an affine approximation of the MTV control moments is given by

$$\boldsymbol{\tau}_\mathrm{T} = -\mathrm{T}d_n\begin{bmatrix}0\\ \delta_\mathrm{ptv}\\ \delta_\mathrm{ytv}\end{bmatrix} \tag{5.7}$$

The MTV vector is subject to a circular constraint imposed over the ℓ_2 norm of the vector $\boldsymbol{\delta}_\mathrm{tv} = (\delta_\mathrm{ptv}, \delta_\mathrm{ytv})$. When the MTV vector violates the circular constraint, it is re-scaled into the boundary of the feasible subspace by keeping the original direction of $\boldsymbol{\delta}_\mathrm{tv}$ (see Figure 5.3):

$$\boldsymbol{\delta}'_\mathrm{tv} = \frac{\boldsymbol{\delta}_{\mathrm{tv}_\mathrm{max}}}{||\delta_\mathrm{tv}||}\delta_\mathrm{tv} \tag{5.8}$$

Wrapping up the control derivative terms into a control effectiveness matrix $B(\mathbf{x})$, the aerodynamic moments can be expressed in input-affine form as

$$\boldsymbol{\tau} = \boldsymbol{\tau}_a + \boldsymbol{\tau}_e = \frac{1}{2}\rho V^2 S\left(\begin{bmatrix}bC_{l_a}(\mathbf{x})\\ \bar{c}C_{m_a}(\mathbf{x})\\ bC_{n_a}(\mathbf{x})\end{bmatrix} + B(\mathbf{x})\,\boldsymbol{\delta}\right) \tag{5.9}$$

5.1.2 Angular Rate Control Loop

The innermost control loop controls the body angular rates $\boldsymbol{\omega} = [p\ q\ r]$ through commanded moments $\boldsymbol{\tau}_c$. Consider the aircraft rotational dynamic equations

$$\dot{\boldsymbol{\omega}} = J^{-1}\left(\boldsymbol{\tau} - \boldsymbol{\omega}\times J\boldsymbol{\omega}\right) = J^{-1}\boldsymbol{\tau}_e + J^{-1}\left(\boldsymbol{\tau}_a - \boldsymbol{\omega}\times I\boldsymbol{\omega}\right) \tag{5.10}$$

The aerodynamic moments produced by the airframe include the contributions from the trim positions of the actuators:

$$\boldsymbol{\tau}_a = \frac{1}{2}\rho V^2 S\left(\begin{bmatrix}bC_{l_a}(\mathbf{x})\\ \bar{c}C_{m_a}(\mathbf{x})\\ bC_{n_a}(\mathbf{x})\end{bmatrix} + B(\mathbf{x})\,\boldsymbol{\delta}_\mathrm{trim}\right) \tag{5.11}$$

Setting the angular acceleration as a virtual control input $\boldsymbol{\nu}_\omega(\mathbf{x}) = \dot{\boldsymbol{\omega}}$ and solving Eq. (5.10) for the required moments $\boldsymbol{\tau}_c = \boldsymbol{\tau}_e$ leads to the model-based inversion control law

$$\boldsymbol{\tau}_c = I\boldsymbol{\nu}_\omega(\mathbf{x}) - \frac{1}{2}\rho V^2 S\left(\begin{bmatrix}bC_{l_a}(\mathbf{x})\\ \bar{c}C_{m_a}(\mathbf{x})\\ bC_{n_a}(\mathbf{x})\end{bmatrix} + B(\mathbf{x})\,\boldsymbol{\delta}_\mathrm{trim}\right) + \boldsymbol{\omega}\times I\boldsymbol{\omega} \tag{5.12}$$

which linearizes the system between the virtual control input $\boldsymbol{\nu}_\omega(\mathbf{x})$ and $\boldsymbol{\omega}$. The required moments $\boldsymbol{\tau}_c$ are distributed over $\boldsymbol{\delta}$ by a linear control allocator. The linearized system can now be controlled through the virtual control input $\boldsymbol{\nu}_\omega(\mathbf{x})$ such that the output follows a reference command $\boldsymbol{\omega}_c$, by using an outer state-feedback linear control law

$$\boldsymbol{\nu}_\omega(\mathbf{x}) = \mathbf{K}_{\omega_P}\left(\boldsymbol{\omega} - \boldsymbol{\omega}_c\right) + \mathbf{K}_{\omega_I}\int\left(\boldsymbol{\omega} - \boldsymbol{\omega}_c\right)dt + \mathbf{K}_{\omega_D}\left(\dot{\boldsymbol{\omega}} - \dot{\boldsymbol{\omega}}_c\right) \tag{5.13}$$

5.1.3 Adaptation of the Linear Model

As previously shown, the identified affine model fails to capture nonlinear moments, which is particularly critical for parabolic and non-monotonic moment curves (e.g. those shown in Figures 5.2b-5.2d). Since such errors can cause instability of the closed loop, the linear model needs to be adapted to ensure minimally acceptable performance.

The AMT, inboard LEF and SSD are restricted to deflect in one direction only. Thus, their yawing moment curves are half-parabolas, which can be approximated with a linear model accepting a reasonable mismatch, which can be absorbed by the robustness of the controller. The elevons and outboard LEF, however, can deflect in two directions, thus having parabolic yawing moment curves. Since these actuators are not primary sources of directional control power, their yawing moment derivatives were set to zero in the control effectiveness matrix. As a consequence, these effectors are used to produce pitching and rolling moments only, whereas their secondary-axis yawing moments are seen by the control system as external disturbances, which need to be compensated by other yawing moment-generating actuators.

These necessary simplifications of the model have two detrimental consequences on the overall performance of the flight control system. First, the potential of the ICE control effectors suite is underexploited (e.g. elevons cannot be used to produce yawing moments, which might be necessary in failure conditions or extreme maneuvers). Second, the yawing moments produced by the elevons and outboard LEF are seen as external disturbances, and need to be continuously suppressed by other control effectors.

5.2 INCA-Based Flight Control System Design

The INCA-based flight control system implements the incremental control scheme derived in Chapter 4. This section discusses the Jacobian model used in the INCA algorithm and the derivation of the INCA angular rate control law.

5.2.1 Multivariate Simplex Spline-Based Jacobian Model

As discussed in Chapter 4, the INCA method has a more relaxed dependency on an on-board aerodynamic model and therefore is more robust against model uncertainties. Instead of a full aerodynamic model, INCA is based on a control effectiveness Jacobian model $\nabla_{\boldsymbol{\delta}}\Phi\left(\mathbf{x}, \boldsymbol{\delta}\right)$ that includes the directional derivatives of $\boldsymbol{\tau}_e$ with respect to $\boldsymbol{\delta}$.

In this thesis, the Jacobian control effectiveness matrix is derived from a multivariate simplex spline-based aerodynamic model of the ICE aircraft identified from the high-fidelity aerodynamic database described in Chapter 3. This spline model preserves the original model structure of the nonlinear aerodynamic coefficients:

$$\begin{aligned} C_i = {} & + C^s_{i_1}(\alpha, M) + C^s_{i_2}(\alpha, \beta, M) + C^s_{i_3}(\alpha, \delta_{\text{ls}}, \delta_{\text{le}}, M) + C^s_{i_4}(\alpha, \delta_{\text{rs}}, \delta_{\text{re}}, M) \\ & + C^s_{i_5}(\alpha, \beta, \delta_{\text{lfi}}) + C^s_{i_6}(\alpha, \beta, \delta_{\text{rfi}}) + C^s_{i_7}(\alpha, \beta, \delta_{\text{lfi}}, \delta_{\text{lfo}}, M) + C^s_{i_8}(\alpha, \beta, \delta_{\text{rfi}}, \delta_{\text{rfo}}, M) \\ & + C^s_{i_9}(\alpha, \delta_{\text{lfo}}, \delta_{\text{la}}) + C^s_{i_{10}}(\alpha, \delta_{\text{rfo}}, \delta_{\text{ra}}) + C^s_{i_{11}}(\alpha, \delta_{\text{la}}, \delta_{\text{le}}) + C^s_{i_{12}}(\alpha, \delta_{\text{ra}}, \delta_{\text{re}}) \\ & + C^s_{i_{13}}(\alpha, \delta_{\text{rs}}, \delta_{\text{ls}}, \delta_{\text{pf}}, M) + C^s_{i_{14}}(\alpha, \beta, \delta_{\text{la}}) + C^s_{i_{15}}(\alpha, \beta, \delta_{\text{ra}}) + C^s_{i_{16}}(\alpha, \beta, \delta_{\text{ls}}) \\ & + C^s_{i_{17}}(\alpha, \beta, \delta_{\text{rs}}) + \frac{pb}{2V} C^s_{i_{18}}(\alpha, M) + \frac{q\bar{c}}{2V} C^s_{i_{19}}(\alpha, M) + \frac{rb}{2V} C^s_{i_{20}}(\alpha, M) \end{aligned} \tag{5.14}$$

with $i = \{l, m, n, X, Y, Z\}$, where every model term $C^s_{i_n}$ is a multivariate B-spline defined over a simplex triangulation with 0th-order continuity. This model was identified from the original ICE aerodynamic database in (van der Peijl, de Visser, & Niestroy, 2017) following the linear regression techniques presented in (de Visser, Chu, & Mulder, 2009). Including all the model terms corresponding to every dimensionless aerodynamic moment and force coefficients, the spline model consists on 108 spline functions.

From this model, the directional derivatives of every term $C^s_{i_j}$ in the directions of $\boldsymbol{\delta}$ can be computed in a computationally efficient way with the method for model reduction of parabolic partial differential equations presented in (Tol et al., 2014; Tol, de Visser, & Kotsonis, 2016). This yields 13 partial derivatives of each of the 108 spline models, from which the control effectiveness Jacobian matrix is constructed as:

$$\nabla_{\boldsymbol{\delta}} \Phi(\alpha, \beta, M, \boldsymbol{\delta}) = \begin{bmatrix} \sum_{j=1}^{20} \frac{\partial C^s_{l_j}(\mathbf{x}, \boldsymbol{\delta})}{\partial \delta_1} & \sum_{j=1}^{20} \frac{\partial C^s_{l_j}(\mathbf{x}, \boldsymbol{\delta})}{\partial \delta_2} & \cdots & \sum_{j=1}^{20} \frac{\partial C^s_{l_j}(\mathbf{x}, \boldsymbol{\delta})}{\partial \delta_{13}} \\ \sum_{j=1}^{20} \frac{\partial C^s_{m_j}(\mathbf{x}, \boldsymbol{\delta})}{\partial \delta_1} & \sum_{j=1}^{20} \frac{\partial C^s_{m_j}(\mathbf{x}, \boldsymbol{\delta})}{\partial \delta_2} & \cdots & \sum_{j=1}^{20} \frac{\partial C^s_{m_j}(\mathbf{x}, \boldsymbol{\delta})}{\partial \delta_{13}} \\ \sum_{j=1}^{20} \frac{\partial C^s_{n_j}(\mathbf{x}, \boldsymbol{\delta})}{\partial \delta_1} & \sum_{j=1}^{20} \frac{\partial C^s_{n_j}(\mathbf{x}, \boldsymbol{\delta})}{\partial \delta_2} & \cdots & \sum_{j=1}^{20} \frac{\partial C^s_{n_j}(\mathbf{x}, \boldsymbol{\delta})}{\partial \delta_{13}} \end{bmatrix} \tag{5.15}$$

The Jacobian calculation was implemented on a real-time, highly optimized routine that can provide in the order of 10^4 Jacobian calculations per second.

To ensure that the Jacobian terms provide correct signs, the zero-crossing points were imposed as a constraint in the model identification process. Note that a key factor for the accuracy of the Jacobian terms is the continuity order between simplices. In this case, 0th-order continuity was used, and therefore the model represents the worst possible case in terms of continuity. This implies that the performance achieved in this thesis can be substantially improved by increasing the continuity order of the spline model.

Note that with the general formulation of the INCA method presented here, the Jacobian model is not restricted to spline-based models. For instance, a locally linear numerical differentiation approach with a lookup table-based aerodynamic model could also be used to approximate the nonlinear Jacobian. In such a case, the spline model would not be necessary. A spline model was used in this thesis because it provides an elegant way to

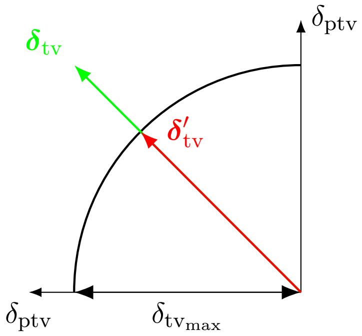

Figure 5.3: Thrust vector constraints in absolute form.

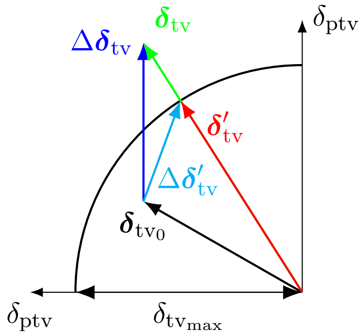

Figure 5.4: Thrust vector constraints in incremental form.

extend the INCA-based FCS into a fault-tolerant flight control system in future work. Splines are function approximators that can be used in an on-line system identification framework, in contrast to lookup table-based models.

5.2.2 Multi-Axis Thrust Vectoring Jacobian Model

A Jacobian model providing the directional derivatives of the control moments produced by MTV can be obtained analytically by deriving the Jacobian matrix of $\boldsymbol{\tau}_T$ in Eq. (3.5):

$$\nabla_{\delta_{\text{tv}}}\boldsymbol{\tau}_{\text{T}}(\delta_{\text{ptv}},\delta_{\text{ytv}}) = \text{T}d_n \begin{bmatrix} 0 & 0 \\ -\cos(\delta_{\text{ptv}}) & 0 \\ \sin(\delta_{\text{ptv}})\tan(\delta_{\text{ytv}}) & -\cos(\delta_{\text{ptv}})/\cos^2(\delta_{\text{ytv}}) \end{bmatrix} \tag{5.16}$$

The MTV circular constraints in incremental form require further consideration. In an incremental control allocation scheme, the control allocator provides a commanded increment $\Delta\boldsymbol{\delta}_{\text{tv}}$ over the current actuator position $\boldsymbol{\delta}_{\text{tv}_0}$. If the resulting MTV deflection vector $\boldsymbol{\delta}_{\text{tv}} = \boldsymbol{\delta}_{\text{tv}_0} + \Delta\boldsymbol{\delta}_{\text{tv}}$ violates the circular constraint, then a new increment $\Delta\boldsymbol{\delta}'_{\text{tv}}$ must be computed such that the new resulting vector $\boldsymbol{\delta}'_{\text{tv}} = \boldsymbol{\delta}_{\text{tv}_0} + \Delta\boldsymbol{\delta}'_{\text{tv}}$ satisfies the circular constraint while preserving the original direction of $\boldsymbol{\delta}_{\text{tv}}$. This usually involves changing the modulus and direction of $\Delta\boldsymbol{\delta}_{\text{tv}}$, as depicted in Figure (5.4). The new deflection increment is computed as

$$\Delta\boldsymbol{\delta}'_{\text{tv}} = \frac{\delta_{\text{tv}_{\max}}}{||\boldsymbol{\delta}_{\text{tv}_\mathbf{0}} + \Delta\boldsymbol{\delta}_{\text{tv}}||}\left(\boldsymbol{\delta}_{\text{tv}_\mathbf{0}} + \Delta\boldsymbol{\delta}_{\text{tv}}\right) - \boldsymbol{\delta}_{\text{tv}_\mathbf{0}} \tag{5.17}$$

5.2.3 Angular Rate Control Loop

INCA is implemented at the innermost control loop for body angular rate control. Consider the aircraft rotational dynamic equations, where $\boldsymbol{\tau}_e$ is now replaced by the nonlinear control effector model $\boldsymbol{\Phi}(\mathbf{x},\boldsymbol{\delta})$:

$$\dot{\boldsymbol{\omega}} = J^{-1}\left(\boldsymbol{\tau} - \boldsymbol{\omega}\times J\boldsymbol{\omega}\right) = J^{-1}\boldsymbol{\Phi}(\mathbf{x},\boldsymbol{\delta}) + J^{-1}\left(\boldsymbol{\tau}_a - \boldsymbol{\omega}\times J\boldsymbol{\omega}\right) \tag{5.18}$$

For a given time step, the incremental form of the rotational dynamics as a first-order Taylor expansion at the operating point $(\mathbf{x}_0, \boldsymbol{\delta}_0)$ is:

$$\begin{aligned}\dot{\boldsymbol{\omega}} \simeq \dot{\boldsymbol{\omega}}_0 &+ \frac{\partial}{\partial \boldsymbol{\omega}} \left[J^{-1}\boldsymbol{\Phi}(\mathbf{x}, \boldsymbol{\delta}) + J^{-1}\left(\boldsymbol{\tau}_a - \boldsymbol{\omega} \times J\boldsymbol{\omega}\right)\right]\Big|_{\substack{\boldsymbol{\delta}=\boldsymbol{\delta}_0 \\ \mathbf{x}=\mathbf{x}_0}} (\boldsymbol{\omega} - \boldsymbol{\omega}_0) \\ &+ \frac{\partial}{\partial \boldsymbol{\delta}} \left[J^{-1}\boldsymbol{\Phi}(\mathbf{x}, \boldsymbol{\delta}) + J^{-1}\left(\boldsymbol{\tau}_a - \boldsymbol{\omega} \times J\boldsymbol{\omega}\right)\right]\Big|_{\substack{\boldsymbol{\delta}=\boldsymbol{\delta}_0 \\ \mathbf{x}=\mathbf{x}_0}} (\boldsymbol{\delta} - \boldsymbol{\delta}_0)\end{aligned} \tag{5.19}$$

where the angular accelerations at the current step $\dot{\boldsymbol{\omega}}_0$ can be obtained from angular accelerometers, signal processing or acceleration estimation methods.

According to the previously discussed time scale separation principle, the second term of the right-hand side of Eq. (5.19), i.e. the changes in angular acceleration due to changes in angular rates, is negligible for high sampling rates in comparison to the input-dependent term. This was explained by Sieberling et al. (2010) as follows. Increments in actuator positions directly cause angular accelerations. Angular rates, however, only vary as a consequence of integrating angular accelerations, i.e. integrating the actuator deflection contributions. Therefore, when the sampling frequency of the FCC is high enough[1], the assumption $(\boldsymbol{\omega} - \boldsymbol{\omega}_0) \approx 0$ is valid.

Applying time scale separation and operating the partial derivatives, the incremental dynamic rotational equations are obtained as a function of the current angular accelerations and actuator positions:

$$\dot{\boldsymbol{\omega}} = \dot{\boldsymbol{\omega}}_0 + J^{-1}\nabla_{\boldsymbol{\delta}}\boldsymbol{\Phi}(\mathbf{x}_0, \boldsymbol{\delta}_0)\,\Delta\boldsymbol{\delta} \tag{5.20}$$

Setting the angular acceleration as a virtual control input $\boldsymbol{\nu}_\omega(\mathbf{x}) = \dot{\boldsymbol{\omega}}$ and solving for $\boldsymbol{\Phi}(\mathbf{x}_0, \boldsymbol{\delta}_0)\,\Delta\boldsymbol{\delta}$, the INCA formulation in Eq. (4.11) is found for the body angular rate control problem:

$$\boldsymbol{\Phi}(\mathbf{x}_0, \boldsymbol{\delta}_0)\,\Delta\boldsymbol{\delta} = I\left[\boldsymbol{\nu}_\omega(\mathbf{x}) - \dot{\boldsymbol{\omega}}_0\right] = \Delta\boldsymbol{\tau}_c \tag{5.21}$$

where the pseudo-control input $\mathbf{d}_c$ corresponds to the required increments of control-induced moments $\Delta\boldsymbol{\tau}_c$. At this point, the required control-induced moment increments $\Delta\boldsymbol{\tau}_c$ are allocated into actuator position increments $\Delta\boldsymbol{\delta}$ by a linear control allocator, where the CA problem is formulated in incremental form as: given the current state $\mathbf{x}_0$, the current actuator positions $\boldsymbol{\delta}_0$ and a required increment of control-induced moments $\Delta\boldsymbol{\tau}_c$, determine an increment in the control effector positions $\Delta\boldsymbol{\delta}$ such that

$$\begin{gathered}\nabla_{\boldsymbol{\delta}}\boldsymbol{\Phi}(\mathbf{x}_0, \boldsymbol{\delta}_0)\,\Delta\boldsymbol{\delta} = \Delta\boldsymbol{\tau}_c \\ \text{subject to} \quad \underline{\boldsymbol{\Delta\delta}} \leq \boldsymbol{\Delta\delta} \leq \overline{\boldsymbol{\Delta\delta}}\end{gathered} \tag{5.22}$$

Here, the inner control law

$$\Delta\boldsymbol{\tau}_c = I\left[\boldsymbol{\nu}_\omega(\mathbf{x}) - \dot{\boldsymbol{\omega}}_0\right] \tag{5.23}$$

linearizes the system between the virtual control input $\boldsymbol{\nu}_\omega(\mathbf{x})$ and the required moment increments $\Delta\boldsymbol{\tau}_c$. The linearized system can now be controlled through the virtual control input such that it follows a command $\boldsymbol{\omega}_c$ by using the outer state-feedback linear control law in Eq. (5.13). The absolute actuator position commands are computed as $\boldsymbol{\delta} = \boldsymbol{\delta}_0 + \Delta\boldsymbol{\delta}$.

---

[1] Practical implementation of incremental attitude control in fast-dynamics aerospace vehicles has proven that FCC frequencies of about 100 Hz are high enough for the time scale separation principle to hold, see (Smeur et al., 2016).

5.2.4 Global Convergence and SSDs

Since INCA dynamically drives the actuator vector towards the direction that best fulfills moment increment commands, it is possible that it converges to local minima. This is not a problem if the assumption that the optimal control distribution lies within the neighbourhood of the current actuator positions is valid. This assumption holds true for most of the ICE actuators, since their moment curves do not have local minima in the directions of $\boldsymbol{\delta}$ (local minima in the directions of α, β and M are irrelevant to the control allocator, since they are not control variables). However, the SSDs have a dramatic impact on the control effectiveness of trailing-edge control effectors, and therefore globally optimal control distributions might be available far away from the current SSD positions.

It is worth noting that, besides providing lateral-directional control at high AoA, an important function of the SSDs is to redirect the airflow towards the upper wing skin at high AoA to recover control effectiveness of trailing-edge devices. In contrast, deflecting the SSDs at low AoA destroys the control effectiveness of downstream actuators. Therefore, it is reasonable to assume that globally optimal control distributions will have small SSD deflections at low AoA and large SSD deflections at high AoA. Hence, convergence towards global optima can be subserved by forcing the SSDs to remain as closed as possible at low AoA, and as open as possible at high AoA. This can be achieved by scheduling the penalizing weights of the SSDs in the weighting matrix $W_{\boldsymbol{\delta}}$ as a function of α. In this case, the SSD penalties $W_{\boldsymbol{\delta}_{\text{SSD}}}(\alpha)$ were scheduled as the exponential function

$$W_{\boldsymbol{\delta}_{\text{SSD}}}(\alpha) = \left[-0.25 + 0.35 \exp\left(1.6\alpha\right)\right]^{-1} \tag{5.24}$$

Whereas penalties are set to 1 for all control effectors, $W_{\boldsymbol{\delta}_{\text{SSD}}}$ is 10 at $\alpha = 0$ deg, becomes 1 at $\alpha \approx 45$ deg and goes to 0 at $\alpha \geq 90$ deg. Although this scheduling is valid for the ICE configuration, the characteristics of each particular controlled system shall be studied in order to favour global convergence.

5.3 Control Allocation Solvers

As mentioned above, both LCA- and INCA-based flight control systems rely on a linear control allocator as a core module to distribute the absolute or incremental moment commands over absolute or incremental control effector positions. The CA module was implemented with two typical linear CA algorithms that are known to provide real-time performance for flight control. These two algorithms are briefly described in this section.

In order to keep the discussion general, the definitions below refer to $\mathbf{u}$ as a generic pseudo-control input vector, which corresponds to $\boldsymbol{\delta}$ in LCA and to $\Delta\boldsymbol{\delta}$ in INCA. Also, the generic matrix G refers to the control effectiveness matrix $B(\mathbf{x})$ in LCA and to the Jacobian control effectiveness matrix $\nabla_{\boldsymbol{\delta}}\Phi(\mathbf{x}, \boldsymbol{\delta})$ in INCA. The generic pseudo-control command $\mathbf{d}_c$ refers to a control moment command $\boldsymbol{\tau}_c$ in LCA and to a control moment increment command $\Delta\boldsymbol{\tau}_c$ in INCA.

5.3.1 Redistributed Weighted Pseudo-Inverse (RWPI)

The RWPI algorithm was discussed in detail in Section 4.4. For the sake of completeness, the RWPI method is described here in general terms in order to describe its practical implementation in the linear CA module of the LCA- and the INCA-based flight control systems. The derivation in Section 4.4 leads to the explicit solution to the unconstrained control allocation problem

$$\mathbf{u} = \mathbf{u}_p + G^\sharp \left(\mathbf{d}_c - G\mathbf{u}_p\right) \tag{5.25}$$

with

$$G^\sharp = W_\mathbf{u}^{-1} G^T \left(G W_\mathbf{u}^{-1} G^T\right)^{-1} \tag{5.26}$$

a generalized weighted pseudo-inverse.

The RWPI method computes the unconstrained solution with Eq. (5.26). If one or more effectors are saturated, the corresponding columns in G are set to zero to form G_{sat}, the saturated values are placed in the preference vector $\mathbf{u}_p$ to form $\mathbf{u}_{p,\text{sat}}$ and the redistributed weighted pseudo-inverse solution is computed as

$$\mathbf{u} = \mathbf{u}_{p,\text{sat}} + G_{\text{sat}}^\sharp \left(\mathbf{d}_c - G\mathbf{u}_{p,\text{sat}}\right) \tag{5.27}$$

This process is repeated until the pseudo-control command $\mathbf{d}_c$ is attained or all the control effectors are saturated.

5.3.2 Active Set-Based Quadratic Programming (QP)

The QP formulation of the control allocation problem is derived by formulating an ℓ_2-norm cost function for the multi-objective constrained optimization problem:

$$\begin{gathered} \min_{\mathbf{u}} \;\; \mathcal{J} = W_\mathbf{d} \left|\left| G\mathbf{u} - \mathbf{d}_c \right|\right|_2 + \epsilon \; W_\mathbf{u} \left|\left| \mathbf{u} - \mathbf{u}_p \right|\right|_2 \\ \text{subject to} \quad \underline{\mathbf{u}} \leq \mathbf{u} \leq \overline{\mathbf{u}} \end{gathered} \tag{5.28}$$

where $W_\mathbf{d}$ and $W_\mathbf{u}$ are nonsingular weighting matrices and ϵ is a scalar, selected sufficiently small to prioritize the minimization of the allocation error $(G\mathbf{u}-\mathbf{d}_c)$ over the secondary objective of minimizing $(\mathbf{u}-\mathbf{u}_p)$.

Many numerical algorithms are available to solve the QP problem, such as fixed-point methods (Burken et al., 1999, 2001), active set methods (Harkegard, 2002) and interior-point methods (Petersen & Bodson, 2005, 2006). Petersen and Bodson (2006) concluded that the active set algorithm converges exactly to the optimal solution in a finite number of steps and is computationally efficient for control allocation problems of small and medium size. For this reason, the active set algorithm for QP-based control allocation proposed by Harkegard (2002) was used in this thesis.

Consider the reformulation of the minimization problem in Eq. (5.28) in the form

$$\begin{gathered} \min_{\mathbf{u}} \left|\left| \begin{bmatrix} W_\mathbf{u} G \\ \epsilon W_\mathbf{u} \end{bmatrix} \mathbf{u} - \begin{bmatrix} W_\mathbf{d} \mathbf{d}_c \\ \epsilon W_\mathbf{u} \mathbf{u}_p \end{bmatrix} \right|\right|_2 \\ \text{subject to} \quad G\mathbf{u} = \mathbf{d}_c, \quad C\mathbf{u} \geq U \end{gathered} \tag{5.29}$$

where $C = [I \; -I]^T$ and $U = [\underline{\mathbf{u}} \; \overline{\mathbf{u}}]$. The active set algorithm consists on solving a sequence of equality constrained problems, where in every iteration some inequality constraints are regarded as equality constraints and form a working set $\mathcal{W}$, whereas the remaining inequality constraints are disregarded. The working set at the optimum is known as the

Algorithm 2 Active set algorithm for QP-based control allocation (Harkegard, 2002).

```
Let $\mathbf{u}_0$ be a feasible starting point. A point is feasible if satisfies $G\mathbf{u} = \mathbf{d}_c$ and $C\mathbf{u} \geq U$.
Let the working set $\mathcal{W}$ contain a subset of the active inequality constraints at $\mathbf{u}_0$. Let
$N$ be the maximum number of iterations.
for $k = 0, 1, 2...N - 1$ do
    Given $\mathbf{u}^k$, find the optimal perturbation $\mathbf{p}$, considering the constraints in the
    working set as equality constraints and disregarding the remaining inequality constraints, by solving
        $$\min_{\mathbf{p}} \left\| \begin{bmatrix} W_{\mathbf{u}}G \\ \epsilon W_{\mathbf{u}} \end{bmatrix} \left(\mathbf{u}^k + \mathbf{p}\right) - \begin{bmatrix} W_{\mathbf{d}}\mathbf{d}_c \\ \epsilon W_{\mathbf{u}}\mathbf{u}_p \end{bmatrix} \right\| \qquad (5.30)$$
        $$\text{subject to} \quad G\mathbf{p} = 0, \quad \mathbf{p}_i = 0, i \in \mathcal{W}$$
    if $\mathbf{u}^k + \mathbf{p}$ is feasible then
        Set $\mathbf{u}^{k+1} = \mathbf{u}^k + \mathbf{p}$ and compute the Lagrange multipliers $[\mu \ \lambda]^T$ using Eq. (5.31),
        where $\mu$ is associated with $G\mathbf{u} = \mathbf{d}_c$ and $\lambda$ with the active constraints in $C\mathbf{u} \geq U$.
        if All $\lambda \geq 0$ then
            $\mathbf{u}^{k+1}$ is the optimal solution to (5.29).
        else
            Remove the constraint associated with the most negative $\lambda$ from $\mathcal{W}$.
        end if
    else
        Determine the maximum step length $\alpha$ such that $\mathbf{u}^{k+1} = \mathbf{u}^k + \alpha\mathbf{p}$ is feasible. Add
        the primary bounding constraint to the working set.
    end if
end for
```

active set of the solution. The active set algorithm taken from (Harkegard, 2002) is given in pseudocode in Algorithm 2.

The Lagrange multipliers are determined by

$$\begin{bmatrix} W_{\mathbf{u}}G \\ \epsilon W_{\mathbf{u}} \end{bmatrix}^T \left(\begin{bmatrix} W_{\mathbf{u}}G \\ \epsilon W_{\mathbf{u}} \end{bmatrix} \mathbf{u} - \begin{bmatrix} W_{\mathbf{d}}\mathbf{d}_c \\ \epsilon W_{\mathbf{u}}\mathbf{u}_p \end{bmatrix} \right) = \begin{bmatrix} G^T & C_0^T \end{bmatrix} \begin{bmatrix} \mu \\ \lambda \end{bmatrix} \tag{5.31}$$

where C_0 contains the rows of C that correspond to constraints in $\mathcal{W}$.

5.4 Pseudo-Control Hedging

Actuator saturation represents a problem when control commands exceed the capabilities of the actuators under rate and position constraints. When physically unachievable control commands are given, the system can run into command windup problems, which compromises the overall performance and stability of the system. To overcome this problem, pseudo-control hedging (PCH) was proposed in (Johnson & Calise, 2000) and developed in (Johnson & Kannan, 2005; Lam & Barkana, 2005) as an adaptation system to hedge the pseudo-control input of the control system to accommodate the commands to the physical limitations of the actuators, thus avoiding physically unachievable commands. PCH has been successfully used as a partial form of flight envelope protection and anti-windup system in (T. Lombaerts, Looye, Chu, & Mulder, 2010; Simplício et al., 2013). In addition to ensuring physically achievable commands, the first-order reference model used in PCH is useful to compute the derivatives of the commanded variables, which can be used as feedforward terms in the control system to improve tracking performance (Simplício et al., 2013).

PCH was implemented in this thesis to shape the virtual control command $\boldsymbol{\nu}_\omega(\mathbf{x})$ by substracting the difference between the commanded $\boldsymbol{\nu}_\omega(\mathbf{x})$ and the actual virtual control achieved, estimated with fed-back actuator positions $\boldsymbol{\delta}_0$ as $\hat{\boldsymbol{\nu}}_\omega(\mathbf{x}) = \mathbf{f}(\mathbf{x}_0, \boldsymbol{\delta}_0)$, where $\mathbf{f}(\mathbf{x}, \boldsymbol{\delta})$ is the virtual control law. The pseudo-control hedge is computed as

$$\boldsymbol{\nu}_h(\mathbf{x}) = \boldsymbol{\nu}_\omega(\mathbf{x}) - \hat{\boldsymbol{\nu}}_\omega(\mathbf{x}) \tag{5.32}$$

The hedge $\boldsymbol{\nu}_h(\mathbf{x})$ is fed back into a first-order reference model (RM) as a compensation signal. The reference model $\boldsymbol{\nu}_{\mathrm{rm}}(\mathbf{x})$ is given by

$$\boldsymbol{\nu}_{\mathrm{rm}}(\mathbf{x}) = K_{\mathrm{rm}} \left(\boldsymbol{\omega}_c - \boldsymbol{\omega}_{\mathrm{rm}}\right) \tag{5.33}$$

with K_{rm} a diagonal matrix. The hedged reference signal fed as a control input into the attitude control system is the state vector of the reference model

$$\boldsymbol{\omega}_{\mathrm{rm}} = \frac{1}{s} \left(\boldsymbol{\nu}_{\mathrm{rm}}(\mathbf{x}) - \boldsymbol{\nu}_h(\mathbf{x})\right) \tag{5.34}$$

When no saturation occurs, $\boldsymbol{\nu}_h(\mathbf{x}) = 0$ and the reference model behaves as a low-pass filter of bandwidth K_{rm_i} for the i-th component of $\boldsymbol{\omega}_{\mathrm{rm}}$. Under actuator saturation, the pseudo-control hedge $\boldsymbol{\nu}_h(\mathbf{x})$ corresponds to the difference between the commanded virtual control input and the estimated virtual control achieved, based on the actual positions of the control effectors. The hedge signal $\boldsymbol{\nu}_h(\mathbf{x})$ is used to reshape the reference and avoid unfeasible commands. The reference model $\boldsymbol{\nu}_{\mathrm{rm}}(\mathbf{x})$ corresponds to the first-order derivatives of the commanded variables, which can be used as a feedforward term added to $\boldsymbol{\nu}_\omega(\mathbf{x})$ to improve tracking performance (Simplício et al., 2013).

For the LCA-based controller the virtual control input is given by the control law

$$\boldsymbol{\nu}_\omega(\mathbf{x}) = \frac{1}{2}\rho V^2 S J^{-1} B(\mathbf{x})\, \boldsymbol{\delta} + J^{-1} \left(\boldsymbol{\tau}_a - \boldsymbol{\omega} \times J\boldsymbol{\omega}\right) \tag{5.35}$$

and therefore the pseudo-control hedge is given by

$$\begin{aligned} \boldsymbol{\nu}_{h_{\mathrm{LCA}}}(\mathbf{x}) = {} & \left[\frac{1}{2}\rho V^2 S J^{-1} B(\mathbf{x})\, \boldsymbol{\delta}_c + J^{-1} \left(\boldsymbol{\tau}_a - \boldsymbol{\omega} \times J\boldsymbol{\omega}\right)\right] \\ & - \left[\frac{1}{2}\rho V^2 S J^{-1} B(\mathbf{x})\, \boldsymbol{\delta} + J^{-1} \left(\boldsymbol{\tau}_a - \boldsymbol{\omega} \times J\boldsymbol{\omega}\right)\right] \end{aligned} \tag{5.36}$$

$$\boldsymbol{\nu}_{h_{\mathrm{LCA}}}(\mathbf{x}) = \frac{1}{2}\rho V^2 S J^{-1} B(\mathbf{x}) \left(\boldsymbol{\delta}_c - \boldsymbol{\delta}\right) \tag{5.37}$$

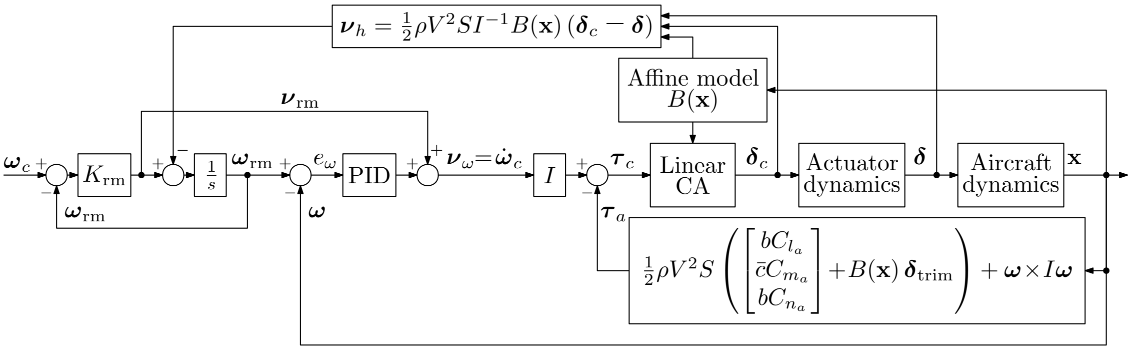

Figure 5.5: Schematic of the LCA-based angular rate control system with PCH.

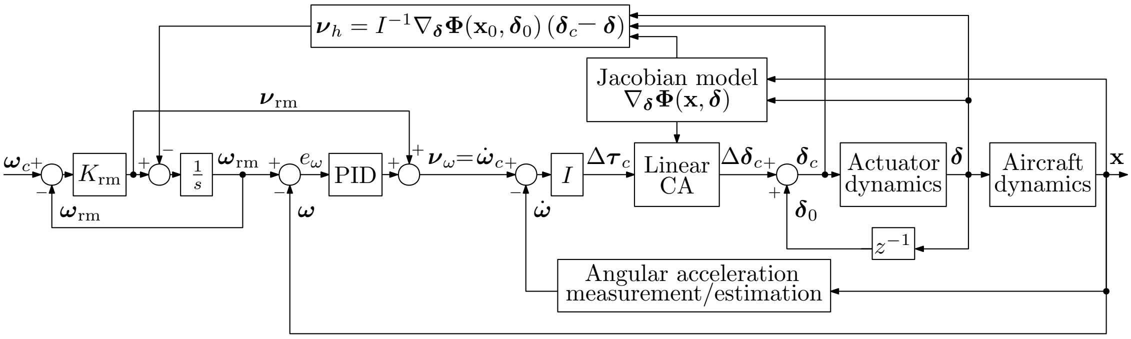

Figure 5.6: Schematic of the INCA-based angular rate control system with PCH.

For the INCA-based controller the virtual control input is given by the control law

$$\boldsymbol{\nu}_\omega(\mathbf{x}) = \dot{\boldsymbol{\omega}}_0 + J^{-1}\nabla_{\boldsymbol{\delta}}\boldsymbol{\Phi}(\mathbf{x}_0,\boldsymbol{\delta}_0)\,(\boldsymbol{\delta} - \boldsymbol{\delta}_0) \tag{5.38}$$

and therefore the pseudo-control hedge is given by

$$\boldsymbol{\nu}_{h_{\mathrm{INCA}}}(\mathbf{x}) = \left[\dot{\boldsymbol{\omega}}_0 + J^{-1}\nabla_{\boldsymbol{\delta}}\boldsymbol{\Phi}(\mathbf{x}_0,\boldsymbol{\delta}_0)\,(\boldsymbol{\delta}_c - \boldsymbol{\delta}_0)\right] - \left[\dot{\boldsymbol{\omega}}_0 + J^{-1}\nabla_{\boldsymbol{\delta}}\boldsymbol{\Phi}(\mathbf{x}_0,\boldsymbol{\delta}_0)\,(\boldsymbol{\delta} - \boldsymbol{\delta}_0)\right] \tag{5.39}$$

$$\boldsymbol{\nu}_{h_{\mathrm{INCA}}}(\mathbf{x}) = J^{-1}\nabla_{\boldsymbol{\delta}}\boldsymbol{\Phi}(\mathbf{x}_0,\boldsymbol{\delta}_0)\,(\boldsymbol{\delta}_c - \boldsymbol{\delta}) \tag{5.40}$$

The internal structures of the LCA-based and the INCA-based angular rate control systems, including PCH, are given in Figures 5.5 and 5.6 respectively.

5.5 Outer Control Loops

The reference maneuvers used to assess the performance of the LCA-based and the INCA-based controllers were coded as predefined reference signals. In order to fly these maneuvers, a series of outer loops were designed to track each kind of reference. Three different outer loops were designed to fly different types of reference trajectories: a sideslip compensation loop with body rate commands in roll and pitch, an aerodynamic inversion loop with bank angle ϕ, α and β as input commands, and an Euler angle inversion loop with flight path guidance variables as inputs. Note that these loops do not work simultaneously, but a different outer loop was used depending on the type of reference trajectory followed. In order to make a fair comparison, the same outer loops were used with both the LCA-based and the INCA-based controllers. The design and implementation of these outer loops is discussed in this section.

5.5.1 Sideslip Inversion Outer Loop

The sideslip dynamic inversion loop compensates the sideslip angle to perform coordinated turns whereas leaving roll and pitch rates as directly controlled variables. This loop was implemented in the yaw rate channel with β as a reference and r as control input. For this, a dynamic inversion of the sideslip angle was performed. The sideslip angle β can be computed as

$$\beta = \arcsin \frac{v}{V} \tag{5.41}$$

The first derivative of Eq. (5.41) is

$$\dot{\beta} = \frac{\dot{v}V - v\dot{V}}{V\sqrt{u^2+w^2}} = \frac{\dot{v}}{\sqrt{u^2+w^2}} - \frac{v\left(u\dot{u} + v\dot{v} + w\dot{w}\right)}{\left(u^2+v^2+w^2\right)\sqrt{u^2+w^2}} \tag{5.42}$$

The accelerations in aerodynamic frame are given by

$$\begin{aligned} \dot{u} &= A_x - g\sin\theta + rv - qw \\ \dot{v} &= A_y + g\sin\phi\cos\theta - ru + pw \\ \dot{w} &= A_z + g\cos\theta\cos\phi + qu - pv \end{aligned} \tag{5.43}$$

Substituting Eqs. (5.43) into Eq. (5.42) gives

$$\dot{\beta} = \left(\frac{1}{\sqrt{u^2+w^2}}\right)\left(F_x + F_y + F_z\right) + \begin{bmatrix} \frac{w}{\sqrt{u^2+w^2}} & 0 & \frac{-u}{\sqrt{u^2+w^2}} \end{bmatrix} \begin{bmatrix} p \\ q \\ r \end{bmatrix} \tag{5.44}$$

with

$$\begin{aligned} F_x &= -\frac{uv}{V^2}\left(A_x - g\sin\theta\right) \\ F_y &= \left(1 - \frac{v}{V^2}\right)\left(A_y + g\sin\phi\cos\theta\right) \\ F_z &= -\frac{vw}{V^2}\left(A_z + g\cos\phi\cos\theta\right) \end{aligned} \tag{5.45}$$

Introducing the virtual control input $\nu_\beta(\mathbf{x}) = \dot{\beta}$ and solving for the input r the sideslip dynamic inversion law is obtained:

$$\begin{aligned} r_c &= \underbrace{\left(\frac{-u}{\sqrt{u^2+w^2}}\right)}_{a_\beta(\mathbf{x})}^{-1} \left[\nu_\beta(\mathbf{x}) - \underbrace{\frac{1}{\sqrt{u^2+w^2}}\left(F_x + F_y + F_z + wp_c\right)}_{b_\beta(\mathbf{x})}\right] \\ &= a_\beta(\mathbf{x})^{-1}\left[\nu_\beta(\mathbf{x}) - b_\beta(\mathbf{x})\right] \end{aligned} \tag{5.46}$$

The structure of the sideslip compensation loop is shown in Figure 5.7.

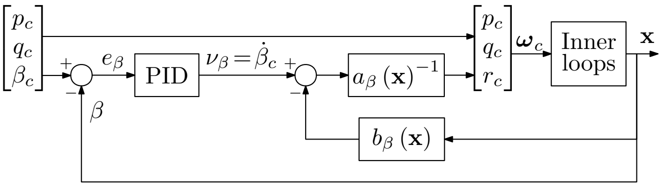

Figure 5.7: Schematic of the outer sideslip dynamic inversion loop.

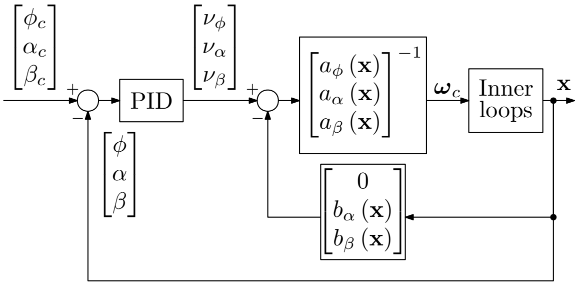

Figure 5.8: Schematic of the outer aerodynamic inversion loop.

5.5.2 Aerodynamic Inversion Loop

Similarly, a dynamic inversion loop can be set up to control the aerodynamic angles ϕ, α and β. The dynamics of the bank angle are given by

$$\dot{\phi} = \begin{bmatrix} 1 & \sin\phi\tan\theta & \cos\phi\tan\theta \end{bmatrix} \begin{bmatrix} p \\ q \\ r \end{bmatrix} \tag{5.47}$$

Introducing the virtual control input $\nu_\phi(\mathbf{x}) = \dot{\phi}$ and solving for the body rates as control inputs, the bank angle dynamic inversion law is obtained:

$$\begin{bmatrix} p_c \\ q_c \\ r_c \end{bmatrix} = \underbrace{\begin{bmatrix} 1 & \sin\phi\tan\theta & \cos\phi\tan\theta \end{bmatrix}}_{a_\phi(\mathbf{x})}^{-1} \nu_\phi(\mathbf{x}) = a_\phi(\mathbf{x})^{-1}\,\nu_\phi(\mathbf{x}) \tag{5.48}$$

The dynamics of the angle of attack α are given by

$$\dot{\alpha} = \arcsin\frac{w}{V} = \frac{u\dot{w} - w\dot{u}}{u^2 + w^2} \tag{5.49}$$

Substituting Eqs. (5.43) into Eq. (5.49) gives

$$\dot{\alpha} = \left(\frac{1}{u^2+w^2}\right)\left(u\left(A_z + g\cos\theta\cos\phi\right) - w\left(A_x - g\sin\theta\right)\right) + \begin{bmatrix} \frac{-uv}{u^2+w^2} & 1 & \frac{-vw}{u^2+w^2} \end{bmatrix} \begin{bmatrix} p \\ q \\ r \end{bmatrix} \tag{5.50}$$

Introducing the virtual control input $\nu_\alpha(\mathbf{x}) = \dot{\alpha}$ and solving for the body rates as control inputs, the angle of attack dynamic inversion law is obtained:

$$\begin{bmatrix} p_c \\ q_c \\ r_c \end{bmatrix} = \underbrace{\begin{bmatrix} \dfrac{-uv}{u^2+w^2} & 1 & \dfrac{-vw}{u^2+w^2} \end{bmatrix}}_{a_\alpha(\mathbf{x})}^{-1} \underbrace{- \left(\frac{1}{u^2+w^2}\right) \left(u\left(A_z + g\cos\theta\cos\phi\right) - w\left(A_x - g\sin\theta\right)\right)}_{b_\alpha(\mathbf{x})}$$

$$= a_\alpha(\mathbf{x})^{-1}\left[\nu_\alpha(\mathbf{x}) - b_\alpha(\mathbf{x})\right] \quad (5.51)$$

The sideslip angle dynamic inversion law for the aerodynamic inversion loop can be obtained by re-arranging Eq. (5.44) with the three body rates as control inputs:

$$\begin{bmatrix} p_c \\ q_c \\ r_c \end{bmatrix} = \underbrace{\begin{bmatrix} \dfrac{w}{u^2+w^2} & 0 & \dfrac{-u}{u^2+w^2} \end{bmatrix}}_{a_\beta(\mathbf{x})}^{-1} - \underbrace{\left(\frac{1}{\sqrt{u^2+w^2}}\right) \left(F_x + F_y + F_z\right)}_{b_\beta(\mathbf{x})}$$

$$= a_\beta(\mathbf{x})^{-1}\left[\nu_\beta(\mathbf{x}) - b_\beta(\mathbf{x})\right] \quad (5.52)$$

Combining the three control channels, the aerodynamic inversion control law is

$$\begin{bmatrix} p_c \\ q_c \\ r_c \end{bmatrix} = \begin{bmatrix} a_\phi\left(\mathbf{x}\right) \\ a_\alpha\left(\mathbf{x}\right) \\ a_\beta\left(\mathbf{x}\right) \end{bmatrix}^{-1} \left(\begin{bmatrix} \nu_\phi\left(\mathbf{x}\right) \\ \nu_\alpha\left(\mathbf{x}\right) \\ \nu_\beta\left(\mathbf{x}\right) \end{bmatrix} - \begin{bmatrix} 0 \\ b_\alpha\left(\mathbf{x}\right) \\ b_\beta\left(\mathbf{x}\right) \end{bmatrix} \right) \tag{5.53}$$

The structure of the outer aerodynamic inversion loop is shown in Figure 5.8.

5.5.3 Flight Path Guidance Loop with Euler Angle Inversion

A guidance loop was designed in order to use flight path angle γ and bank angle ϕ as control inputs from a reference trajectory with a sideslip compensator in the directional channel. For this, first an Euler angle dynamic inversion loop was set up, whose pseudo-control inputs were provided by an outer linear loop controlling ϕ, γ and β.

The relationship between body angular rates and Euler angular rates in the lateral and longitudinal channels is

$$\begin{bmatrix} \dot{\phi} \\ \dot{\theta} \end{bmatrix} = \begin{bmatrix} 1 & \sin\phi\tan\theta & \cos\phi\tan\theta \\ 0 & \cos\theta & -\sin\phi \end{bmatrix} \begin{bmatrix} p \\ q \end{bmatrix} \tag{5.54}$$

setting the virtual control inputs $\nu_\phi(\mathbf{x}) = \dot{\phi}$ and $\nu_\theta(\mathbf{x}) = \dot{\theta}$ and solving for the body rates as control inputs, the Euler dynamic inversion law is obtained:

$$\begin{bmatrix} p_c \\ q_c \end{bmatrix} = \underbrace{\begin{bmatrix} 1 & \sin\phi\tan\theta & \cos\phi\tan\theta \\ 0 & \cos\theta & -\sin\phi \end{bmatrix}}_{\left[a_\phi(\mathbf{x}) \;\; a_\theta(\mathbf{x})\right]^T}^{-1} \begin{bmatrix} \nu_\phi(\mathbf{x}) \\ \nu_\theta(\mathbf{x}) \end{bmatrix} \tag{5.55}$$

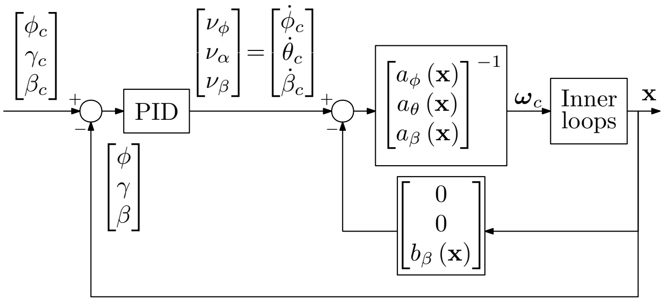

Figure 5.9: Schematic of the outer guidance loop with Euler angle inversion.

Including the sideslip inversion law in Eq. (5.52), the Euler angle inversion law is

$$\begin{bmatrix}p_c\\ q_c\\ r_c\end{bmatrix} = \begin{bmatrix}a_\phi(\mathbf{x})\\ a_\theta(\mathbf{x})\\ a_\beta(\mathbf{x})\end{bmatrix}^{-1}\left(\begin{bmatrix}\nu_\phi(\mathbf{x})\\ \nu_\theta(\mathbf{x})\\ \nu_\beta(\mathbf{x})\end{bmatrix} - \begin{bmatrix}0\\ 0\\ b_\beta(\mathbf{x})\end{bmatrix}\right) \tag{5.56}$$

The references for the pseudo-control input $\boldsymbol{\nu}_{\text{guid}}(\mathbf{x}) = \begin{bmatrix}\dot\phi_c & \dot\theta_c & \dot\beta_c\end{bmatrix}$ are provided by a linear outer loop with ϕ_c, γ_c and β_c as references:

$$\begin{bmatrix}\dot\phi_c\\ \dot\theta_c\\ \dot\beta_c\end{bmatrix} = \mathbf{K}_{\text{guid}_P}\begin{bmatrix}(\phi-\phi_c)\\ (\gamma-\gamma_c)\\ (\beta-\beta_c)\end{bmatrix} + \mathbf{K}_{\text{guid}_I}\begin{bmatrix}\int(\phi-\phi_c)\,dt\\ \int(\gamma-\gamma_c)\,dt\\ \int(\beta-\beta_c)\,dt\end{bmatrix} + \mathbf{K}_{\text{guid}_D}\begin{bmatrix}(\dot\phi-\dot\phi_c)\\ (\dot\gamma-\dot\gamma_c)\\ (\dot\beta-\dot\beta_c)\end{bmatrix} \tag{5.57}$$

The structure of the outer guidance loop is shown in Figure 5.9. The full INCA-based flight control system including PCH with the flight path guidance controller as outer loop is given in Figure 5.10. Note that any of the three loops described above can be used as outer loop depending on the type of reference trajectory to follow.

5.5.4 Auto-Throttle Loop

Finally, an auto-throttle (A/T) control loop was implemented to keep the true airspeed constant to its initial value. This system was implemented as a simple linear feedback loop with a PID controller. The throttle dynamics are also subject to absolute limits as described in Chapter 3.

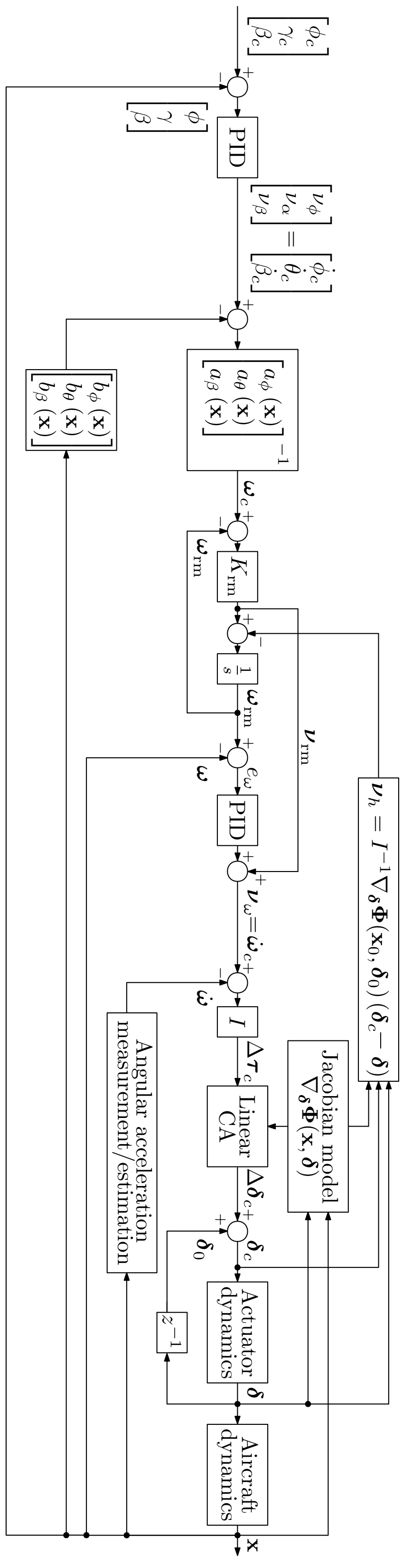

Figure 5.10: INCA-based flight control system with PCH and guidance outer loop.

Chapter 6

Simulations and Results

The evaluation of the performance of INCA with respect to traditional LCA methods was based on a real-time simulation setup with the high-fidelity ICE model described in Chapter 3 and the LCA- and INCA-based flight control systems described in Chapter 5. The assessment was made for both CA schemes solved with the RWPI and the active set-based QP algorithms described in the latter chapter. The metrics used to assess the performance of the tested systems were the control allocation performance, the overall tracking performance, the control effort and the number of iterations per time step of the core CA algorithms. First, the body rate tracking performance was tested with a simple maneuver with direct body rate inputs. Then the control systems were tested against aggressive flight maneuvers with increasing level of control effort demand, using different outer loops. Additionally, a robustness analysis was carried out in order to assess the sensitivity of INCA to Jacobian model mismatch.

This chapter presents the simulation setup and the results obtained from the simulations. The simulation environment and setup are described in Section 6.1. Section 6.2 presents the results of the preliminary performance evaluation with a simple baseline trajectory. The results of the sensitivity analysis of INCA to Jacobian model mismatch are presented in Section 6.3. Section 6.4 presents the results of the four tested aggressive flight maneuvers. Finally, the overall performance of each system is assessed and discussed in Section 6.5. The results not included in this chapter can be found in Appendix C.

6.1 Simulation Setup

The flight simulations were set up in a Matlab/Simulink framework using the high-fidelity ICE aerodynamic model described in Chapter 3. Both LCA- and INCA-based flight control systems were implemented with the RWPI and the active set-based QP solvers described in Chapter 5. The simulations were run in real time with a 4th-order Runge-Kutta solver with a fixed sampling rate of 100Hz. The simulations were performed in a 64-bit computer with four Intel(R) Core(TM) i7-4702MQ CPU @ 2.20GHz processors and 16.0 Gb RAM.

The simulation environment included a 1976 COESA-Extended U.S. Standard Atmosphere, an horizontal and shear wind model, a Dryden MIL-F-8785C wind turbulence model and a discrete wind gust model with gust length of 4 ft and gust amplitude of 10 ft/s. The flight simulations were initialized in trim conditions at an altitude of 20000 ft and $M = 0.85$. The initial true airspeed of 880 ft/sec was set as a constant reference to the A/T controller. In all the simulations, the linear gains of the innermost body rate control loop were set to the values listed in Table 6.1. The reference model gains K_{rm} were all set to 10. The penalization gains in $W_{\boldsymbol{\delta}}$ were set to 1 for all control effectors except for the AMTs, which were set to 0.5, and for the SSDs, which were scheduled as a function of α with Eq. (5.24). The penalization gains in $W_{\boldsymbol{\tau}}$ were all set to 1. The control preference vector $\boldsymbol{\delta}_p$ was set to 0 for all control effectors in all cases.

Table 6.1: Gains used in the linear controller of the body rate loop.

Channel	p	q	r
K_{ω_P}	6.5	6.5	5.8
K_{ω_I}	0.0	0.0	0.0
K_{ω_D}	0.5	0.5	0.5

6.2 3211 Maneuver with Sideslip Compensation

The first set of simulations was set up with the sideslip inversion loop, using roll and pitch body rates and sideslip angle as control input commands. The control inputs were simultaneous 3211 signals with amplitudes of 10 deg/sec for the roll and pitch channels and 3 deg for the sideslip channel. 3211 inputs consist of two consecutive pulse doublets, the pulses of which have durations of 3, 2, 1 and 1 seconds. These inputs are known to excite a significant frequency range of the aircraft operational bandwidth (Mulder, 1986). The gains used for the sideslip loop were $K_{\beta_P} = 1.60$, $K_{\beta_I} = 0.30$ and $K_{\beta_D} = 0.00$.

6.2.1 Simulation Results with RWPI

The tracking histories of the controlled variables with LCA and INCA solved with RWPI are displayed and compared in Figure 6.1. Evident deficiencies are observed for the LCA controller, which exhibits large excursions from the commanded values, including overshoots and oscillations. This behaviour can be explained by the fact that many aerodynamic effects of the control effectors are neglected in the linear control effectors model, including effector nonlinearities, interaction effects and the secondary-axis yawing moment contributions of both the elevons and outboard LEF. The fact that these effects need to be compensated with other actuators, which in turn have nonlinear effects and cause interactions, results in a substantial degradation of the tracking performance. In contrast, INCA performs with considerably superior tracking accuracy. It exhibits overshoots, although to a lower extent. It is worth highlighting that the tracking performance of LCA in the directional r and β channels is particularly low, since most important nonlinearities and model inaccuracies occur for directional dynamics.

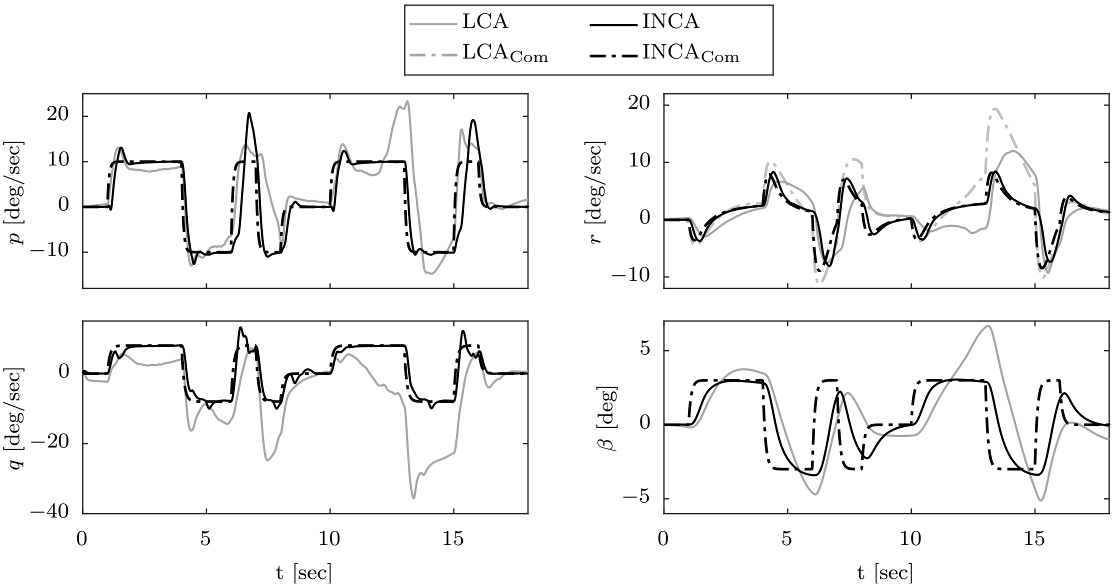

Figure 6.1: Tracking performance of LCA and INCA solved with RWPI.

A key performance metric of control allocation systems is their allocation performance, which refers to their capability of attaining the control moments required by the high-level flight control system, i.e. minimizing the allocation error $\boldsymbol{\tau} - \boldsymbol{\tau}_c$. The time histories of the commanded and attained control moments for the 3211 maneuver with LCA and INCA solved with RWPI are given in Figure 6.2. Large excursions in commanded moments are observed for LCA, especially in the longitudinal and directional channels. Similarly to the tracking case, this low performance is due to the necessity of the LCA-based FCS to compensate inaccuracies in the control effector model. In contrast, the moments required to satisfy the same control commands are significantly smaller with INCA, and these are attained with a substantially higher performance.

Finally, the time histories of the 13 control effector positions along the 3211 maneuver are given in Figure 6.3. Severe oscillations in the control effectors with lateral-directional control authority can be observed with LCA due to control effector interactions. Note that these couplings are not observed with INCA, since the Jacobian model captures these interactions. In addition, LCA places bigger control effort on the AMTs, since the linear control effector model lacks information about other sources of directional control power such as the elevons and outboard LEF.

Since the main advantage of INCA is its suitability for real-time applications, another key performance metric is computational complexity. The computational complexities of the RWPI and the active set-based QP algorithms were evaluated in (Bodson, 2002; Harkegard, 2002). Both studies concluded that these CA algorithms are well-suited for real-time control allocation in flight control systems. Thus, further analysis of the computational complexity of these CA algorithms is not required here. However, in order to evaluate whether INCA is suitable or not for real-time implementation, it is necessary to demonstrate that INCA does not increase the computational load on these algorithms in

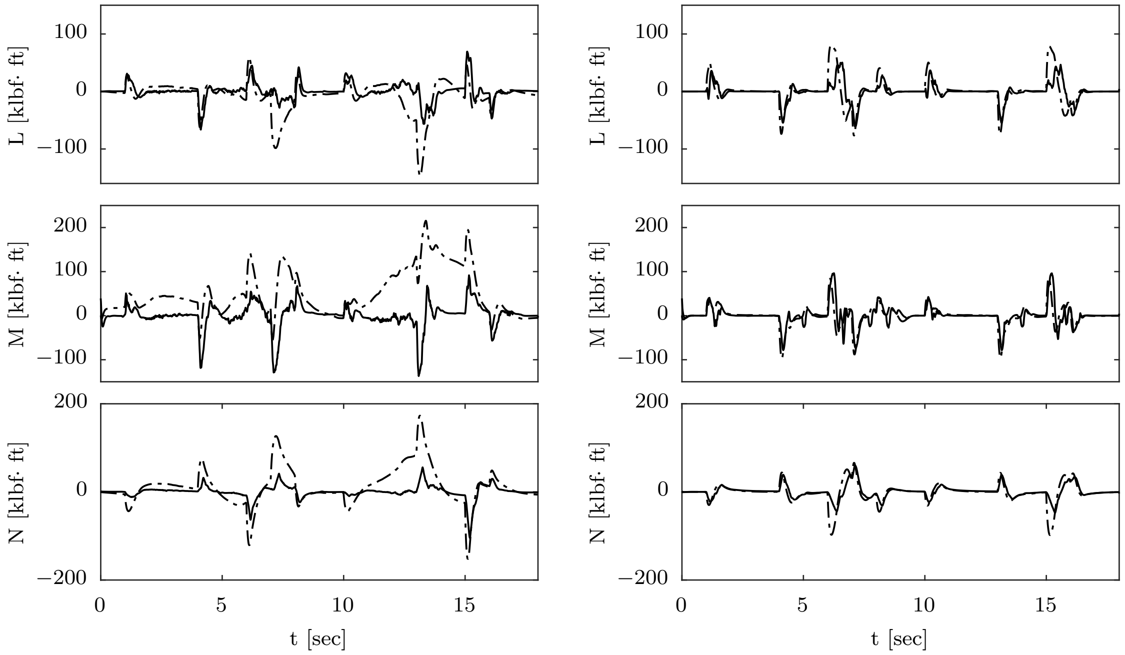

(a) LCA-based FCS. (b) INCA-based FCS.

Figure 6.2: Commanded (dot-dashed line) and attained (solid line) control-induced moments for the 3211 maneuver with RWPI.

comparison with traditional LCA schemes. Since an iteration implies the same number of operations for both LCA and INCA, it suffices to demonstrate that the number of iterations required per time step is statistically comparable for both control allocation methods.

The number of iterations per time step n_i of LCA and INCA solved with RWPI along the 3211 maneuver are shown in Figure 6.7a. It can be observed that both methods require a similar number of iterations per time step for this trajectory. It is important noting that the maximum number of iterations of RWPI is 14 and therefore 50% of the maximum number of iterations is rarely reached by both systems. Quantitative statistical data on n_i will be given at the end of this chapter. The spatial trajectories of the 3211 maneuvers solved with RWPI are given in Figure 6.8a.

6.2.2 Simulation Results with Active Set-Based QP

The time histories of the control variables of LCA and INCA solved with the active set-based QP algorithm are given in Figure 6.4. A significant improvement with respect to RWPI is observed for both LCA and INCA. This is consistent with previous research (Bodson, 2002; Harkegard, 2002; Johansen & Fossen, 2013) which concluded that, despite its simplicity, the RWPI method may yield suboptimal solutions and does not guarantee convergence to a feasible solution, even if it exists.

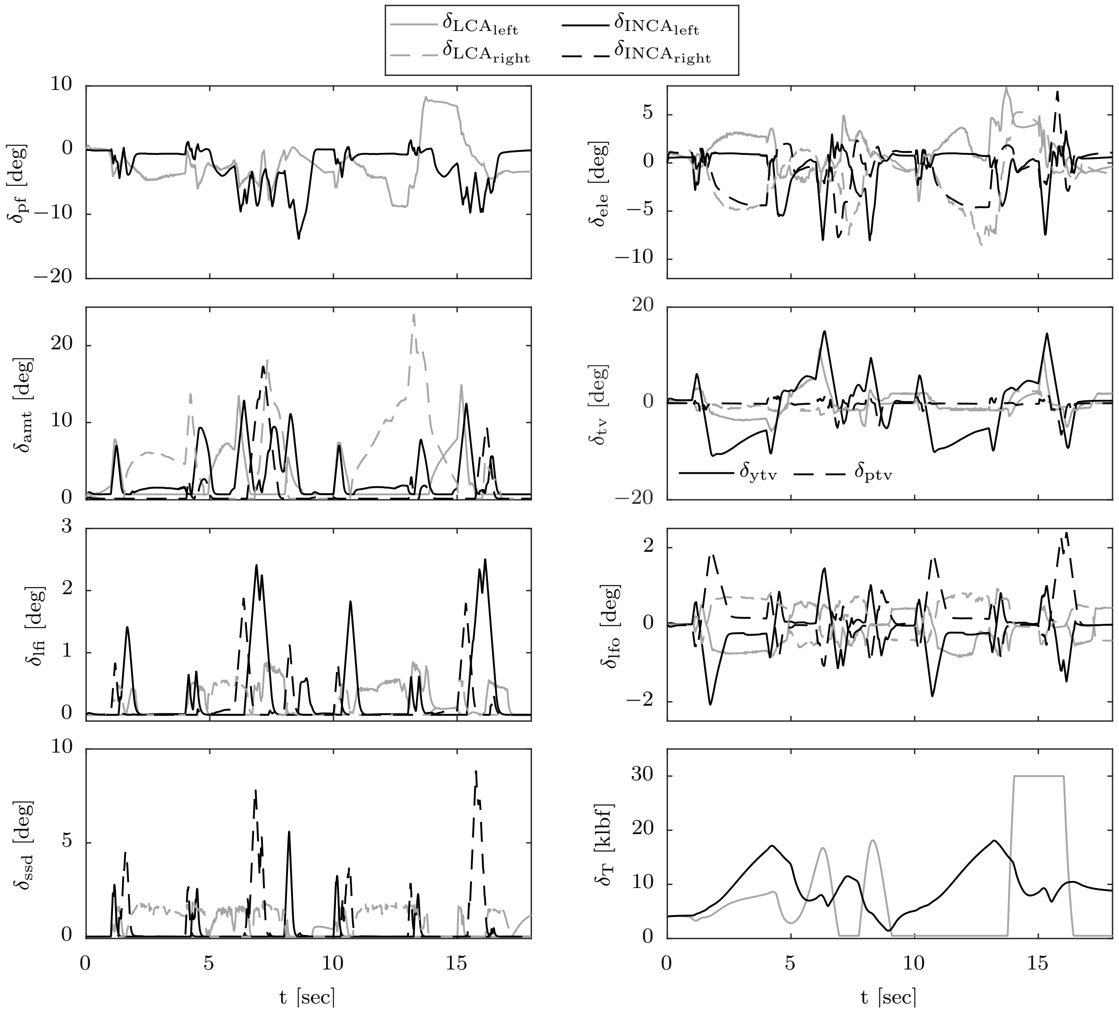

Figure 6.3: Control effector positions with LCA and INCA solved with RWPI.

In spite of this substantial improvement, the performance of LCA with QP is still poor: the controlled variables exhibit large excursions, overshoots and oscillations in all axes. In contrast, the INCA-based control system performs with substantially superior performance, tracking the reference quickly and without significant excursions or oscillations.

Figure 6.5 shows the commanded and attained moments along the trajectory for both systems. The LCA-based system still presents important allocation error in the form of offsets and excursions from the commanded values, whereas INCA exhibits substantially higher performance, requiring small moments to achieve the control commands and attaining the commanded moments quickly and accurately.

The time histories of the control effector positions are given in Figure 6.6. Note that the active set-based QP approach alleviates the problems regarding oscillations observed with LCA/RWPI. Consequently, the control effort of the LCA-based system is substantially reduced in this case.

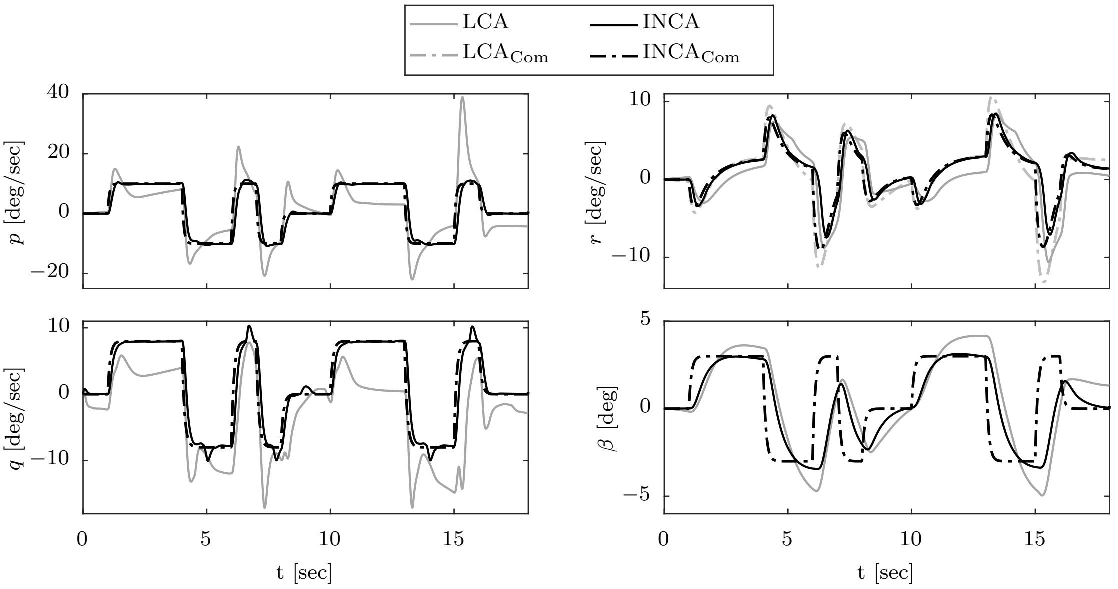

Figure 6.4: Tracking performance of LCA and INCA solved with active set-based QP.

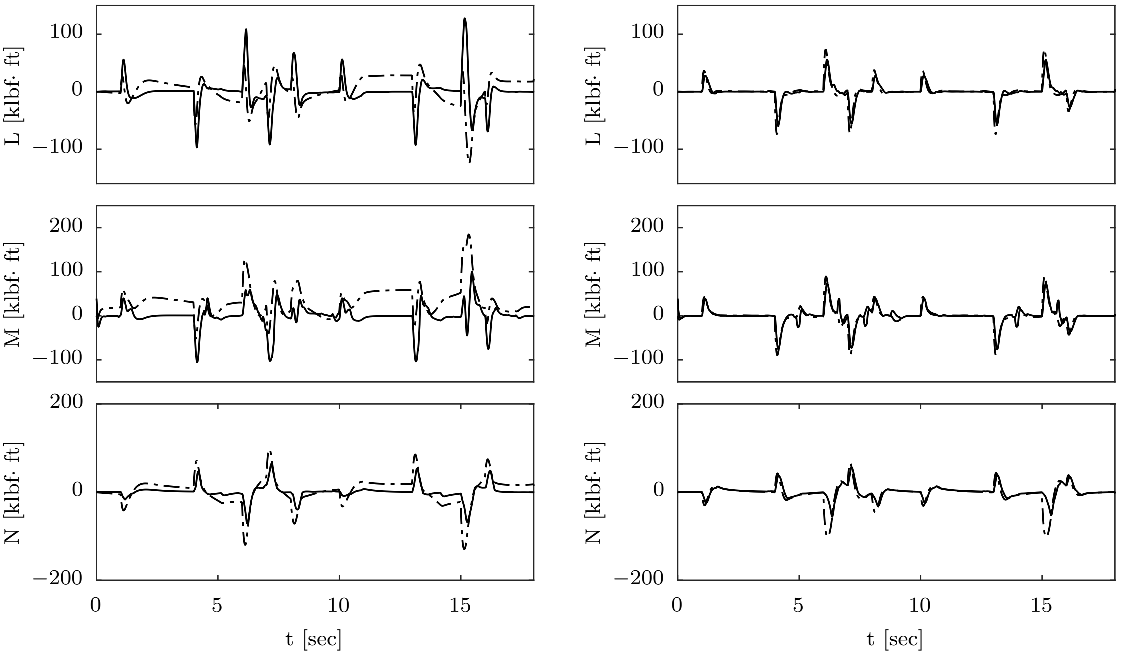

(a) LCA-based FCS.

(b) INCA-based FCS.

Figure 6.5: Commanded (dot-dashed line) and attained (solid line) control-induced moments for the 3211 maneuver with QP.

Figure 6.7b shows that approximately the same number of iterations per time step are executed for INCA and LCA with the active set algorithm. Additionally, since the maximum number of iterations was set to 100, 20% of the iteration limit are rarely reached, which demonstrates satisfactory convergence along the trajectory under consideration. The spatial trajectories of the 3211 maneuvers with active set-based QP are given in Figure 6.8b.

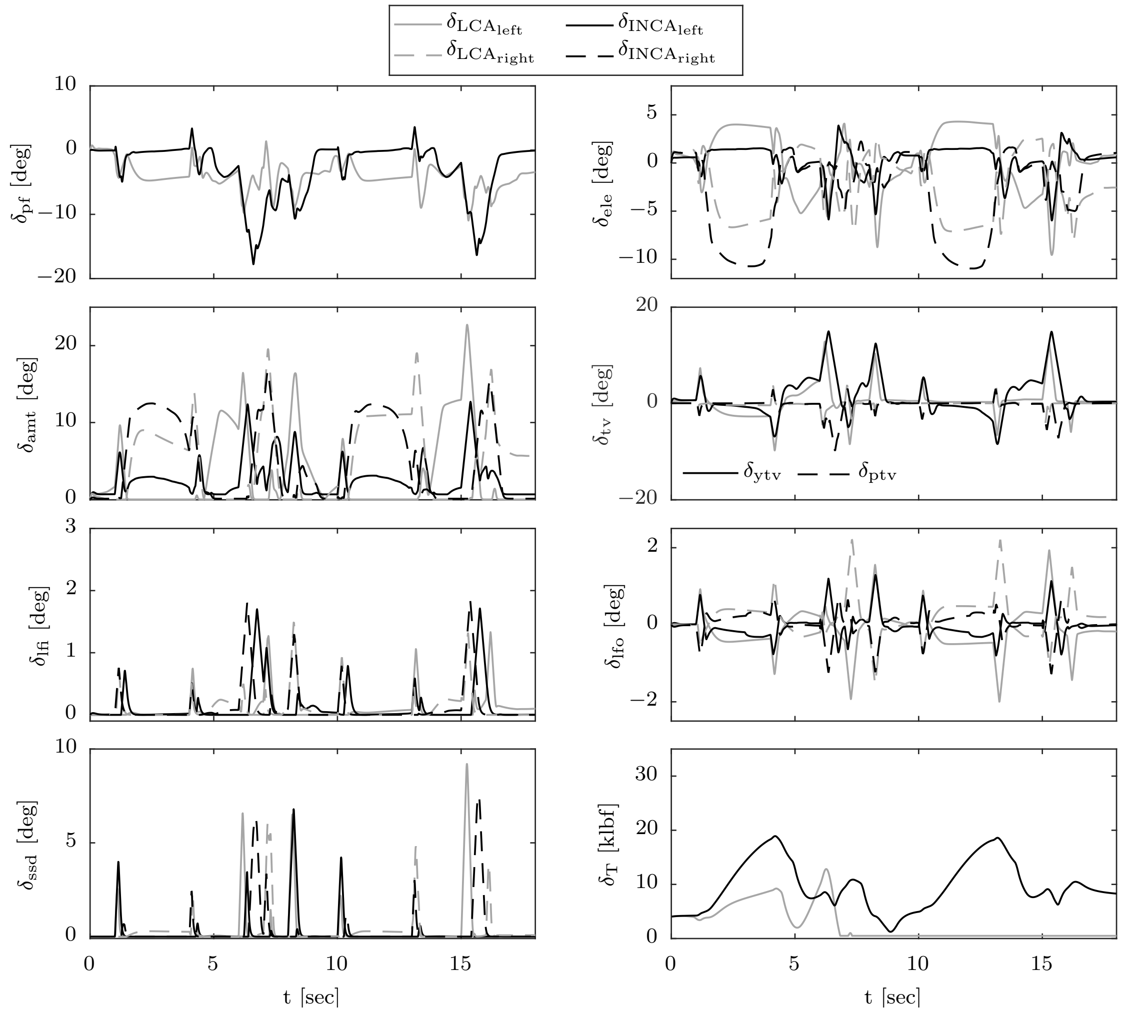

Figure 6.6: Control effector positions with LCA and INCA solved with QP.

6.2.3 Performance Comparison

The quantitative performance metrics used in this thesis to evaluate the overall performance of the flight control systems are:

- **Tracking error:** Evaluates the overall ability of the FCS to track the reference input commands:
$$\varepsilon_{\mathrm{Track}} = \mathrm{RMS}\left(\mathbf{u} - \mathbf{u}_c\right) \tag{6.1}$$
where $\mathbf{u}$ is the vector of control input variables of the FCS under consideration.
- **Allocation error:** Evaluates the ability of a control allocation algorithm to attain the control-induced moments required by the high-level FCS:
$$\varepsilon_{\mathrm{Alloc}} = \mathrm{RMS}\left(\boldsymbol{\tau} - \boldsymbol{\tau}_c\right) \tag{6.2}$$
- **Control effort:** Evaluates the amount of deflection of the control effectors required to satisfy the control commands:
$$\mathrm{Ceff} = \mathrm{RMS}\left(\boldsymbol{\delta} - \boldsymbol{\delta}_p\right) \tag{6.3}$$

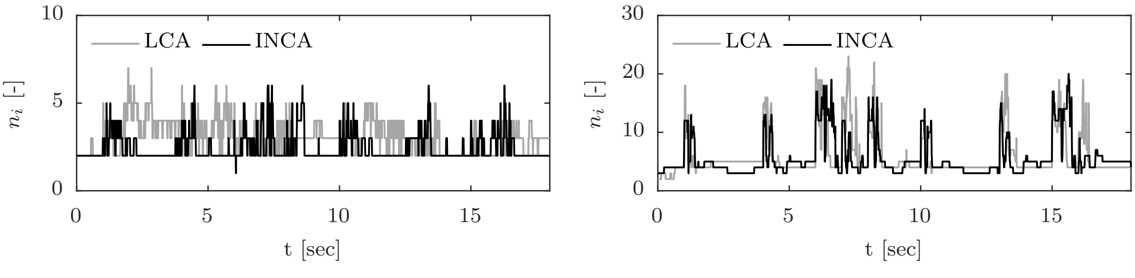

(a) RWPI solver.

(b) QP solver.

Figure 6.7: Number of iterations per time step of the 3211 maneuver with RWPI and QP.

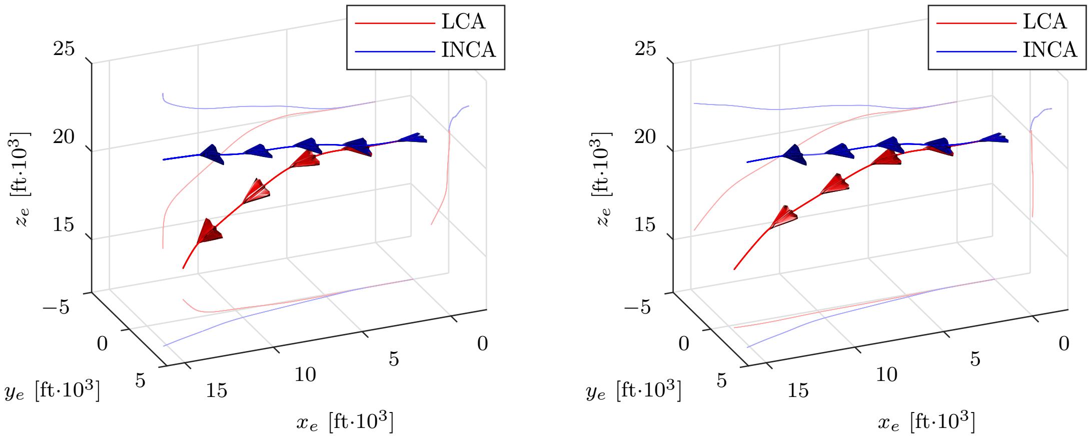

(a) RWPI solver.

(b) QP solver.

Figure 6.8: Trajectories of the 3211 maneuver with RWPI and QP.

The allocation error assesses the ability to fulfill of the primary CA objective, the control effort refers to the degree of fulfilment of the secondary CA objective, and the tracking error refers to the overall performance of the closed loop control system.

The RMS tracking errors along the 3211 maneuver are given in Table 6.2 for both LCA and INCA solved with RWPI and QP. As expected, the tracking error is reduced in both cases with the QP solver with respect to RWPI. However, INCA outperforms LCA in terms of overall tracking performance by a factor of about 2.3 with both solvers. Table 6.3 compares the allocation error of LCA and INCA with RWPI and QP. Although, as in the case of tracking performance, the allocation error is reduced with QP in both cases, the INCA-based system outperforms LCA by a factor of 3 with both solvers.

Table 6.4 lists the control effort per control effector and in total for the whole set of control effectors. Note that INCA makes more extensive use of MTV for yaw control than LCA. Since the on-board model of INCA captures parabolic yawing moments, it makes sense that it prioritizes the use of uncoupled control effectors for pitch control to minimize secondary-axis yawing contributions. In spite of the differences of the distributions of control effort, with no remarkable particularities, it is observed that both systems use

Table 6.2: Tracking error for the 3211 maneuver with LCA and INCA.

	RMS($\varepsilon_{\text{Track}}$)			
Solver	RWPI		QP	
CA Method	LCA	INCA	LCA	INCA
p [deg/sec]	6.01	4.27	5.65	2.69
q [deg/sec]	9.19	2.06	5.47	1.87
r [deg/sec]	4.36	1.81	2.77	1.80
Total	6.82	2.93	4.81	2.15

Table 6.3: Allocation error for the 3211 maneuver with LCA and INCA.

	RMS($\varepsilon_{\text{Alloc}}$)			
Solver	RWPI		QP	
CA Method	LCA	INCA	LCA	INCA
L [klbf·ft]	25.0	17.8	31.1	7.35
M [klbf·ft]	72.6	16.7	44.9	10.4
N [klbf·ft]	35.4	14.4	20.3	14.7
Total	48.8	16.4	33.6	11.2

Table 6.4: Control effort for the 3211 maneuver with LCA and INCA.

	Ceff = RMS $(\delta - \delta_p)$													
	Total	δ_{lfi}	δ_{lfo}	δ_{la}	δ_{le}	δ_{ls}	δ_{pf}	δ_{rfi}	δ_{rfo}	δ_{ra}	δ_{re}	δ_{rs}	δ_{ptv}	δ_{ytv}
LCA/RWPI	2.8	0.3	0.5	3.4	2.3	0.5	4.1	0.2	0.5	6.7	3.3	1.0	1.1	2.7
INCA/RWPI	2.6	0.7	0.6	3.8	2.0	0.7	3.9	0.3	0.6	3.1	2.5	1.6	1.0	6.0
LCA/QP	3.3	0.2	0.5	6.0	3.1	1.2	4.5	0.2	0.5	6.9	4.0	0.8	0.7	3.0
INCA/QP	3.4	0.3	0.3	3.5	1.5	0.8	5.1	0.3	0.3	7.2	5.5	1.2	1.6	4.2

a similar amount of control effort in total. An important conclusion is that, for the trajectory under study, INCA achieves a significant improvement in performance with no significant increase of control effort.

Finally, basic statistical metrics of the number of iterations per time step are given in Table 6.5. The number of iterations required per time step is similar for both methods, which reveals that no added computational complexity is implied by INCA for this maneuver.

To sum up, the preliminary simulations showed a substantial improvement in tracking and allocation performance of INCA over LCA, with no significant increase in control effort and computational load. Additionally, notable improvements in tracking and allocation performance are observed with QP over RWPI in both cases, with only slight increases in control effort and computational load.

6.3 Robustness Analysis to Jacobian Model Mismatch

As discussed earlier, the sensitivity of the performance of INCA to mismatch in the control effectiveness Jacobian model $\nabla_{\boldsymbol{\delta}}\Phi(\mathbf{x}, \boldsymbol{\delta})$ is a relevant subject of study. As deducted in the theoretical development of the method, it is expected that the acceleration feedback provides considerable robustness against model mismatch. In order to support this hypothesis and quantify the degree of robustness, a sensitivity analysis was carried out.

Table 6.5: Iterations per time step for the 3211 maneuver with LCA and INCA.

	n_i			
Solver	RWPI		QP	
CA Method	LCA	INCA	LCA	INCA
Min.	2	1	2	3
Avg.	3.1	2.4	5.8	5.6
Max.	7	6	23	20

There are three ways in which mismatch can be introduced in the Jacobian model. The first one is by changing the order of continuity between simplices of the original spline model $\Phi(\mathbf{x}, \boldsymbol{\delta})$. Abrupt discontinuities in the aerodynamic model cause undesirable peaks in the Jacobian function. The spline model used in this thesis has 0th-order continuity between simplices, and therefore represents the worst case scenario. Any variation in the model continuity order can only lead to improvement in the accuracy of the Jacobian function.

The two other possible alterations of the model accuracy are the application of offset and scaling to the Jacobian terms. To analyse model sensitivity, offset and scaling were introduced in the Jacobian function as follows:

$$\nabla_{\boldsymbol{\delta}}\Phi'\left(\mathbf{x}, \boldsymbol{\delta}\right) = m_{\Phi}\nabla_{\boldsymbol{\delta}}\Phi_{\max} + n_{\Phi}\nabla_{\boldsymbol{\delta}}\Phi\left(\mathbf{x}, \boldsymbol{\delta}\right) \tag{6.4}$$

where $\nabla_{\boldsymbol{\delta}}\Phi_{\max}$ is a matrix containing the maximum values of the Jacobian terms obtained along the 3211 reference trajectory in Section 6.2, m_{Φ} represents the fraction of the maximum Jacobian values introduced as offset and n_{Φ} represents the scaling factor of the original Jacobian function.

The sensitivity analysis consisted on simulating the 3211 maneuver described in Section 6.2 with INCA/QP by varying the model offset and scaling between simulations. The scale factor n_{Φ} was varied from 0.6 to 1.4 in steps of 0.01 taking a total of 81 values, and the offset m_{Φ} was varied between -0.5 and 0.5 in steps of 0.01 taking a total of 101 values. This led to a total amount of 8181 simulations. The tracking and allocation errors and the control effort were recorded for each simulation in order to study the effect of model offset and scaling on performance.

The obtained performance metrics are displayed as a function of the introduced model offset and scaling in Figures 6.9 to 6.11. Note that the range of model offset was reduced to ±30% in these figures to exclude large peaks in extreme regions and improve resolution within the shown region. Figure 6.9 shows that the allocation error only varies between 10 and 14 klbf·ft for the study region shown. It is worth pointing out that, whereas performance is slightly deteriorated as offset deviates from 0%, it significantly improves for decreasing scaling factors. Maximum performance is reached for the minimum scaling applied and within the region close to 0% offset. This reveals that the INCA system benefits from underestimation of the magnitude of the Jacobian terms, whereas overestimation results detrimental.

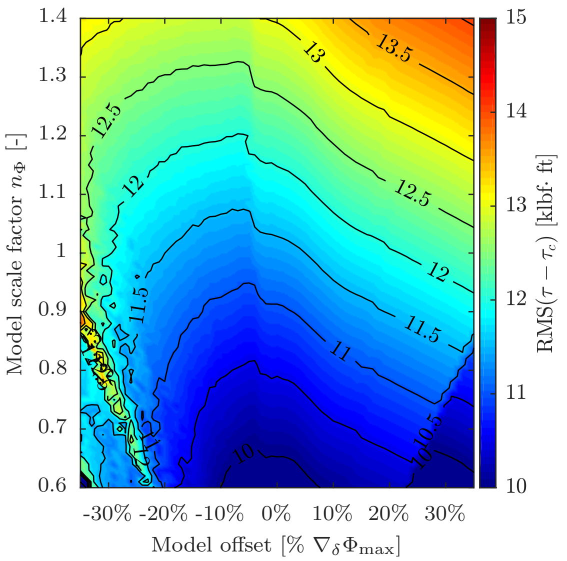

Figure 6.9: Effect of model mismatch on allocation performance.

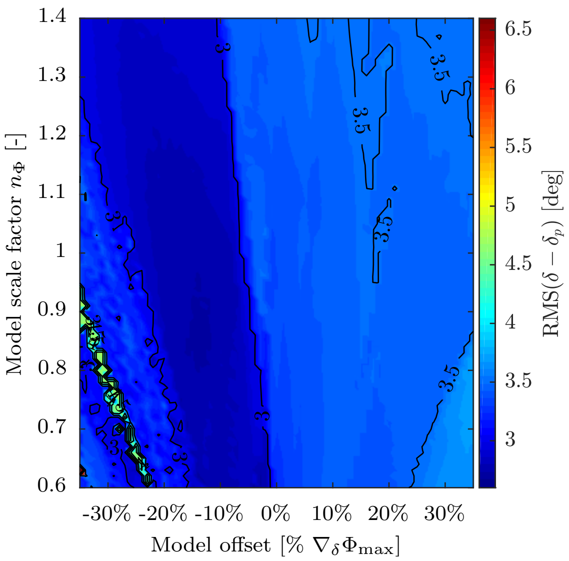

Figure 6.10: Effect of model mismatch on control effort.

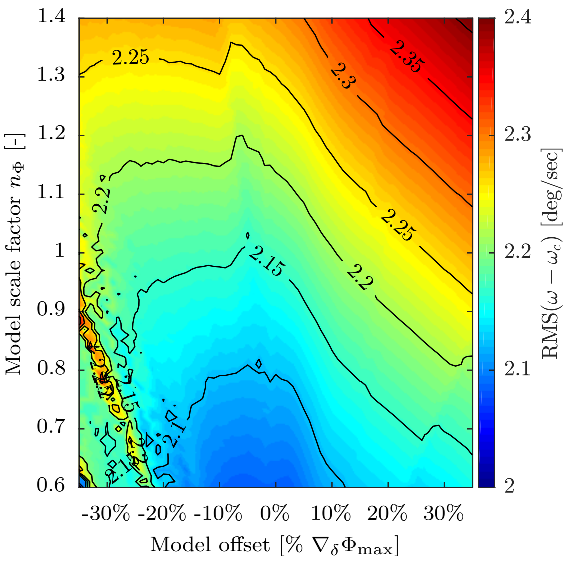

Figure 6.11: Effect of model mismatch on tracking performance.

Figure 6.10 shows a mostly uniform control effort between 3 and 3.5 deg along the shown range of study, except for a region with offsets between -30% and -20% and scaling factors between 0.6 and 0.9. Note, however, that a local minimum exists in a region with scalings between 0.8 and 0.9 and offsets between -15% and -10%. This reveals a possible mismatch of the Jacobian model used in the simulations. However, the overall variation in control effort is very small within most of the study region shown.

Figure 6.11 shows a similar effect of model mismatch on the tracking performance than observed on the allocation performance. Tracking performance improves when the magnitude of the Jacobians is underestimated, whereas overestimation increases the tracking error. Maximal performance is also observed for the smallest scaling factor applied, close

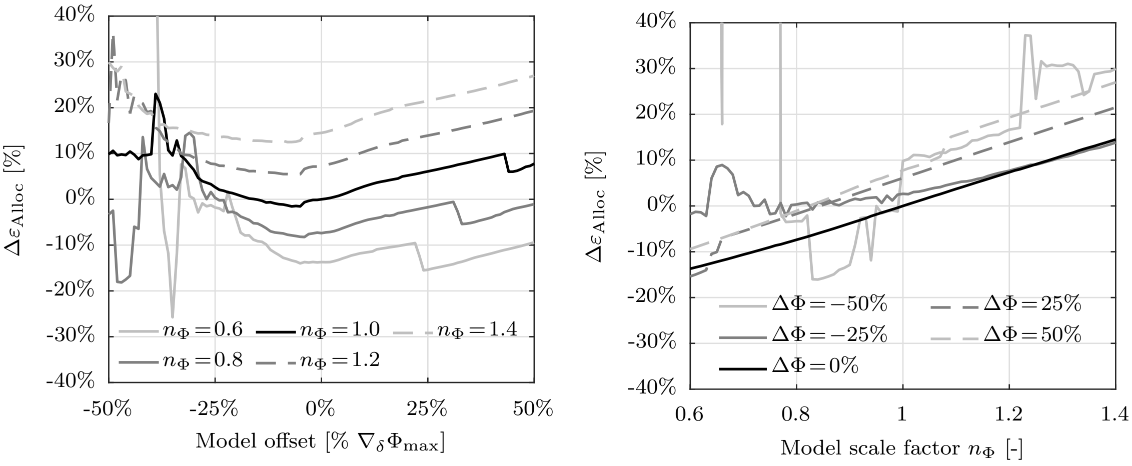

(a) Allocation error with model offset.

(b) Allocation error with model scaling.

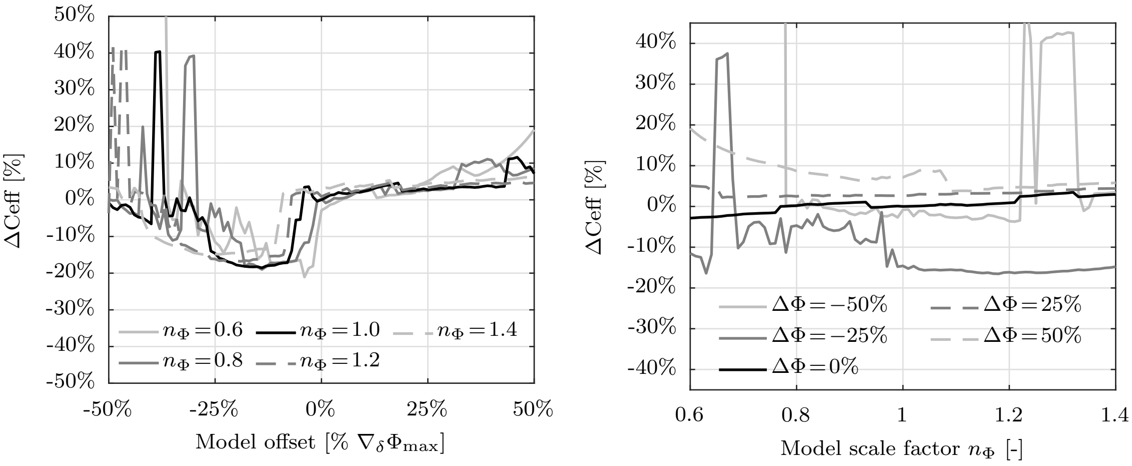

(c) Control effort with model offset.

(d) ontrol effort with model scaling.

Figure 6.12: Performance degradation due to model scaling and offset with respect to the baseline study case with $m_\Phi = 0$ and $n_\Phi = 1$.

to the region of 0% offset. It is worth noting, however, that the variation of the tracking error ranges only between 2 and 2.4 for the shown region, demonstrating a strong robustness of the overall tracking performance to model mismatch.

Figure 6.12 shows the performance degradation as a percentage of the error of the baseline case with unit model scaling and zero offset. In this case, the performance degradation is shown for the whole range of tested model offsets. Figures 6.12a and 6.12b show the previously remarked behaviour: a slight improvement in allocation performance for a small negative offset but degradation for higher offset values, and a close-to-linear improvement of the allocation performance with decreasing scaling factors. Degradation of the allocation performance reaches a maximum of about 30% for a 50% positive offset and a scale factor of 1.2, which demonstrates strong robustness. The system becomes unstable for negative offsets below -30% when the scaling factor is smaller than 0.8. Finally, Figures 6.12c and 6.12d show the effect of model mismatch on control effort. The previously mentioned local minimum can be observed here, revealing a possible mismatch of the model used in the simulations.

In conclusion, the INCA-based controller showed very slight performance degradation for offsets of $\pm 30\%$ and scalings between 0.6 and 1.4. The overall performance of the controller improves when the magnitude of the Jacobians is underestimated, leading to maximal performance at scalings of 0.6 close to the 0% offset region. Observed local minima reveal a possible mismatch of the current model of about 15% in magnitude and 15% in offset. Allocation performance degrades only on a 20% for the maximum tested offset and scaling, but the system becomes unstable at negative offsets of -30% for scalings below 0.8. Overall, the INCA system demonstrated strong robustness against Jacobian model mismatch.

6.4 Aggressive Flight Maneuvers

The ICE aircraft is a highly maneuverable fighter designed for air combat, and therefore its design, including flight control and stability systems, must demonstrate high maneuverability and stability in extreme regions of its flight envelope. In order to assess the performance of the INCA-based and the LCA-based flight control systems when the aircraft is pushed towards the limits of its operational range, four tests were designed with aggressive air combat aerobatic maneuvers. The designed trajectories include barrel rolls, asymmetric loopings, Immelmann turns and more. These maneuvers were coded as predefined reference trajectories using the control inputs to the different outer loops described in Chapter 5. All aggressive maneuvers were flown with both LCA- and INCA-based controllers solved with both RWPI and active set-based QP. The most relevant results of these simulations are presented and discussed in this section. The results not shown here are included in Appendix C.

6.4.1 Maneuver A: High-Bank Climbing Spiral

The high-bank climbing spiral maneuver uses the flight path guidance outer loop with Euler angle inversion, using bank angle ϕ, glide path angle γ and sideslip β as control inputs. The reference trajectory consists of a constant bank angle reference of 80 deg with a constant flight path angle reference of 15 deg and zero sideslip. This results in a high-bank coordinated turn while climbing.

The linear gains of the outer guidance loop used for the INCA-based system are listed in Tale 6.6. The LCA-based flight control systems were not able to follow the trajectory with this set of gains, so the gains of the γ channel were lowered to $K_{\gamma_P} = 0.15$, $K_{\gamma_I} = 0.03$ and $K_{\gamma_D} = 0.35$ in order to obtain a stable trajectory.

Table 6.6: Gains used in the outer guidance loop for maneuver A.

Channel	ϕ	γ	β
K_{g_P}	1.00	0.20	1.00
K_{g_I}	1.00	0.05	0.35
K_{g_D}	1.00	0.40	0.00

Since the best performance was obtained with the active set QP solver for both LCA and INCA, only the simulation results with the LCA/QP and INCA/QP systems are shown here. The results with the RWPI solver can be found in Section C.1 of Appendix C. The time histories of the outer loop and inner loop control variables along the trajectory are given in Figures 6.13 and 6.14 respectively. These results show the inability of the LCA-based system to properly track the flight path angle reference, resulting in severe oscillations and excursions along the maneuver. Due to the high bank angle used during the spiral climb, flight path angle control is mostly performed through the yaw body axis. Due to the limitations of LCA methods with regards to directional control authority in tailles configurations, this results in extremely poor performance when performing high-bank climbs. Note, however, the remarkably superior performance obtained with the INCA method. The tracking errors for the outer and inner loop control variables are given for all the tested conditions in tables 6.7 and 6.8 respectively. INCA improves the tracking performance of the inner loop variables by a factor of about 10 with respect to LCA methods for this trajectory.

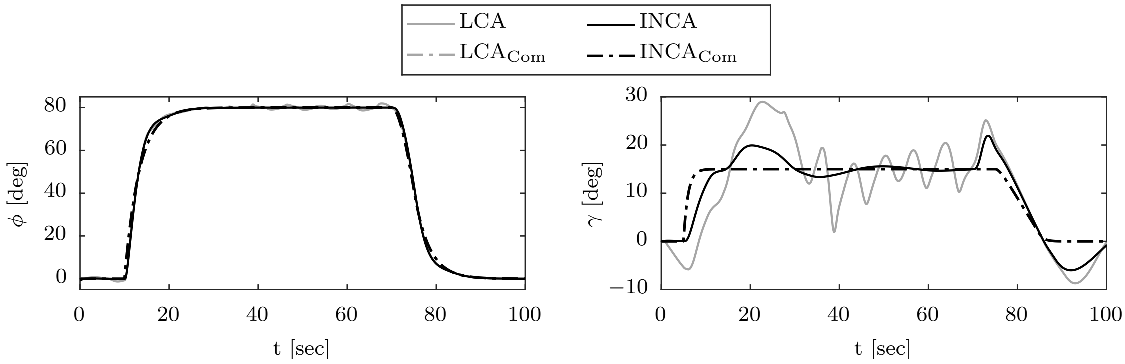

Figure 6.13: Outer loop control variables of maneuver A with LCA and INCA with QP.

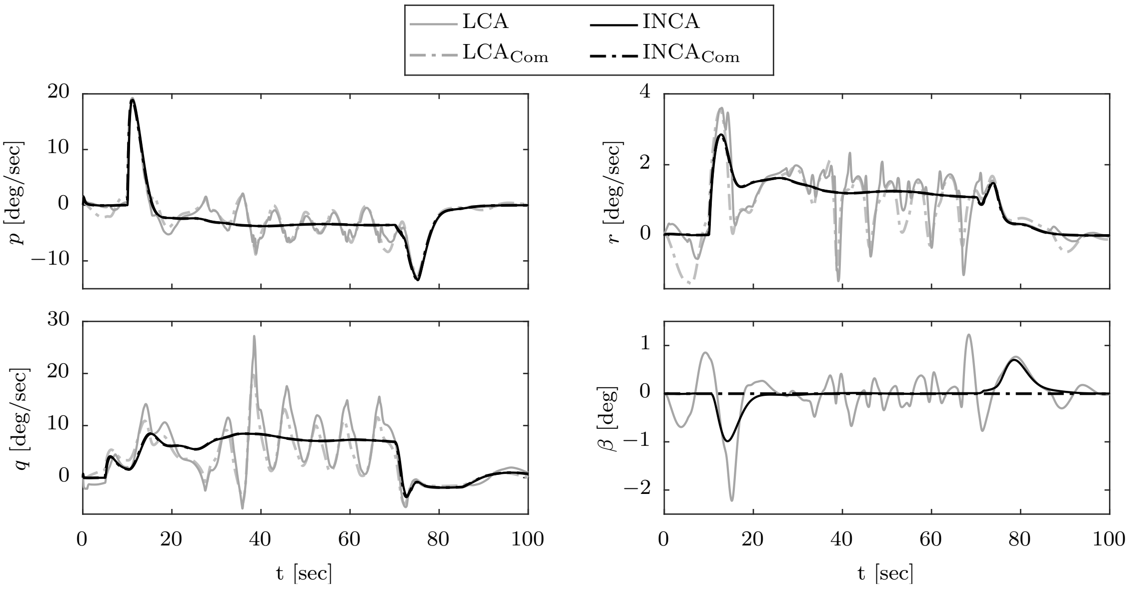

Figure 6.14: Inner loop control variables of maneuver A with LCA and INCA with QP.

Table 6.7: Tracking error of the outer loop control variables of maneuver A.

	RMS($\varepsilon_{\text{Track}}$)			
Solver	RWPI		QP	
CA Method	LCA	INCA	LCA	INCA
ϕ [deg]	1.53	1.49	1.48	1.49
γ [deg]	6.08	3.02	6.68	3.02
β [deg]	0.44	0.25	0.47	0.25
Total	3.63	1.95	3.96	1.95

Table 6.8: Tracking error of the inner loop control variables of maneuver A.

	RMS($\varepsilon_{\text{Track}}$)			
Solver	RWPI		QP	
CA Method	LCA	INCA	LCA	INCA
p [deg/sec]	0.79	0.29	0.91	0.29
q [deg/sec]	1.86	0.14	2.05	0.14
r [deg/sec]	0.44	0.03	0.47	0.03
Total	1.19	0.19	1.32	0.19

The commanded and attained control-induced moments are given in Figure 6.15. LCA is unable to produce the required moments, which causes big oscillations and excursions. INCA, however, is able to produce the required moments quickly and accurately, which results in smaller moments required to satisfy the control commands. The allocation errors are given in Table 6.15. These results show that INCA improves the allocation performance by a factor of 16 in this case.

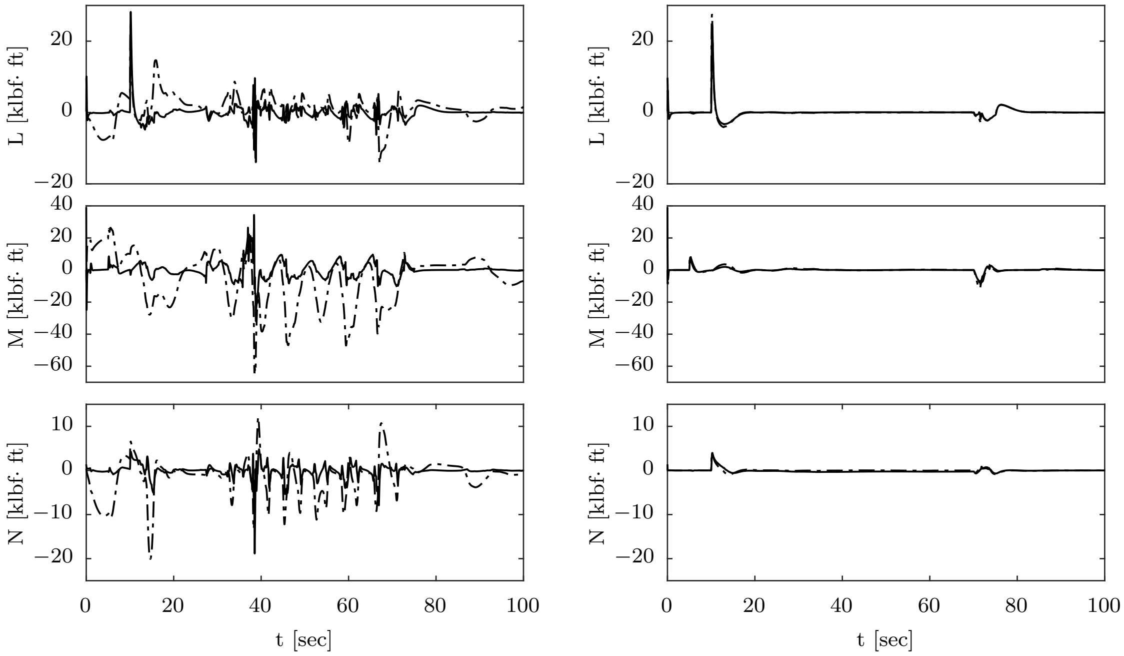

Figure 6.15: Commanded (dot-dashed line) and attained (solid line) control-induced moments of maneuver A with LCA and INCA with QP.

Finally, the time histories of the control effector positions are given in Figure 6.16. Given the high bank angle at which the spiral climb occurs, INCA makes extensive use of the pitch flap to perform the turn. In this case, sideslip is kept to zero by using a constant AMT deflection, and roll axis commands are attained by combining elevons and outboard LEFs. The SSDs remain closed along the whole trajectory. On the other hand, the LCA-based controller experiments strong interactions between control effectors (note that the SSDs start to open in several occasions), causing severe oscillations in all axes. The pitch flap is barely used, and extensive use is made of thrust vectoring in the pitch axis instead.

Table 6.9: Allocation error of maneuver A.

	RMS($\varepsilon_{\text{Alloc}}$)			
Solver	RWPI		QP	
CA Method	LCA	INCA	LCA	INCA
L [klbf·ft]	3.32	0.41	3.75	0.41
M [klbf·ft]	13.6	0.87	15.2	0.87
N [klbf·ft]	3.86	0.23	4.05	0.23
Total	8.40	0.57	9.31	0.57

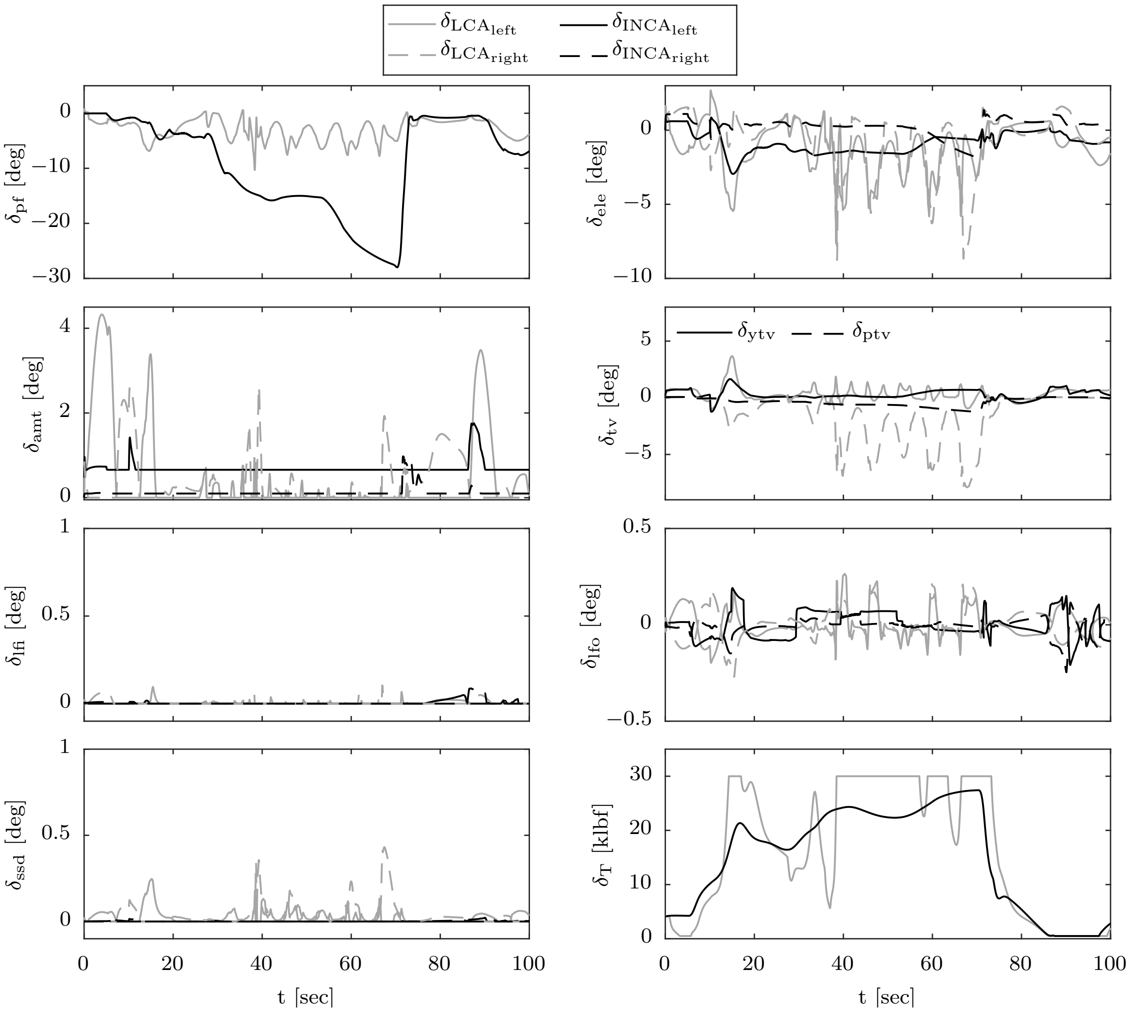

Figure 6.16: Control effector positions of maneuver A with LCA and INCA with QP.

The control efforts of this maneuver are given in Table 6.10. Note that the total control effort is higher for INCA with both solvers. This is justified by an extensive and constant use by INCA of the pitch flap to turn, which is a reasonable turning strategy given the large bank angle of the maneuver. Instead of using the pitch flap, LCA places higher control effort on the rest of actuators, especially on the elevons and pitch thrust vectoring.

Table 6.10: Control effort of maneuver A.

	Ceff = RMS $(\delta - \delta_p)$													
Actuator	Total	δ_{lfi}	δ_{lfo}	δ_{la}	δ_{le}	δ_{ls}	δ_{pf}	δ_{rfi}	δ_{rfo}	δ_{ra}	δ_{re}	δ_{rs}	δ_{ptv}	δ_{ytv}
LCA/RWPI	1.4	0.0	0.1	1.1	1.9	0.1	3.4	0.0	0.1	0.6	2.0	0.1	2.4	0.7
INCA/RWPI	3.5	0.0	0.1	0.7	1.1	0.0	12.5	0.0	0.0	0.2	0.7	0.0	0.5	0.5
LCA/QP	1.5	0.0	0.1	1.1	2.0	0.0	3.5	0.0	0.1	0.7	2.1	0.1	2.6	0.7
INCA/QP	3.5	0.0	0.1	0.7	1.1	0.0	12.5	0.0	0.0	0.2	0.7	0.0	0.5	0.5

The spatial trajectories of maneuver A are shown in Figure 6.17. The time histories of the number of iterations per time step with RWPI and QP are given in Figure 6.18, and their statistical metrics are listed in Table 6.11. As in previous cases, no significant effect of using INCA is observed on the computational load.

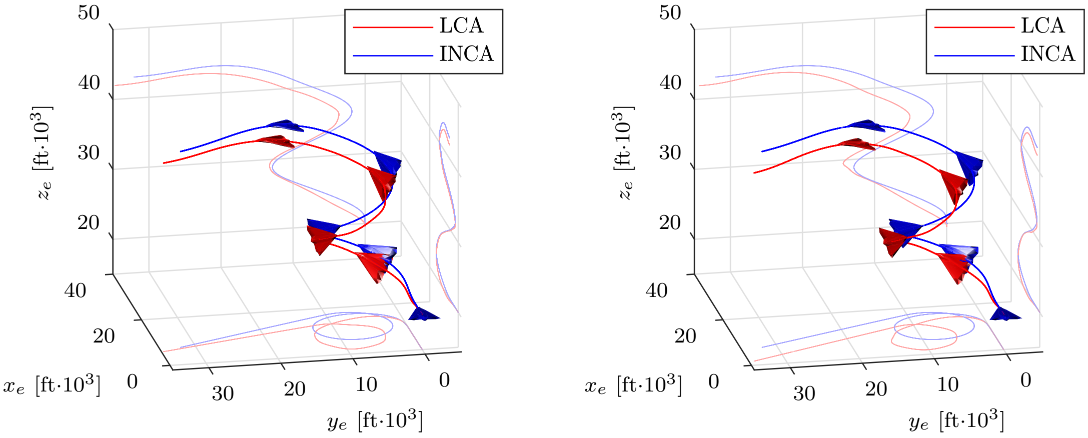

(a) RWPI solver.

(b) QP solver.

Figure 6.17: Trajectories of maneuver A with RWPI and QP.

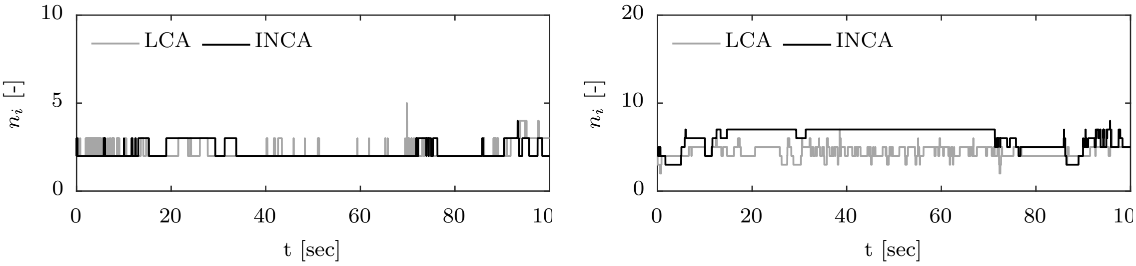

(a) RWPI solver.

(b) QP solver.

Figure 6.18: Number of iterations per time step of maneuver A with RWPI and QP.

Table 6.11: Iterations per time step for maneuver A with LCA and INCA.

	n_i			
Solver	RWPI		QP	
CA Method	LCA	INCA	LCA	INCA
Min.	2	2	2	3
Avg.	2.2	2.3	4.4	6.1
Max.	5	4	7	8

6.4.2 Maneuver B: Barrel Roll

The barrel roll maneuver uses the sideslip compensation outer loop with direct roll and pitch body rate control inputs. It consists of constant pitch and roll rate inputs, synchronized to complete two barrel rolls and exit the maneuver with the initial heading and zero flight path angle (straight and level flight). The gains used for the sideslip compensation loop are those listed in Table 6.6.

Since the best performance was obtained with the active set QP solver for both LCA and INCA, only the simulation results with the LCA/QP and INCA/QP systems are shown here. The results with the RWPI solver can be found in Section C.2 of Appendix C. The time histories of the control variables are given in Figure 6.19. It can be observed that LCA is unable to keep a constant pitch rate, and exhibits bad tracking performance in all axes, especially in the lateral-directional channels. In contrast, the tracking performance of INCA is excellent with no noticeable deviations from the commanded references. This difference in performance is quantified in Table 6.12, which shows a reduction in tracking error of INCA with respect to LCA by a factor of 5.5 for this trajectory.

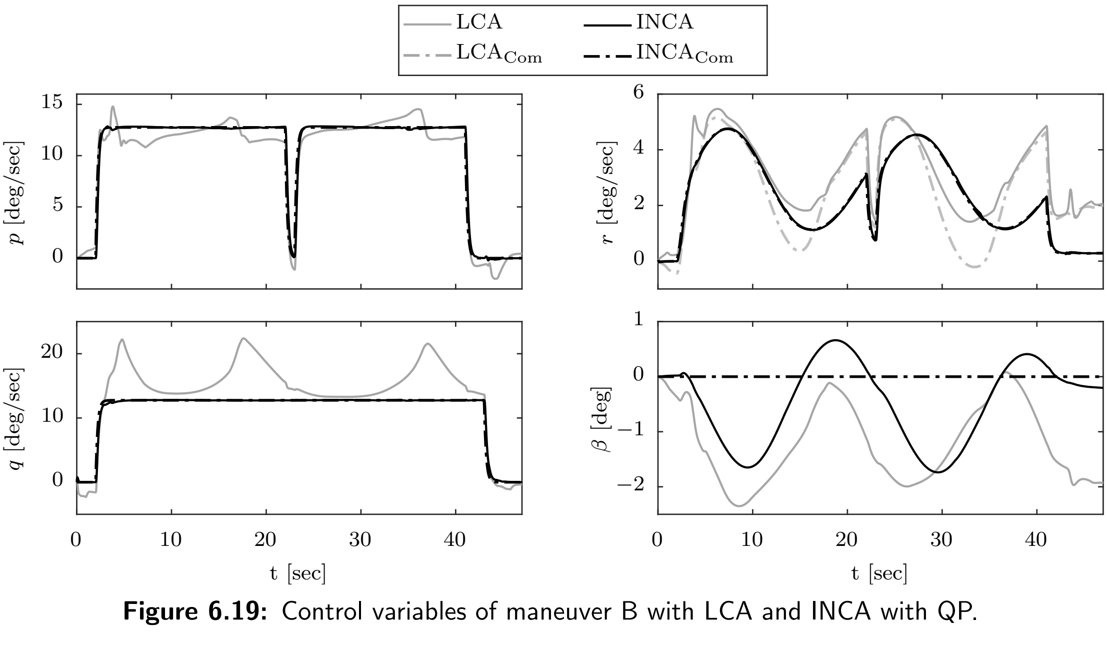

Figure 6.19: Control variables of maneuver B with LCA and INCA with QP.

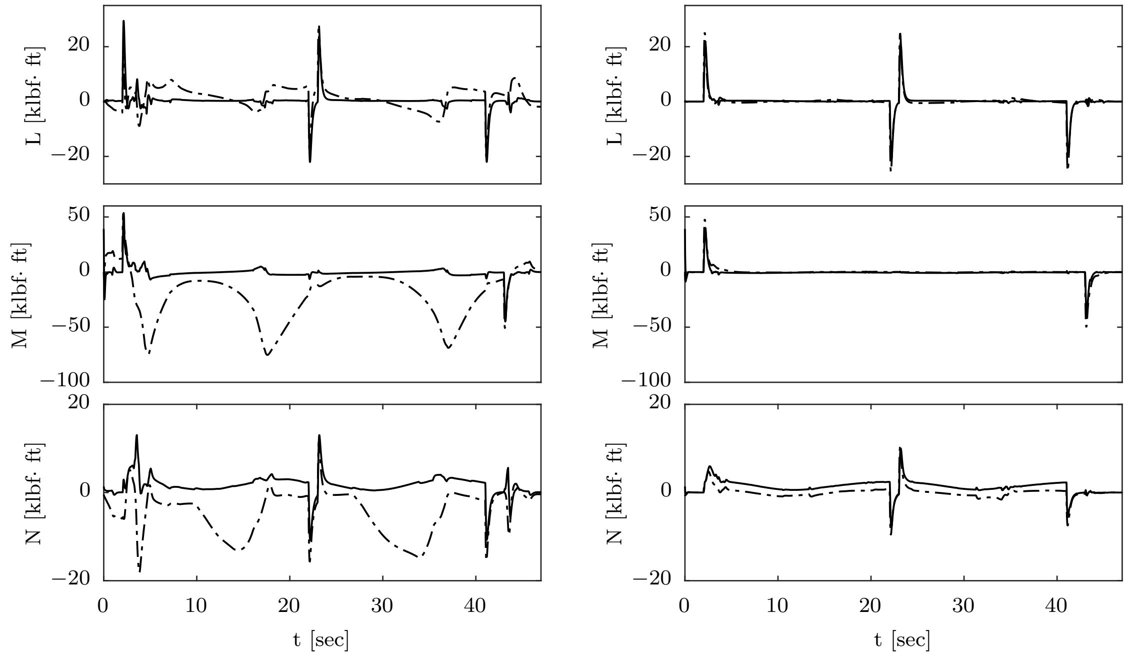

Figure 6.20: Commanded (dot-dashed line) and attained (solid line) control-induced moments of maneuver B with LCA and INCA with QP.

Table 6.12: Tracking error of maneuver B.

	$\mathrm{RMS}(\varepsilon_{\mathrm{Track}})$			
Solver	RWPI		QP	
CA Method	LCA	INCA	LCA	INCA
p [deg/sec]	0.88	0.58	1.03	0.58
q [deg/sec]	3.99	0.46	3.91	0.46
r [deg/sec]	0.85	0.10	0.76	0.10
Total	2.41	0.43	2.37	0.43

Table 6.13: Allocation error of maneuver B.

	$\mathrm{RMS}(\varepsilon_{\mathrm{Alloc}})$			
Solver	RWPI		QP	
CA Method	LCA	INCA	LCA	INCA
L [klbf·ft]	3.41	1.10	4.04	1.09
M [klbf·ft]	30.2	2.16	29.6	2.15
N [klbf·ft]	8.71	1.52	7.87	1.52
Total	18.3	1.66	17.8	1.65

The time histories of the commanded and attained moments are given in Figure 6.20. INCA shows substantially superior performance with respect to LCA, which is unable to produce the required moments. Allocation performance metrics are given in Table 6.13, which shows an improvement of allocation performance of INCA with respect to LCA by a factor of 10 in this case.

The time histories of the control effector positions along the trajectory are given in Figure 6.21. It is observed that INCA makes more extensive use of the pitch flap for longitudinal control, whereas LCA places more control effort on pitch thrust vectoring. Also, LCA uses the elevons to a larger extent. INCA compensates for sideslip in the directional channel with a constant deflection of the left AMT, whereas LCA opens the left SSD, provoking interactions with the elevons resulting in the oscillations observed in both actuators. The control efforts for this trajectory are given in Table 6.14. The total control effort of INCA is again higher, although LCA allocates larger control effort on all the individual control effectors except on the pitch flap.

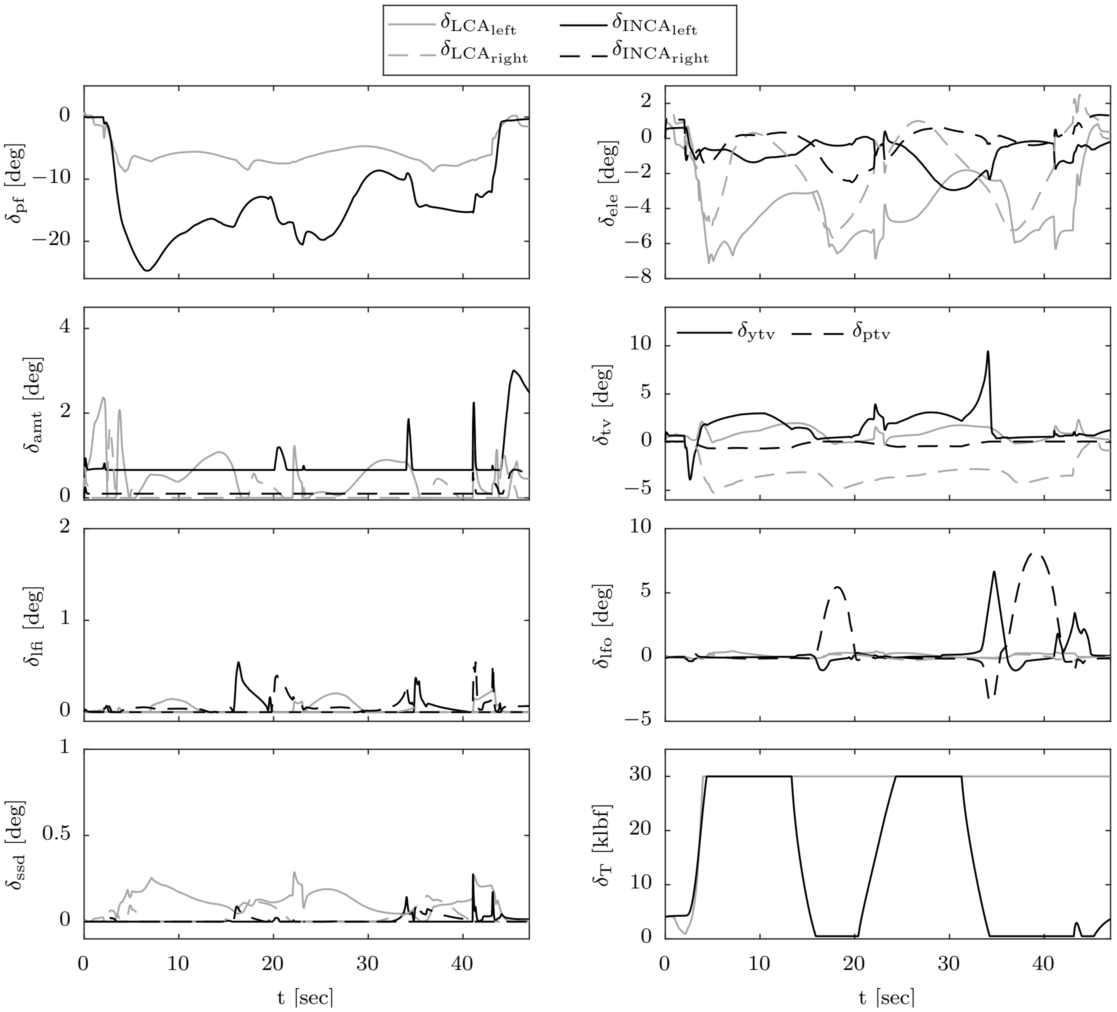

Figure 6.21: Control effector positions of maneuver B with LCA and INCA with QP.

Table 6.14: Control effort of maneuver B.

							Ceff = RMS $(\delta - \delta_p)$							
Actuator	Total	δ_{lfi}	δ_{lfo}	δ_{la}	δ_{le}	δ_{ls}	δ_{pf}	δ_{rfi}	δ_{rfo}	δ_{ra}	δ_{re}	δ_{rs}	δ_{ptv}	δ_{ytv}
LCA/RWPI	2.5	0.1	0.2	0.9	4.5	0.1	6.2	0.0	0.1	0.2	2.6	0.1	3.4	1.3
INCA/RWPI	4.3	0.1	1.1	0.9	1.2	0.1	15	0.2	2.5	0.2	0.9	0.0	0.3	2.5
LCA/QP	2.4	0.1	0.2	0.6	4.3	0.1	6.1	0.0	0.1	0.2	2.7	0.1	3.4	1.1
INCA/QP	4.3	0.1	1.1	0.9	1.2	0.0	15	0.1	2.5	0.2	0.9	0.0	0.3	2.2

The spatial trajectories of maneuver B are given in Figure 6.22. The time histories of the number of iterations per time step are given in Figure 6.23, and its statistical metrics are listed in Table 6.15. No significant effect of using INCA is observed on the computational load for this maneuver.

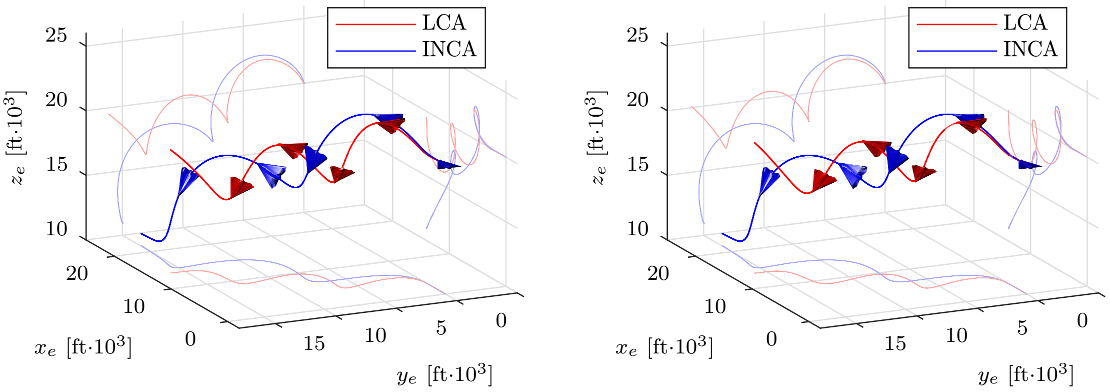

(a) RWPI solver.

(b) QP solver.

Figure 6.22: Trajectories of maneuver B with RWPI and QP.

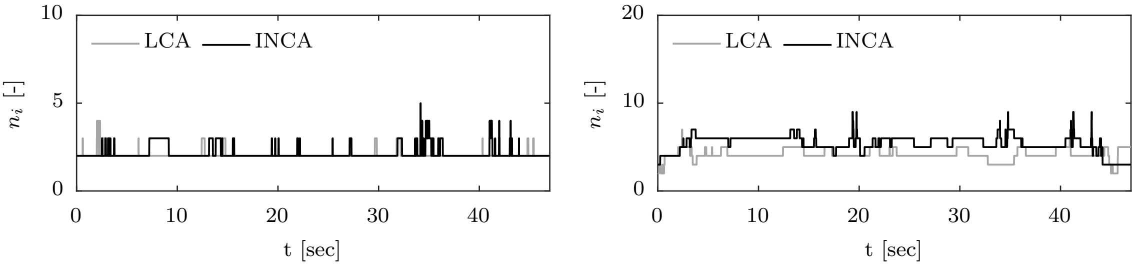

(a) RWPI solver.

(b) QP solver.

Figure 6.23: Number of iterations per time step of maneuver B with RWPI and QP.

Table 6.15: Number of iterations per time step of maneuver B.

	n_i			
Solver	RWPI		QP	
CA Method	LCA	INCA	LCA	INCA
Min.	2	2	2	3
Avg.	2.0	2.1	4.1	5.4
Max.	4	5	7	9

6.4.3 Maneuver C: High AoA and High Sideslip Commands

This maneuver is intended to test the behaviour of the flight control systems at high AoA and high sideslip, since most nonlinearities and interactions occur within these regions of the flight envelope. The simulations were performed using the aerodynamic inversion outer loop with the aerodynamic angles α and β and the bank angle ϕ as control inputs. The reference consists of a doublet α input of ± 40 deg followed by a doublet β input of ± 25 deg, while keeping the bank angle reference at 0 deg. Since the controller with

Table 6.16: Gains used in the aerodynamic inversion loop for maneuver C.

Channel	ϕ	α	β
K_{a_P}	1.50	2.40	1.65
K_{a_I}	0.00	0.20	0.00
K_{a_D}	0.00	0.10	0.00

LCA/QP resulted in unstable flight with stall, only the results with the RWPI solver are shown in this section. The results with QP can be found in Section C.3 of Appendix C. The gains used in the aerodynamic inversion loop are given in Table 6.16. Since the main interest of this maneuver was to study the nonlinearities and interactions of the aerodynamic actuators at high aerodynamic angles, the penalization gains of MTV on the weighting matrix $W_{\boldsymbol{\delta}}$ were set to 20 to prioritize the use of aerodynamic control effectors.

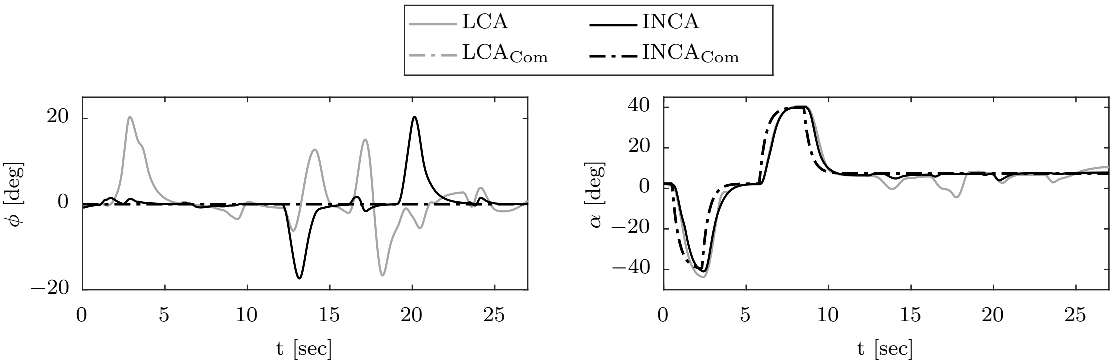

Figure 6.24: Outer loop control variables of maneuver C with LCA and INCA with RWPI.

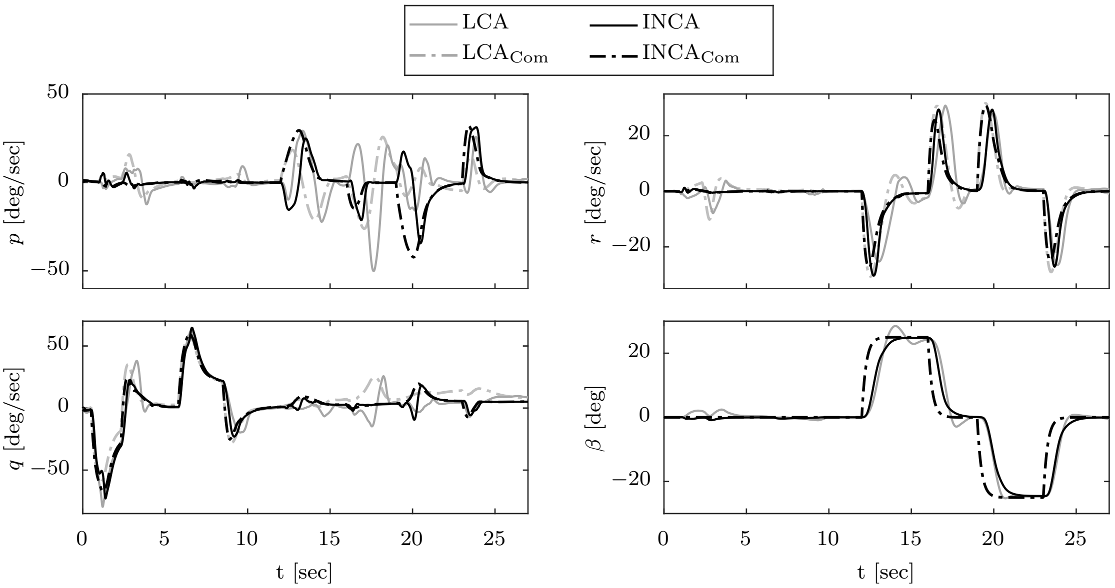

Figure 6.25: Inner loop control variables of maneuver C with LCA and INCA with RWPI.

Table 6.17: Tracking error of the outer loop control variables of maneuver C.

	RMS($\varepsilon_{\text{Track}}$)			
Solver	RWPI		QP	
CA Method	LCA	INCA	*LCA**	INCA
ϕ [deg]	5.84	4.56	*37.1*	4.56
α [deg]	6.65	5.80	*8.72*	5.80
β [deg]	6.19	5.63	*6.33*	5.63
Total	6.24	5.36	*22.3*	5.36

* *Unstable trajectory.*

Table 6.18: Tracking error of the inner loop control variables of maneuver C.

	RMS($\varepsilon_{\text{Track}}$)			
Solver	RWPI		QP	
CA Method	LCA	INCA	*LCA**	INCA
p [deg/sec]	13.1	11.2	*278*	1.92
q [deg/sec]	10.9	5.93	*70.2*	4.89
r [deg/sec]	7.25	4.62	*97.0*	3.72
Total	10.7	7.78	*175*	3.72

* *Unstable trajectory.*

The time histories of the controlled variables are given in Figures 6.24 and 6.25, and the tracking performances are listed in Tables 6.17 and 6.18. In the α doublet part of the trajectory, the tracking performance in the longitudinal channel is poorer with LCA than with INCA. It can be observed that within the first part of the maneuver the required rolling moments are successfully attained by both control allocation systems. However, directional moments are also required in the longitudinal maneuver due to the unstable lateral-directional eigenmodes of the ICE aircraft. Unlike INCA, LCA fails to produce the required stabilizing moments in the directional channel. It is worth pointing out the large excursion of up to 20 deg in bank angle observed in Figure 6.24 with LCA. This excursion is suppressed by INCA, which successfully produces the required lateral-directional moments. The control effector positions in Figure 6.27 show that more extensive use of the pitch flap is made by LCA in this case.

In the second part of the trajectory with the sideslip doublet, worse performance is obtained with LCA, which exhibits excursions and oscillations in all channels. Figure 6.26 shows that LCA does not attain the required lateral-directional moments, whereas allocation performance is considerably superior with INCA. Excursions in rolling moment are observed for both INCA and LCA.

In Figure 6.27 it can be observed that INCA makes more extensive use of innovative nonlinear control effectors for lateral-directional control such as SSDs and outboard LEFs. Since the parabolic yawing moments of the outboard LEFs had to be removed from the linear control effector model, LCA does not use these effectors for lateral-directional control (it is worth recalling that LEFs are an excellent source of lateral-directional control power at high AoA). Since the positive effect of opening the SSDs at high AoA on the control effectiveness of trailing-edge actuators is not captured by the linear control effector model, SSDs are barely used in LCA. As a result, LCA allocates a higher control load on the AMTs for directional control and uses the elevons to compensate for secondary moments in the roll axis. All these effects can be observed in the allocation errors in Table 6.19 and the control efforts in Table 6.20.

The spatial trajectories of maneuver C are given in Figure 6.28. The number of iterations per time step are plotted in Figure 6.29 and listed in Table 6.21. It is worth highlighting that, although only results with RWPI were shown here to ensure a fair comparison, the performance of INCA with QP for this trajectory is notably superior. This is reflected in Tables 6.17 to 6.19 and in the results shown in Section C.3 of Appendix C.

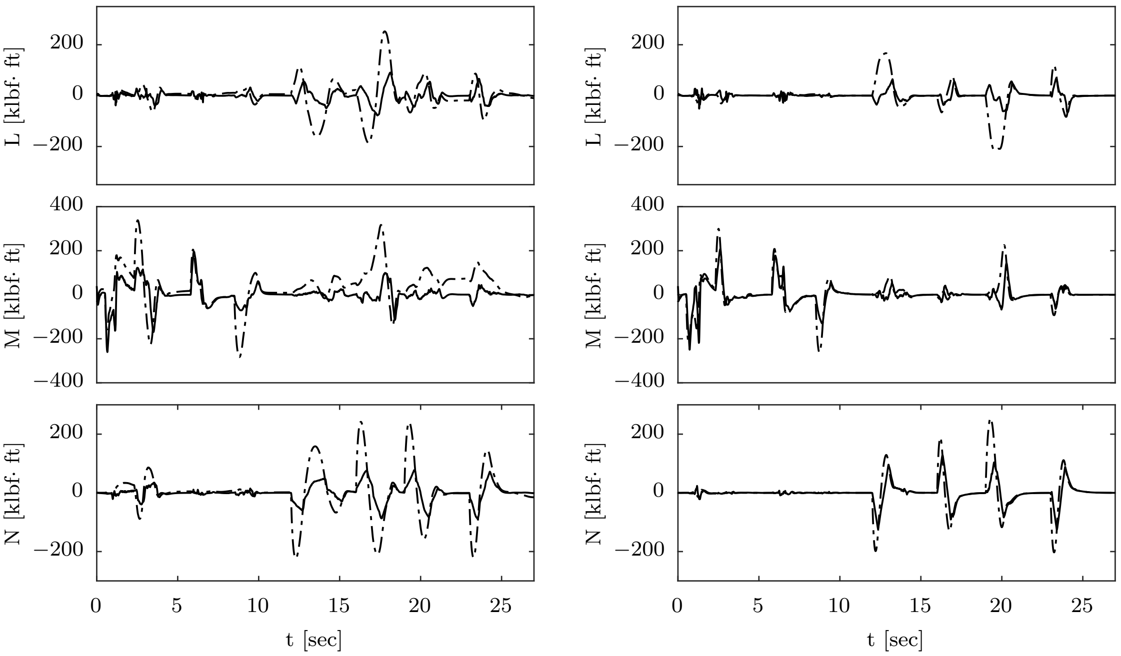

Figure 6.26: Commanded (dot-dashed line) and attained (solid line) control-induced moments of maneuver C with LCA and INCA with RWPI.

Table 6.19: Allocation error of maneuver C.

	RMS($\varepsilon_{\text{Alloc}}$)			
Solver	RWPI		QP	
CA Method	LCA	INCA	*LCA**	INCA
L [klbf·ft]	55.1	46.7	*1.69E+03*	6.68
M [klbf·ft]	81.4	40.0	*7.97E+02*	27.0
N [klbf·ft]	59.2	37.8	*1.38E+03*	29.2
Total	66.2	41.7	*1.34E+03*	23.3

* *Unstable trajectory.*

Table 6.20: Control effort of maneuver C.

	Ceff = RMS $(\delta - \delta_p)$													
Actuator	Total	δ_{lfi}	δ_{lfo}	δ_{la}	δ_{le}	δ_{ls}	δ_{pf}	δ_{rfi}	δ_{rfo}	δ_{ra}	δ_{re}	δ_{rs}	δ_{ptv}	δ_{ytv}
LCA/RWPI	6.5	0.4	1.0	9.3	9.3	0.8	10.2	1.4	0.9	14.2	8.4	1.2	1.0	1.2
INCA/RWPI	5.6	0.5	1.8	6.8	8.6	2.4	6.2	2.6	6.8	9.6	8.4	4.6	2.2	2.2
*LCA/QP**	*10*	*1.0*	*1.5*	*15*	*12*	*11*	*13*	*1.5*	*2.8*	*18*	*12*	*16*	*3.8*	*4.6*
INCA/QP	5.9	0.6	1.7	7.4	7.9	3.9	7.2	2.1	2.3	11.3	9.8	4.0	2.3	2.2

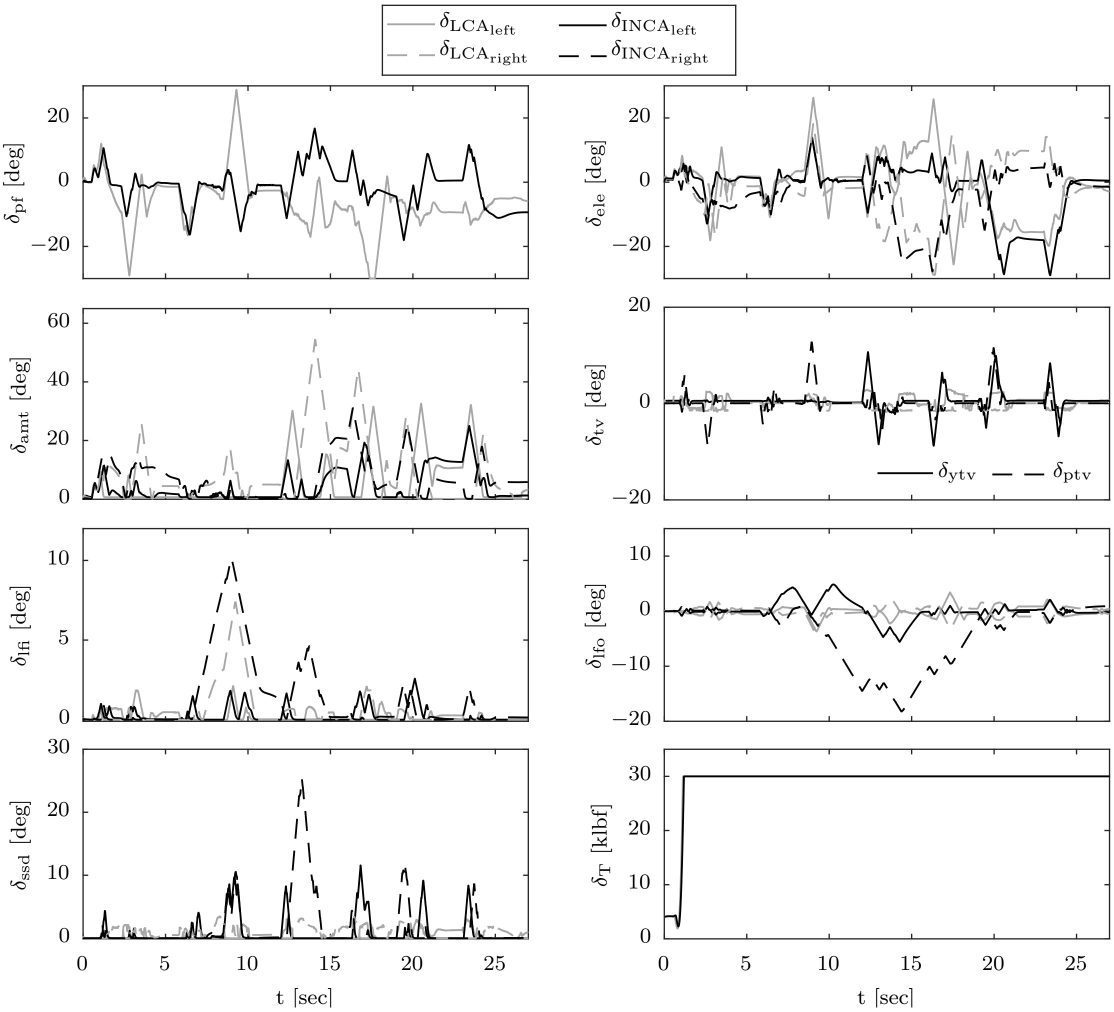

Figure 6.27: Control effector positions of maneuver C with LCA and INCA with RWPI.

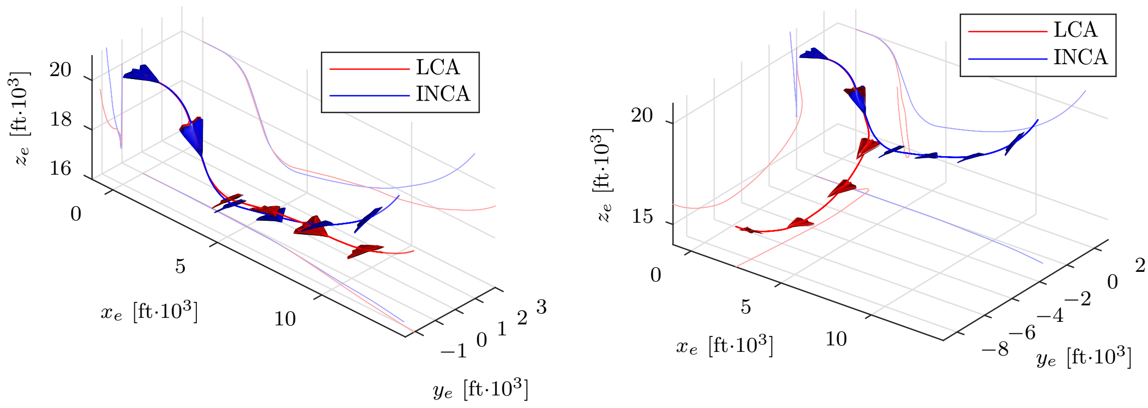

(a) RWPI solver.

(b) QP solver.

Figure 6.28: Trajectories of maneuver C with RWPI and QP.

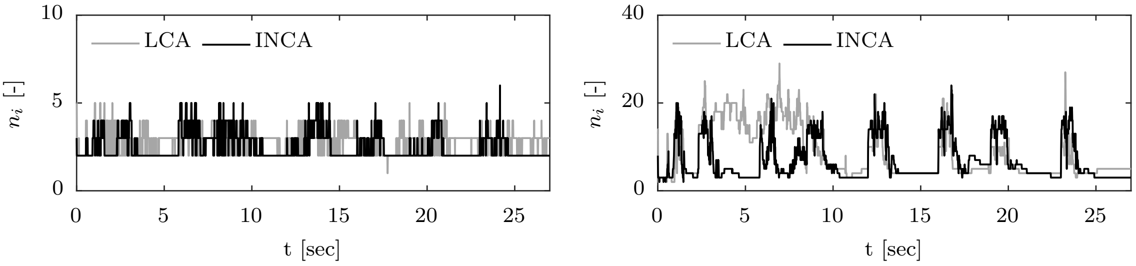

(a) RWPI solver. (b) QP solver.

Figure 6.29: Number of iterations per time step of maneuver C with RWPI and QP.

Table 6.21: Number of iterations per time step of maneuver C.

	n_i			
Solver	RWPI		QP	
CA Method	LCA	INCA	*LCA**	INCA
Min.	1	2	*2*	2
Avg.	2.8	2.5	*8.4*	6.7
Max.	5	6	*29*	24

* *Unstable trajectory.*

6.4.4 Maneuver D: Aerobatics Sequence

Maneuver D is the most demanding test performed in this thesis, consisting on a sequence of aggressive aerobatic maneuvers: aileron roll, asymmetric looping with sideslip, half 8-point hesitation roll and Immelmann turn. These maneuvers are flown with the sideslip compensation outer loop with direct roll and pitch body rate control inputs. The aileron roll consists on an aggressive roll input of 180 deg/sec resulting in two full turns around the body x-axis in 4 seconds. The asymmetric looping consists on a pitch rate input of 18 deg/sec, resulting in a full looping performed in 20 sec. During the first 10 seconds of the looping a 5 deg sideslip input is given, which returns to 0 deg for the last 10 seconds of the looping maneuver. This results in lateral displacement during the looping. The half 8-piont hesitation roll consists on four quick roll rate step inputs of 90 deg/sec with a duration of 0.5 sec each and with a separation of 1 sec, resulting in four quick steps in roll of 45 deg each, holding constant roll angle for 1 second after each step, and finishing the maneuver with a roll angle of 180 deg. At this position, a downward half-looping follows, completing an Immelmann turn and ending the trajectory in straight-and-level flight, flying in the opposite direction at a lower altitude than initially.

This maneuver is highly demanding, and the LCA/QP and INCA/RWPI systems failed to keep stable flight throughout the simulation. Consequently, only the results for the systems that managed to finish the aerobatics sequence with stable flight are shown here, i.e. LCA/RWPI and INCA/QP. The results for the unstable trajectories can be found in Section C.4 of Appendix C.

The time histories of the controlled variables are given in Figure 6.30. LCA exhibits very poor performance in the form of oscillations and very large excursions from the reference values, amounting up to errors of 50 deg/sec in the longitudinal channel and of ± 10 deg in the sideslip channel. In contrast, INCA shows excellent performance, with an accurate and fast tracking of the references with no remarkable deviations from the commanded values. The tracking errors listed in Table 6.22 show the superior performance of INCA/QP over LCA/RWPI, especially on the longitudinal and directional channels.

The time histories of the control moments are given in Figure 6.31. As observed in the previous cases, important deficiencies of LCA are especially relevant in the longitudinal and directional axes. INCA requires smaller moments to follow the commands, and those are tracked faster and more accurately. The allocation errors are given in Table 6.23, which shows significantly better performance for INCA/QP.

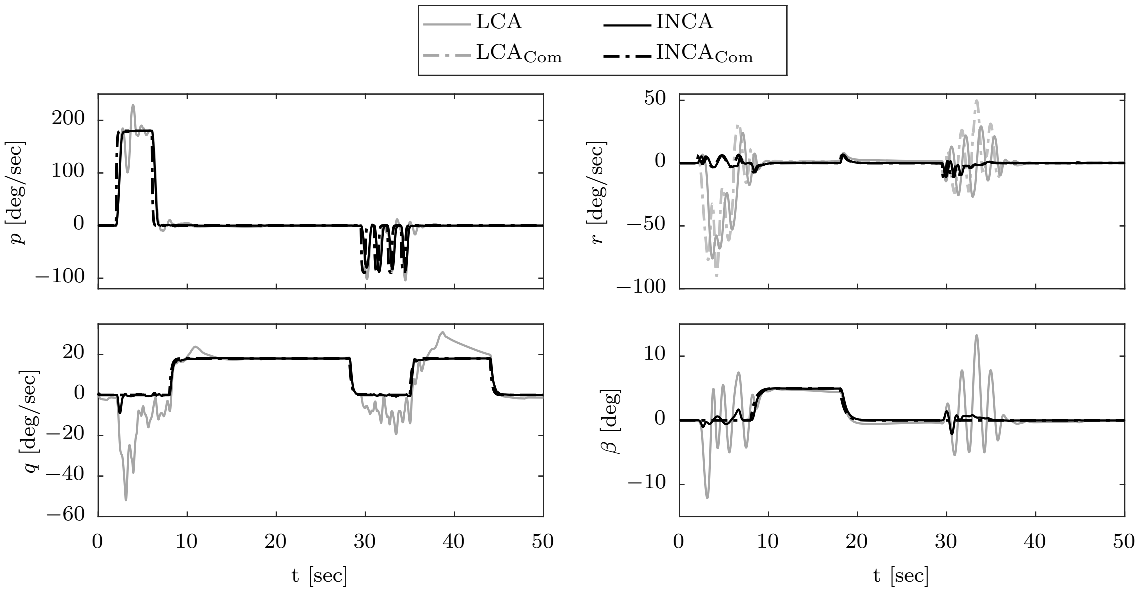

Figure 6.30: Control variables of maneuver B with LCA/RWPI and INCA/QP.

Table 6.22: Tracking error of maneuver D.

	RMS($\varepsilon_{\text{Track}}$)			
Solver	RWPI		QP	
CA Method	LCA	*INCA**	*LCA**	INCA
p [deg/sec]	23.0	*71.1*	*55.8*	21.2
q [deg/sec]	8.58	*1050*	*39.4*	1.10
r [deg/sec]	14.6	*8120*	*11197*	1.65
Total	16.5	*4727*	*6465*	12.3

* *Unstable trajectory.*

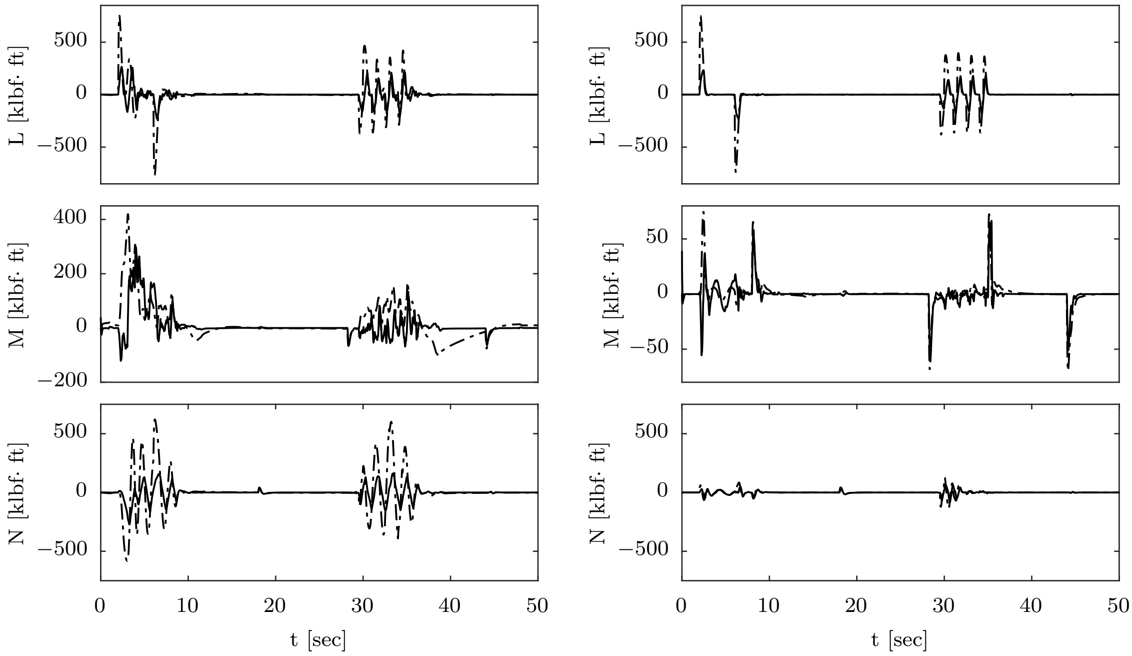

Figure 6.31: Commanded (dot-dashed line) and attained (solid line) control-induced moments of maneuver D with LCA/RWPI and INCA/QP.

Table 6.23: Allocation error of maneuver D.

	RMS($\varepsilon_{\text{Alloc}}$)			
Solver	RWPI		QP	
CA Method	LCA	*INCA**	*LCA**	INCA
L [klbf·ft]	93.3	*4.11E+06*	*5.57E+02*	81.4
M [klbf·ft]	63.9	*2.53E+06*	*3.41E+02*	8.85
N [klbf·ft]	129	*1.63E+06*	*1.62E+05*	15.4
Total	99.0	*2.94E+06*	*9.36E+04*	48.1

* *Unstable trajectory.*

The control effector positions and control efforts are given in Figure 6.32 and Table 6.24. Although the control distributions are in general similar, INCA makes more extensive use of the pitch flap and innovative nonlinear control effectors such as the SSDs, which open up to 30 degrees during the 8-point hesitation roll, and both inboard and outboard LEFs. In contrast, LCA allocates more control effort on the AMTs, since secondary sources of yawing moment are not captured in the linear control effector model. Note that rate saturation of the actuators occurs often.

Finally, the spatial trajectories of maneuver D are shown in Figure 6.33. Note that INCA/QP performs the maneuver with excellent precision, keeping a straight looping with lateral displacement, suffering no deviation after the hesitation roll, and ending the maneuver in straight-and-level flight. Although LCA manages to end the trajectory with stable flight, the flown path has deviations from the intended trajectory (tilted looping, loss of altitude, deviation after the hesitation roll, and non-level flight at the end of the maneuver).

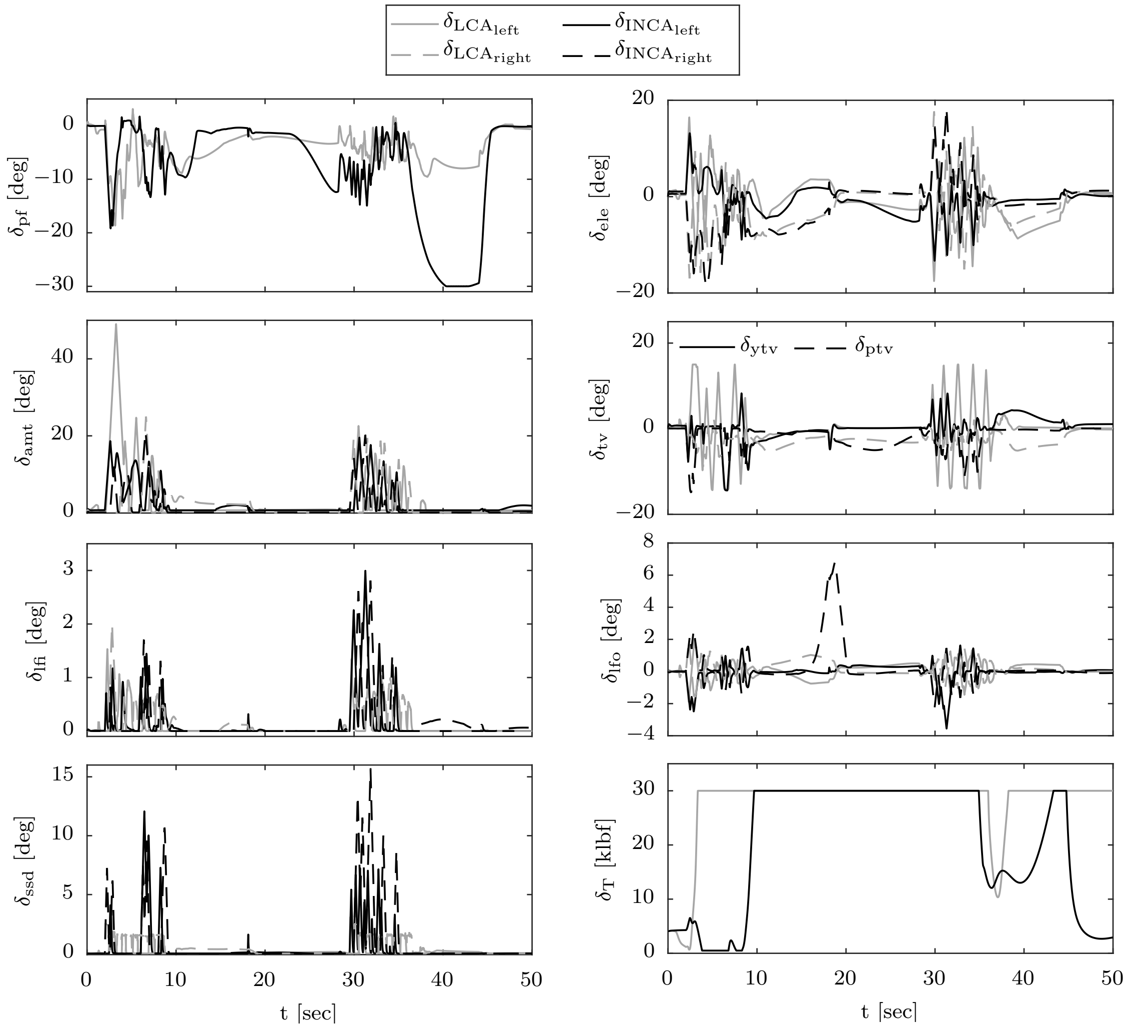

Figure 6.32: Control effector positions of maneuver D with LCA/RWPI and INCA/QP.

Table 6.24: Control effort of maneuver D.

	Ceff = RMS $(\delta - \delta_p)$													
Actuator	Total	δ_{lfi}	δ_{lfo}	δ_{la}	δ_{le}	δ_{ls}	δ_{pf}	δ_{rfi}	δ_{rfo}	δ_{ra}	δ_{re}	δ_{rs}	δ_{ptv}	δ_{ytv}
LCA/RWPI	3.6	0.3	0.5	7.2	4.4	0.5	5.2	0.2	0.5	4.1	4.8	0.6	3.0	4.8
*INCA/RWPI**	*20*	*14*	*6.5*	*39*	*16*	*28*	*9.8*	*9.5*	*8.9*	*27*	*19*	*30*	*7.9*	*8.8*
*LCA/QP**	*18*	*14*	*4.1*	*28*	*16*	*24*	*9.5*	*12*	*3.8*	*30*	*16*	*26*	*6.1*	*9.3*
INCA/QP	4.3	0.4	0.6	4.5	3.1	1.5	12	0.4	1.3	3.7	5.1	2.4	3.0	2.7

* *Unstable trajectory.*

The number of iterations per time step are given in Figure 6.34 and Table 6.25. The fact that this maneuver is highly demanding and actuator saturation occurs often is reflected in n_i. For LCA/RWPI the iteration limit of 14 is reached, although the average n_i is 15% of this limit. For INCA/QP the maximum number of iterations is only 27% of the iteration limit of the active set algorithm, and the average n_i is 6.8% of the iteration limit. This result suggests that INCA does not increase the computational complexity of the QP algorithm in this highly-demanding maneuver where actuator saturation occurs.

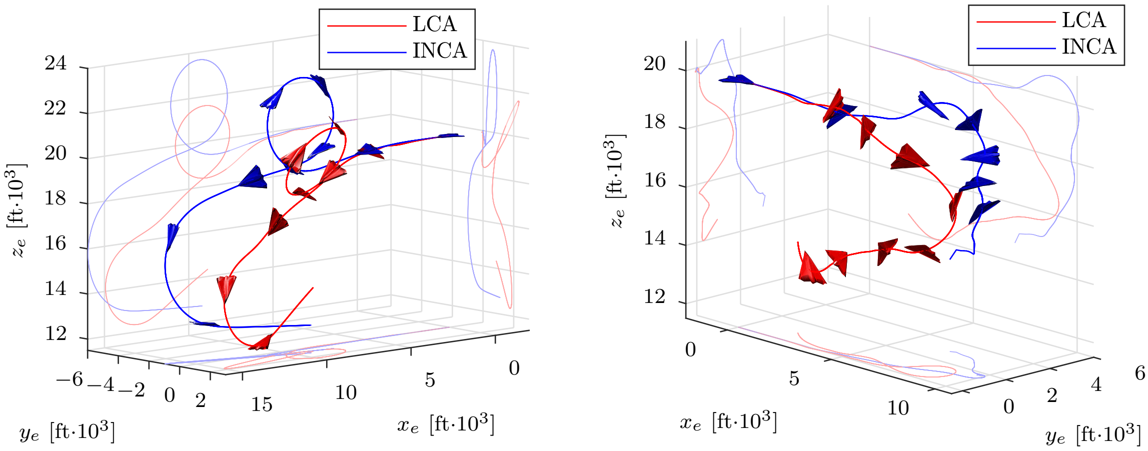

(a) Stable: LCA/RWPI and INCA/QP. (b) Unstable: LCA/QP and INCA/RWPI.

Figure 6.33: Trajectories of maneuver D for the stable trajectories (left) and for the unstable trajectories (right).

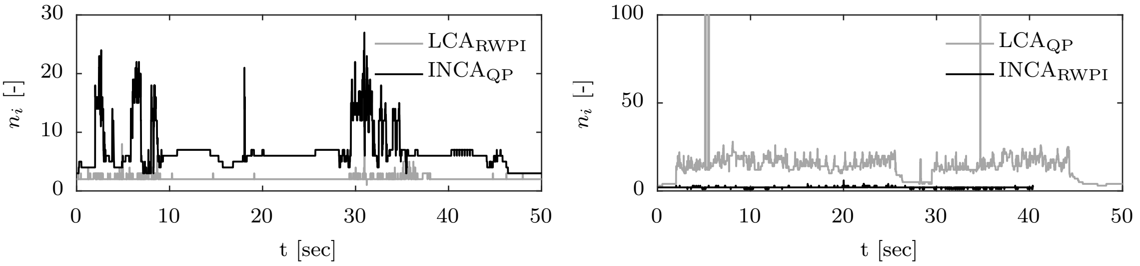

(a) Stable: LCA/RWPI and INCA/QP. (b) Unstable: LCA/QP and INCA/RWPI.

Figure 6.34: Number of iterations per time step of maneuver D for the stable trajectories (left) and for the unstable trajectories (right).

Table 6.25: Number of iterations per time step of maneuver D.

	n_i			
Solver	RWPI		QP	
CA Method	LCA	*INCA**	*LCA**	INCA
Min.	1	*1*	*2*	3
Avg.	2.1	*1.9*	*13.5*	6.8
Max.	14	*6*	*100*	27

* *Unstable trajectory.*

6.5 Overall Performance Assessment

In this section the data from all the simulations performed and discussed previously are combined to compute overall performance metrics. The data used for this analysis includes the maneuvers flown with LCA/RWPI, LCA/QP, INCA/RWPI and INCA/QP, i.e. all the results presented in this Chapter and in Appendix C. Since maneuvers C and D resulted in unstable trajectories for some of the tested systems, only the maneuvers 3211, A and B were included in the overall analysis in order to ensure a fair comparison.

The overall tracking errors for the four tested systems are listed in Table 6.26. As observed in previous results, the overall tracking performance is better with QP for both LCA and INCA. In both cases, INCA outperforms LCA in terms of tracking performance by a factor of 2.5 with RWPI and of 3.0 with QP. Furthermore, LCA performs worst in the longitudinal channel, in which INCA improves performance by a factor of 4.7 with QP.

Table 6.26: Overall tracking error combining maneuvers 3211, A and B.

	RMS($\varepsilon_{\text{Track}}$)			
Solver	RWPI		QP	
CA Method	LCA	INCA	LCA	INCA
p [deg/sec]	2.13	1.46	2.07	0.97
q [deg/sec]	3.98	0.73	3.19	0.67
r [deg/sec]	1.55	0.60	1.07	0.60
Total	2.76	1.01	2.28	0.76

Table 6.27 provides the overall allocation errors for the different tested systems. It can be observed that the improvement of INCA with respect to LCA is remarkably high in terms of allocation performance. INCA outperforms LCA by a factor of 3.6 with RWPI and of 4.5 with QP. As in the case of tracking performance, LCA performs worst in the longitudinal channel, where INCA shows an improvement in allocation performance by a factor of 5.34 with RWPI and of 6.7 with QP.

Table 6.27: Overall allocation error combining maneuvers 3211, A and B.

	RMS($\varepsilon_{\text{Alloc}}$)			
Solver	RWPI		QP	
CA Method	LCA	INCA	LCA	INCA
L [klbf·ft]	8.85	5.93	10.9	2.52
M [klbf·ft]	30.8	5.67	24.7	3.69
N [klbf·ft]	12.9	4.81	8.52	4.92
Total	19.9	5.49	16.3	3.84

The overall control efforts per control effector and in total are listed in Table 6.28. It can be observed that the overall control effort is higher for INCA than for LCA by a factor of 1.8. However the differences in the control effort allocated to each individual control effector reveal interesting trends. First, the elevons are more extensively used with LCA than with INCA. Since the parabolic yawing moments of the elevons were removed from the linear model used in LCA but are taken into account by INCA, it is reasonable that INCA tries to place more effort on control effectors with quasi-uncoupled moment contributions, in order to avoid secondary-axis moments. This explains the considerably higher use of the pitch flaps by INCA for longitudinal control, since they do not have secondary contributions in the lateral-directional axes. Also, the parabolic yawing moments of the outboard LEFs were removed from the LCA model. In contrast to the elevons, the outboard LEFs are one of the primary sources of lateral-directional control power at high AoA, but are weak sources of longitudinal control power. Since directional contributions of the outboard LEF were removed from the linear model and their contributions on other axes are weak, these effectors are underexploited by LCA. However, since these moments are considered in INCA, this system places higher control effort on outboard LEF.

Table 6.28: Overall control effort combining maneuvers 3211, A and B.

	Ceff = RMS $(\delta - \delta_p)$													
Actuator	Total	δ_{lfi}	δ_{lfo}	δ_{la}	δ_{le}	δ_{ls}	δ_{pf}	δ_{rfi}	δ_{rfo}	δ_{ra}	δ_{re}	δ_{rs}	δ_{ptv}	δ_{ytv}
LCA/RWPI	2.0	0.1	0.2	1.5	2.9	0.2	4.4	0.1	0.2	2.3	2.3	0.3	2.6	1.3
INCA/RWPI	3.7	0.2	0.6	1.5	1.3	0.2	13	0.1	1.4	1.0	1.1	0.5	0.6	2.4
LCA/QP	2.0	0.1	0.2	2.2	2.9	0.4	4.5	0.1	0.2	2.4	2.5	0.3	2.7	1.3
INCA/QP	3.7	0.1	0.6	1.4	1.2	0.3	13	0.1	1.3	2.4	2.0	0.4	0.7	1.9

Finally, Figure 6.35 shows the distributions of the number of iterations per time step for each trajectory with the RWPI and QP solvers. It can be noted that the number of iterations per time step are very similar in every case. The fact that n_i is higher for LCA in some cases is due to the large excursions and unstable flight conditions observed in some trajectories. The maximum number of iterations possible with RWPI is 14, although the maximum iteration count reached was 7. On the other hand, the iteration limit set for the active set algorithm was 100, although the maximum iteration count reached was 23. This proves that INCA has a computational load on the RWPI and active set-based QP algorithms statistically similar to traditional LCA, and therefore the INCA method is well-suited for real-time applications.

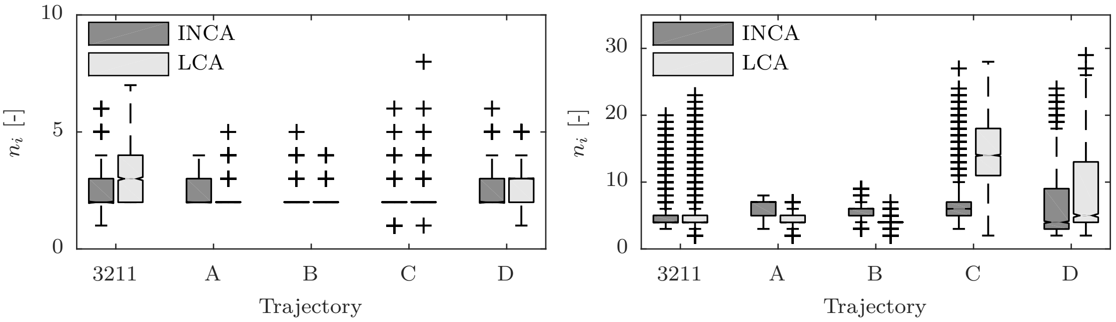

(a) RWPI solver. (b) Active set-based QP solver.

Figure 6.35: Distributions of the number of iterations per time step per trajectory.

Chapter 7

Conclusions and Final Remarks

Existing control allocation (CA) methods have a number of deficiencies that make them unable to provide satisfactory performance in advanced control effector suites where nonlinearities and interactions between control effectors are not negligible. This is particularly true for tailless configurations such as Lockheed Martin's Innovative Control Effectors (ICE) aircraft. Most conventional linear control allocation (LCA) methods work under the assumption of linearity of the control effectors, which fails to capture important nonlinear phenomena: parabolic yawing moment curves produced by horizontal control surfaces, nonlinearities in extreme regions of the operational range of the actuators, and interactions between control effectors. In addition to being strongly detrimental for the overall performance of the flight control system (FCS), neglecting these effects results in underexploiting the potential of highly redundant and coupled control effector suites in terms of maneuverability and recoverability in faulty conditions. Previous research has demonstrated the potential benefits of nonlinear CA, but the methods used were computationally complex and not suitable for real-time implementation.

In this thesis an incremental CA concept has been implemented to perform accurate, robust and computationally efficient nonlinear control allocation, which is suitable for real-time implementation in flight control systems of highly manoeuvrable tailless aircraft. This incremental nonlinear control allocation (INCA) concept works in an incremental scheme, in which the high-level control system provides required increments in control-induced moments that are mapped into commanded increments in control effector positions by an incremental nonlinear control allocator. The developed INCA system is based on a control effectiveness Jacobian model that accounts for aerodynamic nonlinearities and interactions between control effectors, and does not require any further aerodynamic model. An angular acceleration feedback loop reduces model dependency and provides strong robustness against aerodynamic model mismatch. The incremental control allocation problem can be solved with typical linear control allocation solvers, which are computationally efficient enough for real-time implementation. In addition, an actuator position feedback mitigates the coupling effects between control allocator and actuator dynamics, typically problematic in conventional static control allocation methods.

The incremental scheme requires some implementation particularities. First, measurements or estimations of the aircraft angular accelerations are required. These can be achieved through state estimation methods or by direct measurement using angular accelerometers. Both methods have been successfully applied in practice for incremental control of aerospace vehicles in previous research. Second, a measurement or estimation of the current control effector positions is required, which does not suppose major technical difficulties. Finally, the INCA method requires a nonlinear Jacobian model of the control effectiveness of the control effectors. In this thesis, a Jacobian model derived from a simplex B-spline aerodynamic model with 0th-order continuity between simplices has been proven to provide excellent control allocation performance for the ICE aircraft. This Jacobian model can provide in the order of 10^4 Jacobian calculations per second in real time.

The performance of the INCA system in flight control systems was assessed and compared to conventional LCA methods by designing an LCA- and an INCA-based flight control systems for the ICE aircraft using a high-fidelity simulation model mainly produced from wind tunnel empirical data. Both the LCA and INCA concepts were implemented with two common linear control allocation solvers: the redistributed weighted pseudo-inverse (RWPI) and quadratic programming (QP) solved with the active-set algorithm. The controllers were implemented for body angular rate control in conjunction with outer control loops. Actuator saturation and partial envelope protection were handled through pseudo-control hedging (PCH).

A robustness analysis performed with INCA solved with active set-based QP showed that the angular acceleration feedback provides the INCA-based control system with strong robustness against Jacobian model mismatch in the form of model scaling and offset. The control system showed very slight degradation in terms of control allocation performance, smaller than 10% for offsets in the Jacobian model of ±30% of the maximum observed values and scaling factors between 0.6 and 1.4. Control allocation performance degraded to a maximum of 20% for the highest offset and scaling factors tested, of 50% and 1.4 respectively. However, the system became unstable along the tested trajectory for negative offsets of -30% and scaling factors below 0.8. The analysis also revealed that the overall performance of INCA improves when the magnitude of the Jacobian terms is underestimated (i.e. for scaling factors lower than 1), achieving maximum performance at the lowest scaling factor tested of 0.6, close to the region of 0% offset. Magnitude overestimation, in contrast, degrades the overall performance of the system. An observed local minimum in the control effort revealed a possible mismatch in the Jacobian model used in the simulations of about 15% in magnitude and 15% in offset.

The capabilities of the LCA- and INCA-based control systems were assessed by simulating aggressive air combat aerobatic maneuvers with increasing control demands including loopings, barrel rolls, aileron rolls and more. Four metrics were used to assess the performance of the control systems: tracking error as an indicator of the overall performance of the control system, allocation error as an indicator of the capability of the control allocator to produce the required control moments, control effort as an indicator of the capability of fulfilling the secondary objective of minimizing control effector deflections, and the number of iterations per time step to compare computational load.

In all the tested maneuvers the performance of both LCA and INCA systems was considerably better with the active set-based QP solver than with RWPI. The results showed substantial improvement of INCA in terms of tracking and control allocation performance with respect to LCA. Due to the simplifications made to linearize the control effectors model for LCA, several negative effects were observed. First, neglecting control effector interactions led to undesired oscillations, large excursions of the controlled variables from the reference commands, an instability in the most demanding maneuvers. Second, neglected parabolic yawing moments of the elevons and leading edge flaps were seen by the LCA-based system as external disturbances which had to be compensated by other control effectors, difficulting adequate production of the required control moments. Last, due to model simplifications, LCA underexploited available sources of control power such as elevons and leading edge flaps in the lateral-directional channels. In contrast, INCA exploited the most nonlinear and coupled control effectors such that the control commands could be achieved with smaller moments, and these were produced faster and more accurately. The overall control performance observed with INCA was excellent and remarkably superior than the observed in the results obtained with LCA.

Overall, with the QP solver INCA outperforms LCA by a factor of 3.0 in terms of tracking performance and by a factor of 4.5 in terms of control allocation performance. This improvement is particularly relevant in the longitudinal and directional channels. In two occasions INCA was capable of following with excellent performance maneuvers that could not be followed by the LCA-based controller. The total control effort increased by a factor of 1.8 with INCA with respect to LCA, mostly due to a substantially larger use of the pitch flap by the former. Also, more extensive use of nonlinear control effectors such as the outboard leading edge flaps was observed with INCA. The number of iterations per time step was statistically similar for both LCA and INCA with RWPI and QP, demonstrating that INCA has no effect on the computational load of the solvers tested in the studied cases. This proves that INCA is well-suited for real-time applications in FCS.

In sight of the promising results obtained in this research, the INCA concept offers many possibilities for future improvement and testing. First, in fault-tolerant flight control systems the control effectors are usually forced to operate in extreme nonlinear regions of their operational range, where INCA performs substantially better than LCA. In addition, INCA can capture secondary-axis parabolic yawing moments and beneficial control interactions such as flow redirection using spoiler-slot deflectors. This opens new possibilities for fault-tolerant flight control systems by making available additional sources of redundant control power to be used to recover flight in faulty conditions. For these reasons, INCA is expected to be highly beneficial in terms of recoverability of fault-tolerant control systems under failure conditions by better exploiting the available redundancy of the control effectors suite. Hence, it is highly recommended to extend the INCA-based control system into a fault-tolerant flight control system with online model identification. Second, the order of continuity of the spline model used in this thesis was 0, and therefore the overall performance of the INCA-based control system can be further improved by increasing the order of continuity of the aerodynamic spline model of the ICE aircraft. This refinement of the model is also recommended as future work. Third, this thesis has focused on attitude control, whereas translational control is only addressed with a simple auto-throttle controller. However, the ICE control suite offers a lot of promising capabilities for translational control, especially with spoiler-slot deflectors, which are the most nonlinear and coupled control effectors. Thus, expanding the current control system with a translational control module is proposed as future work. Fourth, further and most sophisticated flight envelope protection is expected to be highly beneficial to the overall performance of the control system in extreme maneuvers. Flight envelope estimation and protection is also recommended as future work. Finally, full state feedback was assumed in this thesis. However, sensor dynamics, delays, noise and the presence of sensor fusion and state estimation algorithms in the control loop are expected to have a strong impact on the performance of the system. Thus, it is highly recommended to include all aspects regarding sensors and state estimation issues in future research.

Finally, the most promising perspectives in terms of further study, research and development of the INCA concept are regarding practical implementation through prototyping and flight testing. In sight of the promising results obtained in this thesis, Lockheed Martin showed interest in the possibility of setting up a collaboration framework to test the INCA-based flight control system in a 1:7 scale model of the ICE aircraft, which is planned to be manufactured by the US Air Force Academy in the upcoming years. Working towards this goal is strongly recommended as the main direction of this new research project, implying a great deal of fruitful research to be conducted on the way. Not only eventual flight tests would contribute towards the goal of practical implementation of incremental flight control and nonlinear control allocation systems in the aerospace field, but would also suppose a meaningful scientific contribution towards advanced, robust, fault-tolerant, safe and high-performance vehicle control in its broadest sense.

References

Addington, G. A., & Myatt, J. H. (2000). *Control-Surface Deflection Effects on the Innovative Control Effectors (ICE 101) Design* (Tech. Rep.).

Alwi, H., & Edwards, C. (2006). Sliding Mode FTC With On-line Control Allocation. In *Proceedings of the 45th ieee conference on decision and control* (pp. 5579–5584). San Diego, CA.

Bacon, B. J., & Ostroff, A. J. (2000). Reconfigurable flight control using nonlinear dynamic inversion with a special accelerometer implementation. In *Proceedings of the aiaa guidance, navigation, and control conference and exhibit.*

Bodson, M. (2002). Evaluation of Optimization Methods for Control Allocation. *Journal of Guidance, Control, and Dynamics*, *25*(4), 703–711.

Bolender, M. A., & Doman, D. B. (2004a). Method for Determination of Nonlinear Attainable Moment Sets. *Journal of Guidance, Control, and Dynamics*, *27*(5), 907–914.

Bolender, M. A., & Doman, D. B. (2004b). Nonlinear Control Allocation Using Piecewise Linear Functions. *Journal of Guidance, Control, and Dynamics*, *27*(6), 1017–1027.

Bordignon, K. (1996). *Constrained Control Allocation for Systems with Redundant Control Effectors* (PhD Thesis). Virginia Polytechnic Institute and State University.

Bowlus, J., Multhopp, D., & Banda, S. (1997). Challenges and Opportunities in Tailless Aircraft Stability and Control. In *Guidance, navigation, and control conference* (pp. 1713–1718).

Buffington, J. M. (1997). Tailless aircraft control allocation. *AIAA Guidance, Navigation, and Control Conference*, 737–747.

Buffington, J. M. (1999). *Modular Control Law Design for the Innovative Control Aircraft Effectors (ICE) Tailless Fighter Configuration* (Tech. Rep.).

Buffington, J. M., & Enns, D. F. (1996). Lyapunov stability analysis of daisy chain control allocation. *Journal of Guidance, Control, and Dynamics*, *19*(6), 1226–1230.

Burken, J. J., Lu, P., Wu, Z., & Bahm, C. (2001). Two Reconfigurable Flight-Control Design Methods: Robust Servomechanism and Control Allocation. *Journal of Guidance, Control, and Dynamics*, *24*(3), 482–493.

Burken, J. J., Lu, P., & Wu, Z. L. (1999). Reconfigurable flight control designs with application to the X-33 vehicle. In *Aiaa guidance, navigation, and control conference* (pp. 951–965).

Davidson, J. B., Lallman, F. J., & Bundick, W. T. (2001a). Integrated reconfigurable control allocation. In *Aiaa guidance, navigation and control conference and exhibit.* Montreal, Canada.

Davidson, J. B., Lallman, F. J., & Bundick, W. T. (2001b). Real-Time Adaptive Control Allocation applied to a High Performance Aircraft. In *5-th siam conference on control & its applications.*

de Visser, C. C., Chu, Q. P., & Mulder, J. A. (2009). A New Approach to Linear Regression with Multivariate Splines. *Automatica*, *45*(12), 2903–2909.

Doman, D. B., & Oppenheimer, M. (2002). Improving Control Allocation Accuracy for Nonlinear Aircraft Dynamics. In *Aiaa guidance, navigation, and control conference and exhibit.* Monterey, California.

Doman, D. B., & Sparks, A. G. (2002). Concepts for Constrained Control Allocation of Mixed Quadratic and Linear Effectors. In *Proceedings of the american control conference* (pp. 3729–3734). Anchorage, AK.

Dorsett, K. M., Fears, S. P., & Houlden, H. P. (1997). *Innovative Control Effectors (ICE) Phase II* (Tech. Rep.).

Dorsett, K. M., & Mehl, D. R. (1996). *Innovative Control Effectors (ICE) Phase I* (Tech. Rep.). Lockheed Martin Tactical Aircraft Systems.

Ducard, G. (2009). Control Allocation. In *Fault-tolerant flight control and guidance systems* (pp. 89–106). Springer.

Durham, W. C. (1993). Constrained Control Allocation. *Journal of Guidance, Control, and Dynamics*, *16*(4), 717–725.

Durham, W. C. (1994a). Attainable Moments for the Constrained Control Allocation Problem. *Journal of Guidance, Control, and Dynamics*, *17*(6), 1371–1373.

Durham, W. C. (1994b). Constrained Control Allocation: Three Moment Problem. *Journal of Guidance, Control, and Dynamics*, *17*(2), 330–336.

Durham, W. C. (1999). Efficient, Near-Optimal Control Allocation. *Journal of Guidance, Control, and Dynamics*, *22*(2), 369–372.

Durham, W. C. (2001). Computationally Efficient Control Allocation. *Journal of Guidance, Control, and Dynamics*, *24*(3), 519–524.

Eberhardt, R., & Ward, D. (1999). Indirect Adaptive Flight Control of a Tailless Fighter Aircraft. In *Guidance, navigation, and control conference and exhibit* (pp. 466–476).

Enns, D. (1998). Control allocation approaches. *Guidance, Navigation, and Control Conference and Exhibit*, 98–108.

Enns, D., Bugajski, D., Hendrick, R., & Stein, G. (1994). Dynamic inversion: an evolving methodology for flight control design. *International Journal of Control*, *59*(1), 71–91.

Gillard, W. J., & Dorsett, K. M. (1997). Directional Control for Tailless Aircraft Using All Moving Wing Tips. In *22nd atmospheric flight mechanics conference* (pp. 51–58).

Hanger, M. B. (2011). *Model Predictive Control Allocation* (PhD Thesis). Norwegian University of Science and Technology.

Harkegard, O. (2002). Efficient Active Set Algorithms for Solving Constrained Least Squares Problems in Aircraft Control Allocation. In *41st ieee conference on decision and control* (pp. 1295–1300).

Harkegard, O. (2004). Dynamic Control Allocation Using Constrained Quadratic Programming. *Journal of Guidance Control and Dynamics*, *27*(6), 1028–1034.

Hodel, S. (2000). Robust Inversion and Data Allocation Compression in Control. In *Aiaa guidance, navigation, and control conference.*

Johansen, T. A. (2004). Optimizing Nonlinear Control Allocation. In *43rd ieee conference on decision and control* (pp. 3435–3440).

Johansen, T. A., & Fossen, T. I. (2013). Control allocation - A survey. *Automatica*, *49*(5), 1087–1103.

Johansen, T. A., Fossen, T. I., & Berge, S. P. (2004). Constrained nonlinear control allocation with singularity avoidance using sequential quadratic programming. *Control Systems Technology, IEEE Transactions on*, *12*(1), 211–216.

Johnson, E. N., & Calise, A. J. (2000). Pseudo-Control Hedging : a New Method for Adaptive Control. In *Advances in navigation guidance and control technology workshop.*

Johnson, E. N., & Kannan, S. K. (2005). Adaptive Trajectory Control for Autonomous Helicopters. *Journal of Guidance, Control, and Dynamics*, *28*(3), 524–538.

Lam, Q., & Barkana, I. (2005). Direct Adaptive Control Treatment to Flight Control Input Saturation. In *Aiaa guidance, navigation, and control conference and exhibit.*

Lewis, F. L., & Syrmos, V. L. (1995). *Optimal Control.* New York, NY: John Wiley & Sons, Inc.

Li, P., Qin, W. W., & Zheng, Z. Q. (2009). Nonlinear disturbance observer-based finite-time convergent second order sliding mode control for a tailless aircraft. In *2009 ieee international conference on mechatronics and automation, icma 2009* (pp. 4572–4576). Changchun, China.

Lombaerts, T., Looye, G., Chu, Q., & Mulder, J. (2010). Pseudo Control Hedging and its Application for Safe Flight Envelope Protection. In *Aiaa guidance, navigation, and control conference.*

Lombaerts, T. J. J., Looye, G. H. N., Chu, Q. P., & Mulder, J. A. (2012). Design and simulation of fault tolerant flight control based on a physical approach. *Aerospace Science and Technology*, *23*(1), 151–171.

Lu, P. (1996). Constrained Tracking Control of Nonlinear Systems. *Systems & Control Letters*, *27*, 305–314.

Luo, Y., Serrani, A., Yurkovich, S., Doman, D. B., & Oppenheimer, M. W. (2004). Model Predictive Dynamic Control Allocation with Actuator Dynamics. In *American control conference* (pp. 1695 –1700). Boston, Massachusetts.

Luo, Y., Serrani, A., Yurkovich, S., Oppenheimer, M. W., & Doman, D. B. (2007). Model-Predictive Dynamic Control Allocation Scheme for Reentry Vehicles. *Journal of Guidance, Control, and Dynamics*, *30*(1), 100–113.

Marquardt, D. W. (1963). An Algorithm for Least-Squares Estimation of Nonlinear Parameters. *Journal of the Society for Industrial and Applied Mathematics*, *11*(2).

Mulder, J. A. (1986). Design and evaluation of dynamic flight test manoeuvres. *Technical Report*.

Ngo, A. D., Reigelsperger, W., Banda, S., & Bessolo, J. (1996). Multivariable Control Law Design for a Tailless Airplane. In *Aiaa guidance, navigation and control conference.* San Diego, CA.

Niestroy, M. A., Dorsett, K. M., & Markstein, K. (2017). A Tailless Fighter Aircraft Model for Control-Related Research and Development. In *Aiaa modeling and simulation* *technologies conference.*

Oppenheimer, M. W., & Doman, D. B. (2004). Methods for Compensating for Control Allocator and Actuator Interactions. *Journal of Guidance, Control, and Dynamics*, *27*(5), 922–927.

Oppenheimer, M. W., & Doman, D. B. (2007). A Method for Including Control Effector Interactions in the Control Allocation Problem. In *Proceedings of the aiaa guidance, navigation, and control conference and exhibit.* Hilton Head, South Carolina.

Oppenheimer, M. W., Doman, D. B., & Bolender, M. A. (2006). Control Allocation for Over-Actuated Systems. In *2006 14th mediterranean conference of control and automation.* IEEE.

Oppenheimer, M. W., Doman, D. B., & Bolender, M. A. (2010). Control Allocation. In L. S. Levine (Ed.), *The control handbook: Control system applications* (2nd ed., chap. 8).

Ostroff, A. J., & Bacon, B. J. (2002). Enhanced NDI Strategies for Reconfigurable Flight Control. In *American control conference* (pp. 3631–3636).

Page, A., & Steinberg, M. (2000). A closed-loop comparison of control allocation methods. In *Aiaa guidance, navigation, and control conference and exhibit.* Denver, CO.

Paradiso, J. (1989). A Highly Adaptable Method of Managing Jets and Aerosurfaces for Control of Aerospace Vehicles. In *Proceedings of the 1989 guidance, navigation and control conference* (pp. 35–44).

Paradiso, J. (1991). Adaptable Method of Managing Jets and Aerosurfaces for Aerospace Vehicle Control. *Journal of Guidance Control and Dynamics*, *14*(1), 44–50.

Petersen, J. A. M., & Bodson, M. (2005). Interior-Point Algorithms for Control Allocation. *Journal of Guidance, Control, and Dynamics*, *28*(3), 471–480.

Petersen, J. A. M., & Bodson, M. (2006). Constrained Quadratic Programming Techniques for Control Allocation. *Ieee Transactions on Control Systems Technology*, *14*(1), 91–98.

Poonamallee, V. L., Yurkovich, S., Serrani, A., Doman, D. B., & Oppenheimer, M. W. (2004). A Nonlinear Programming Approach for Control Allocation. In *American control conference* (pp. 1689–1694). Boston, Massachusetts.

Schierman, J., Hull, J., & Ward, D. (2003). On-Line Trajectory Command Reshaping for Reusable Launch Vehicles. In *Aiaa guidance, navigation, and control conference and exhibit.* Austin, Texas.

Shtessel, Y., Buffington, J., & Banda, S. (2002). Tailless Aircraft Flight Control Using Multiple Time Scale Reconfigurable Sliding Modes. *IEEE Transactions on Control Systems Technology*, *10*(2), 288–296.

Sieberling, S., Chu, Q. P., & Mulder, J. a. (2010). Robust Flight Control Using Incremental Nonlinear Dynamic Inversion and Angular Acceleration Prediction. *Journal of Guidance, Control, and Dynamics*, *33*(6), 1732–1742.

Simplício, P., Pavel, M. D., van Kampen, E., & Chu, Q. P. (2013). An Acceleration Measurements-Based Approach for Helicopter Nonlinear Flight Control Using Incremental Nonlinear Dynamic Inversion. *Control Engineering Practice*, *21*(8), 1065–1077.

Smeur, E. J. J., Chu, Q. P., & de Croon, G. C. H. E. (2016). Adaptive Incremental Nonlinear Dynamic Inversion for Attitude Control of Micro Aerial Vehicles. *Journal of Guidance, Control, and Dynamics*, *39*(3), 450–461.

Snell, S. A., Garrard, W. L., & Enns, D. F. (1990). Nonlinear inversion flight control for a supermaneuverable aircraft. *Journal of Guidance Control and Dynamics*, *15*(4), 976–984.

Tavasoli, A., & Naraghi, M. (2011). Comparison of Static and Dynamic Control Allocation Techniques for Integrated Vehicle Control. In *18th ifac world congress* (Vol. 44, pp. 7180–7186). Milano: IFAC.

Tol, H. J., De Visser, C. C., Van Kampen, E., & Chu, Q. P. (2014). Nonlinear Multivariate Spline-Based Control Allocation for High-Performance Aircraft. *Journal of Guidance, Control, and Dynamics*, *37*(6), 1840–1862.

Tol, H. J., de Visser, C. C., & Kotsonis, M. (2016). Model Reduction of Parabolic PDEs Using Multivariate Splines. *International Journal of Control*.

van der Peijl, I., de Visser, C., & Niestroy, M. A. (2017). Physical Splines for Aerodynamic Modelling of Innovative Control Effectors. *Unpublished MSc Thesis*.

Appendix A

Conference Paper

Incremental Nonlinear Control Allocation for a Tailless Aircraft with Innovative Control Effectors

I. Matamoros[*] and C.C. de Visser[†]
Delft University of Technology, 2629HS Delft, The Netherlands.

Conventional linear control allocation (LCA) methods fail to provide satisfactory performance in flight control systems (FCS) for aircraft with highly nonlinear and coupled control effector suites, especially for tailless aircraft with strong interactions between control effectors. This is due to the inability of linear effector models to capture nonlinear and coupled control forces and moments. This paper implements an incremental nonlinear control allocation (INCA) approach, which can capture nonlinearities and interactions of control effectors while being solvable with simple and computationally efficient linear control allocation algorithms. This makes INCA suitable for real-time control allocation in FCS. This incremental reformulation of the control allocation problem is based on a Jacobian model of the control effectors, and relies on angular acceleration measurements to reduce model dependency. In addition, it operates based on real-time measurements of the actuator positions, which mitigates typical problems related to couplings between control allocators and actuator dynamics. In this paper, LCA- and INCA-based nonlinear FCS are designed for the Innovative Control Effectors (ICE) aircraft, a highly maneuverable tailless aircraft with 13 highly nonlinear, interacting and axis-coupled control effectors. Real-time simulation results show that INCA dramatically improves tracking and control allocation performance, thus improving maneuverability and exploiting the full potential of innovative control effector suites.

Nomenclature

A_x, A_y, A_z	Specific forces in body frame
b	Wingspan
B	Control effectiveness matrix
$\bar{c}$	Mean aerodynamic chord
C	Dimensionless aerodynamic coefficients
$\mathbf{d}_c$	Pseudo-control input
g	Gravitational acceleration
I	Aircraft inertia matrix
$\mathcal{J}$	Cost function
l, m, n	Aerodynamic moments in body frame
M	Mach number
p, q, r	Pitch, roll and yaw angular rates
S	Wing surface
$\mathbf{T}$	Thrust force vector
t	Time
$\mathbf{u}$	Control input vector
u, v, w	Airspeed components
V	True airspeed

---

[*] MSc Student, Control and Simulation Division, Faculty of Aerospace Engineering, Kluyverweg 1, 2629HS Delf, The Netherlands, i.matamoroscid@student.tudelft.nl. AIAA Member.

[†] Assistant Professor, Control and Simulation Division, Faculty of Aerospace Engineering, Kluyverweg 1, 2629HS Delft, The Netherlands, c.c.devisser@tudelft.nl. AIAA Member.

X, Y, Z	Aerodynamic forces in body frame
$\mathbf{x}$	State vector

Symbols

α	Angle of attack
β	Sideslip angle
$\boldsymbol{\delta}$	Control effector positions
$\boldsymbol{\nu}$	Virtual control input
$\boldsymbol{\omega}$	Body angular rates
$\boldsymbol{\tau}$	Aerodynamic moments
∇	Jacobian matrix
ϕ, θ, ψ	Roll, pitch and yaw angles
ρ	Atmospheric pressure

I. Introduction

Given the inherent benefits of highly redundant and axis-coupled control effector suites, aircraft over-actuation is an increasingly common practice in aerospace design. Over-actuated systems have more control inputs than controlled variables, and therefore a given control command can usually be achieved by multiple combinations of control effector positions. Control allocation (CA) algorithms automatically distribute control commands over the available set of control effectors, aiming to optimally exploit the potential of the redundant control suite in terms of manoeuvrability and efficiency.

Most conventional control allocation methods operate under the assumption that a linear relationship exists between actuator positions and control-induced moments. Common examples of such methods are the redistributed weighted pseudo-inverse,[1, 2] daisy chaining,[3] direct allocation[4–10] and numerical optimization-based approaches such as linear programming[11–14] and quadratic programming.[10, 13] The assumption of linearity yields a very tractable affine formulation of the control allocation problem, which can be solved with efficient linear algorithms suitable for real-time implementation in flight control systems. This assumption, however, has important shortcomings.

First, linear models are unable to capture interactions between control effectors. Although such couplings are usually negligible in conventional actuator suites, more innovative configurations feature actuators positioned downstream of others, resulting in important nonlinear interactions. In some cases, such interactions can be positively exploited such as in the case of slots, which can be used to recover control effectiveness of trailing-edge control surfaces at high angles-of-attack (AoA). In other cases, these interactions can have negative effects on control effectiveness, such as in the case of leading-edge actuators that disturb the downstream airflow. Although the issue of control effector interactions was noticed and addressed in Ref. 15, the applicability of the proposed method is limited to interactions between two control effectors that can be described by a bilinear function.

Second, independently-moving control surfaces produce secondary-axis yawing moments by generating drag through a lever arm with respect to the aircraft longitudinal axis. Although conventional aircraft use a rudder for directional control, tailless configurations exploit these secondary-axis moments as a main source of directional control power. These moments can also be used in conventional actuator suites to regain directional controllability after rudder failure. Common actuators using this principle are all-moving wing tips, ailerons and elevons.[16, 17] Whereas they produce locally linear rolling moments, they have highly nonlinear contributions to yawing moment, especially at low AoA where parasitic drag dominates induced drag effects. Secondary-axis yawing moments are generally asymmetric parabolic functions of the actuator deflections, which cannot be captured with linear effector models. This shortcoming has two negative effects on control allocation performance. First, the yawing moments not included in the on-board aerodynamic model are seen as external disturbances by the control system, and need to be mitigated with other sources of directional control power. Second, the ability to positively exploit these sources of yawing moment is lost, which is particularly critical in tailless configurations. This problem was addressed in Ref. 18 by modelling the control effectors with piecewise linear functions. Although the potential benefits of nonlinear CA with respect to linear methods were clearly demonstrated, the proposed method required solving a mixed-integer programming problem, which is extremely slow due to its computational complexity, and therefore not suitable for real-time implementation.

Finally, although the control moment curves of conventional actuators are locally linear for small deflections, nonlinearities exist in extreme regions of their operational range. Failing to capture such nonlinearities results in a model mismatch causing control allocation error, which needs to be mitigated by the robustness of the flight control laws.[19] This is detrimental to the overall performance of the system, especially in faulty conditions where the non-faulty actuators are forced to operate within extreme regions of their moment curves. This problem was addressed in Ref. 19 by introducing an affine control effector model with intercept correction. This method is not applicable when the control-induced moments are quadratic, have non-monotonic behaviour, or when the slope of the control effectiveness curves becomes small. Despite its limited applicability, this method demonstrated the potential benefits of considering nonlinearities in control moment curves.

In most conventional aircraft configurations the inaccuracies introduced by the assumption of linearity are relatively small and can be acceptably absorbed by robust control systems. However, linear control allocation fails to provide adequate performance in more advanced and innovative designs, especially in tailless aircraft, which achieve directional control mainly through secondary-axis parabolic yawing moments. A very relevant example is Lockheed Martin's Innovative Control Effectors (ICE) research aircraft, a tailless flying wing with a highly redundant control effector suite of 13 actuators, which produce highly nonlinear and cross-axis coupled moments and exhibit strong interactions.

Nonlinear control allocation has been explored as a solution with different approaches such as nonlinear direct allocation,[16] mixed-integer programming[17] and nonlinear programming.[20] Although the proposed methods clearly demonstrated important improvements over linear approaches, nonlinear optimization algorithms are highly computationally complex and not suitable for implementation in real-time systems.

This paper implements an incremental nonlinear control allocation (INCA) method based on a reformulation of the control allocation problem in incremental form, exploiting the time scale separation principle. This method is based on a nonlinear Jacobian model of the control effectors, which can capture actuator nonlinearities, including interactions between control effectors. This, in turn, reduces the model dependency of the nonlinear flight control system, which makes it more robust against model uncertainties. The crux of this method is that it operates in an incremental scheme, which allows the nonlinear CA problem to be solved with typical linear control allocation algorithms that are computationally efficient enough for real-time implementation. Moreover, unlike most typical CA algorithms, INCA uses information of the current position of the actuators, which are dynamically driven towards their optimal positions through small increments. This mitigates the negative impact of actuator dynamics in control allocation, which has been focus of extensive research in the past.[22–26]

This paper demonstrates substantial benefits of INCA in terms of flight control and control allocation performance for innovative aircraft designs with respect to linear control allocation (LCA) methods. For this, an LCA-based and an INCA-based nonlinear flight control systems were designed for the ICE aircraft, and their performance was evaluated through simulation using the high-fidelity simulation model described in Ref. 27. The simulation model includes actuator dynamics, in addition to position and rate constraints. Both LCA- and INCA-based flight control systems were implemented with two typical linear control allocation solvers to compare performance.

II. The Control Allocation Problem

Consider the aircraft dynamics expressed in the general form

$$\dot{\mathbf{x}} = \mathbf{f}(\mathbf{x}) + \mathbf{g}(\mathbf{x})\,\boldsymbol{\tau} \tag{1}$$

where $\mathbf{x} \in \mathbb{R}^n$ is the state vector and $\boldsymbol{\tau} \in \mathbb{R}^m$ the aerodynamic inputs to the equations of motion. Control allocation in aerospace applications typically concerns attitude control, $\boldsymbol{\tau} \in \mathbb{R}^3$ being the aerodynamic moments in body frame. This problem is commonly referred to as the three-moment problem. The aerodynamic moments are generally nonlinear functions of the states and the control effector positions $\boldsymbol{\delta} \in \mathbb{R}^p$:

$$\boldsymbol{\tau} = \mathbf{h}(\mathbf{x}, \boldsymbol{\delta}) \tag{2}$$

The control effectors are subject to rate and position constraints

$$\boldsymbol{\delta}_{\min} \leq \boldsymbol{\delta} \leq \boldsymbol{\delta}_{\max} \tag{3}$$

$$|\dot{\boldsymbol{\delta}}| \leq \dot{\boldsymbol{\delta}}_{\max} \tag{4}$$

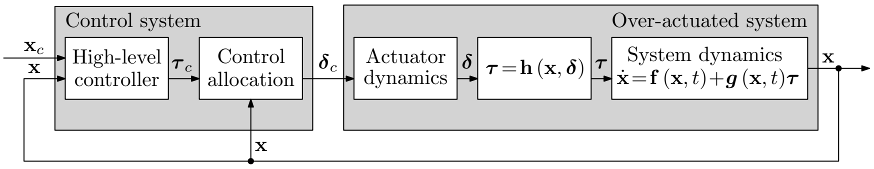

Figure 1. Classical control scheme for over-actuated systems.

The control allocation problem consists on determining the control effector positions $\boldsymbol{\delta}$ that produce a given moment command $\boldsymbol{\tau}_c$. Over-actuated systems have more control effectors than controlled variables, i.e. $p > m$, and therefore the system of Eqs. (2) is underdetermined with $p-m$ degrees of freedom. When multiple solutions that satisfy $\boldsymbol{\tau}_c$ exist, secondary objectives might be defined to determine an optimal solution. As shown in the classical control scheme for over-actuated systems in Figure 1, the moment commands are typically provided by a high-level control system. The choice of a suitable control allocation approach is strongly application-dependent. Very extensive surveys giving a broad overview of currently available CA methods exist in the literature, see Refs. 1, 2, 13, 28.

In aerospace systems, control allocation algorithms are run in flight control computers (FCC) in discrete-time, and the control distribution is computed at each time step for the current state $\mathbf{x}_0$. Given a measured or estimated $\mathbf{x}_0$, the control effectiveness function $\mathbf{h}(\mathbf{x}, \boldsymbol{\delta})$ becomes a generally nonlinear static mapping $\mathbf{h}(\mathbf{x}_0) : \mathbb{R}^p \to \mathbb{R}^m$. Thus, the actuator rate limits can be translated into local position limits for the current time step as

$$\Delta\boldsymbol{\delta}_{\max} = \dot{\boldsymbol{\delta}}_{\max}\Delta t \tag{5}$$

The effective local position limits at a given time step are

$$\underline{\boldsymbol{\delta}} \leq \boldsymbol{\delta} \leq \overline{\boldsymbol{\delta}} \tag{6}$$

with

$$\begin{aligned} \overline{\boldsymbol{\delta}} &= \min\left(\boldsymbol{\delta}_{\max},\ \boldsymbol{\delta}_0 + \dot{\boldsymbol{\delta}}_{\max}\Delta t\right) \\ \underline{\boldsymbol{\delta}} &= \max\left(\boldsymbol{\delta}_{\min},\ \boldsymbol{\delta}_0 - \dot{\boldsymbol{\delta}}_{\max}\Delta t\right) \end{aligned} \tag{7}$$

the local upper and lower bounds of the actuator positions.

For a given time step, the static control allocation problem is formulated as: given the current state $\mathbf{x}_0$, the control effector model $\boldsymbol{\tau} = \mathbf{h}(\mathbf{x}_0, \boldsymbol{\delta})$ and a moment command $\boldsymbol{\tau}_c$, determine a control vector $\boldsymbol{\delta}$ such that

$$\begin{gathered} \mathbf{h}(\mathbf{x}_0, \boldsymbol{\delta}) = \boldsymbol{\tau}_c \\ \text{subject to} \quad \underline{\boldsymbol{\delta}} \leq \boldsymbol{\delta} \leq \overline{\boldsymbol{\delta}} \end{gathered} \tag{8}$$

Note that the inverse problem of computing $\boldsymbol{\delta}$ given $\boldsymbol{\tau}_c$ is ill-posed and generally its solution is not unique. In order to solve the inverse CA problem in Eq. (8), commonly used approaches assume that $\mathbf{h}(\mathbf{x}, \boldsymbol{\delta})$ is linear in the inputs, and thus can be expressed using a control effectiveness matrix $B(\mathbf{x}) \in \mathbb{R}^{m\times p}$ in the form

$$\boldsymbol{\tau} = \mathbf{h}(\mathbf{x}, \boldsymbol{\delta}) = B(\mathbf{x})\,\boldsymbol{\delta} \tag{9}$$

This formulation of the problem enables the use of computationally efficient linear solvers such as generalized pseudo-inverses, linear programming or quadratic programming. However, as discussed above, the assumption of linearity neglects interactions between control effectors, fails to capture parabolic moment curves and neglects nonlinearities in the control-induced moments. Although the assumption is acceptable for conventional control effector configurations, it is not valid for advanced configurations such as the ICE aircraft. In aerospace control CA algorithms are required to run in real time at frequencies in the order of 100Hz,[10] a requirement that is not met by current nonlinear control allocation approaches.

III. Incremental Nonlinear Control Allocation

The incremental control allocation approach implemented in this paper is based on a reformulation of the control allocation problem in incremental form and the application of the time scale separation principle. Incremental nonlinear control has been successfully implemented in aerospace applications under the incremental nonlinear dynamic inversion (INDI) scheme,[29–32] showing very promising advantages such as a substantial reduction of model dependency.

III.A. The Control Problem in Incremental Form

Consider again the nonlinear system dynamics in Eq. (1). The aerodynamic moment inputs $\boldsymbol{\tau}$ can be separated into an exclusively state-dependent part and an input-depended part

$$\boldsymbol{\tau} = \boldsymbol{\tau}_a + \boldsymbol{\tau}_\delta \tag{10}$$

where $\boldsymbol{\tau}_a$ contains the aerodynamic moments generated by the airframe, and $\boldsymbol{\tau}_\delta$ is the control effector model, providing the control-induced moments produced by the actuators. The control effector model can be generally expressed as the nonlinear mapping

$$\boldsymbol{\tau}_\delta = \boldsymbol{\Phi}(\mathbf{x}, \boldsymbol{\delta}) \tag{11}$$

Thus, the system dynamics can be rewritten as

$$\dot{\mathbf{x}} = [\mathbf{f}(\mathbf{x}) + \mathbf{g}(\mathbf{x})\,\boldsymbol{\tau}_a] + \mathbf{g}(\mathbf{x})\,\boldsymbol{\Phi}(\mathbf{x}, \boldsymbol{\delta}) = \mathbf{F}(\mathbf{x}) + \mathbf{g}(\mathbf{x})\,\boldsymbol{\Phi}(\mathbf{x}, \boldsymbol{\delta}) \tag{12}$$

When the control system works in a discrete-time scheme, the dynamic equations of the system can be locally linearized at every time step around the current state $\mathbf{x}_0$ and actuator positions $\boldsymbol{\delta}_0$ as a first-order Taylor expansion:

$$\dot{\mathbf{x}} \approx \dot{\mathbf{x}}_0 + \frac{\partial}{\partial \mathbf{x}} \left[\mathbf{F}(\mathbf{x}) + \mathbf{g}(\mathbf{x})\,\boldsymbol{\Phi}(\mathbf{x}, \boldsymbol{\delta})\right]\Bigg|_{\substack{\boldsymbol{\delta}=\boldsymbol{\delta}_0 \\ \mathbf{x}=\mathbf{x}_0}} (\mathbf{x} - \mathbf{x}_0) + \frac{\partial}{\partial \boldsymbol{\delta}} \left[\mathbf{F}(\mathbf{x}) + \mathbf{g}(\mathbf{x})\,\boldsymbol{\Phi}(\mathbf{x}, \boldsymbol{\delta})\right]\Bigg|_{\substack{\boldsymbol{\delta}=\boldsymbol{\delta}_0 \\ \mathbf{x}=\mathbf{x}_0}} (\boldsymbol{\delta} - \boldsymbol{\delta}_0) \tag{13}$$

The time scale separation principle states that, for systems where the derivatives of the states have significantly faster dynamics than the states themselves, the term $(\mathbf{x}-\mathbf{x}_0)$ is small enough to be neglected at high sampling rates. This principle commonly applies to systems where $\boldsymbol{\delta}$ can change significantly faster than $\mathbf{x}$ over a time step, which is the case when the influence of $\boldsymbol{\delta}$ on the derivatives of the states is significantly higher than the influence of the states. This has been proven to be true for aerial vehicles such as aircraft,[30] helicopters[31] and quadrotors[32] at common sampling frequencies of 100 Hz.

Applying the time scale separation principle and introducing the virtual control input $\boldsymbol{\nu}(\mathbf{x}) = \dot{\mathbf{x}}$, Eq. (13) can be simplified to

$$\boldsymbol{\nu}(\mathbf{x}) = \dot{\mathbf{x}} \approx \dot{\mathbf{x}}_0 + \mathbf{g}(\mathbf{x}_0)\,\frac{\partial \boldsymbol{\Phi}(\mathbf{x}_0, \boldsymbol{\delta}_0)}{\partial \boldsymbol{\delta}}\Delta\boldsymbol{\delta} \tag{14}$$

At this point, the system dynamics can be linearized with an incremental nonlinear dynamic inversion loop by inverting the dynamics in Eq. (14):

$$\Delta\boldsymbol{\delta}_c = \left[\frac{\partial \boldsymbol{\Phi}(\mathbf{x}_0, \boldsymbol{\delta}_0)}{\partial \boldsymbol{\delta}}\right]^{-1} \mathbf{g}(\mathbf{x})^{-1}\left[\boldsymbol{\nu}(\mathbf{x}) - \dot{\mathbf{x}}_0\right] \tag{15}$$

This control law linearizes the response between the virtual control input $\boldsymbol{\nu}(\mathbf{x})$ and $\mathbf{x}$. Moreover, model dependency is significantly reduced with respect to typical nonlinear dynamic inversion (NDI) control laws,[33–35] since the INDI control law is independent of the aerodynamic derivatives in $\boldsymbol{\tau}_a$. This reduction in model dependency is compensated by feeding back acceleration measurements $\dot{\mathbf{x}}_0$.

In over-actuated systems the Jacobian $\partial\boldsymbol{\Phi}(\mathbf{x}, \boldsymbol{\delta})\,/\partial\boldsymbol{\delta}$ is a non-square $m{\times}p$ matrix, and therefore it cannot be inverted to implement the incremental control law in Eq. (15). However, a control allocation scheme can be implemented by reformulating the control allocation problem in incremental form with Eq. (14).

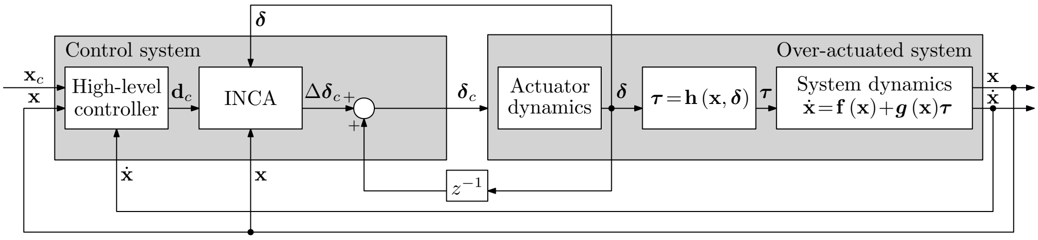

Figure 2. Incremental nonlinear control allocation-based control scheme for over-actuated systems.

III.B. The Control Allocation Problem in Incremental Form

Note that Eq. (14) establishes an affine relationship between the virtual control input $\boldsymbol{\nu}(\mathbf{x})$ and increments in actuator positions $\Delta\boldsymbol{\delta}$. The nonlinearities and interactions of the control effectors are still captured by the Jacobian matrix $\partial\boldsymbol{\Phi}(\mathbf{x}_0,\boldsymbol{\delta}_0)/\partial\boldsymbol{\delta}$, which can be updated for the current state and actuator positions at every time step. To simplify notation, let the Jacobian matrix of $\boldsymbol{\Phi}(\mathbf{x},\boldsymbol{\delta})$ with respect to $\boldsymbol{\delta}$ be denoted as

$$\nabla_{\boldsymbol{\delta}}\boldsymbol{\Phi}(\mathbf{x},\boldsymbol{\delta}) = \frac{\partial\boldsymbol{\Phi}(\mathbf{x},\boldsymbol{\delta})}{\partial\boldsymbol{\delta}} \tag{16}$$

and define the pseudo-control input $\mathbf{d}_c \in \mathbb{R}^n$

$$\mathbf{d}_c = \mathbf{g}(\mathbf{x})^{-1}\left[\boldsymbol{\nu}(\mathbf{x}) - \dot{\mathbf{x}}_0\right] \tag{17}$$

The INCA problem is formulated as: given the current state $\mathbf{x}_0$, the current actuator positions $\boldsymbol{\delta}_0$, acceleration measurements $\dot{\mathbf{x}}_0$ and a pseudo-control input command $\mathbf{d}_c = \mathbf{g}(\mathbf{x})^{-1}\left[\boldsymbol{\nu}(\mathbf{x}) - \dot{\mathbf{x}}_0\right]$, determine an increment in the control input vector $\Delta\boldsymbol{\delta}$ such that

$$\begin{gathered} \nabla_{\boldsymbol{\delta}}\boldsymbol{\Phi}(\mathbf{x}_0,\boldsymbol{\delta}_0)\,\Delta\boldsymbol{\delta} = \mathbf{d}_c \\ \text{subject to} \quad \underline{\boldsymbol{\Delta\delta}} \leq \boldsymbol{\Delta\delta} \leq \overline{\boldsymbol{\Delta\delta}} \end{gathered} \tag{18}$$

where $\underline{\boldsymbol{\Delta\delta}}$ and $\overline{\boldsymbol{\Delta\delta}}$ are the most restrictive upper and lower bounds of the local position and rate constraints of the actuators, translated into local incremental constraints. Note that the INCA control allocator provides required increments of the actuator positions, which are added to the current actuator positions to reach the absolute position vector: $\boldsymbol{\delta} = \boldsymbol{\delta}_0 + \Delta\boldsymbol{\delta}$. The top-level INCA-based control scheme is depicted in Figure 2.

The main advantage of INCA is that the incremental problem formulated in Eq. (18) is linear in the increments of actuator positions, and therefore can be solved with simple and efficient linear methods, such as the redistributed weighted pseudo-inverse or quadratic programming. The fact that only local increments $\Delta\boldsymbol{\delta}$ are determined at each time step implies that the Jacobian $\nabla_{\boldsymbol{\delta}}\boldsymbol{\Phi}(\mathbf{x},\boldsymbol{\delta})$, which captures nonlinearities and control effector interactions, can be updated for the new actuator positions at every time step while the actuators are dynamically driven towards their optimal positions. Thus, the direction of the increments of the control vector may change at every time step, in contrast to conventional LCA methods, which compute absolute positions at each time step. Additionally, note that actual actuator positions $\boldsymbol{\delta}_0$ are fed back into the system, and therefore the allocation is always performed based on actual actuator position measurements, which mitigates the negative impact of actuator dynamics. Most conventional CA methods, in contrast, assume $\boldsymbol{\delta}_c = \boldsymbol{\delta}_0$, resulting in negative coupling effects between control allocators and actuator dynamics.[36]

Note that an incremental formulation of the control allocation problem was derived for the particular case of multivariate spline-based control systems in Ref. 21. In this paper, the method is generalized to incremental flight control systems based on any kind of on-board aerodynamic model, and focuses on controller-related aspects such as real-time performance, robustness, model dependency, actuator dynamics and saturation handling.

III.C. Actuator Constraints in Incremental Form

The incremental formulation of the control allocation problem requires the absolute position and rate constraints of the actuators to be translated into equivalent local constraints in incremental form. Under a discrete-time scheme, rate limits are directly mapped into position limits over a time step Δt as

$$\begin{aligned} \Delta\boldsymbol{\delta}^r_{\max} &= \dot{\boldsymbol{\delta}}_{\max}\Delta t \\ \Delta\boldsymbol{\delta}^r_{\min} &= -\dot{\boldsymbol{\delta}}_{\max}\Delta t \end{aligned} \tag{19}$$

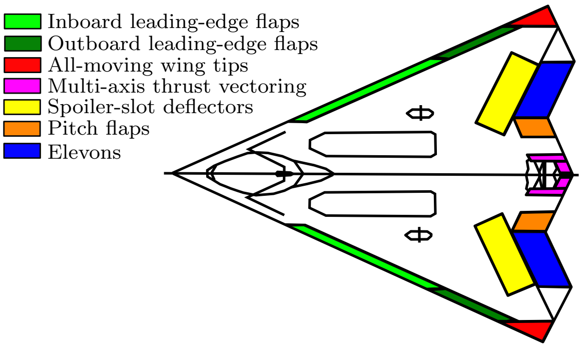

Figure 3. ICE control effectors suite.

Similarly, absolute position limits can be translated into local constraints imposed over a time step as

$$\begin{aligned} \Delta\boldsymbol{\delta}^p_{\text{max}} &= \boldsymbol{\delta}_{\text{max}} - \boldsymbol{\delta}_0 \\ \Delta\boldsymbol{\delta}^p_{\text{min}} &= \boldsymbol{\delta}_{\text{min}} - \boldsymbol{\delta}_0 \end{aligned} \tag{20}$$

The local upper and lower bounds of the actuator position increments at a given time step are the most restrictive of the local rate and position limits:

$$\begin{aligned} \overline{\Delta\boldsymbol{\delta}} &= \min\left(\dot{\boldsymbol{\delta}}_{\text{max}}\Delta t_s,\ \boldsymbol{\delta}_{\text{max}} - \boldsymbol{\delta}_0\right) \\ \underline{\Delta\boldsymbol{\delta}} &= \max\left(-\dot{\boldsymbol{\delta}}_{\text{max}}\Delta t_s,\ \boldsymbol{\delta}_{\text{min}} - \boldsymbol{\delta}_0\right) \end{aligned} \tag{21}$$

IV. The ICE Aircraft Model

The INCA method was implemented in a simulation framework to design a flight control system for Lockeed Martin's ICE aircraft, a highly manoeuvrable tailless aircraft with an unconventional suite of control effectors. This configuration presents substantial control challenges for which LCA methods are obsolete. In this section the ICE configuration is presented, and a description of the high-fidelity model used in simulations the is given.

IV.A. The ICE Control Effectors Suite

The ICE configuration was developed as one of the design concepts for the ICE program conceived in 1993 by the Flight Control Division of the U.S. Flight Dynamics Directorate, which aimed to meet new requirements in terms of improved stealth characteristics, reduction of airframe weight, improvement of lift-to-drag ratio and high manoeuvrability.[37] The result was an over-actuated 65-deg sweep, highly maneuverable, supersonic tailless flying wing with 13 innovative control effectors. Refs. 38,39 provide technical insight on this program.

The ICE control effectors suite includes inboard and outboard leading-edge flaps (LEF) providing lateral-directional control power at high AoA, all-moving wing tips (AMT) as one of the main sources of lateral-directional control, and fluidic multi-axis thrust vectoring (MTV) as an additional source of directional and longitudinal control power. It also includes pitch flaps (PF) for longitudinal control (only symmetric deflections are possible) and independent elevons, mainly producing longitudinal and lateral control power. Finally, the ICE aircraft has two spolier-slot deflectors (SSD). Unlike conventional spoilers, SSDs open a slot between the lower and upper wing skins when deflected, allowing the redirection of the air flow at high AoA to recover control effectiveness of the trailing-edge actuators. SSDs provide improved lateral-directional control effectiveness at high AoA and transonic flight with respect to conventional spoilers. The SSDs are placed upstream of most trailing-edge control surfaces, and therefore have a strong influence on their control effectiveness at low AoA. The configuration of the ICE control effectors is shown in Figure 3.

The dynamics of the control effectors are modeled as second-order transfer functions. A low-bandwidth and a high-bandwidth transfer functions are used depending on the effectors:

$$H_l(s) = \frac{(18)(100)}{(s+18)(s+100)} \qquad (22) \qquad\qquad H_h(s) = \frac{(40)(100)}{(s+40)(s+100)} \qquad (23)$$

The position limits, no-load rate limits and dynamics of the ICE control effectors are listed in Table 1.

IV.B. Control Challenges

The ICE configuration presents a series of challenges regarding flight control and stability. In conventional control suites, lateral-directional stability is mainly provided by the vertical stabilizer, and quasi-uncoupled yaw control power is generated by the rudder. The elimination of a vertical tail in tailless designs implies a substantial relaxation of directional stability and a reduction of directional control power.[40] Control and stability issues have been extensively addressed for the ICE aircraft.[14,37,41–44]

A more unaddressed challenge of the ICE configuration is the impossibility to successfully use linear control allocation methods to optimally distribute control commands and fully exploit the capabilities of its control suite. This impossibility is due to a number of reasons. First, as is common in tailless configurations, directional control power is mainly produced with horizontal control surfaces, and therefore yawing moment curves are mainly parabolic. These cannot be captured by linear effector models unless the concerned actuators are restricted to operate in one direction, so LCA methods have serious issues regarding directional control in tailless configurations. An example of a parabolic yawing moment curve of the left elevon influenced by the AMT deflection from the ICE aerodynamic database is shown in Figure 4(a).

Second, due to the high number of control effectors, the mechanisms used to produce control moments and the proximity between some control surfaces, the actuators exhibit strong nonlinear interactions. This is particularly notable for trailing-edge actuators. In some cases, such interactions may even cause a change of sign in the slope of the moment curves of some actuators, such as in the examples shown in Figures 4(a)-4(c). Also, note that control effectiveness of trailing-edge surfaces is rapidly lost for even small deflections of the SSDs at low AoA, as observed in Figure 4(b).

Finally, nonlinearities at the extreme regions of the control moment curves are observed in Figure 4(b). The dashed line represents a linear approximation of the control moment curve for $\delta_{\mathrm{s}} = 0$ deg. It is shown that that the model mismatch becomes significant close to the actuator position limits. This error is particularly critical in failure conditions, where the non-faulty actuators are forced to operate in extreme regions of the moment curve. The factors discussed above make the assumption of linearity in control allocation obsolete in the case of the ICE aircraft.

IV.C. The ICE High-Fidelity Simulation Model

The high-fidelity nonlinear simulation model used in this paper was released by Lockheed Martin to encourage control-related research. It is a six degrees-of-freedom (6-DoF) aerodynamic model developed mainly from wind tunnel data, and includes nonlinear control effector interaction effects, dynamic derivatives, aeroelastic effects and hinge moment derivatives. The aerodynamic model provides dimensionless coefficients for aerodynamic forces and moments as a summation of nonlinear terms:

$$C_i = \sum_{j=1}^{19} C_{ij}\left(\boldsymbol{\delta}, \alpha, \beta, M, \boldsymbol{\omega}\right) \tag{24}$$

with $i = \{l, m, n, X, Y, Z\}$ and where the nonlinear terms $C_{ij}(\boldsymbol{\delta}, \alpha, \beta, M, \boldsymbol{\omega})$ are stored in lookup tables. A detailed description of the model is given in Ref. 27.

Table 1. Dynamic properties of the ICE control effectors.

Control effector	Notation	Position limits [deg]	Rate limit [deg/sec]	Dynamics
Inboard LEF	$\delta_{\mathrm{lfi}}, \delta_{\mathrm{rfi}}$	[0, 40]	40	$H_l(s)$
Outboard LEF	$\delta_{\mathrm{lfo}}, \delta_{\mathrm{rfo}}$	[-40, 40]	40	$H_l(s)$
AMT	$\delta_{\mathrm{la}}, \delta_{\mathrm{ra}}$	[0, 60]	150	$H_h(s)$
Elevons	$\delta_{\mathrm{le}}, \delta_{\mathrm{re}}$	[-30, 30]	150	$H_h(s)$
SSD	$\delta_{\mathrm{ls}}, \delta_{\mathrm{rs}}$	[0, 60]	150	$H_h(s)$
PF	δ_{pf}	[-30, 30]	150	$H_h(s)$
MTV	$\delta_{\mathrm{ptv}}, \delta_{\mathrm{ytv}}$	[-15, 15]	150	$H_h(s)$

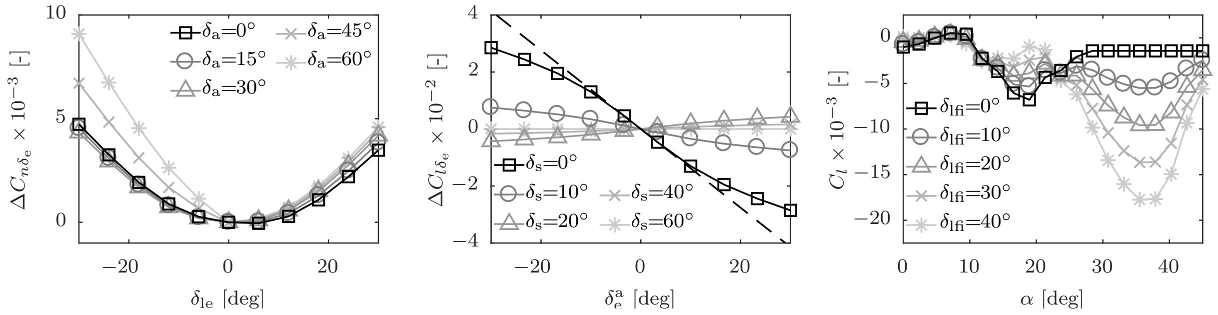

(a) Yawing moment curve of the left elevon, influenced by the deflection of the AMTs.

(b) Rolling momentcurve of the elevons with asymmetric deflections, influenced by the SSDs. The dashed line represents a linear approximation for $\delta_s = 0$.

(c) Total rolling moment coefficient, including moments from the airframe, for $\delta_{lfo} = 30$ deg, influenced by the inboard LEF. $\beta = 0$.

Figure 4. Examples of control effectiveness from the ICE aerodynamic database.

IV.D. Multi-Axis Thrust Vectoring Model

The MTV model considers the direction of the pitch δ_{ptv} and yaw δ_{ytv} deflection angles of the thrust vector such that positive deflections produce negative pitching and yawing moments. Using this convention, the projections of the thrust vector $\mathbf{T}$ onto the body frame for arbitrary deflections δ_{ptv} and δ_{ytv} are represented in the diagram in Figure 5. The MTV force $\mathbf{T}$ and moment $\boldsymbol{\tau}_T$ vectors are given by Equations (25) and (26), where d_n=18.75 ft is the moment arm of the thrust force.

$$\mathbf{T} = \begin{bmatrix} T_x \\ T_y \\ T_z \end{bmatrix} = \mathrm{T} \begin{bmatrix} \cos(\delta_{ptv})/\cos(\delta_{ytv}) \\ \cos(\delta_{ptv})\tan(\delta_{ytv}) \\ \sin(\delta_{ptv}) \end{bmatrix} \quad (25)$$

$$\boldsymbol{\tau}_T = \begin{bmatrix} \tau_{x_T} \\ \tau_{y_T} \\ \tau_{z_T} \end{bmatrix} = -\mathrm{T}d_n \begin{bmatrix} 0 \\ \sin(\delta_{ptv}) \\ \cos(\delta_{ptv})\tan(\delta_{ytv}) \end{bmatrix} \quad (26)$$

V. Control Allocation Solvers

The LCA- and INCA-based flight control systems designed in this paper were implemented with two typical LCA methods that have been proven to be suitable for real-time implementation. The selected methods are the redistributed weighted pseudo-inverse (RWPI) and quadratic programming (QP) solved with the active set algorithm. These methods are described in this section.

V.A. Redistributed Weighted Pseudo-Inverse

The RWPI method consists on using an explicit solution of the unconstrained LCA problem and iterating over the result if actuator constraints are violated. The explicit solution to the unconstrained problem can be derived analytically if the constraints from Eq. (8) are removed.

The unconstrained control allocation problem consists on finding a control vector $\mathbf{u}$ that satisfies a control demand $\mathbf{d}_c$ while minimizing a secondary objective formulated as a quadratic cost function that penalizes displacement from a preferred control vector $\mathbf{u}_p$. A linear relationship $G\mathbf{u} = \mathbf{d}_c$ is assumed. Note that here the control vector is denoted as $\mathbf{u}$ to keep de discussion general, and corresponds to $\boldsymbol{\delta}$ for LCA and to $\Delta\boldsymbol{\delta}$ for INCA. Also, the matrix G corresponds to the control effectiveness matrix $B(\mathbf{x})$ in LCA and to the Jacobian matrix $\nabla_{\boldsymbol{\delta}}\boldsymbol{\Phi}(\mathbf{x}, \boldsymbol{\delta})$ in INCA; and the pseudo-control input $\mathbf{d}_c$ corresponds to an absolute moment command $\boldsymbol{\tau}_c$ in LCA and to an incremental moment command $\Delta\boldsymbol{\tau}_c$ in INCA.

The minimization problem is formulated using a ℓ_2 norm cost function as: given an operating point $\mathbf{x}_0$, an affine relationship $G\mathbf{u} = \mathbf{d}_c$, a control demand $\mathbf{d}_c$ and a preference vector $\mathbf{u}_p$ determine a control input $\mathbf{u}$ such that

$$\begin{aligned} \min_{\mathbf{u}} \ \mathcal{J} &= \frac{1}{2}\left(\mathbf{u} - \mathbf{u}_p\right)^T W_{\mathbf{u}} \left(\mathbf{u} - \mathbf{u}_p\right) \\ \text{subject to} \quad & G\mathbf{u} = \mathbf{d}_c \end{aligned} \quad (27)$$

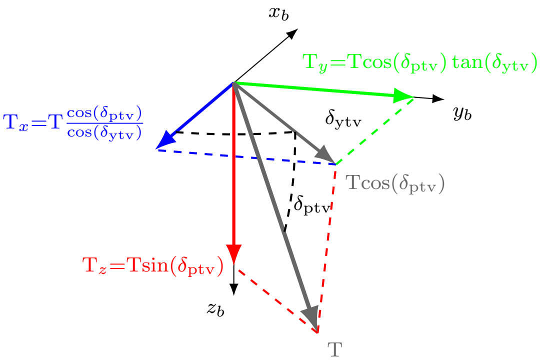

Figure 5. Projections of the thrust vector in body frame.

where $W_{\mathbf{u}}$ is a weighting matrix that penalizes to the use of some effectors over others. For the secondary objective, the most common approach is minimizing the control effort by setting $\mathbf{u}_p = 0$.

Analytically solving (27) with Lagrange multipliers[1, 13, 45] the explicit biased weighted pseudo-inverse solution is found:

$$\mathbf{u} = \mathbf{u}_p + G^{\sharp} \left(\mathbf{d}_c - G\mathbf{u}_p\right) \tag{28}$$

with

$$G^{\sharp} = W_{\mathbf{u}}^{-1} G^T \left(G W_{\mathbf{u}}^{-1} G^T\right)^{-1} \tag{29}$$

a generalized weighted pseudo-inverse. This method provides a solution to the unconstrained problem as long as it exists and GG^T is not rank-deficient[a]. Note that the weighted pseudo-inverse solution does not consider local position and rate constraints, and hence it requires further processing.

The RWPI method consists on first computing the weighted pseudo-inverse solution with Eq. (28). If the found $\mathbf{u}$ is within the local actuator limits, the solution is kept. Otherwise, if one or more effectors violate constraints, the next steps are followed. First, the columns in G corresponding to the actuators that violate the limits are zeroed, forming an auxiliary matrix G_{sat}. Second, the values of the saturated effectors are placed in the preference vector $\mathbf{u}_p$, forming an auxiliary preference vector $\mathbf{u}_{p,\mathrm{sat}}$. Then, the redistributed weighted pseudo-inverse solution is re-computed as follows:

$$\mathbf{u} = \mathbf{u}_{p,\mathrm{sat}} + G^{\sharp}_{\mathrm{sat}} \left(\mathbf{d}_c - G\mathbf{u}_{p,\mathrm{sat}}\right) \tag{30}$$

This process is repeated until all effectors are saturated or a solution within the local limits is found. The maximum number of iterations within a time step corresponds to the number of control effectors available plus one. Despite being suboptimal,[10] the pseudo-inverse method is a very popular[44, 46–49] solution for real-time control allocation in safety-critical systems due to its simplicity, reliability and computational efficiency.

V.B. Quadratic Programming

The CA problem can be also solved as a numerical optimization problem with explicit constraints. In such cases, the common approach is to minimize a multi-objective cost function defined with a given norm, subject to local actuator constraints. When the ℓ_1 norm is chosen, the optimization problem can be solved as a linear program (LP).[11–14] However, as discussed in Ref. 10, LP-based solutions tend to exploit a smaller number of control effectors, whereas solutions found using ℓ_2 and ℓ_∞ norms tend to distribute the control effort over a larger number of actuators. For this reason, ℓ_2- and ℓ_∞-based solutions are more popular.[28]

A very common approach is using the ℓ_2 norm to formulate the control allocation problem as a multi-objective constrained optimization problem, solved as a quadratic program:

$$\begin{aligned} \min_{\mathbf{u}} \ \ \mathcal{J} = W_{\mathbf{d}} \left|\left|G\mathbf{u} - \mathbf{d}_c\right|\right|_2^2 + \epsilon \ W_{\mathbf{u}} \left|\left|\mathbf{u} - \mathbf{u}_p\right|\right|_2^2 \\ \text{subject to} \quad \underline{\mathbf{u}} \leq \mathbf{u} \leq \overline{\mathbf{u}} \end{aligned} \tag{31}$$

---

[a] Control suites for mechanical systems usually avoid control effector deficiencies by design.

where ϵ is a scalar, selected sufficiently small to prioritize the minimization of the allocation error $(G\mathbf{u}-\mathbf{d}_c)$ over the secondary objective of minimizing $(\mathbf{u}-\mathbf{u}_p)$, and $W_{\mathbf{d}}$ and $W_{\mathbf{u}}$ are nonsingular weighting matrices.

Many numerical algorithms are available to solve the QP problem in real time, such as fixed-point methods,[50,51] active set methods[52] and interior-point methods.[53,54] In Ref. 54, the authors concluded that the active set algorithm converges exactly to the optimal solution in a finite number of steps and is computationally efficient for control allocation problems of small and medium size, whereas interior-point algorithms perform better in problems of larger size, despite requiring significantly more computations. In this paper, the QP problem is implemented with the active set algorithm described in Ref. 52.

VI. LCA-Based Flight Control System Design

A conventional nonlinear attitude control system based on aerodynamic model inversion and LCA was designed for the ICE aircraft as a baseline to assess the performance of INCA-based flight control systems. The control system, including the linear control effector model, its adaptation and the inner loop control laws is described in this section.

VI.A. Linear Control Effectors Model

As discussed above, LCA methods require an aerodynamic model in which the control-induced moments are affine in the actuator positions. Note, however that the aerodynamic and control derivatives can remain nonlinear functions of α, β, M and $\boldsymbol{\omega}$. In order to de-couple the inputs, the interaction effects between control effectors were eliminated from the original database. Linear regressors were used to identify the aerodynamic coefficients and control derivatives as functions of α, β, M and $\boldsymbol{\omega}$ at the data points available in the ICE aerodynamic database. The obtained derivatives were stored in lookup tables. The structure of the affine model is

$$\begin{aligned} C_l &= C_{l_a}(\alpha,\beta,M,\boldsymbol{\omega}) + \sum_{i=1}^{13} \Delta C_{l,\delta_i}(\alpha,\beta,M)\,\delta_i \\ C_m &= C_{m_a}(\alpha,\beta,M,\boldsymbol{\omega}) + \sum_{i=1}^{13} \Delta C_{m,\delta_i}(\alpha,\beta,M)\,\delta_i \\ C_n &= C_{n_a}(\alpha,\beta,M,\boldsymbol{\omega}) + \sum_{i=1}^{13} \Delta C_{n,\delta_i}(\alpha,\beta,M)\,\delta_i \end{aligned} \tag{32}$$

with $\Delta C_{j,\delta_i}$ the control derivative of $j=\{l,m,n\}$ with respect to the control effector δ_i, and

$$\begin{aligned} C_{l_a}(\alpha,\beta,M,\boldsymbol{\omega}) &= C_{l,\alpha}(\alpha,M) + C_{l,\beta}(\alpha,\beta,M) + \frac{pb}{2V}C_{l,p}(\alpha,M) + \frac{rb}{2V}C_{l,r}(\alpha,M) \\ C_{m_a}(\alpha,\beta,M,\boldsymbol{\omega}) &= C_{m,\alpha}(\alpha,M) + C_{m,\beta}(\alpha,\beta,M) + \frac{q\bar{c}}{2V}C_{m,q}(\alpha,M) \\ C_{n_a}(\alpha,\beta,M,\boldsymbol{\omega}) &= C_{n,\alpha}(\alpha,M) + C_{n,\beta}(\alpha,\beta,M) + \frac{pb}{2V}C_{n,p}(\alpha,M) + \frac{rb}{2V}C_{n,r}(\alpha,M) \end{aligned} \tag{33}$$

the dimensionless nonlinear moments generated by the airframe. Examples of identified control derivatives scheduled for α and β are shown in Figure 6.

As discussed earlier, the assumption of linearity in control-induced moments is accurate enough in some cases (see the pitching moment characteristic of the pitch flap in Figure 7(a)), but in other cases it fails to capture important effects. See, for instance, the rolling moment characteristic of the outboard LEF in Figure 7(b) and the parabolic yawing moment curve of the right elevon in Figure 7(c).

The control derivative terms of the MTV can be derived by taking a first-order Taylor expansion of the terms τ_{y_T} and τ_{z_T} in Eq. (26) around $\delta_{\text{ptv}}=\delta_{\text{ytv}}=0$, yielding the affine approximation

$$\boldsymbol{\tau}_T = -Td_n \begin{bmatrix} 0 \\ \delta_{\text{ptv}} \\ \delta_{\text{ytv}} \end{bmatrix} \tag{34}$$

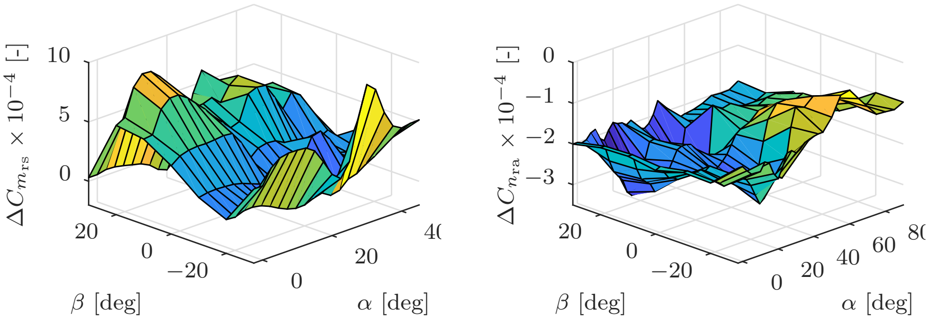

(a) Pitching moment derivative of right SSD. (b) Yawing moment derivative of right AMT.

Figure 6. Examples of control derivatives scheduled for α and β.

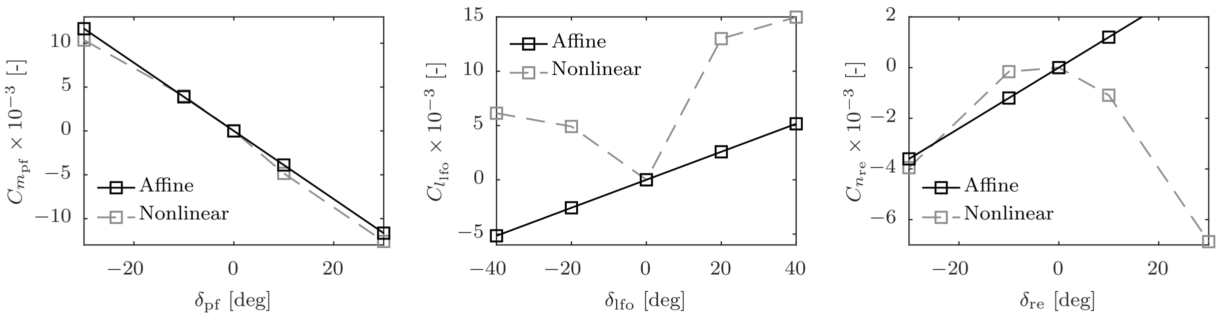

(a) Pitching moment of pitch flaps. (b) Rolling moment of outboard LEF. (c) Yawing moment of right elevon.

Figure 7. Affine control effector model compared to original aerodynamic data.

Wrapping up the control derivative terms into a control effectiveness matrix $B(\mathbf{x})$, the aerodynamic moments can be expressed in control-affine form as

$$\boldsymbol{\tau} = \boldsymbol{\tau}_a + \boldsymbol{\tau}_e = \frac{1}{2}\rho V^2 S \left(\begin{bmatrix} bC_{l_a} \\ \bar{c}C_{m_a} \\ bC_{n_a} \end{bmatrix} + B(\mathbf{x})\, \boldsymbol{\delta} \right) \tag{35}$$

The actuator constraints are translated into local constraints as in Eq. (7). The MTV vector is subject to a circular constraint imposed over the ℓ_2 norm of the vector $\boldsymbol{\delta}_{\mathrm{tv}} = (\delta_{\mathrm{ptv}}, \delta_{\mathrm{ytv}})$. When the MTV vector violates the circular constraint, it is re-scaled into the boundary of the feasible subspace by keeping the original direction of $\boldsymbol{\delta}_{\mathrm{tv}}$:

$$\boldsymbol{\delta}'_{\mathrm{tv}} = \frac{\boldsymbol{\delta}_{\mathrm{tv}_{\mathrm{max}}}}{||\delta_{\mathrm{tv}}||}\delta_{\mathrm{tv}} \tag{36}$$

VI.B. Angular Rate Control Loop

The innermost control loop controls the body angular rates $\boldsymbol{\omega} = [p\ q\ r]$ through commanded moments $\boldsymbol{\tau}_c$. Consider the aircraft rotational dynamic equations

$$\dot{\boldsymbol{\omega}} = I^{-1}\left(\boldsymbol{\tau} - \boldsymbol{\omega}\times I\boldsymbol{\omega}\right) = I^{-1}\boldsymbol{\tau}_e + I^{-1}\left(\boldsymbol{\tau}_a - \boldsymbol{\omega}\times I\boldsymbol{\omega}\right) \tag{37}$$

where I is the aircraft inertia matrix. The aerodynamic moments produced by the airframe include the contributions from the trim positions of the actuators:

$$\boldsymbol{\tau}_a = \frac{1}{2}\rho V^2 S \left(\begin{bmatrix} bC_{l_a} \\ \bar{c}C_{m_a} \\ bC_{n_a} \end{bmatrix} + B(\mathbf{x})\, \boldsymbol{\delta}_{\mathrm{trim}} \right) \tag{38}$$

Setting the angular acceleration as a virtual control input $\boldsymbol{\nu}_\omega(\mathbf{x}) = \dot{\boldsymbol{\omega}}$ and solving Eq. (37) for the required moments $\boldsymbol{\tau}_c = \boldsymbol{\tau}_e$ leads to the model-based inversion control law

$$\boldsymbol{\tau}_c = I\boldsymbol{\nu}_\omega(\mathbf{x}) - \frac{1}{2}\rho V^2 S \left(\begin{bmatrix} bC_{l_a} \\ \bar{c}C_{m_a} \\ bC_{n_a} \end{bmatrix} + B(\mathbf{x})\,\boldsymbol{\delta}_{\text{trim}} \right) + \boldsymbol{\omega} \times I\boldsymbol{\omega} \tag{39}$$

which linearizes the system between the virtual control input $\boldsymbol{\nu}_\omega(\mathbf{x})$ and $\boldsymbol{\omega}$. The required moments $\boldsymbol{\tau}_c$ are distributed over $\boldsymbol{\delta}$ by a linear control allocator. The linearized system can now be controlled through the virtual control input $\boldsymbol{\nu}_\omega(\mathbf{x})$ such that the output follows a reference command $\boldsymbol{\omega}_c$, by using an outer state-feedback linear control law

$$\boldsymbol{\nu}_\omega(\mathbf{x}) = \boldsymbol{K}_{\omega_P}(\boldsymbol{\omega} - \boldsymbol{\omega}_c) + \boldsymbol{K}_{\omega_I}\int(\boldsymbol{\omega} - \boldsymbol{\omega}_c)\,dt + \boldsymbol{K}_{\omega_D}(\dot{\boldsymbol{\omega}} - \dot{\boldsymbol{\omega}}_c) \tag{40}$$

VI.C. Adaptation of the Linear Model

As previously shown, the identified linear model fails to capture nonlinear moments, which is particularly critical for parabolic and non-monotonic moment curves (e.g. those shown in Figures 7(b) and 7(c)). Since such errors can cause instability of the closed loop, the linear model needs to be adapted to ensure minimally acceptable performance.

The AMT, inboard LEF and SSD are restricted to deflect in one direction only. Thus, their yawing moment curves are half-parabolas, which can be approximated with a linear model. The model mismatch is then compensated by the robustness of the controller. The elevons and outboard LEF, however, can deflect in two directions, thus having parabolic yawing moment curves. Since these actuators are not primary sources of directional control power, their yawing moment derivatives were set to zero in the control effectiveness matrix. As a consequence, these effectors are used to produce pitch and roll only, and their secondary-axis yawing moments are seen by the control system as external disturbances, which need to be compensated by other yaw-generating actuators.

These necessary simplifications of the model have two detrimental consequences on the overall performance of the flight control system. First, the potential of the ICE control suite is underexploited (e.g. elevons cannot be used to produce yawing moments, which might be necessary in failure conditions or extreme maneuvers). Second, the yawing moments produced by the elevons and outboard LEF are seen as external disturbances, and need to be continuously suppressed by other control effectors.

VII. INCA-Based Flight Control System Design

In order to evaluate the performance of INCA as a control allocator, an INCA-based flight control system was designed for the ICE aircraft. The control system, including the Jacobian model, inner loop control laws and control allocation-related particularities of the INCA method are discussed in this section.

VII.A. Multivariate Simplex Spline-Based Jacobian Model

As shown in Section III, the INCA method has a more relaxed dependency on an on-board aerodynamic model and therefore is more robust against model uncertainties. Instead of a full aerodynamic model, INCA is based on a control effectiveness Jacobian model $\nabla_{\boldsymbol{\delta}}\Phi(\mathbf{x}, \boldsymbol{\delta})$ that includes the directional derivatives of $\boldsymbol{\tau}_e$ with respect to $\boldsymbol{\delta}$.

In this paper, the Jacobian control effectiveness matrix is derived from a multivariate simplex B spline-based aerodynamic model of the ICE aircraft identified from the high-fidelity aerodynamic database described in Section IV. This spline model preserves the original model structure of aerodynamic terms:

$$\begin{aligned} C_i = \; & + C^s_{i_1}(\alpha, M) + C^s_{i_2}(\alpha, \beta, M) + C^s_{i_3}(\alpha, \delta_{\text{ls}}, \delta_{\text{le}}, M) + C^s_{i_4}(\alpha, \delta_{\text{rs}}, \delta_{\text{re}}, M) \\ & + C^s_{i_5}(\alpha, \beta, \delta_{\text{lfi}}) + C^s_{i_6}(\alpha, \beta, \delta_{\text{rfi}}) + C^s_{i_7}(\alpha, \beta, \delta_{\text{lfi}}, \delta_{\text{lfo}}, M) + C^s_{i_8}(\alpha, \beta, \delta_{\text{rfi}}, \delta_{\text{rfo}}, M) \\ & + C^s_{i_9}(\alpha, \delta_{\text{lfo}}, \delta_{\text{la}}) + C^s_{i_{10}}(\alpha, \delta_{\text{rfo}}, \delta_{\text{ra}}) + C^s_{i_{11}}(\alpha, \delta_{\text{la}}, \delta_{\text{le}}) + C^s_{i_{12}}(\alpha, \delta_{\text{ra}}, \delta_{\text{re}}) \\ & + C^s_{i_{13}}(\alpha, \delta_{\text{rs}}, \delta_{\text{ls}}, \delta_{\text{pf}}, M) + C^s_{i_{14}}(\alpha, \beta, \delta_{\text{la}}) + C^s_{i_{15}}(\alpha, \beta, \delta_{\text{ra}}) + C^s_{i_{16}}(\alpha, \beta, \delta_{\text{ls}}) \\ & + C^s_{i_{17}}(\alpha, \beta, \delta_{\text{rs}}) + \frac{pb}{2V}C^s_{i_{18}}(\alpha, M) + \frac{q\bar{c}}{2V}C^s_{i_{19}}(\alpha, M) + \frac{rb}{2V}C^s_{i_{20}}(\alpha, M) \end{aligned} \tag{41}$$

with $i = \{l, m, n, X, Y, Z\}$, where every model term $C^s_{i_n}$ is a multivariate B-spline defined over a simplex triangulation with 0th-order continuity. This model was identified from the original ICE aerodynamic database in Ref. 55 following the linear regression techniques presented in Ref. 56. T he directional derivatives of every model term $C^s_{i_j}$ in the directions of $\boldsymbol{\delta}$ can be computed in a computationally efficient way with the method for model reduction of parabolic partial differential equations presented in Ref. 57. This yields 13 partial derivatives of each of the 108 spline models, from which the control effectiveness Jacobian matrix is constructed as:

$$\nabla_{\boldsymbol{\delta}} \Phi\left(\alpha, \beta, M, \boldsymbol{\delta}\right) = \begin{bmatrix} \sum_{j=1}^{20} \frac{\partial C^s_{l_j}(\mathbf{x},\boldsymbol{\delta})}{\partial \delta_1} & \sum_{j=1}^{20} \frac{\partial C^s_{l_j}(\mathbf{x},\boldsymbol{\delta})}{\partial \delta_2} & \cdots & \sum_{j=1}^{20} \frac{\partial C^s_{l_j}(\mathbf{x},\boldsymbol{\delta})}{\partial \delta_{13}} \\ \sum_{j=1}^{20} \frac{\partial C^s_{m_j}(\mathbf{x},\boldsymbol{\delta})}{\partial \delta_1} & \sum_{j=1}^{20} \frac{\partial C^s_{m_j}(\mathbf{x},\boldsymbol{\delta})}{\partial \delta_2} & \cdots & \sum_{j=1}^{20} \frac{\partial C^s_{m_j}(\mathbf{x},\boldsymbol{\delta})}{\partial \delta_{13}} \\ \sum_{j=1}^{20} \frac{\partial C^s_{n_j}(\mathbf{x},\boldsymbol{\delta})}{\partial \delta_1} & \sum_{j=1}^{20} \frac{\partial C^s_{n_j}(\mathbf{x},\boldsymbol{\delta})}{\partial \delta_2} & \cdots & \sum_{j=1}^{20} \frac{\partial C^s_{n_j}(\mathbf{x},\boldsymbol{\delta})}{\partial \delta_{13}} \end{bmatrix} \tag{42}$$

The Jacobian calculation was implemented on a real-time, highly optimized routine that can provide in the order of 10^4 Jacobian calculations per second. A key factor for the accuracy of the Jacobians is the continuity order between simplices. In this case, 0th-order continuity was used, and therefore the model represents the worst possible case in terms of continuity. This implies that the performance achieved in this thesis can be substantially improved by increasing the continuity order of the spline model.

The Jacobian model is not restricted to spline-based models. For instance, a locally linear numerical differentiation approach with a lookup table-based aerodynamic model could also be used to approximate the nonlinear Jacobian. A spline model was used in this thesis because it provides an elegant way to extend the INCA-based FCS into a fault-tolerant flight control system. Splines are function approximators that can be used in an on-line system identification framework, in contrast to lookup table-based models.

VII.B. Multi-Axis Thrust Vectoring Jacobian Model

A Jacobian model providing the directional derivatives of the control moments produced by MTV can be obtained analytically by deriving the Jacobian matrix of $\boldsymbol{\tau}_T$ in Eq. (26):

$$\nabla_{\delta_{\text{tv}}} \boldsymbol{\tau}_{\text{T}}(\delta_{\text{ptv}}, \delta_{\text{ytv}}) = \text{T} d_n \begin{bmatrix} 0 & 0 \\ -\cos(\delta_{\text{ptv}}) & 0 \\ \sin(\delta_{\text{ptv}})\tan(\delta_{\text{ytv}}) & -\cos(\delta_{\text{ptv}})/\cos^2(\delta_{\text{ytv}}) \end{bmatrix} \tag{43}$$

The MTV circular constraints in incremental form require further consideration. In an incremental control allocation scheme, the control allocator provides a commanded increment $\Delta\boldsymbol{\delta}_{\text{tv}}$ over the current actuator position $\boldsymbol{\delta}_{\text{tv}_0}$. If the resulting MTV deflection vector $\boldsymbol{\delta}_{\text{tv}} = \boldsymbol{\delta}_{\text{tv}_0} + \Delta\boldsymbol{\delta}_{\text{tv}}$ violates the circular constraint, then a new increment $\Delta\boldsymbol{\delta}'_{\text{tv}}$ must be computed such that the new resulting vector $\boldsymbol{\delta}'_{\text{tv}} = \boldsymbol{\delta}_{\text{tv}_0} + \Delta\boldsymbol{\delta}'_{\text{tv}}$ satisfies the circular constraint while preserving the original direction of $\boldsymbol{\delta}_{\text{tv}}$. This usually involves changing the modulus and direction of $\Delta\boldsymbol{\delta}_{\text{tv}}$. The new deflection increment is computed as

$$\Delta\boldsymbol{\delta}'_{\text{tv}} = \frac{\delta_{\text{tv}_{\max}}}{||\boldsymbol{\delta}_{\text{tv}_0} + \Delta\boldsymbol{\delta}_{\text{tv}}||} \left(\boldsymbol{\delta}_{\text{tv}_0} + \Delta\boldsymbol{\delta}_{\text{tv}}\right) - \boldsymbol{\delta}_{\text{tv}_0} \tag{44}$$

VII.C. Angular Rate Control Loop

INCA is implemented at the innermost control loop for body-frame angular rate control. Consider the aircraft rotational dynamic equations, where $\boldsymbol{\tau}_e$ is substituted by the nonlinear control effector model $\boldsymbol{\Phi}(\mathbf{x}, \boldsymbol{\delta})$:

$$\dot{\boldsymbol{\omega}} = I^{-1}\left(\boldsymbol{\tau} - \boldsymbol{\omega} \times I\boldsymbol{\omega}\right) = I^{-1}\boldsymbol{\Phi}(\mathbf{x}, \boldsymbol{\delta}) + I^{-1}\left(\boldsymbol{\tau}_a - \boldsymbol{\omega} \times I\boldsymbol{\omega}\right) \tag{45}$$

For a given time step, the incremental form of the rotational dynamics as a first-order Taylor expansion at the operating point $(\mathbf{x}_0, \boldsymbol{\delta}_0)$ is:

$$\begin{aligned} \dot{\boldsymbol{\omega}} \simeq \dot{\boldsymbol{\omega}}_0 &+ \frac{\partial}{\partial \boldsymbol{\omega}} \left[I^{-1}\boldsymbol{\Phi}(\mathbf{x}, \boldsymbol{\delta}) + I^{-1}\left(\boldsymbol{\tau}_a - \boldsymbol{\omega} \times I\boldsymbol{\omega}\right)\right]\Bigg|_{\substack{\boldsymbol{\delta}=\boldsymbol{\delta}_0 \\ \mathbf{x}=\mathbf{x}_0}} (\boldsymbol{\omega} - \boldsymbol{\omega}_0) \\ &+ \frac{\partial}{\partial \boldsymbol{\delta}} \left[I^{-1}\boldsymbol{\Phi}(\mathbf{x}, \boldsymbol{\delta}) + I^{-1}\left(\boldsymbol{\tau}_a - \boldsymbol{\omega} \times I\boldsymbol{\omega}\right)\right]\Bigg|_{\substack{\boldsymbol{\delta}=\boldsymbol{\delta}_0 \\ \mathbf{x}=\mathbf{x}_0}} (\boldsymbol{\delta} - \boldsymbol{\delta}_0) \end{aligned} \tag{46}$$

where the angular accelerations at the current step $\dot{\boldsymbol{\omega}}_0$ can be obtained from angular accelerometers, signal processing or acceleration estimation methods.

According to the previously discussed time-scale separation principle, the second term of the right-hand side of Eq. (46), i.e. the changes in angular acceleration due to changes in angular rates, is negligible for high sampling rates in comparison to the control-dependent term. This is explained in Ref. 30 as follows. Increments in actuator positions directly cause angular accelerations. Angular rates, however, only vary as a consequence of integrating angular accelerations, i.e. integrating the actuator deflection contributions. Therefore, when the sampling frequency of the FCC is high enough[b], the assumption $(\boldsymbol{\omega} - \boldsymbol{\omega}_0) \approx 0$ is valid.

Applying time-scale separation and operating the partial derivatives, the incremental dynamic rotational equations are obtained as a function of the current angular accelerations and actuator positions:

$$\dot{\boldsymbol{\omega}} = \dot{\boldsymbol{\omega}}_0 + I^{-1} \nabla_{\boldsymbol{\delta}} \boldsymbol{\Phi}(\mathbf{x}_0, \boldsymbol{\delta}_0)\, \Delta\boldsymbol{\delta} \tag{47}$$

Setting the angular acceleration as a virtual control input $\boldsymbol{\nu}_\omega(\mathbf{x}) = \dot{\boldsymbol{\omega}}$ and solving for $\nabla_{\boldsymbol{\delta}} \boldsymbol{\Phi}(\mathbf{x}_0, \boldsymbol{\delta}_0)\, \Delta\boldsymbol{\delta}$, the INCA formulation in Eq. (18) is found for the angular rate control problem:

$$\nabla_{\boldsymbol{\delta}} \boldsymbol{\Phi}(\mathbf{x}_0, \boldsymbol{\delta}_0)\, \Delta\boldsymbol{\delta} = I \left[\boldsymbol{\nu}_\omega(\mathbf{x}) - \dot{\boldsymbol{\omega}}_0\right] = \Delta\boldsymbol{\tau}_c \tag{48}$$

where the pseudo-control input $\mathbf{d}_c$ corresponds to the required increments of control-induced moments $\Delta\boldsymbol{\tau}_c$. At this point, the required control-induced moment increments $\Delta\boldsymbol{\tau}_c$ are allocated into actuator position increments $\Delta\boldsymbol{\delta}$ by a linear control allocator, where the CA problem is formulated in incremental form as: given the current state $\mathbf{x}_0$, the current actuator positions $\boldsymbol{\delta}_0$ and a required increment of control-induced moments $\Delta\boldsymbol{\tau}_c$, determine an increment in the control effector positions $\Delta\boldsymbol{\delta}$ such that

$$\begin{gathered} \nabla_{\boldsymbol{\delta}} \boldsymbol{\Phi}(\mathbf{x}_0, \boldsymbol{\delta}_0)\, \Delta\boldsymbol{\delta} = \Delta\boldsymbol{\tau}_c \\ \text{subject to} \quad \underline{\boldsymbol{\Delta\delta}} \leq \boldsymbol{\Delta\delta} \leq \overline{\boldsymbol{\Delta\delta}} \end{gathered} \tag{49}$$

Here, the inner control law

$$\Delta\boldsymbol{\tau}_c = I \left[\boldsymbol{\nu}_\omega(\mathbf{x}) - \dot{\boldsymbol{\omega}}_0\right] \tag{50}$$

linearizes the system between the virtual control input $\boldsymbol{\nu}_\omega(\mathbf{x})$ and $\boldsymbol{\omega}$. The linearized system can now be controlled through the virtual control input such that it follows a command $\boldsymbol{\omega}_c$ by using the outer state-feedback linear control law in Eq. (40).

The absolute actuator position commands are computed as $\boldsymbol{\delta} = \boldsymbol{\delta}_0 + \Delta\boldsymbol{\delta}$. Note that the Jacobian matrix is also a function of the actuator positions, and therefore interactions between control effectors are considered in the control allocation process. Also, note that actual actuator position measurements $\boldsymbol{\delta}_0$ are fed back into the control system at each time step, and therefore the Jacobian matrix is always computed with the actual actuator positions. This also implies that the required increments $\Delta\boldsymbol{\delta}$ are always calculated over the actual actuator positions, avoiding couplings between control allocator and actuator dynamics typical of LCA-based control systems.[36]

VII.D. Preference Vector in Incremental Form

The INCA scheme requires a re-formulation of the preference vector used in the control allocation algorithms, since under the INCA formulation the preference vector refers to a preferred actuator position increment $\Delta\boldsymbol{\delta}_0$. If the preferred increment is set to $\Delta\boldsymbol{\delta}_p = 0$, the actuators are forced to remain at a constant, possibly nonzero position whenever it is possible. It has been observed that this can lead to complementary actuators (those producing moments of equal magnitude but opposite sign) diverging to asymmetric nonzero deflections while still producing a resultant moment of zero. To avoid this situation and minimize the control effort, the control effectors must be driven to their preferred position whenever it is possible. Thus, the preferred position increment in each time step must be the increment that brings the actuators closest to their preferred positions. This is achieved by calculating the incremental preference vector $\Delta\boldsymbol{\delta}_p$ at each time step as

$$\Delta\boldsymbol{\delta}_p = \min\left(\left|\boldsymbol{\delta}_p - \boldsymbol{\delta}_0\right|,\ \left|\overline{\boldsymbol{\Delta\delta}}\right|,\ \left|\underline{\boldsymbol{\Delta\delta}}\right|\right) \cdot \operatorname{sign}\left(\boldsymbol{\delta}_p - \boldsymbol{\delta}_0\right) \tag{51}$$

---

[b] Practical implementation of incremental attitude control in fast-dynamics aerospace vehicles has proven that FCC frequencies of about 100 Hz are high enough for the time-scale separation principle to hold.[32]

VII.E. Global Convergence and SSDs

Since INCA dynamically drives the actuator vector towards the direction that best fulfills local moment increment commands, it is possible that it converges to local optima. This is not a problem if it is valid to assume that the optimal control distribution lies within the neighbourhood of the current actuator positions. This assumption is valid for most of the ICE actuators, since their moment curves do not have local minima in the directions of $\boldsymbol{\delta}$ (local minima in the directions of α, β and M are irrelevant to the control allocator, since they are not control variables). However, the SSDs have a dramatic impact on the control effectiveness of trailing-edge control effectors, and therefore globally optimal control distributions might be available far away from the current control distribution.

It is worth noting that, besides providing lateral-directional control at high AoA, an important function of the SSDs is to redirect the airflow towards the upper wing skin at high AoA to recover control effectiveness of trailing-edge devices. In contrast, deflecting the SSDs at low AoA destroys the control effectiveness of downstream actuators. Therefore, it is reasonable to assume that globally optimal control distributions will have small SSD deflections at low AoA and big deflections at high AoA. Hence, convergence towards global optima can be subserved by forcing the SSDs to remain as closed as possible at low AoA, and as open as possible at high AoA. This can be achieved by scheduling the penalizing weights of the SSDs in the weighting matrix $W_{\mathbf{u}}$ as a function of α. In this case, the SSD penalties $W_{\mathbf{u}_{\mathrm{SSD}}}(\alpha)$ were scheduled as the exponential function

$$W_{\mathbf{u}_{\mathrm{SSD}}}(\alpha) = \left[-0.25 + 0.35 \exp\left(1.6\alpha\right)\right]^{-1} \tag{52}$$

Whereas penalties are set to 1 for all control effectors, $W_{\mathbf{u}_{\mathrm{SSD}}}$ is 10 for $\alpha = 0$ deg, becomes 1 at $\alpha \approx 45$ deg and goes to 0 at $\alpha \geq 90$ deg. Although this scheduling is valid for the ICE configuration, the characteristics of each particular controlled system shall be studied in order to favour global convergence.

VIII. Saturation Handling: Pseudo-Control Hedging

Actuator saturation represents a problem when control commands exceed the capabilities of the actuators under rate and position constraints. When physically unachievable control commands are given, the system can run into command windup problems, which compromises the overall performance and stability of the system. To overcome this problem, pseudo-control hedging (PCH) was proposed[58] and developed[59,60] as an adaptation system to hedge the pseudo-control input of the control system to accommodate the commands to the limitations of the actuators set, thus avoiding physically unachievable commands. PCH has been successfully used as a partial form of flight envelope protection and anti-windup system in Refs. 31, 61. In addition to ensuring physically achievable commands, the first-order reference model used in PCH is useful to compute the derivatives of the commanded variables, which can be used as feedforward terms in the control system to improve tracking performance.[31]

PCH was implemented in the designed ICE flight control systems to shape the virtual control command $\boldsymbol{\nu}_\omega(\mathbf{x})$ by substracting the difference between the commanded $\boldsymbol{\nu}_\omega(\mathbf{x})$ and the actual virtual control achieved, estimated with measured actuator positions $\boldsymbol{\delta}_0$ as $\hat{\boldsymbol{\nu}}_\omega(\mathbf{x}) = \mathbf{f}(\mathbf{x}_0, \boldsymbol{\delta}_0)$, where $\mathbf{f}(\mathbf{x}, \boldsymbol{\delta})$ is the virtual control law. The pseudo-control hedge is computed as

$$\boldsymbol{\nu}_h(\mathbf{x}) = \boldsymbol{\nu}_\omega(\mathbf{x}) - \hat{\boldsymbol{\nu}}_\omega(\mathbf{x}) \tag{53}$$

The hedge $\boldsymbol{\nu}_h(\mathbf{x})$ is fed back into a first-order reference model (RM) as a compensation signal. The reference model $\boldsymbol{\nu}_{\mathrm{rm}}(\mathbf{x})$ is given by

$$\boldsymbol{\nu}_{\mathrm{rm}}(\mathbf{x}) = K_{\mathrm{rm}} \left(\boldsymbol{\omega}_c - \boldsymbol{\omega}_{\mathrm{rm}}\right) \tag{54}$$

with K_{rm} a diagonal matrix. The hedged reference signal fed as a control input into the attitude control system is the state vector of the reference model

$$\boldsymbol{\omega}_{\mathrm{rm}} = \frac{1}{s} \left(\boldsymbol{\nu}_{\mathrm{rm}}(\mathbf{x}) - \boldsymbol{\nu}_h(\mathbf{x})\right) \tag{55}$$

When no saturation occurs, $\boldsymbol{\nu}_h(\mathbf{x}) = 0$ and the reference model behaves as a low-pass filter of bandwidth K_{rm_i} for the i-th component of $\boldsymbol{\omega}_{\mathrm{rm}}$. Under actuator saturation, the pseudo-control hedge $\boldsymbol{\nu}_h(\mathbf{x})$ corresponds to the difference between the commanded virtual control input and the estimated virtual control achieved, based on the actual positions of the control effectors. The hedge signal $\boldsymbol{\nu}_h(\mathbf{x})$ is used to reshape the reference

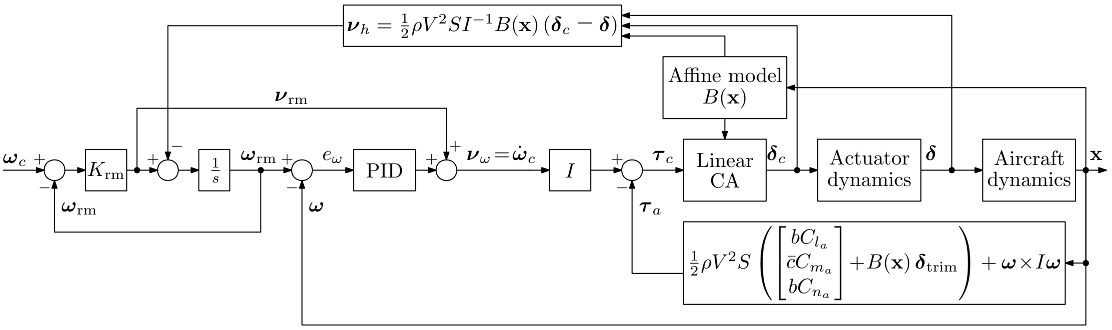

Figure 8. Schematic of the LCA-based angular rate control system with PCH.

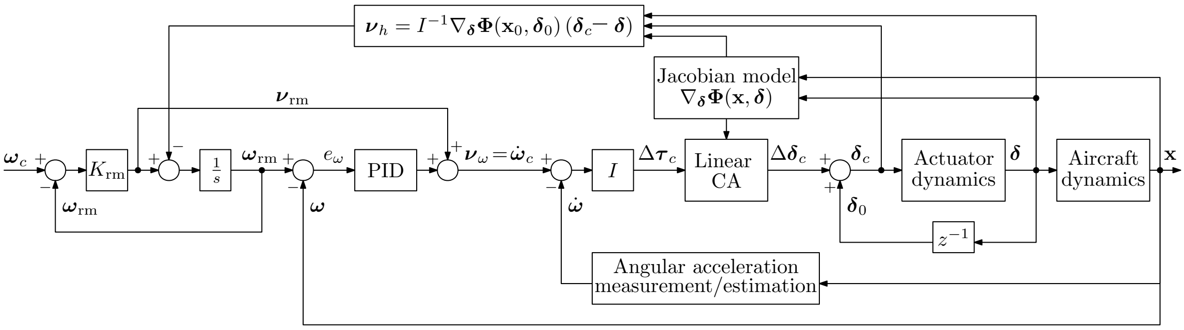

Figure 9. Schematic of the INCA-based angular rate control system with PCH.

and avoid unfeasible commands. The reference model $\boldsymbol{\nu}_{\mathrm{rm}}(\mathbf{x})$ corresponds to the first-order derivatives of the commanded variables, which can be used as a feedforward term added to $\boldsymbol{\nu}_\omega(\mathbf{x})$ to improve tracking performance.[31]

For the LCA-based controller the virtual control input is given by the control law

$$\boldsymbol{\nu}_\omega(\mathbf{x}) = \frac{1}{2}\rho V^2 S I^{-1} B(\mathbf{x})\,\boldsymbol{\delta} + I^{-1}\left(\boldsymbol{\tau}_a - \boldsymbol{\omega} \times I\boldsymbol{\omega}\right) \tag{56}$$

and therefore the pseudo-control hedge is given by

$$\boldsymbol{\nu}_{h_{\mathrm{LCA}}}(\mathbf{x}) = \left[\frac{1}{2}\rho V^2 S I^{-1} B(\mathbf{x})\,\boldsymbol{\delta}_c + I^{-1}\left(\boldsymbol{\tau}_a - \boldsymbol{\omega} \times I\boldsymbol{\omega}\right)\right] - \left[\frac{1}{2}\rho V^2 S I^{-1} B(\mathbf{x})\,\boldsymbol{\delta} + I^{-1}\left(\boldsymbol{\tau}_a - \boldsymbol{\omega} \times I\boldsymbol{\omega}\right)\right] \tag{57}$$

$$\boldsymbol{\nu}_{h_{\mathrm{LCA}}}(\mathbf{x}) = \frac{1}{2}\rho V^2 S I^{-1} B(\mathbf{x})\,(\boldsymbol{\delta}_c - \boldsymbol{\delta}) \tag{58}$$

For the INCA-based controller the virtual control input is given by the control law

$$\boldsymbol{\nu}_\omega(\mathbf{x}) = \dot{\boldsymbol{\omega}}_0 + I^{-1}\nabla_{\boldsymbol{\delta}}\boldsymbol{\Phi}(\mathbf{x}_0, \boldsymbol{\delta}_0)\,(\boldsymbol{\delta} - \boldsymbol{\delta}_0) \tag{59}$$

and therefore the pseudo-control hedge is given by

$$\boldsymbol{\nu}_{h_{\mathrm{INCA}}}(\mathbf{x}) = \left[\dot{\boldsymbol{\omega}}_0 + I^{-1}\nabla_{\boldsymbol{\delta}}\boldsymbol{\Phi}(\mathbf{x}_0, \boldsymbol{\delta}_0)\,(\boldsymbol{\delta}_c - \boldsymbol{\delta}_0)\right] - \left[\dot{\boldsymbol{\omega}}_0 + I^{-1}\nabla_{\boldsymbol{\delta}}\boldsymbol{\Phi}(\mathbf{x}_0, \boldsymbol{\delta}_0)\,(\boldsymbol{\delta} - \boldsymbol{\delta}_0)\right] \tag{60}$$

$$\boldsymbol{\nu}_{h_{\mathrm{INCA}}}(\mathbf{x}) = I^{-1}\nabla_{\boldsymbol{\delta}}\boldsymbol{\Phi}(\mathbf{x}_0, \boldsymbol{\delta}_0)\,(\boldsymbol{\delta}_c - \boldsymbol{\delta}) \tag{61}$$

The internal structures of the LCA-based and the INCA-based angular rate control systems, including PCH, are given in Figures 8 and 9 respectively.

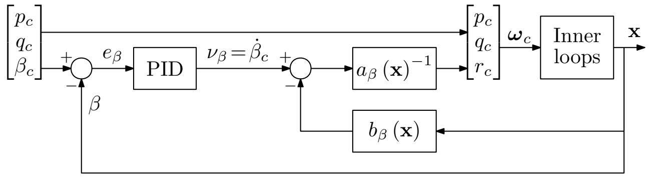

Figure 10. Schematic of the outer sideslip dynamic inversion loop.

IX. Sideslip Dynamic Inversion Outer Loop

In order to compensate sideslip angle to perform coordinated turns, a sideslip control outer loop was implemented in the yaw rate channel with β as a reference and r as control input. For this, a dynamic inversion of the sideslip angle was performed. The sideslip angle β can be computed as

$$\beta = \arcsin \frac{v}{V} \tag{62}$$

where V is the true airspeed $V = \sqrt{u^2 + v^2 + w^2}$. The first derivative of Eq. (62) is

$$\dot{\beta} = \frac{\dot{v}V - v\dot{V}}{V\sqrt{u^2 + w^2}} = \frac{\dot{v}}{\sqrt{u^2 + w^2}} - \frac{v\left(u\dot{u} + v\dot{v} + w\dot{w}\right)}{\left(u^2 + v^2 + w^2\right)\sqrt{u^2 + w^2}} \tag{63}$$

The accelerations in aerodynamic frame are given by

$$\begin{aligned} \dot{u} &= A_x - g\sin\theta + rv - qw \\ \dot{v} &= A_y + g\sin\phi\cos\theta - ru + pw \\ \dot{w} &= A_z + g\cos\theta\cos\phi + qu - pv \end{aligned} \tag{64}$$

Substituting Eqs. (64) into (63) gives

$$\dot{\beta} = \left(\frac{1}{\sqrt{u^2 + w^2}}\right)\left(F_x + F_y + F_z\right) + \begin{bmatrix} \frac{w}{\sqrt{u^2 + w^2}} & 0 & \frac{-u}{\sqrt{u^2 + w^2}} \end{bmatrix} \begin{bmatrix} p \\ q \\ r \end{bmatrix} \tag{65}$$

with

$$\begin{aligned} F_x &= -\frac{uv}{V^2}\left(A_x - g\sin\theta\right) \\ F_y &= \left(1 - \frac{v}{V^2}\right)\left(A_y + g\sin\phi\cos\theta\right) \\ F_z &= -\frac{vw}{V^2}\left(A_z + g\cos\phi\cos\theta\right) \end{aligned} \tag{66}$$

Introducing the virtual control input $\boldsymbol{\nu}_\beta(\mathbf{x}) = \dot{\beta}$ and solving for the input r the sideslip loop dynamic inversion law is obtained:

$$r_c = \left(\frac{-u}{\sqrt{u^2 + w^2}}\right)^{-1}\left[\nu_\beta(\mathbf{x}) - \frac{1}{\sqrt{u^2 + w^2}}\left(F_x + F_y + F_z + wp_c\right)\right] = a_\beta(\mathbf{x})^{-1}\left[\nu_\beta(\mathbf{x}) - b_\beta(\mathbf{x})\right] \tag{67}$$

The structure of the outer beta loop is shown in Figure 10.

X. Simulations and Results

In order to assess the performance of INCA with respect to conventional LCA approaches, the previously described LCA- and INCA-based attitude control systems were set up in a simulation framework with Matlab and Simulink. Each control system was implemented with an RWPI solver and with a QP solver with the active set algorithm, in order to compare performance using two different linear solvers. The simulations were run in real time with a fixed sampling rate of 100 Hz.

The flight simulations were initialized in trim conditions at an altitude of 20000 ft and M=0.85. A linear auto-throttle (A/T) controller was added to the system to keep the true airspeed at 880 ft/sec. The gains used in the linear control loops are given in Table 2. The reference model gains K_{rm} were all set to 10. The control inputs were simultaneous 3211 signals with amplitudes of 10 deg/sec for the roll and pitch channels and 3 deg for the sideslip channel. 3211 inputs consist of two consecutive pulse doublets, the pulses of which have durations of 3, 2, 1 and 1 seconds. These inputs are known to excite a significant frequency range of the aircraft operational bandwidth.[62]

Table 2. Gains used in the linear controller loops.

	p	q	r	β
K_P	6.5	6.5	5.8	1.0
K_I	0.0	0.0	0.0	0.0
K_D	0.5	0.5	0.5	0.7

Table 3. Root mean square tracking error.

	RMS($\varepsilon_{\text{Track}}$)			
Solver	RWPI		QP	
CA Method	LCA	INCA	LCA	INCA
p [deg/sec]	6.01	4.27	5.65	2.69
q [deg/sec]	9.19	2.06	5.47	1.87
r [deg/sec]	4.36	1.81	2.77	1.80
Total	6.82	2.93	4.81	2.15

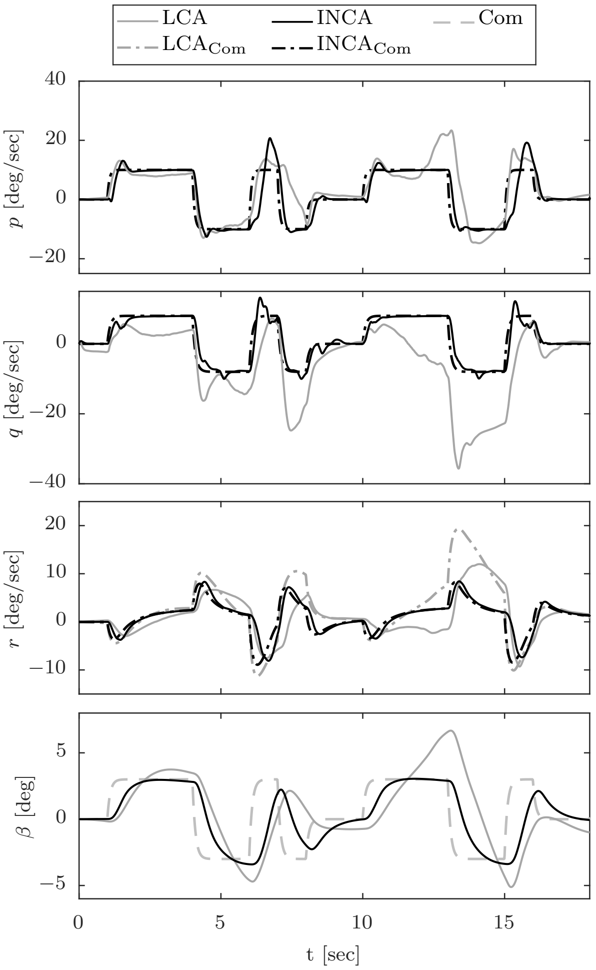

Figure 11. Body angular rates and sideslip angle tracking performance of LCA and INCA with RWPI.

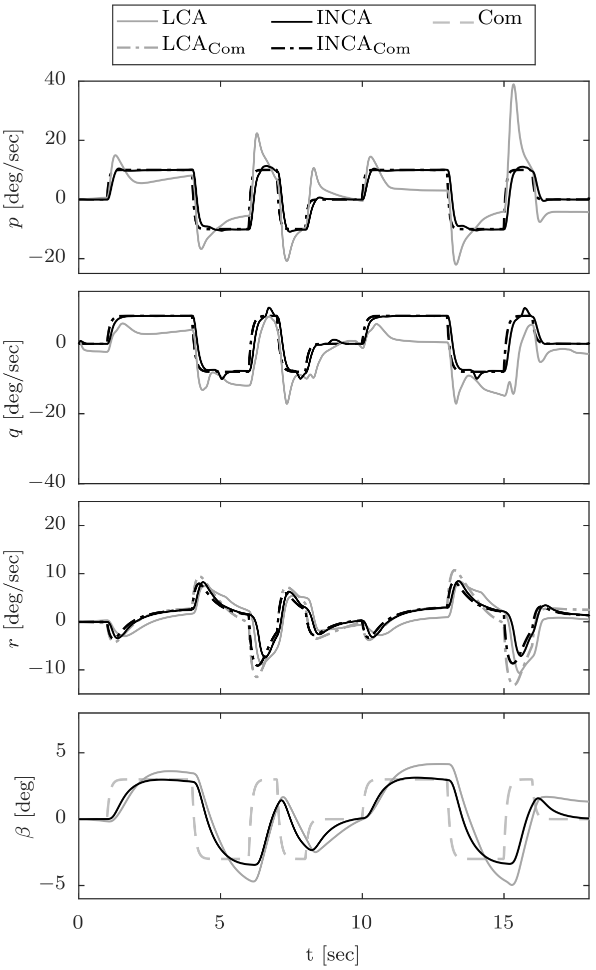

Figure 12. Body angular rates and sideslip angle tracking performance of LCA and INCA with QP.

The tracking histories of the controlled variables for LCA and INCA with RWPI and QP are displayed and compared in Figures 11 and 12 respectively. The deficiencies of LCA are evident in both cases, where large excursions occur from the commanded rates, in addition to overshoot and oscillation. This behaviour can be explained by the fact that several aerodynamic effects of the control effectors are neglected by the linear model, including nonlinearities, effector interactions and secondary-axis yawing moment contributions of the elevons and outboard LEF. These effects need to be compensated with other actuators, which in turn have nonlinear effects. This results in a dramatic degradation of tracking performance. In contrast, INCA performs with superior tracking accuracy, following all commands with slight overshoot for RWPI, and no significant inaccuracies for QP.

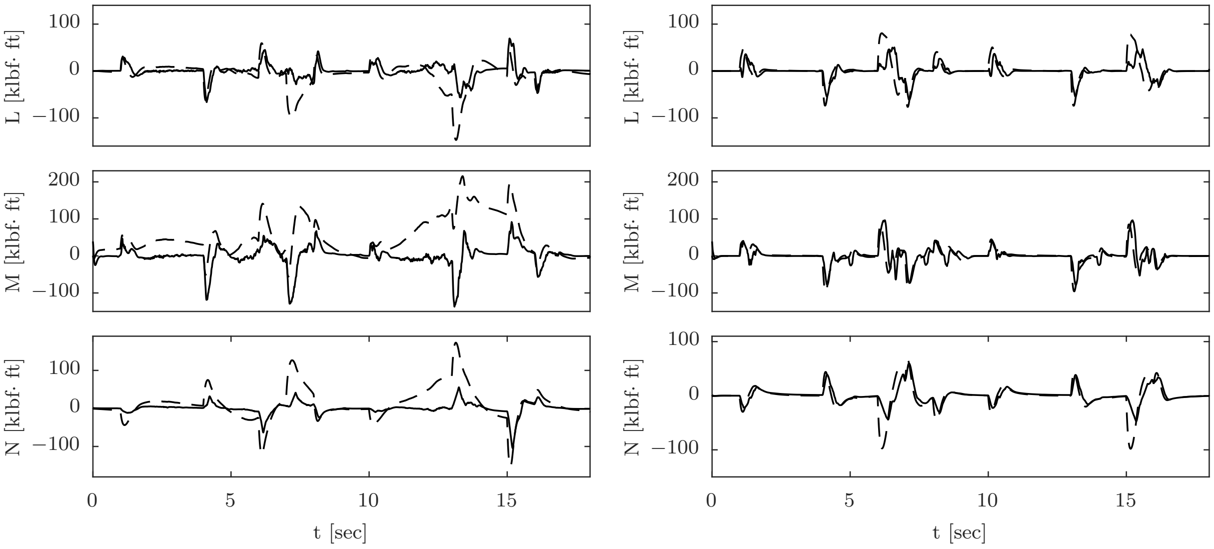

(a) LCA method.

(b) INCA method.

Figure 13. Commanded (dashed line) and attained (solid line) moments using the RWPI solver.

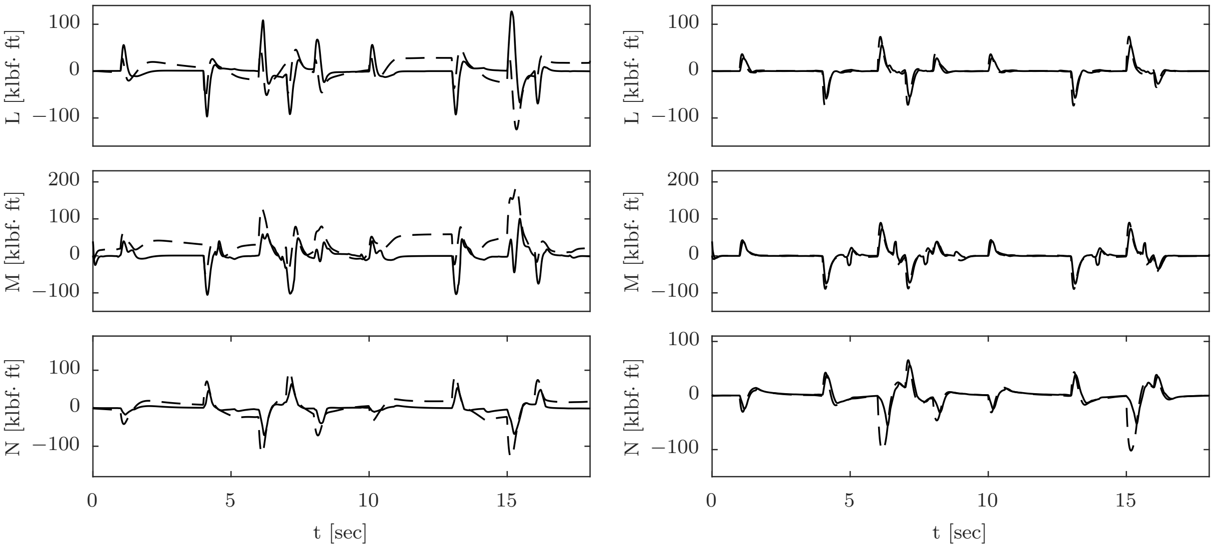

(a) LCA method.

(b) INCA method.

Figure 14. Commanded (dashed line) and attained (solid line) moments using the QP solver.

Table 4. Root mean square allocation error.

	RMS($\varepsilon_{\text{Alloc}}$)			
Solver	RWPI		QP	
CA Method	LCA	INCA	LCA	INCA
L [klbf·ft]	25.0	17.8	31.1	7.35
M [klbf·ft]	72.6	16.7	44.9	10.4
N [klbf·ft]	35.4	14.4	20.3	14.7
Total	48.8	16.4	33.6	11.2

Table 5. Number of iterations per time step.

	n_i			
Solver	RWPI		QP	
CA Method	LCA	INCA	LCA	INCA
Min.	2	1	2	3
Avg.	3.1	2.4	5.8	5.6
Max.	7	6	23	20

The root mean square (RMS) of the tracking errors, defined as $\varepsilon_{\text{Track}} = (\boldsymbol{\omega} - \boldsymbol{\omega}_c)$ and $\varepsilon_{\text{Track}} = (\beta - \beta_c)$ are given in Table 3 for each controller. The tracking error is substantially reduced with INCA by a factor of about 2.3 for both RWPI and QP. It is worth pointing out that the tracking performance with the QP solver is notably better than with RWPI for both LCA and INCA systems. This is consistent with previous research[10, 28, 52] which concluded that, despite its simplicity, the RWPI method may yield suboptimal solutions and does not guarantee convergence to a feasible solution, even if it exists.

A key performance metric to be considered is control allocation performance, which measures the ability of a control allocation system to successfully attain the commanded moments with the available set of control effectors. The commanded an attained moments for LCA and INCA using RWPI and QP are given in Figures 13 and 14 respectively. The RMS of the control allocation errors, defined as $\varepsilon_{\text{Alloc}} = (\boldsymbol{\tau} - \boldsymbol{\tau}_c)$, are given in Table 4. Large excursions in commanded moments are observed for LCA in all channels. Again, these are due to the necessity of compensating for inaccuracies in the linear control effector model. In contrast, the

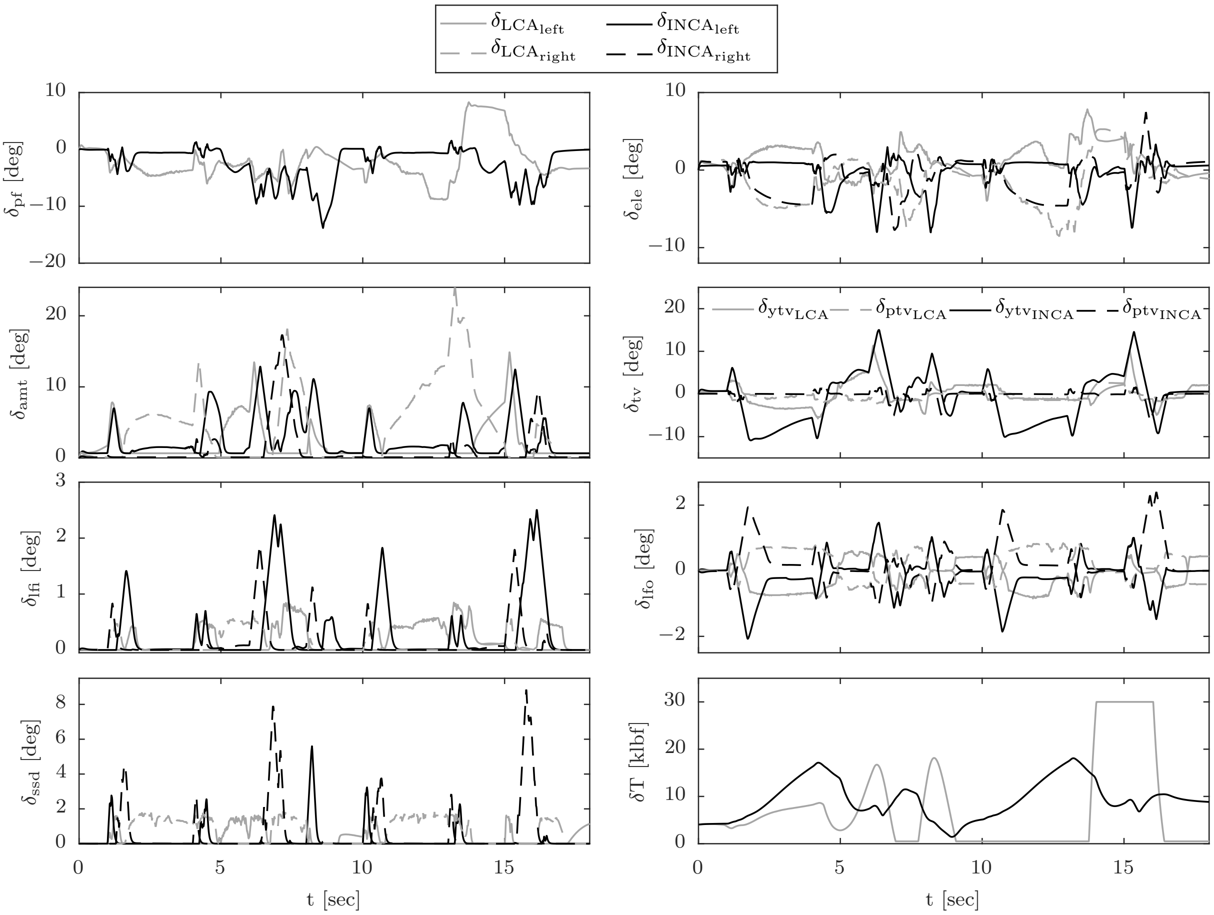

Figure 15. Control effector positions with LCA and INCA solved with RWPI.

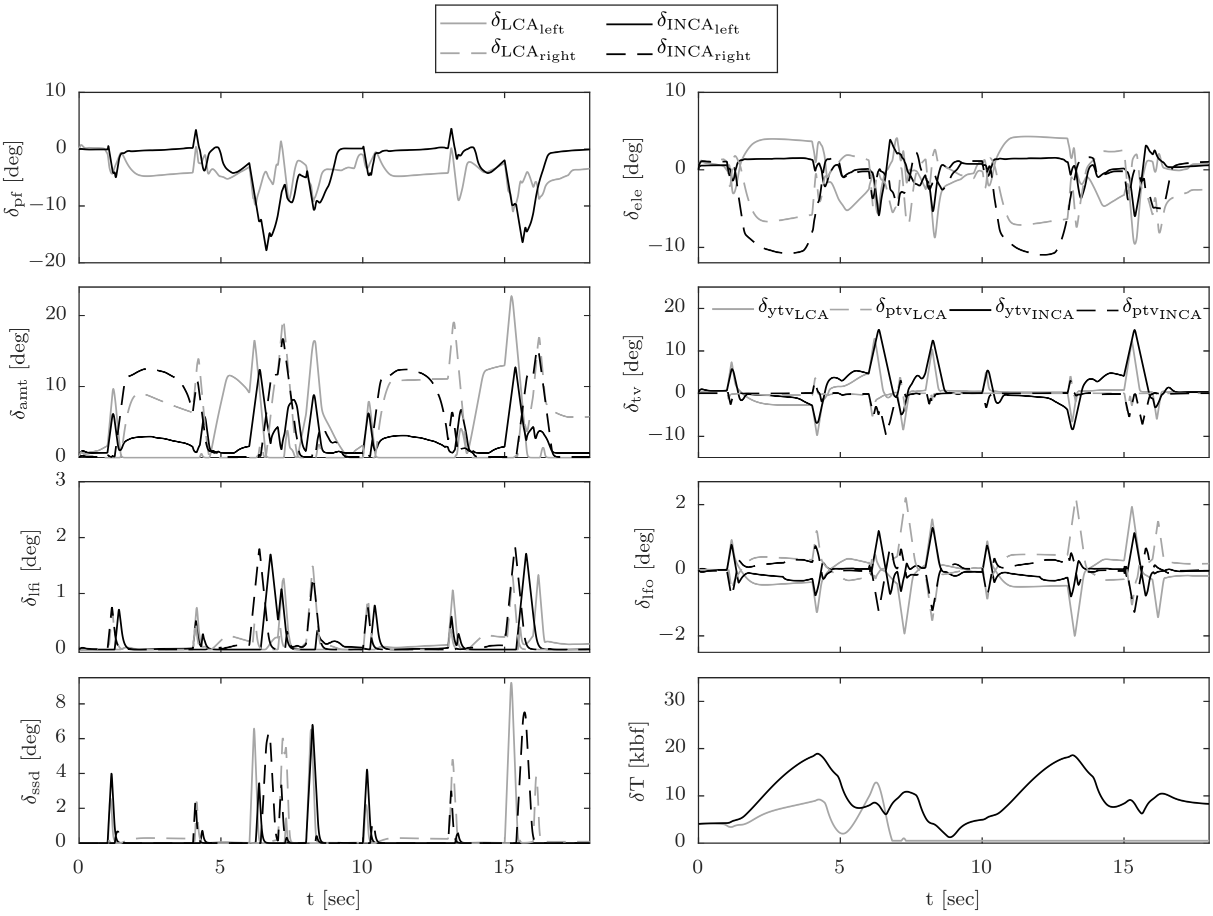

Figure 16. Control effector positions with LCA and INCA solved with QP.

Table 6. Control effort.

	Ceff = RMS $(\delta - \delta_p)$													
	Total	δ_{lfi}	δ_{lfo}	δ_{la}	δ_{le}	δ_{ls}	δ_{pf}	δ_{rfi}	δ_{rfo}	δ_{ra}	δ_{re}	δ_{rs}	δ_{ptv}	δ_{ytv}
LCA/RWPI	2.8	0.3	0.5	3.4	2.3	0.5	4.1	0.2	0.5	6.7	3.3	1.0	1.1	2.7
INCA/RWPI	2.6	0.7	0.6	3.8	2.0	0.7	3.9	0.3	0.6	3.1	2.5	1.6	1.0	6.0
LCA/QP	3.3	0.2	0.5	6.0	3.1	1.2	4.5	0.2	0.5	6.9	4.0	0.8	0.7	3.0
INCA/QP	3.4	0.3	0.3	3.5	1.5	0.8	5.1	0.3	0.3	7.2	5.5	1.2	1.6	4.2

control moment commands with INCA are short and small, with high allocation performance. The control allocation performance metrics in Table 4 show that INCA has a dramatic improvement in control allocation performance with respect to LCA by a factor of 3 with both RWPI and QP.

The time histories of the control effector deflections are shown for RWPI and QP in Figures 15 and 16 respectively. In the RWPI case in Figure 15, severe oscillations of the control effectors with lateral-directional control authority are observed with LCA. This behaviour is most likely due to the strong interference of the SSD on the rest of effectors, which is neglected by the LCA-based control system. Note, however, that these couplings are not observed with INCA, since the Jacobian model captures these interactions. The large excursions with LCA can be explained as a consequence of compensating the unexpected interaction effects of the SSD. LCA places relatively large control effort on the AMTs, since it lacks information about other sources of directional control power such as the elevons and outboard LEF due to the assumption of linearity. As can be observed in Figure 16, the QP solver alleviates the problems regarding oscillations observed with LCA/RWPI.

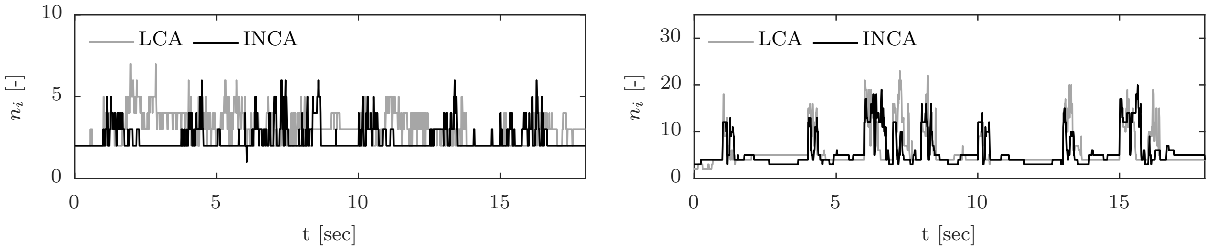

(a) RWPI solver.

(b) QP solver.

Figure 17. Number of iterations per time step with LCA and INCA.

The control efforts, defined as Ceff = RMS $(\boldsymbol{\delta} - \boldsymbol{\delta}_p)$ are listed in Table 6 for each individual actuator and for the whole set of actuators. Note that INCA makes more extensive use of MTV for yaw control than LCA. Since the on-board model of INCA captures parabolic yawing moments, it makes sense that it prioritizes the use of uncoupled control effectors for pitch control to minimize secondary-axis yawing contributions. In spite of the differences of the distributions of control effort, with no remarkable particularities, it is observed that both systems use a similar amount of control effort in total. An important conclusion is that, for the trajectory under study, INCA achieves a substantial improvement in tracking and control allocation performance with no significant increase of control effort.

Finally, as stated above, computational efficiency is an important concern regarding control allocation methods, since these need to run in real time on FCCs at typical rates in the order of 100 Hz. Performance and computational requirements for real time implementation of the RWPI and QP solvers were evaluated in Refs. 10 and 52. In both cases, the authors concluded that RWPI and QP solved with the active set algorithm are well-suited for real-time control allocation in flight control systems. Therefore, further analysis on computational complexity is not required here. However, it is interesting to demonstrate that INCA does not imply an increase in computational load with respect to conventional LCA-based controllers. The number of iterations per time step executed with RWPI and QP are compared for LCA and INCA in Figure 17. Average, minimum and maximum number of iterations are listed in Table 5. In the case of RWPI, the maximum possible number of iterations corresponds to the number of available control effectors, in this case 13. Note that INCA requires slightly less iterations to converge than LCA in average, and the maximum number of iterations does not surpass 7 in neither case. For QP, the maximum number of iterations was set to 100. In this case, INCA and LCA required a similar number iterations in average to converge. The maximum number of iterations in these simulations remains below 25 in both cases. This shows that the computational load when using RWPI and QP with the active set algorithm is similar with LCA and INCA for the considered trajectory.

XI. Conclusions and Final Remarks

Conventional linear control allocation (LCA) methods are unable to provide satisfactory performance in advanced and unconventional control effector configurations due to the impossibility of linear effector models to capture nonlinearities and interactions between control effectors. In this paper, an incremental nonlinear control allocation (INCA) approach is implemented to overcome these issues. The INCA method operates in an incremental scheme based on a Jacobian model of the control effectiveness of the actuators. This way of operation enables the consideration of nonlinear control moment curves such as secondary-axis yawing moments and nonlinear interactions between control effectors. The incremental reformulation of the problem enables the use of simple and computationally efficient linear control allocation solvers, enabling the use of INCA in real-time flight control systems. In addition, INCA dynamically drives the actuators towards their optimal positions and is based on real-time actuator position measurements, mitigating coupling effects between the control allocator and actuator dynamics. Moreover, it uses angular acceleration measurements to reduce its model dependency, improving robustness against aerodynamic uncertainties.

The performance of INCA was assessed against conventional LCA methods by designing two flight control systems based on LCA and INCA for the Innovative Control Effectors (ICE) aircraft, a highly maneuverable tailless aircraft with 13 highly nonlinear, interacting and axis-coupled control effectors. Both control allocation solvers were implemented with two typical control allocation methods. Real-time simulation results showed that INCA dramatically improves tracking and control allocation performance for the ICE aircraft, whereas substantially reducing the control effort.

Future work will focus on the development of outer guidance loops to test the LCA- and INCA-based control systems in extreme flight maneuvers such as loopings, high bank angle turns, high AoA commands or barrel rolls. In addition, flight envelope protection will be included in the control system. It is also of great interest to upgrade the systems for fault-tolerant flight control with on-line system identification. INCA is expected to provide substantial benefits in terms of recoverability in fault conditions. Finally, sensitivity of the INCA allocation performance to Jacobian model uncertainties will be further investigated.

References

[1] Oppenheimer, M. W., Doman, D. B., and Bolender, M. A., "Control Allocation for Over-Actuated Systems," *2006 14th Mediterranean Conference of Control and Automation*, IEEE, 2006.

[2] Oppenheimer, M. W., Doman, D. B., and Bolender, M. A., "Control Allocation," *The Control Handbook: Control System Applications*, edited by L. S. Levine, chap. 8, 2nd ed., 2010.

[3] Buffington, J. M. and Enns, D. F., "Lyapunov stability analysis of daisy chain control allocation," *Journal of Guidance, Control, and Dynamics*, Vol. 19, No. 6, 1996, pp. 1226–1230.

[4] Durham, W. C., "Constrained Control Allocation," *Journal of Guidance, Control, and Dynamics*, Vol. 16, No. 4, 1993, pp. 717–725.

[5] Durham, W. C., "Constrained Control Allocation: Three Moment Problem," *Journal of Guidance, Control, and Dynamics*, Vol. 17, No. 2, 1994, pp. 330–336.

[6] Durham, W. C., "Attainable Moments for the Constrained Control Allocation Problem," *Journal of Guidance, Control, and Dynamics*, Vol. 17, No. 6, 1994, pp. 1371–1373.

[7] Durham, W. C., "Efficient, Near-Optimal Control Allocation," *Journal of Guidance, Control, and Dynamics*, Vol. 22, No. 2, 1999, pp. 369–372.

[8] Durham, W. C., "Computationally Efficient Control Allocation," *Journal of Guidance, Control, and Dynamics*, Vol. 24, No. 3, 2001, pp. 519–524.

[9] Bordignon, K., *Constrained Control Allocation for Systems with Redundant Control Effectors*, Phd thesis, Virginia Polytechnic Institute and State University, 1996.

[10] Bodson, M., "Evaluation of Optimization Methods for Control Allocation," *Journal of Guidance, Control, and Dynamics*, Vol. 25, No. 4, 2002, pp. 703–711.

[11] Paradiso, J., "A Highly Adaptable Method of Managing Jets and Aerosurfaces for Control of Aerospace Vehicles," *Proceedings of the 1989 Guidance, Navigation and Control Conference*, 1989, pp. 35–44.

[12] Paradiso, J., "Adaptable Method of Managing Jets and Aerosurfaces for Aerospace Vehicle Control," *Journal of Guidance Control and Dynamics*, Vol. 14, No. 1, 1991, pp. 44–50.

[13] Enns, D., "Control allocation approaches," *Guidance, Navigation, and Control Conference and Exhibit*, 1998, pp. 98–108.

[14] Buffington, J. M., "Modular Control Law Design for the Innovative Control Aircraft Effectors (ICE) Tailless Fighter Configuration," Tech. rep., 1999.

[15] Oppenheimer, M. W. and Doman, D. B., "A Method for Including Control Effector Interactions in the Control Allocation Problem," *Proceedings of the AIAA Guidance, Navigation, and Control Conference and Exhibit*, No. August, Hilton Head, South Carolina, 2007.

[16] Doman, D. B. and Sparks, A. G., "Concepts for Constrained Control Allocation of Mixed Quadratic and Linear Effectors," *Proceedings of the American Control Conference*, Anchorage, AK, 2002, pp. 3729–3734.

[17] Bolender, M. A. and Doman, D. B., "Nonlinear Control Allocation Using Piecewise Linear Functions," *Journal of Guidance, Control, and Dynamics*, Vol. 27, No. 6, 2004, pp. 1017–1027.

[18] Bolender, M. A. and Doman, D. B., "Method for Determination of Nonlinear Attainable Moment Sets," *Journal of Guidance, Control, and Dynamics*, Vol. 27, No. 5, 2004, pp. 907–914.

[19] Doman, D. B. and Oppenheimer, M., "Improving Control Allocation Accuracy for Nonlinear Aircraft Dynamics," *AIAA Guidance, Navigation, and Control Conference and Exhibit*, Monterey, California, 2002.

[20] Poonamallee, V. L., Yurkovich, S., Serrani, A., Doman, D. B., and Oppenheimer, M. W., "A Nonlinear Programming Approach for Control Allocation," *American Control Conference*, Boston, Massachusetts, 2004, pp. 1689–1694.

[21] Tol, H. J., De Visser, C. C., Van Kampen, E., and Chu, Q. P., "Nonlinear Multivariate Spline-Based Control Allocation for High-Performance Aircraft," *Journal of Guidance, Control, and Dynamics*, Vol. 37, No. 6, 2014, pp. 1840–1862.

[22] Harkegard, O., "Dynamic Control Allocation Using Constrained Quadratic Programming," *Journal of Guidance Control and Dynamics*, Vol. 27, No. 6, 2004, pp. 1028–1034.

[23] Luo, Y., Serrani, A., Yurkovich, S., Doman, D. B., and Oppenheimer, M. W., "Model Predictive Dynamic Control Allocation with Actuator Dynamics," *American Control Conference*, Boston, Massachusetts, 2004, pp. 1695 –1700.

[24] Luo, Y., Serrani, A., Yurkovich, S., Oppenheimer, M. W., and Doman, D. B., "Model-Predictive Dynamic Control Allocation Scheme for Reentry Vehicles," *Journal of Guidance, Control, and Dynamics*, Vol. 30, No. 1, 2007, pp. 100–113.

[25] Hanger, M. B., *Model Predictive Control Allocation*, Phd thesis, Norwegian University of Science and Technology, 2011.

[26] Johansen, T. A., "Optimizing Nonlinear Control Allocation," *43rd IEEE Conference on Decision and Control*, 2004, pp. 3435–3440.

[27] Niestroy, M. A., Dorsett, K. M., and Markstein, K., "A Tailless Fighter Aircraft Model for Control-Related Research and Development," *AIAA Modeling and Simulation Technologies Conference*, 2017.

[28] Johansen, T. A. and Fossen, T. I., "Control allocation - A survey," *Automatica*, Vol. 49, No. 5, 2013, pp. 1087–1103.

[29] Ostroff, A. J. and Bacon, B. J., "Enhanced NDI Strategies for Reconfigurable Flight Control," *American Control Conference*, 2002, pp. 3631–3636.

[30] Sieberling, S., Chu, Q. P., and Mulder, J. a., "Robust Flight Control Using Incremental Nonlinear Dynamic Inversion and Angular Acceleration Prediction," *Journal of Guidance, Control, and Dynamics*, Vol. 33, No. 6, 2010, pp. 1732–1742.

[31] Simplício, P., Pavel, M. D., van Kampen, E., and Chu, Q. P., "An Acceleration Measurements-Based Approach for Helicopter Nonlinear Flight Control Using Incremental Nonlinear Dynamic Inversion," *Control Engineering Practice*, Vol. 21, No. 8, 2013, pp. 1065–1077.

[32] Smeur, E. J. J., Chu, Q. P., and de Croon, G. C. H. E., "Adaptive Incremental Nonlinear Dynamic Inversion for Attitude Control of Micro Aerial Vehicles," *Journal of Guidance, Control, and Dynamics*, Vol. 39, No. 3, 2016, pp. 450–461.

[33] Doman, D. B. and Ngo, A. D., "Dynamic Inversion-Based Adaptive/Reconfigurable Control of the X-33 on Ascent," *Journal of Guidance, Control, and Dynamics*, Vol. 25, No. 2, 2002, pp. 275–284.

[34] da Costa, R. R., Chu, Q. P., and Mulder, J. a., "Reentry Flight Controller Design Using Nonlinear Dynamic Inversion," *Journal of Spacecraft and Rockets*, Vol. 40, No. 1, 2003, pp. 64–71.

[35] Tol, H. J., de Visser, C. C., Sun, L. G., van Kampen, E., and Chu, Q. P., "Multivariate Spline-Based Adaptive Control of High-Performance Aircraft with Aerodynamic Uncertainties," *Journal of Guidance, Control, and Dynamics*, Vol. 39, No. 4, 2016, pp. 781–800.

[36] Oppenheimer, M. W. and Doman, D. B., "Methods for Compensating for Control Allocator and Actuator Interactions," *Journal of Guidance, Control, and Dynamics*, Vol. 27, No. 5, 2004, pp. 922–927.

[37] Bowlus, J., Multhopp, D., and Banda, S., "Challenges and Opportunities in Tailless Aircraft Stability and Control," *Guidance, Navigation, and Control Conference*, 1997, pp. 1713–1718.

[38] Dorsett, K. M. and Mehl, D. R., "Innovative Control Effectors (ICE) Phase I," Tech. rep., Lockheed Martin Tactical Aircraft Systems, 1996.

[39] Dorsett, K. M., Fears, S. P., and Houlden, H. P., "Innovative Control Effectors (ICE) Phase II," Tech. rep., 1997.

[40] Buffington, J. M., "Tailless aircraft control allocation," *AIAA Guidance, Navigation, and Control Conference*, 1997, pp. 737–747.

[41] Ngo, A. D., Reigelsperger, W., Banda, S., and Bessolo, J., "Multivariable Control Law Design for a Tailless Airplane," *AIAA Guidance, Navigation and Control Conference*, San Diego, CA, 1996.

[42] Gillard, W. J. and Dorsett, K. M., "Directional Control for Tailless Aircraft Using All Moving Wing Tips," *22nd Atmospheric Flight Mechanics Conference*, 1997, pp. 51–58.

[43] Eberhardt, R. and Ward, D., "Indirect Adaptive Flight Control of a Tailless Fighter Aircraft," *Guidance, Navigation, and Control Conference and Exhibit*, 1999, pp. 466–476.

[44] Shtessel, Y., Buffington, J., and Banda, S., "Tailless Aircraft Flight Control Using Multiple Time Scale Reconfigurable Sliding Modes," *IEEE Transactions on Control Systems Technology*, Vol. 10, No. 2, 2002, pp. 288–296.

[45] Lewis, F. L. and Syrmos, V. L., *Optimal Control*, John Wiley & Sons, Inc., New York, NY, 1995.

[46] Davidson, J. B., Lallman, F. J., and Bundick, W. T., "Integrated reconfigurable control allocation," *AIAA Guidance, Navigation and Control Conference and Exhibit*, Montreal, Canada, 2001.

[47] Davidson, J. B., Lallman, F. J., and Bundick, W. T., "Real-Time Adaptive Control Allocation applied to a High Performance Aircraft," *5-th SIAM Conference on Control & Its Applications*, 2001.

[48] Alwi, H. and Edwards, C., "Sliding Mode FTC With On-line Control Allocation," *Proceedings of the 45th IEEE Conference on Decision and Control*, San Diego, CA, 2006, pp. 5579–5584.

[49] Lombaerts, T. J. J., Looye, G. H. N., Chu, Q. P., and Mulder, J. A., "Design and simulation of fault tolerant flight control based on a physical approach," *Aerospace Science and Technology*, Vol. 23, No. 1, 2012, pp. 151–171.

[50] Burken, J. J., Lu, P., and Wu, Z. L., "Reconfigurable flight control designs with application to the X-33 vehicle," *AIAA Guidance, Navigation, and Control Conference*, 1999, pp. 951–965.

[51] Burken, J. J., Lu, P., Wu, Z., and Bahm, C., "Two Reconfigurable Flight-Control Design Methods: Robust Servomechanism and Control Allocation," *Journal of Guidance, Control, and Dynamics*, Vol. 24, No. 3, 2001, pp. 482–493.

[52] Harkegard, O., "Efficient Active Set Algorithms for Solving Constrained Least Squares Problems in Aircraft Control Allocation," *41st IEEE Conference on Decision and Control*, 2002, pp. 1295–1300.

[53] Petersen, J. A. M. and Bodson, M., "Interior-Point Algorithms for Control Allocation," *Journal of Guidance, Control, and Dynamics*, Vol. 28, No. 3, 2005, pp. 471–480.

[54] Petersen, J. A. M. and Bodson, M., "Constrained Quadratic Programming Techniques for Control Allocation," *Ieee Transactions on Control Systems Technology*, Vol. 14, No. 1, 2006, pp. 91–98.

[55] van der Peijl, I., de Visser, C., and Niestroy, M. A., "Physical Splines for Aerodynamic Modelling of Innovative Control Effectors," *Unpublished MSc Thesis*, 2017.

[56] de Visser, C. C., Chu, Q. P., and Mulder, J. A., "A New Approach to Linear Regression with Multivariate Splines," *Automatica*, Vol. 45, No. 12, 2009, pp. 2903–2909.

[57] Tol, H. J., de Visser, C. C., and Kotsonis, M., "Model Reduction of Parabolic PDEs Using Multivariate Splines," *International Journal of Control*, 2016.

[58] Johnson, E. N. and Calise, A. J., "Pseudo-Control Hedging : a New Method for Adaptive Control," *Advances in Navigation Guidance and Control Technology Workshop*, 2000.

[59] Johnson, E. N. and Kannan, S. K., "Adaptive Trajectory Control for Autonomous Helicopters," *Journal of Guidance, Control, and Dynamics*, Vol. 28, No. 3, 2005, pp. 524–538.

[60] Lam, Q. and Barkana, I., "Direct Adaptive Control Treatment to Flight Control Input Saturation," *AIAA Guidance, Navigation, and Control Conference and Exhibit*, 2005.

[61] Lombaerts, T., Looye, G., Chu, Q., and Mulder, J., "Pseudo Control Hedging and its Application for Safe Flight Envelope Protection," *AIAA Guidance, Navigation, and Control Conference*, 2010.

[62] Mulder, J. A., "Design and evaluation of dynamic flight test manoeuvres," *Technical Report*, 1986.

Appendix B

Journal Paper Draft

Incremental Nonlinear Control Allocation for a Tailless Aircraft with Innovative Control Effectors

I. Matamoros[a], C.C. de Visser[b] and Q.P. Chu[c]
Delft University of Technology, 2629HS Delft, The Netherlands.

M.A. Niestroy[d]
Lockheed Martin Aero, Fort Worth, TX, 76101.

Conventional linear control allocation (LCA) methods fail to provide satisfactory performance in flight control systems (FCS) for aircraft with highly nonlinear and coupled control effector suites, especially for tailless aircraft with strong interactions between control effectors. This paper implements an incremental nonlinear control allocation (INCA) approach that can capture nonlinearities and interactions of control effectors, while being solvable with computationally efficient LCA algorithms. This makes INCA suitable for real-time control allocation in FCS. This incremental reformulation of the control allocation problem is based on a Jacobian model of the control effectors, and relies on angular acceleration measurements to reduce model dependency. In addition, real-time measurements of the actuator positions mitigate typical problems related to couplings between control allocators and actuator dynamics. In this paper, LCA- and INCA-based nonlinear FCS are designed for the Innovative Control Effectors (ICE) aircraft, a highly maneuverable tailless aircraft with 13 highly nonlinear, interacting and axis-coupled control effectors. Real-time simulation results showed that INCA dramatically improves tracking and control allocation performance with respect to LCA methods, thus improving maneuverability and exploiting the full

---

[a] MSc student, Control and Simulation Division, Faculty of Aerospace Engineering, Kluyverweg 1, 2629HS Delft, The Netherlands, ismaelmatamoros@hotmail.com. AIAA Member.

[b] Assistant Professor, Control and Simulation Division, Faculty of Aerospace Engineering, Kluyverweg 1, 2629HS Delft, The Netherlands, c.c.devisser@tudelft.nl. AIAA Member.

[c] Associate Professor, Control and Simulation Division, Faculty of Aerospace Engineering, Kluyverweg 1, 2629HS Delft, The Netherlands, q.p.chu@tudelft.nl. AIAA Member.

[d] Aeronautical Eng. Manager, Lockheed Martin ADP, P.O. Box 748, Fort Worth, TX 76101. AIAA Associate Fellow.

potential of innovative control effector suites. Additionally, a sensitivity analysis revealed that the INCA method is highly robust against Jacobian model mismatch.

I. Introduction

Given the inherent benefits of highly redundant and axis-coupled control effector suites, aircraft over-actuation is an increasingly common practice in aerospace design. Over-actuated systems have more control inputs than controlled variables, and therefore an attainable control command may be achievable through multiple combinations of actuator positions. In flight control systems (FCS), control allocation (CA) algorithms distribute control commands over the available set of control effectors, aiming to maximally exploit the maneuverability and handling qualities of the aircraft while accounting for the physical limitations of the actuators.

Most conventional CA methods operate under the assumption that a linear relationship exists between actuator positions and control-induced forces and moments. This simplification yields a very tractable affine formulation of the control allocation problem, which can be solved with efficient linear algorithms suitable for real-time implementation in FCS. Common examples of such methods are the redistributed weighted pseudo-inverse [1], daisy chaining [2], direct allocation [3–9] and numerical optimization-based approaches such as linear programming [10–13] and quadratic programming [9, 12]. The assumption of linearity of the control effectors, however, has important shortcomings.

First, linear models are unable to capture interactions between control effectors. Although such interactions are usually negligible in conventional actuator suites, more innovative configurations feature actuators positioned downstream of others, resulting in important nonlinear interactions. In some cases, these can be positively exploited such as in the case of slots, which can be used to recover control effectiveness of trailing-edge control surfaces at high angles-of-attack (AoA). In other cases, these interactions can have negative effects on the control effectiveness of certain actuators, such as in the case of leading-edge control devices that disturb the downstream airflow. Although the issue of control effector interactions was noticed and addressed in [14], the applicability of the proposed method is limited to interactions between two control effectors that can be described by a bilinear function.

Second, independently-moving control surfaces produce secondary-axis yawing moments by generating drag through a lever arm with respect to the aircraft longitudinal axis. Although conventional aircraft use a rudder for directional control, tailless configurations exploit these secondary-axis moments as a main source of directional control power. These moments can also be used in conventional actuator suites to regain directional controllability after rudder failure. Common actuators using this principle are all-moving wing tips and independently-moving ailerons and elevons [15, 16]. Whereas they produce locally linear rolling moments, they have highly nonlinear contributions to yawing moment, especially at low AoA, where parasitic drag dominates induced drag effects. Secondary-axis yawing moments are generally asymmetric parabolic functions of the actuator deflections, which cannot be captured with linear effector models. This shortcoming has two negative effects concerning control allocation. First, the yawing moments not included in the on-board aerodynamic model are seen as external disturbances by the control system, and need to be mitigated with other sources of directional control power. Second, the ability to positively exploit these sources of yawing moment is lost, which is particularly critical in tailless configurations. This problem was addressed in [17] by modelling the control effectors with piecewise linear functions. Although the potential benefits of nonlinear CA were clearly demonstrated, the proposed method required solving a mixed-integer programming problem, which is extremely slow due to its computational complexity, and therefore not suitable for real-time implementation.

Finally, although the control moment curves of conventional actuators are locally linear for small deflections, nonlinearities exist in extreme regions of their operational range. Failing to capture such nonlinearities results in a model mismatch causing control allocation error, which needs to be mitigated by the robustness of the flight control laws [18]. This is detrimental to the overall performance of the system, especially in faulty conditions where the non-faulty actuators are forced to operate within extreme regions of their moment curves. This problem was addressed in [18] by introducing an affine control effector model with intercept correction. This method is not applicable when the control-induced moments are quadratic, have non-monotonic behaviour, or when the slope of the control effectiveness curves becomes small. Despite its limited applicability, this method showed the potential benefits of considering nonlinearities in control moment curves.

In most conventional aircraft configurations the inaccuracies introduced by the assumption of linearity are relatively small and can be acceptably absorbed by robust control systems. However, linear control allocation fails to provide adequate performance in more advanced and innovative designs, especially in tailless aircraft, which produce directional control power mainly through secondary-axis parabolic yawing moments. A very representative example is Lockheed Martin's Innovative Control Effectors (ICE) research aircraft concept, a tailless flying wing with a highly redundant set of 13 control effectors, which produce highly nonlinear and cross-axis coupled moments and exhibit strong interactions.

Nonlinear control allocation methods have been explored as a solution with different approaches, such as nonlinear direct allocation [15], mixed-integer programming [16] and nonlinear programming [19]. Although the methods proposed to date clearly demonstrate important improvements over conventional linear approaches, nonlinear optimization algorithms are highly computationally complex and not suitable for implementation in real-time systems.

This paper implements an incremental nonlinear control allocation (INCA) method based on a reformulation of the control allocation problem in incremental form, exploiting the time scale separation principle. This approach is based on a nonlinear Jacobian model of the control effectors, which can capture actuator nonlinearities, including interactions between control effectors. An angular acceleration feedback loop reduces the model dependency of the nonlinear control system and makes it highly robust against model mismatch. The crux of this method is that it operates in an incremental scheme, which allows the nonlinear CA problem to be solved with simple and efficient linear control allocation algorithms that are well-suited for real-time implementation in FCS. Unlike most typical CA algorithms, INCA uses information of the current position of the actuators, which are dynamically driven towards their optimal positions through small increments. This mitigates the negative impact of actuator dynamics in control allocation, which has been focus of extensive research [20–24].

The results presented in this paper demonstrate substantial benefits of INCA in terms of flight control and control allocation performance for innovative aircraft designs with respect to linear control allocation (LCA) methods. For this, an LCA-based and an INCA-based nonlinear flight control systems were designed for the ICE aircraft, and their performance was evaluated through simulation using the high-fidelity simulation model described in [25]. This model includes actuator dynamics, in addition to position and rate constraints. Both LCA- and INCA-based flight control systems were implemented with two typical LCA solvers to compare performance.

II. The Control Allocation Problem

Consider the aircraft dynamic equations expressed in the general form

$$\dot{\mathbf{x}} = \mathbf{f}(\mathbf{x}) + \mathbf{g}(\mathbf{x})\,\boldsymbol{\tau} \tag{1}$$

where $\mathbf{x} \in \mathbb{R}^n$ is the state vector and $\boldsymbol{\tau} \in \mathbb{R}^m$ the aerodynamic inputs to the equations of motion. Control allocation in aerospace applications typically concerns attitude control, $\boldsymbol{\tau} \in \mathbb{R}^3$ being the aerodynamic moments in body frame. This problem is commonly referred to as the three-moment problem. The aerodynamic moments are generally nonlinear functions of the states and the control effector positions $\boldsymbol{\delta} \in \mathbb{R}^p$:

$$\boldsymbol{\tau} = \mathbf{h}(\mathbf{x}, \boldsymbol{\delta}) \tag{2}$$

The control effectors are subject to rate and position constraints

$$\boldsymbol{\delta}_{\min} \leq \boldsymbol{\delta} \leq \boldsymbol{\delta}_{\max} \tag{3}$$

$$|\dot{\boldsymbol{\delta}}| \leq \dot{\boldsymbol{\delta}}_{\max} \tag{4}$$

The control allocation problem consists on determining the control effector positions $\boldsymbol{\delta}$ that produce a given moment command $\boldsymbol{\tau}_c$. Over-actuated systems have more control effectors than controlled variables, i.e. $p > m$, and therefore the system of Eqs. (2) is underdetermined with $p - m$ degrees of freedom. When multiple solutions that satisfy $\boldsymbol{\tau}_c$ exist, secondary objectives might be defined to determine an optimal solution. As shown in the classical control scheme for over-actuated systems in Figure 1, the moment commands are typically provided by a high-level control system. The choice of a suitable control allocation approach is strongly application-dependent.

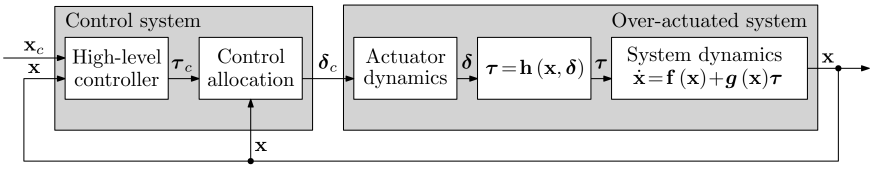

Fig. 1 Classical control scheme for over-actuated systems.

Extensive surveys giving a broad overview of currently available CA methods exist in the literature, see [1, 12, 26].

In aerospace systems, CA algorithms run in flight control computers (FCC) in discrete-time, and the control distribution is computed at each time step for the current state $\mathbf{x}_0$. Given a measured or estimated $\mathbf{x}_0$ at a given time step, the control effectiveness function $\mathbf{h}(\mathbf{x},\boldsymbol{\delta})$ becomes a generally nonlinear static mapping $\mathbf{h}(\mathbf{x}_0):\mathbb{R}^p\rightarrow\mathbb{R}^m$. Thus, the actuator rate limits can be translated into local position limits for the current time step as

$$\Delta\boldsymbol{\delta}_{\max}=\dot{\boldsymbol{\delta}}_{\max}\Delta t \tag{5}$$

The effective local position limits at a given time step are

$$\underline{\boldsymbol{\delta}}\leq\boldsymbol{\delta}\leq\overline{\boldsymbol{\delta}} \tag{6}$$

with

$$\begin{aligned}\overline{\boldsymbol{\delta}}&=\min\left(\boldsymbol{\delta}_{\max},\ \boldsymbol{\delta}_0+\dot{\boldsymbol{\delta}}_{\max}\Delta t\right)\\ \underline{\boldsymbol{\delta}}&=\max\left(\boldsymbol{\delta}_{\min},\ \boldsymbol{\delta}_0-\dot{\boldsymbol{\delta}}_{\max}\Delta t\right)\end{aligned} \tag{7}$$

the local upper and lower bounds of the actuator positions.

For a given time step, the static control allocation problem is formulated as: given the current state $\mathbf{x}_0$, the control effector model $\boldsymbol{\tau}=\mathbf{h}(\mathbf{x}_0,\boldsymbol{\delta})$ and a moment command $\boldsymbol{\tau}_c$, determine a control vector $\boldsymbol{\delta}$ such that

$$\begin{gathered}\mathbf{h}(\mathbf{x}_0,\boldsymbol{\delta})=\boldsymbol{\tau}_c\\ \text{subject to}\quad\underline{\boldsymbol{\delta}}\leq\boldsymbol{\delta}\leq\overline{\boldsymbol{\delta}}\end{gathered} \tag{8}$$

Note that the inverse problem of computing $\boldsymbol{\delta}$ given $\boldsymbol{\tau}_c$ is ill-posed and generally its solution is not unique. In order to solve the inverse CA problem in Eq. (8), commonly used approaches assume that $\mathbf{h}(\mathbf{x}, \boldsymbol{\delta})$ is linear in the inputs, and thus can be expressed using a control effectiveness matrix $B(\mathbf{x}) \in \mathbb{R}^{m \times p}$ in the form

$$\boldsymbol{\tau} = \mathbf{h}(\mathbf{x}, \boldsymbol{\delta}) = B(\mathbf{x})\,\boldsymbol{\delta} \tag{9}$$

This formulation of the problem enables the use of computationally efficient linear solvers such as generalized pseudo-inverses, linear programming or quadratic programming. However, as discussed above, the assumption of linearity neglects interactions between control effectors, fails to capture parabolic moment curves and neglects nonlinearities in the control-induced moments. Although this assumption is acceptable for conventional control effector configurations, it is not valid for advanced configurations such as the ICE aircraft. In aerospace control CA algorithms are required to run real-time at frequencies in the order of 100 Hz [9].

III. Incremental Nonlinear Control Allocation

The incremental control allocation approach implemented in this paper is based on a reformulation of the control allocation problem in incremental form and the application of the time scale separation principle. Incremental nonlinear control has been successfully implemented in aerospace applications under the incremental nonlinear dynamic inversion (INDI) scheme [27–30], showing very promising advantages such as a substantial reduction of model dependency.

A. The Control Problem in Incremental Form

Consider again the nonlinear system dynamics in Eq. (1). The aerodynamic moment inputs $\boldsymbol{\tau}$ can be separated into an exclusively state-dependent part and an input-depended part

$$\boldsymbol{\tau} = \boldsymbol{\tau}_a + \boldsymbol{\tau}_\delta \tag{10}$$

where $\boldsymbol{\tau}_a$ contains the aerodynamic moments generated by the airframe, and $\boldsymbol{\tau}_\delta$ is the control effector model, providing the control-induced moments produced by the actuators. The control effector model can be generally expressed as the nonlinear mapping

$$\boldsymbol{\tau}_\delta = \boldsymbol{\Phi}(\mathbf{x}, \boldsymbol{\delta}) \tag{11}$$

Thus, the system dynamics can be rewritten as

$$\dot{\mathbf{x}} = [\mathbf{f}(\mathbf{x}) + \mathbf{g}(\mathbf{x})\,\boldsymbol{\tau}_a] + \mathbf{g}(\mathbf{x})\,\boldsymbol{\Phi}(\mathbf{x}, \boldsymbol{\delta}) = \mathbf{F}(\mathbf{x}) + \mathbf{g}(\mathbf{x})\,\boldsymbol{\Phi}(\mathbf{x}, \boldsymbol{\delta}) \tag{12}$$

where $\mathbf{F}(\mathbf{x})$ contains all the effects not produced by the control effectors.

When the control system works in discrete time the dynamic equations of the system can be locally linearized at every time step around the current state $\mathbf{x}_0$ and actuator positions $\boldsymbol{\delta}_0$ as a first-order Taylor expansion:

$$\dot{\mathbf{x}} \approx \dot{\mathbf{x}}_0 + \frac{\partial}{\partial \mathbf{x}} \left[\mathbf{F}(\mathbf{x}) + \mathbf{g}(\mathbf{x}) \boldsymbol{\Phi}(\mathbf{x}, \boldsymbol{\delta})\right]\Bigg|_{\substack{\boldsymbol{\delta}=\boldsymbol{\delta}_0 \\ \mathbf{x}=\mathbf{x}_0}} (\mathbf{x} - \mathbf{x}_0) + \frac{\partial}{\partial \boldsymbol{\delta}} \left[\mathbf{F}(\mathbf{x}) + \mathbf{g}(\mathbf{x}) \boldsymbol{\Phi}(\mathbf{x}, \boldsymbol{\delta})\right]\Bigg|_{\substack{\boldsymbol{\delta}=\boldsymbol{\delta}_0 \\ \mathbf{x}=\mathbf{x}_0}} (\boldsymbol{\delta} - \boldsymbol{\delta}_0) \quad (13)$$

The time scale separation principle states that, for systems where the derivatives of the states have significantly faster dynamics than the states themselves, the term $(\mathbf{x} - \mathbf{x}_0)$ is small enough to be neglected at high sampling rates. This principle commonly applies to systems where $\boldsymbol{\delta}$ can change significantly faster than $\mathbf{x}$ over a time step, which is the case when the influence of $\boldsymbol{\delta}$ on the derivatives of the states is significantly higher than the influence of the states. This has been proven to be true for aerial vehicles such as aircraft [28], helicopters [29] and quadrotors [30] at common sampling frequencies of 100 Hz.

Applying the time scale separation principle and introducing the virtual control input $\boldsymbol{\nu}(\mathbf{x}) = \dot{\mathbf{x}}$, Eq. (13) can be simplified to

$$\boldsymbol{\nu}(\mathbf{x}) = \dot{\mathbf{x}} \approx \dot{\mathbf{x}}_0 + \mathbf{g}(\mathbf{x}_0) \frac{\partial \boldsymbol{\Phi}(\mathbf{x}_0, \boldsymbol{\delta}_0)}{\partial \boldsymbol{\delta}} \Delta \boldsymbol{\delta} \quad (14)$$

At this point, the system dynamics can be linearized with an incremental nonlinear dynamic inversion loop by inverting the dynamics in Eq. (14):

$$\Delta \boldsymbol{\delta}_c = \left[\frac{\partial \boldsymbol{\Phi}(\mathbf{x}_0, \boldsymbol{\delta}_0)}{\partial \boldsymbol{\delta}}\right]^{-1} \mathbf{g}(\mathbf{x})^{-1} \left[\boldsymbol{\nu}(\mathbf{x}) - \dot{\mathbf{x}}_0\right] \quad (15)$$

This control law linearizes the response between the virtual control input $\boldsymbol{\nu}(\mathbf{x})$ and $\mathbf{x}$. Moreover, model dependency is significantly reduced with respect to typical nonlinear dynamic inversion (NDI) control laws [31–33], since the INDI control law is independent of the aerodynamic derivatives in $\boldsymbol{\tau}_a$. This reduction in model dependency is compensated by feeding back acceleration measurements $\dot{\mathbf{x}}_0$.

In over-actuated systems the Jacobian $\partial \boldsymbol{\Phi}(\mathbf{x}, \boldsymbol{\delta}) / \partial \boldsymbol{\delta}$ is a non-square $m \times p$ matrix, and therefore it cannot be inverted to implement the incremental control law in Eq. (15). However, a control allocation scheme can be implemented by reformulating the control allocation problem in incremental form with Eq. (14).

B. The Control Allocation Problem in Incremental Form

Note that Eq. (14) establishes an affine relationship between the virtual control input $\boldsymbol{\nu}(\mathbf{x})$ and increments in actuator positions $\Delta\boldsymbol{\delta}$. The nonlinearities and interactions of the control effectors are still captured by the Jacobian matrix $\partial\boldsymbol{\Phi}(\mathbf{x}_0, \boldsymbol{\delta}_0)/\partial\boldsymbol{\delta}$, which can be updated for the current state and actuator positions at every time step. To simplify notation, let the Jacobian matrix of $\boldsymbol{\Phi}(\mathbf{x}, \boldsymbol{\delta})$ with respect to $\boldsymbol{\delta}$ be denoted as

$$\nabla_{\boldsymbol{\delta}}\boldsymbol{\Phi}(\mathbf{x}, \boldsymbol{\delta}) = \frac{\partial\boldsymbol{\Phi}(\mathbf{x}, \boldsymbol{\delta})}{\partial\boldsymbol{\delta}} \tag{16}$$

and define the pseudo-control input $\mathbf{d}_c \in \mathbb{R}^n$

$$\mathbf{d}_c = \mathbf{g}(\mathbf{x})^{-1}\left[\boldsymbol{\nu}(\mathbf{x}) - \dot{\mathbf{x}}_0\right] \tag{17}$$

The INCA problem is formulated as: given the current state $\mathbf{x}_0$, the current actuator positions $\boldsymbol{\delta}_0$, acceleration measurements $\dot{\mathbf{x}}_0$ and a pseudo-control input command $\mathbf{d}_c = \mathbf{g}(\mathbf{x})^{-1}\left[\boldsymbol{\nu}(\mathbf{x}) - \dot{\mathbf{x}}_0\right]$, determine an increment in the control input vector $\Delta\boldsymbol{\delta}$ such that

$$\begin{gathered} \nabla_{\boldsymbol{\delta}}\boldsymbol{\Phi}(\mathbf{x}_0, \boldsymbol{\delta}_0)\Delta\boldsymbol{\delta} = \mathbf{d}_c \\ \text{subject to} \quad \underline{\boldsymbol{\Delta\delta}} \leq \boldsymbol{\Delta\delta} \leq \overline{\boldsymbol{\Delta\delta}} \end{gathered} \tag{18}$$

where $\underline{\boldsymbol{\Delta\delta}}$ and $\overline{\boldsymbol{\Delta\delta}}$ are the most restrictive upper and lower bounds of the local position and rate constraints of the actuators, translated into local incremental constraints. Note that the INCA control allocator provides required increments of the actuator positions, which are added to the current actuator positions to reach the absolute position command: $\boldsymbol{\delta} = \boldsymbol{\delta}_0 + \Delta\boldsymbol{\delta}$. The top-level INCA-based control scheme is depicted in Figure 2.

The main advantage of INCA is that the incremental problem formulated in Eq. (18) is linear in the increments of actuator positions, and therefore can be solved with simple and efficient linear CA methods, such as the redistributed weighted pseudo-inverse or quadratic programming. The fact that only local increments $\Delta\boldsymbol{\delta}$ are determined at each time step implies that the Jacobian $\nabla_{\boldsymbol{\delta}}\boldsymbol{\Phi}(\mathbf{x}, \boldsymbol{\delta})$, which captures nonlinearities and control effector interactions, can be updated for the new actuator positions at every time step while the actuators are dynamically driven towards their optimal positions. Thus, the direction of the increments of the control vector may change at every

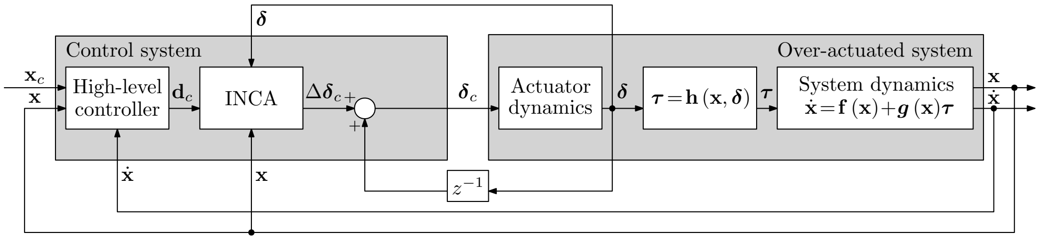

Fig. 2 Incremental nonlinear control allocation scheme for over-actuated systems.

time step in contrast to conventional LCA methods, which compute absolute positions at each time step. Additionally, measured or estimated actuator positions $\boldsymbol{\delta}_0$ are fed back into the system, and therefore the incremental allocation is always based on current actuator positions. This mitigates the negative impact of actuator dynamics. Most conventional CA methods, in contrast, assume $\boldsymbol{\delta}_c = \boldsymbol{\delta}_0$, resulting in negative coupling effects between control allocators and actuator dynamics [34].

Note that an incremental formulation of the control allocation problem was derived for the particular case of multivariate spline-based control systems in [35]. In this paper, the method is generalized to incremental flight control systems based on any kind of on-board aerodynamic model, and focuses on controller-related aspects such as real-time performance, robustness, model dependency, actuator dynamics and saturation handling.

C. Actuator Constraints in Incremental Form

The incremental formulation of the control allocation problem requires translation of the absolute position and rate limits of the actuators into equivalent local incremental constraints. Under a discrete-time scheme, rate limits are directly mapped into position limits over a time step Δt as

$$\begin{aligned} \Delta\boldsymbol{\delta}^r_{\max} &= \dot{\boldsymbol{\delta}}_{\max}\Delta t \\ \Delta\boldsymbol{\delta}^r_{\min} &= -\dot{\boldsymbol{\delta}}_{\max}\Delta t \end{aligned} \tag{19}$$

Similarly, absolute position limits can be translated into local constraints imposed over a time step as

$$\begin{aligned} \Delta\boldsymbol{\delta}^p_{\max} &= \boldsymbol{\delta}_{\max} - \boldsymbol{\delta}_0 \\ \Delta\boldsymbol{\delta}^p_{\min} &= \boldsymbol{\delta}_{\min} - \boldsymbol{\delta}_0 \end{aligned} \tag{20}$$

The local upper and lower bounds of the actuator position increments at a given time step are the most restrictive of the local rate and position limits:

$$\begin{aligned}\overline{\Delta\boldsymbol{\delta}} &= \min\left(\dot{\boldsymbol{\delta}}_{\max}\Delta t_s,\ \boldsymbol{\delta}_{\max} - \boldsymbol{\delta}_0\right)\\ \underline{\Delta\boldsymbol{\delta}} &= \max\left(-\dot{\boldsymbol{\delta}}_{\max}\Delta t_s,\ \boldsymbol{\delta}_{\min} - \boldsymbol{\delta}_0\right)\end{aligned} \tag{21}$$

IV. The ICE Aircraft Model

The INCA method was implemented in this paper on a simulation framework to design a flight control system for Lockeed Martin's ICE aircraft, a highly manoeuvrable tailless aircraft with an unconventional set of control effectors. This configuration presents substantial control challenges for which LCA methods are obsolete. In this section the ICE configuration is presented, and a description of the high-fidelity model used in the simulations is given.

A. The ICE Control Effectors Suite

The ICE configuration was developed as one of the design concepts for the ICE program conceived in 1993 by the Flight Control Division of the U.S. Flight Dynamics Directorate, which aimed to meet new requirements in terms of improved stealth characteristics, reduction of airframe weight, improvement of lift-to-drag ratio and high manoeuvrability [36]. The result was an over-actuated 65-deg sweep, highly maneuverable, supersonic tailless flying wing with 13 innovative control effectors. Refs. [37, 38] provide technical insight on the ICE program.

The ICE control effectors suite includes inboard and outboard leading-edge flaps (LEF) providing lateral-directional control power at high AoA, all-moving wing tips (AMT) as one of the main sources of lateral-directional control, and fluidic multi-axis thrust vectoring (MTV) as an additional source of directional and longitudinal control power. It also includes pitch flaps (PF) for longitudinal control (only symmetric deflections are possible) and independent elevons, mainly producing longitudinal and lateral control power. Finally, the ICE aircraft has two spolier-slot deflectors (SSD). Unlike conventional spoilers, SSDs open a slot between the lower and upper wing skins when deflected, allowing the redirection of the air flow at high AoA to recover control effectiveness of the trailing-edge actuators. SSDs provide improved lateral-directional control effectiveness at high AoA and transonic flight with respect to conventional spoilers. The SSDs are placed upstream of most

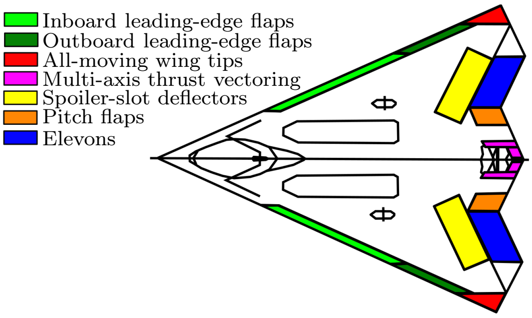

Fig. 3 ICE control effectors suite.

Table 1 Dynamic properties of the ICE control effectors.

Control effector	Notation	Position limits [deg]	Rate limit [deg/sec]	Dynamics
Inboard LEF	$\delta_{\text{lfi}}, \delta_{\text{rfi}}$	[0, 40]	40	$H_l(s)$
Outboard LEF	$\delta_{\text{lfo}}, \delta_{\text{rfo}}$	[-40, 40]	40	$H_l(s)$
AMT	$\delta_{\text{la}}, \delta_{\text{ra}}$	[0, 60]	150	$H_h(s)$
Elevons	$\delta_{\text{le}}, \delta_{\text{re}}$	[-30, 30]	150	$H_h(s)$
SSD	$\delta_{\text{ls}}, \delta_{\text{rs}}$	[0, 60]	150	$H_h(s)$
PF	δ_{pf}	[-30, 30]	150	$H_h(s)$
MTV	$\delta_{\text{ptv}}, \delta_{\text{ytv}}$	[-15, 15]	150	$H_h(s)$

trailing-edge control surfaces, and therefore have a strong influence on their control effectiveness at low AoA. The configuration of the ICE control effectors is shown in Figure 3.

The dynamics of the control effectors are modeled as second-order transfer functions. Either a low-bandwidth and a high-bandwidth transfer function is used depending on the effectors:

$$H_l(s) = \frac{(18)(100)}{(s+18)(s+100)} \qquad (22) \qquad\qquad H_h(s) = \frac{(40)(100)}{(s+40)(s+100)} \qquad (23)$$

The position limits, no-load rate limits and dynamics of the ICE control effectors are listed in Table 1.

B. Control Challenges

The unconventional ICE configuration presents a series of control challenges. Control and stability issues have been extensively addressed for the ICE aircraft in [13, 36, 40–43]. A more unaddressed challenge of the ICE configuration is the impossibility to successfully use linear control allocation methods to optimally distribute control commands and fully exploit the capabilities of its set of control effectors. This is due to a number of reasons.

First, as is common in tailless configurations, directional control power is mainly produced with horizontal control surfaces, and therefore yawing moment curves are mostly parabolic. These curves cannot be captured by linear effector models unless the concerned actuators are restricted to operate in one direction, so LCA methods have serious issues regarding directional control in tailless configurations. An example of a parabolic yawing moment curve of the left elevon influenced by the AMT deflection from the ICE aerodynamic database is shown in Figure 4(a).

Second, due to the high number of control effectors, the mechanisms used to produce control moments and the proximity between some control surfaces, the actuators exhibit strong nonlinear interactions. This is particularly relevant for trailing-edge actuators. In some cases, such interactions may even cause a change of sign in the slope of the moment curves of some actuators, such as in the examples shown in Figures 4(a)-4(c). Also, note that control effectiveness of trailing-edge surfaces is rapidly lost for small deflections of the SSDs at low AoA, as observed in Figure 4(b).

Finally, nonlinearities at the extreme regions of the control moment curves are observed in Figure 4(b). The dashed line represents a linear approximation of the control moment curve for $\delta_{\mathrm{s}} = 0$ deg. It is shown that the model mismatch becomes significant close to the actuator position limits. This error is particularly critical in failure conditions, where the non-faulty actuators are forced to operate in extreme regions of the moment curve. The factors discussed above make the assumption of linearity in control allocation obsolete in the case of the ICE aircraft.

C. The ICE High-Fidelity Simulation Model

The high-fidelity nonlinear simulation model used in this paper was released by Lockheed Martin to encourage control-related research. It is a six degrees-of-freedom (6-DoF) aerodynamic model developed mainly from wind tunnel data, and includes nonlinear interaction effects between control effectors, dynamic derivatives, aeroelastic effects and hinge moment derivatives. The aerodynamic model provides dimensionless coefficients for aerodynamic forces and moments as a summation of

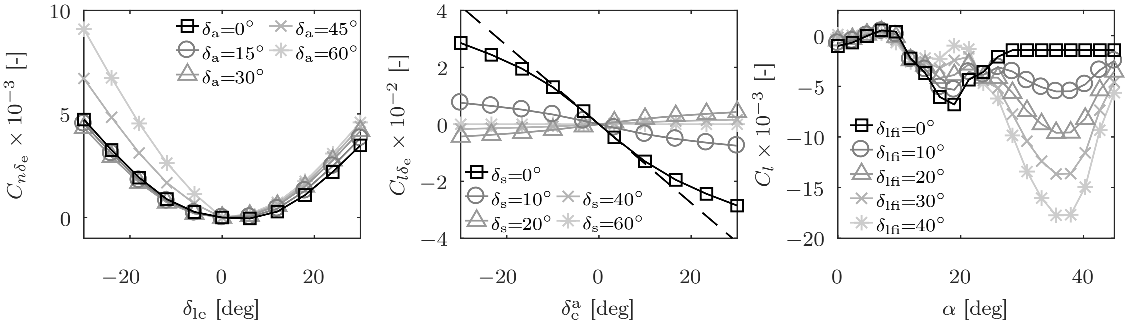

(a)Yawing moment curve of the left elevon, influenced by the deflection of the AMTs.

(b)Rolling moment curve of the elevons with asymmetric deflections, influenced by the SSDs. The dashed line represents a linear approximation for $\delta_s = 0$ deg.

(c)Total rolling moment coefficient, including moments from the airframe, for $\delta_{lfo} = 30$ deg, influenced by the inboard LEF.

Fig. 4 Examples of control moment curves at M = 0.6 and $\alpha = \beta = 0$ deg from the ICE aerodynamic database.

nonlinear terms:

$$C_i = \sum_{j=1}^{19} C_{ij}\left(\boldsymbol{\delta}, \alpha, \beta, M, \boldsymbol{\omega}\right) \tag{24}$$

with $i = \{l, m, n, X, Y, Z\}$ and where the nonlinear terms $C_{ij}\left(\boldsymbol{\delta}, \alpha, \beta, M, \boldsymbol{\omega}\right)$ are stored in lookup tables. A detailed description of the model is given in [25].

D. Multi-Axis Thrust Vectoring Model

The MTV model considers the direction of the pitch δ_{ptv} and yaw δ_{ytv} deflection angles of the thrust vector such that positive deflections produce negative pitching and yawing moments. Using this convention, the MTV force $\mathbf{T}$ and moment $\boldsymbol{\tau}_{\text{T}}$ vectors are given by Equations (25) and (26), where d_n=18.75 ft is the moment arm of the thrust force.

$$\mathbf{T} = \begin{bmatrix} T_x \\ T_y \\ T_z \end{bmatrix} = \mathrm{T} \begin{bmatrix} \cos(\delta_{\text{ptv}})/\cos(\delta_{\text{ytv}}) \\ \cos(\delta_{\text{ptv}})\tan(\delta_{\text{ytv}}) \\ \sin(\delta_{\text{ptv}}) \end{bmatrix} \tag{25}$$

$$\boldsymbol{\tau}_{\text{T}} = \begin{bmatrix} \tau_{x_T} \\ \tau_{y_T} \\ \tau_{z_T} \end{bmatrix} = -\mathrm{T}d_n \begin{bmatrix} 0 \\ \sin(\delta_{\text{ptv}}) \\ \cos(\delta_{\text{ptv}})\tan(\delta_{\text{ytv}}) \end{bmatrix} \tag{26}$$

V. Flight Control Systems Design

In order to test the INCA concept and assess its performance with respect to conventional LCA methods, an LCA-based and an INCA-based fight control systems were designed for the ICE aircraft. The control allocation systems were applied to angular body rate control, the innermost loop of the FCS. The body rate loop was augmented with a pseudo-control hedging loop as a partial fight envelope protection and anti-windup system. The design of both FCS is discussed in this section.

A. LCA-Based Flight Control System Design

The conventional LCA-based flight control system was designed with a typical nonlinear dynamic inversion scheme. This flight control system relies on a nonlinear aerodynamic model of the plant and a linear control effector model for the control allocation module.

1. Linear Control Effectors Model

As discussed above, LCA methods require an aerodynamic model in which the control-induced moments are affine in the actuator positions. Note, however that the aerodynamic and control derivatives can remain nonlinear functions of α, β, M and $\boldsymbol{\omega}$. In order to de-couple the inputs, the interaction effects between control effectors were eliminated from the original database. Linear regressors were used to identify the aerodynamic coefficients and control derivatives as functions of α, β, M and $\boldsymbol{\omega}$ at the data points available in the ICE aerodynamic database. The obtained derivatives were stored in lookup tables. The structure of the affine model is

$$\begin{aligned} C_l &= C_{l_a}\left(\alpha,\beta,M,\boldsymbol{\omega}\right) + \sum_{i=1}^{13} \Delta C_{l,\delta_i}\left(\alpha,\beta,M\right)\delta_i \\ C_m &= C_{m_a}\left(\alpha,\beta,M,\boldsymbol{\omega}\right) + \sum_{i=1}^{13} \Delta C_{m,\delta_i}\left(\alpha,\beta,M\right)\delta_i \\ C_n &= C_{n_a}\left(\alpha,\beta,M,\boldsymbol{\omega}\right) + \sum_{i=1}^{13} \Delta C_{n,\delta_i}\left(\alpha,\beta,M\right)\delta_i \end{aligned} \tag{27}$$

with $\Delta C_{j,\delta_i}$ the control derivative of $j = \{l, m, n\}$ with respect to the control effector δ_i, and

$$\begin{aligned} C_{l_a}\left(\alpha,\beta,M,\boldsymbol{\omega}\right) &= C_{l,\alpha}\left(\alpha,M\right) + C_{l,\beta}\left(\alpha,\beta,M\right) + \frac{pb}{2V}C_{l,p}\left(\alpha,M\right) + \frac{rb}{2V}C_{l,r}\left(\alpha,M\right) \\ C_{m_a}\left(\alpha,\beta,M,\boldsymbol{\omega}\right) &= C_{m,\alpha}\left(\alpha,M\right) + C_{m,\beta}\left(\alpha,\beta,M\right) + \frac{q\bar{c}}{2V}C_{m,q}\left(\alpha,M\right) \\ C_{n_a}\left(\alpha,\beta,M,\boldsymbol{\omega}\right) &= C_{n,\alpha}\left(\alpha,M\right) + C_{n,\beta}\left(\alpha,\beta,M\right) + \frac{pb}{2V}C_{n,p}\left(\alpha,M\right) + \frac{rb}{2V}C_{n,r}\left(\alpha,M\right) \end{aligned} \tag{28}$$

the dimensionless nonlinear moments generated by the airframe. Examples of identified control derivatives scheduled for α and β are shown in Figure 5.

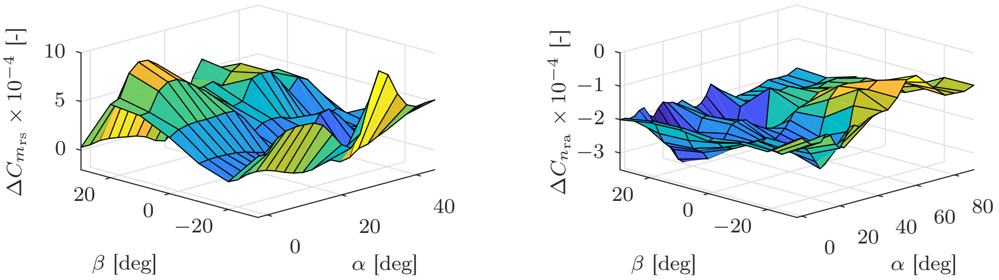

(a)Pitching moment derivative of right SSD.

(b)Yawing moment derivative of right AMT.

Fig. 5 Examples of control derivatives scheduled for α and β.

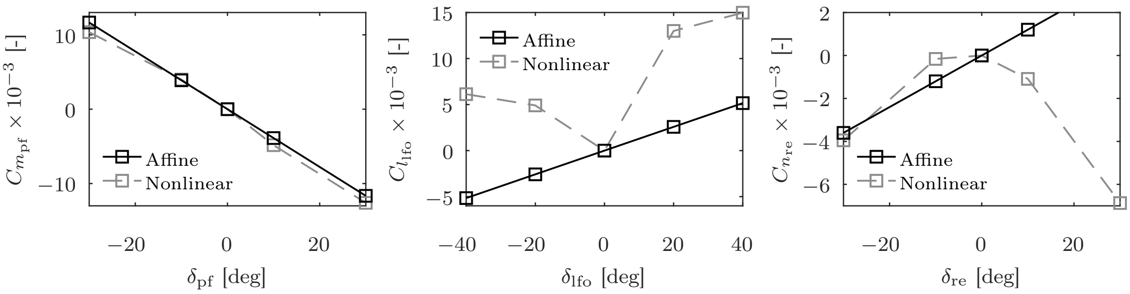

(a)Pitching moment of pitch flaps.

(b)Rolling moment of outboard LEF.

(c)Yawing moment of right elevon.

Fig. 6 Affine control effector model compared to original aerodynamic data.

As discussed earlier, the assumption of linearity in control-induced moments is accurate enough in some cases such as the pitching moment of the pitch flap in Figure 6(a), but in other cases it fails to capture important effects. See, for instance, the rolling moment characteristic of the outboard LEF in Figure 6(b) and the parabolic yawing moment curve of the right elevon in Figure 6(c).

The control derivative terms of the MTV can be derived by taking a first-order Taylor expansion of the terms τ_{y_T} and τ_{z_T} in Eq. (26) around $\delta_{\text{ptv}} = \delta_{\text{ytv}} = 0$, obtaining the affine approximation

$$\boldsymbol{\tau}_T = -T d_n \begin{bmatrix} 0 \\ \delta_{\text{ptv}} \\ \delta_{\text{ytv}} \end{bmatrix} \tag{29}$$

Wrapping up the control derivative terms into a control effectiveness matrix $B(\mathbf{x})$, the aerodynamic moments can be expressed in control-affine form as

$$\boldsymbol{\tau} = \boldsymbol{\tau}_a + \boldsymbol{\tau}_e = \frac{1}{2}\rho V^2 S \left(\begin{bmatrix} b C_{l_a} \\ \bar{c} C_{m_a} \\ b C_{n_a} \end{bmatrix} + B(\mathbf{x})\, \boldsymbol{\delta} \right) \tag{30}$$

The actuator constraints are translated into local constraints as in Eq. (7). The MTV vector is subject to a circular constraint imposed over the ℓ_2 norm of the vector $\boldsymbol{\delta}_{\text{tv}} = (\delta_{\text{ptv}}, \delta_{\text{ytv}})$. When the MTV vector violates the circular constraint, it is re-scaled into the boundary of the feasible subspace by keeping the original direction of $\boldsymbol{\delta}_{\text{tv}}$:

$$\boldsymbol{\delta}'_{\text{tv}} = \frac{\boldsymbol{\delta}_{\text{tv}_{\text{max}}}}{||\delta_{\text{tv}}||}\delta_{\text{tv}} \tag{31}$$

2. Angular Rate Control Loop

The innermost control loop controls the body angular rates $\boldsymbol{\omega} = [p\ q\ r]$ through commanded moments $\boldsymbol{\tau}_c$. Consider the aircraft rotational dynamic equations

$$\dot{\boldsymbol{\omega}} = I^{-1}\left(\boldsymbol{\tau} - \boldsymbol{\omega} \times I\boldsymbol{\omega}\right) = I^{-1}\boldsymbol{\tau}_e + I^{-1}\left(\boldsymbol{\tau}_a - \boldsymbol{\omega} \times I\boldsymbol{\omega}\right) \tag{32}$$

where I is the matrix of inertia of the aircraft. The aerodynamic moments produced by the airframe include the contributions from the trim positions of the actuators:

$$\boldsymbol{\tau}_a = \frac{1}{2}\rho V^2 S \left(\begin{bmatrix} bC_{l_a} \\ \bar{c}C_{m_a} \\ bC_{n_a} \end{bmatrix} + B\left(\mathbf{x}\right)\boldsymbol{\delta}_{\text{trim}} \right) \tag{33}$$

Setting the angular acceleration as a virtual control input $\boldsymbol{\nu}_\omega\left(\mathbf{x}\right) = \dot{\boldsymbol{\omega}}$ and solving Eq. (32) for the required moments $\boldsymbol{\tau}_c = \boldsymbol{\tau}_e$ leads to the model-based inversion control law

$$\boldsymbol{\tau}_c = I\boldsymbol{\nu}_\omega\left(\mathbf{x}\right) - \frac{1}{2}\rho V^2 S \left(\begin{bmatrix} bC_{l_a} \\ \bar{c}C_{m_a} \\ bC_{n_a} \end{bmatrix} + B\left(\mathbf{x}\right)\boldsymbol{\delta}_{\text{trim}} \right) + \boldsymbol{\omega} \times I\boldsymbol{\omega} \tag{34}$$

which linearizes the system between the virtual control input $\boldsymbol{\nu}_\omega\left(\mathbf{x}\right)$ and $\boldsymbol{\omega}$. The required moments $\boldsymbol{\tau}_c$ are distributed over $\boldsymbol{\delta}$ by a linear control allocator. The linearized system can now be controlled through the virtual control input $\boldsymbol{\nu}_\omega\left(\mathbf{x}\right)$ such that the output follows a reference command $\boldsymbol{\omega}_c$, by using an outer state-feedback linear control law

$$\boldsymbol{\nu}_\omega\left(\mathbf{x}\right) = \boldsymbol{K}_{\omega_P}\left(\boldsymbol{\omega} - \boldsymbol{\omega}_c\right) + \boldsymbol{K}_{\omega_I}\int\left(\boldsymbol{\omega} - \boldsymbol{\omega}_c\right)dt + \boldsymbol{K}_{\omega_D}\left(\dot{\boldsymbol{\omega}} - \dot{\boldsymbol{\omega}}_c\right) \tag{35}$$

3. *Adaptation of the Linear Model*

As previously shown, the identified linear model fails to capture important nonlinear effects, which is particularly critical for parabolic and non-monotonic moment curves (e.g. those shown in Figures 6(b) and 6(c)). Since such errors can cause instability of the closed loop, the linear model needs to be adapted to ensure minimally acceptable performance.

The AMT, inboard LEF and SSD are restricted to deflect in one direction only. Thus their yawing moment curves are half-parabolas that can be approximated with a linear model with a reasonable mismatch, which can be absorbed by the robustness of the controller. The elevons and outboard LEF, however, can deflect in two directions, thus having parabolic yawing moment curves. Since these actuators are not primary sources of directional control power, their yawing moment derivatives were set to zero in the control effectiveness matrix. As a consequence, these effectors are used to produce pitching and rolling moments only, whereas their secondary-axis yawing moments are seen by the control system as external disturbances, which need to be compensated by other yawing moment-generating actuators.

These necessary simplifications of the model have two detrimental consequences on the overall performance of the FCS. First, the potential of the ICE control suite is underexploited (e.g. elevons cannot be used to produce yawing moments, which might be necessary in failure conditions or extreme maneuvers). Second, the yawing moments produced by the elevons and outboard LEF are seen as external disturbances, and need to be continuously suppressed by other control effectors.

B. INCA-Based Flight Control System Design

The INCA-based flight control system was designed with an incremental control scheme. This scheme relies upon angular acceleration and actuator position feedback loops, whereas model dependency is limited to a Jacobian model of the control-induced moments.

1. *Multivariate Simplex Spline-Based Jacobian Model*

As shown in Section III, the INCA method has a more relaxed dependency on an on-board aerodynamic model and therefore is more robust against model uncertainties. Instead of a full aerodynamic model, INCA is based on a control moment Jacobian model $\nabla_{\boldsymbol{\delta}} \Phi(\mathbf{x}, \boldsymbol{\delta})$ that includes the directional derivatives of $\boldsymbol{\tau}_e$ with respect to $\boldsymbol{\delta}$.

In this paper, the Jacobian control effectiveness matrix is derived from a multivariate simplex B-spline aerodynamic model of the ICE aircraft identified from the high-fidelity aerodynamic database described in Section IV. This spline model preserves the original model structure of aerodynamic terms:

$$\begin{aligned}
C_i = & + C^s_{i_1}(\alpha, M) + C^s_{i_2}(\alpha, \beta, M) + C^s_{i_3}(\alpha, \delta_{\text{ls}}, \delta_{\text{le}}, M) + C^s_{i_4}(\alpha, \delta_{\text{rs}}, \delta_{\text{re}}, M) \\
& + C^s_{i_5}(\alpha, \beta, \delta_{\text{lfi}}) + C^s_{i_6}(\alpha, \beta, \delta_{\text{rfi}}) + C^s_{i_7}(\alpha, \beta, \delta_{\text{lfi}}, \delta_{\text{lfo}}, M) + C^s_{i_8}(\alpha, \beta, \delta_{\text{rfi}}, \delta_{\text{rfo}}, M) \\
& + C^s_{i_9}(\alpha, \delta_{\text{lfo}}, \delta_{\text{la}}) + C^s_{i_{10}}(\alpha, \delta_{\text{rfo}}, \delta_{\text{ra}}) + C^s_{i_{11}}(\alpha, \delta_{\text{la}}, \delta_{\text{le}}) + C^s_{i_{12}}(\alpha, \delta_{\text{ra}}, \delta_{\text{re}}) \\
& + C^s_{i_{13}}(\alpha, \delta_{\text{rs}}, \delta_{\text{ls}}, \delta_{\text{pf}}, M) + C^s_{i_{14}}(\alpha, \beta, \delta_{\text{la}}) + C^s_{i_{15}}(\alpha, \beta, \delta_{\text{ra}}) + C^s_{i_{16}}(\alpha, \beta, \delta_{\text{ls}}) \\
& + C^s_{i_{17}}(\alpha, \beta, \delta_{\text{rs}}) + \frac{pb}{2V} C^s_{i_{18}}(\alpha, M) + \frac{q\bar{c}}{2V} C^s_{i_{19}}(\alpha, M) + \frac{rb}{2V} C^s_{i_{20}}(\alpha, M)
\end{aligned} \tag{36}$$

with $i = \{l, m, n, X, Y, Z\}$, where every model term $C^s_{i_n}$ is a multivariate B-spline defined over a simplex triangulation with 0th-order continuity. This model was identified with the original ICE aerodynamic database in [44] following the linear regression techniques presented in [45]. Including all the model terms corresponding to every dimensionless aerodynamic moment and force coefficients, the spline model consists on 108 spline functions.

From this model, the directional derivatives of every model term $C^s_{i_j}$ in the directions of $\boldsymbol{\delta}$ can be computed in a computationally efficient way with the method of model reduction of parabolic partial differential equations presented in [46]. This yields 13 partial derivatives of each of the 108 spline models, from which the control effectiveness Jacobian matrix is constructed as:

$$\nabla_{\boldsymbol{\delta}} \Phi(\alpha, \beta, M, \boldsymbol{\delta}) = \begin{bmatrix} \sum_{j=1}^{20} \frac{\partial C^s_{l_j}(\mathbf{x}, \boldsymbol{\delta})}{\partial \delta_1} & \sum_{j=1}^{20} \frac{\partial C^s_{l_j}(\mathbf{x}, \boldsymbol{\delta})}{\partial \delta_2} & \cdots & \sum_{j=1}^{20} \frac{\partial C^s_{l_j}(\mathbf{x}, \boldsymbol{\delta})}{\partial \delta_{13}} \\ \sum_{j=1}^{20} \frac{\partial C^s_{m_j}(\mathbf{x}, \boldsymbol{\delta})}{\partial \delta_1} & \sum_{j=1}^{20} \frac{\partial C^s_{m_j}(\mathbf{x}, \boldsymbol{\delta})}{\partial \delta_2} & \cdots & \sum_{j=1}^{20} \frac{\partial C^s_{m_j}(\mathbf{x}, \boldsymbol{\delta})}{\partial \delta_{13}} \\ \sum_{j=1}^{20} \frac{\partial C^s_{n_j}(\mathbf{x}, \boldsymbol{\delta})}{\partial \delta_1} & \sum_{j=1}^{20} \frac{\partial C^s_{n_j}(\mathbf{x}, \boldsymbol{\delta})}{\partial \delta_2} & \cdots & \sum_{j=1}^{20} \frac{\partial C^s_{n_j}(\mathbf{x}, \boldsymbol{\delta})}{\partial \delta_{13}} \end{bmatrix} \tag{37}$$

The Jacobian calculation was implemented on a real-time, highly optimized routine that can provide in the order of 10^4 Jacobian calculations per second. A key factor for the accuracy of the Jacobians is the continuity order between simplices. In this case, 0th-order continuity was used, and therefore the model represents the worst possible case in terms of continuity. This implies that the performance achieved in this paper can be improved by increasing the continuity order of the spline model.

The Jacobian model is not restricted to spline-based models. For instance, a locally linear numerical differentiation approach with a lookup table-based aerodynamic model could also be used to approximate the nonlinear Jacobian. A spline model was used in this thesis because it provides an elegant way to extend the INCA-based FCS into a fault-tolerant flight control system. Splines are function approximators that can be used in an on-line system identification framework, in contrast to lookup table-based models.

2. Multi-Axis Thrust Vectoring Jacobian Model

A Jacobian model providing the directional derivatives of the control moments produced by MTV can be obtained analytically by deriving the Jacobian matrix of $\boldsymbol{\tau}_T$ in Eq. (26):

$$\nabla_{\delta_{\rm tv}}\boldsymbol{\tau}_{\rm T}(\delta_{\rm ptv},\delta_{\rm ytv}) = {\rm T}d_n \begin{bmatrix} 0 & 0 \\ -\cos(\delta_{\rm ptv}) & 0 \\ \sin(\delta_{\rm ptv})\tan(\delta_{\rm ytv}) & -\cos(\delta_{\rm ptv})/\cos^2(\delta_{\rm ytv}) \end{bmatrix} \tag{38}$$

The MTV circular constraints in incremental form require further consideration. In an incremental control allocation scheme, the control allocator provides a commanded increment $\Delta\boldsymbol{\delta}_{\rm tv}$ over the current actuator position $\boldsymbol{\delta}_{{\rm tv}_0}$. If the resulting MTV deflection vector $\boldsymbol{\delta}_{\rm tv} = \boldsymbol{\delta}_{{\rm tv}_0} + \Delta\boldsymbol{\delta}_{\rm tv}$ violates the circular constraint, then a new increment $\Delta\boldsymbol{\delta}'_{\rm tv}$ must be computed such that the new resulting vector $\boldsymbol{\delta}'_{\rm tv} = \boldsymbol{\delta}_{{\rm tv}_0} + \Delta\boldsymbol{\delta}'_{\rm tv}$ satisfies the circular constraint while preserving the original direction of $\boldsymbol{\delta}_{\rm tv}$. This implies changing the modulus and direction of $\Delta\boldsymbol{\delta}_{\rm tv}$:

$$\Delta\boldsymbol{\delta}'_{\rm tv} = \frac{\delta_{{\rm tv}_{\max}}}{||\boldsymbol{\delta}_{{\rm tv}_0} + \Delta\boldsymbol{\delta}_{\rm tv}||}\left(\boldsymbol{\delta}_{{\rm tv}_0} + \Delta\boldsymbol{\delta}_{\rm tv}\right) - \boldsymbol{\delta}_{{\rm tv}_0} \tag{39}$$

3. Angular Rate Control Loop

INCA is implemented at the innermost control loop for body-frame angular rate control. Consider the aircraft rotational dynamic equations, where $\boldsymbol{\tau}_e$ is substituted by the nonlinear control effector model $\boldsymbol{\Phi}(\mathbf{x},\boldsymbol{\delta})$:

$$\dot{\boldsymbol{\omega}} = I^{-1}\left(\boldsymbol{\tau} - \boldsymbol{\omega}\times I\boldsymbol{\omega}\right) = I^{-1}\boldsymbol{\Phi}(\mathbf{x},\boldsymbol{\delta}) + I^{-1}\left(\boldsymbol{\tau}_a - \boldsymbol{\omega}\times I\boldsymbol{\omega}\right) \tag{40}$$

For a given time step, the incremental form of the rotational dynamics as a first-order Taylor expansion at the operating point $(\mathbf{x}_0, \boldsymbol{\delta}_0)$ is

$$\begin{aligned}\dot{\boldsymbol{\omega}} \simeq \dot{\boldsymbol{\omega}}_0 &+ \frac{\partial}{\partial \boldsymbol{\omega}} \left[I^{-1} \boldsymbol{\Phi} \left(\mathbf{x}, \boldsymbol{\delta} \right) + I^{-1} \left(\boldsymbol{\tau}_a - \boldsymbol{\omega} \times I \boldsymbol{\omega} \right) \right] \Big|_{\substack{\boldsymbol{\delta}=\boldsymbol{\delta}_0 \\ \mathbf{x}=\mathbf{x}_0}} \left(\boldsymbol{\omega} - \boldsymbol{\omega}_0 \right) \\ &+ \frac{\partial}{\partial \boldsymbol{\delta}} \left[I^{-1} \boldsymbol{\Phi} \left(\mathbf{x}, \boldsymbol{\delta} \right) + I^{-1} \left(\boldsymbol{\tau}_a - \boldsymbol{\omega} \times I \boldsymbol{\omega} \right) \right] \Big|_{\substack{\boldsymbol{\delta}=\boldsymbol{\delta}_0 \\ \mathbf{x}=\mathbf{x}_0}} \left(\boldsymbol{\delta} - \boldsymbol{\delta}_0 \right) \quad (41)\end{aligned}$$

where the angular accelerations at the current step $\dot{\boldsymbol{\omega}}_0$ can be obtained from angular accelerometers, signal processing or acceleration estimation methods.

According to the previously discussed time scale separation principle, the second term of the right-hand side of Eq. (41), i.e. the changes in angular acceleration due to changes in angular rates, is negligible for high sampling rates in comparison to the control-dependent term. This is explained in [28] as follows. Increments in actuator positions directly cause angular accelerations. Angular rates, however, only vary as a consequence of integrating angular accelerations, i.e. integrating the actuator deflection contributions. Therefore, when the sampling frequency of the FCC is high enough, the assumption $(\boldsymbol{\omega} - \boldsymbol{\omega}_0) \approx 0$ is valid. Practical implementation of incremental attitude control in fast-dynamics aerospace vehicles has proven that FCC frequencies of about 100 Hz are high enough for the time scale separation principle to hold [30].

Applying time scale separation and operating the partial derivatives, the incremental dynamic rotational equations are obtained as a function of the current angular accelerations and actuator positions:

$$\dot{\boldsymbol{\omega}} = \dot{\boldsymbol{\omega}}_0 + I^{-1} \nabla_{\boldsymbol{\delta}} \boldsymbol{\Phi} \left(\mathbf{x}_0, \boldsymbol{\delta}_0 \right) \Delta \boldsymbol{\delta} \quad (42)$$

Setting the angular acceleration as a virtual control input $\boldsymbol{\nu}_\omega (\mathbf{x}) = \dot{\boldsymbol{\omega}}$ and solving for $\nabla_{\boldsymbol{\delta}} \boldsymbol{\Phi} (\mathbf{x}_0, \boldsymbol{\delta}_0) \Delta \boldsymbol{\delta}$, the INCA formulation in Eq. (18) is found for the angular rate control problem:

$$\nabla_{\boldsymbol{\delta}} \boldsymbol{\Phi} \left(\mathbf{x}_0, \boldsymbol{\delta}_0 \right) \Delta \boldsymbol{\delta} = I \left[\boldsymbol{\nu}_\omega \left(\mathbf{x} \right) - \dot{\boldsymbol{\omega}}_0 \right] = \Delta \boldsymbol{\tau}_c \quad (43)$$

where the pseudo-control input $\mathbf{d}_c$ corresponds to the required increments of control-induced moments $\Delta \boldsymbol{\tau}_c$. At this point, the required control-induced moment increments $\Delta \boldsymbol{\tau}_c$ are allocated into actuator position increments $\Delta \boldsymbol{\delta}$ by a linear control allocator, where the CA problem is formulated in incremental form at every time step as: given the current state $\mathbf{x}_0$, the current actuator positions

$\boldsymbol{\delta}_0$ and a required increment of control-induced moments $\Delta\boldsymbol{\tau}_c$, determine an increment in the control effector positions $\Delta\boldsymbol{\delta}$ such that

$$\begin{gathered}\nabla_{\boldsymbol{\delta}}\boldsymbol{\Phi}\left(\mathbf{x}_0,\boldsymbol{\delta}_0\right)\Delta\boldsymbol{\delta}=\Delta\boldsymbol{\tau}_c\\ \text{subject to}\quad \underline{\boldsymbol{\Delta\delta}}\leq\boldsymbol{\Delta\delta}\leq\overline{\boldsymbol{\Delta\delta}}\end{gathered}\tag{44}$$

Here, the inner control law

$$\Delta\boldsymbol{\tau}_c=I\left[\boldsymbol{\nu}_\omega\left(\mathbf{x}\right)-\dot{\boldsymbol{\omega}}_0\right]\tag{45}$$

linearizes the system between the virtual control input $\boldsymbol{\nu}_\omega\left(\mathbf{x}\right)$ and $\boldsymbol{\omega}$. The linearized system can now be controlled through the virtual control input such that it follows a command $\boldsymbol{\omega}_c$ by using the outer state-feedback linear control law in Eq. (35).

The absolute actuator position commands are computed as $\boldsymbol{\delta}=\boldsymbol{\delta}_0+\Delta\boldsymbol{\delta}$. Note that the Jacobian matrix is also a function of the actuator positions, and therefore interactions between control effectors are considered in the control allocation process. Also, note that actual actuator position measurements $\boldsymbol{\delta}_0$ are fed back into the control system at each time step, and therefore the Jacobian matrix is always computed with the actual actuator positions. This also implies that the required increments $\Delta\boldsymbol{\delta}$ are always calculated over the actual actuator positions, avoiding couplings between control allocator and actuator dynamics typical of LCA-based control systems [34].

4. Global Convergence and SSDs

Since INCA dynamically drives the actuator vector towards the direction that best fulfills local moment increment commands, it is possible that it converges to local optima. This is not a problem if it is valid to assume that the optimal control distribution lies within the neighbourhood of the current actuator positions. This assumption is valid for most of the ICE actuators, since their moment curves do not have local minima in the directions of $\boldsymbol{\delta}$, and local minima in the directions of α, β and M are irrelevant to the control allocator since they are not control variables. However, the SSDs have a dramatic impact on the control effectiveness of trailing-edge control effectors, and therefore globally optimal control distributions might be available far away from the current control distribution.

It is worth noting that, besides providing lateral-directional control at high AoA, an important function of the SSDs is to redirect the airflow towards the upper wing skin at high AoA to recover control effectiveness of trailing-edge devices. In contrast, deflecting the SSDs at low AoA destroys the control effectiveness of downstream actuators. Therefore, it is reasonable to assume that globally optimal control distributions will have small SSD deflections at low AoA and big deflections at high AoA. Hence, convergence towards global optima can be subserved by forcing the SSDs to remain as closed as possible at low AoA, and as open as possible at high AoA. This can be achieved by scheduling the penalizing weights of the SSDs in the weighting matrix $W_{\mathbf{u}}$ as a function of α. In this case, the SSD penalties $W_{\mathbf{u}_{\mathrm{SSD}}}(\alpha)$ were scheduled as the exponential function

$$W_{\mathbf{u}_{\mathrm{SSD}}}(\alpha) = \left[-0.25 + 0.35\exp\left(1.6\alpha\right)\right]^{-1} \tag{46}$$

Although this scheduling is valid for the ICE configuration, the characteristics of each particular controlled system shall be studied in order to favour global convergence.

VI. Control Allocation Solvers

As described in Section V, the innermost loop of the designed FCSs relies upon a linear control allocator that distributes control moments into actuator positions in the LCA-based FCS and control moment increments into actuator position increments in the INCA-based FCS. In this paper, both FCS were implemented with two different linear CA solvers: the redistributed weighted pseudo-inverse (RWPI) and quadratic programming (QP) solved with the active set algorithm. These CA methods are briefly discussed in this section.

A. Redistributed Weighted Pseudo-Inverse

The RWPI method consists on using an explicit solution of the unconstrained LCA problem and iterating over the result by clipping saturated actuators. The explicit solution to the unconstrained problem can be derived analytically if the constraints from Eq. (8) are removed. The unconstrained control allocation problem consists on finding a control vector $\mathbf{u}$ that satisfies a control demand $\mathbf{d}_c$ while minimizing a secondary objective formulated as a quadratic cost function that penalizes displacement from a preferred control vector $\mathbf{u}_p$. A linear relationship $G\mathbf{u} = \mathbf{d}_c$ is assumed. Note that here the control vector is denoted as $\mathbf{u}$ to keep de discussion general, and corresponds to $\boldsymbol{\delta}$

for LCA and to $\Delta\boldsymbol{\delta}$ for INCA. Also, the matrix G corresponds to the control effectiveness matrix $B(\mathbf{x})$ in LCA and to the Jacobian matrix $\nabla_{\boldsymbol{\delta}}\boldsymbol{\Phi}(\mathbf{x},\boldsymbol{\delta})$ in INCA; and the pseudo-control input $\mathbf{d}_c$ corresponds to an absolute moment command $\boldsymbol{\tau}_c$ in LCA and to an incremental moment command $\Delta\boldsymbol{\tau}_c$ in INCA.

The minimization problem is formulated using a ℓ_2 norm cost function as: given an operating point $\mathbf{x}_0$, an affine relationship $G\mathbf{u} = \mathbf{d}_c$, a control demand $\mathbf{d}_c$ and a preference vector $\mathbf{u}_p$ determine a control input $\mathbf{u}$ such that

$$\begin{gathered}\min_{\mathbf{u}} \;\; \mathcal{J} = \frac{1}{2}\left(\mathbf{u}-\mathbf{u}_p\right)^T W_{\mathbf{u}}\left(\mathbf{u}-\mathbf{u}_p\right) \\ \text{subject to} \quad G\mathbf{u} = \mathbf{d}_c\end{gathered} \tag{47}$$

where $W_{\mathbf{u}}$ is a weighting matrix that penalizes to the use of some effectors over others. For the secondary objective, the most common approach is minimizing the control effort by setting $\mathbf{u}_p = 0$.

Analytically solving (47) with Lagrange multipliers [1, 12, 51] the explicit biased weighted pseudo-inverse solution is found:

$$\mathbf{u} = \mathbf{u}_p + G^{\sharp}\left(\mathbf{d}_c - G\mathbf{u}_p\right) \tag{48}$$

with

$$G^{\sharp} = W_{\mathbf{u}}^{-1}G^T\left(GW_{\mathbf{u}}^{-1}G^T\right)^{-1} \tag{49}$$

a generalized weighted pseudo-inverse. This method provides a solution to the unconstrained problem as long as it exists and GG^T is not rank-deficient.

The weighted pseudo-inverse solution does not consider local position and rate constraints, and hence it requires further processing. If the found $\mathbf{u}$ is within the local actuator limits, the solution is kept. Otherwise, if one or more effectors violate constraints, the next steps are followed. First, the columns in G corresponding to the actuators that violate the limits are zeroed, forming an auxiliary matrix G_{sat}. Second, the values of the saturated effectors are placed in the preference vector $\mathbf{u}_p$, forming an auxiliary preference vector $\mathbf{u}_{p,\text{sat}}$. Then, the redistributed weighted pseudo-inverse solution is re-computed as follows:

$$\mathbf{u} = \mathbf{u}_{p,\text{sat}} + G_{\text{sat}}^{\sharp}\left(\mathbf{d}_c - G\mathbf{u}_{p,\text{sat}}\right) \tag{50}$$

This process is repeated until all effectors are saturated or a solution within the local limits is found.

B. Quadratic Programming

The CA problem can be also solved as a numerical optimization problem with explicit constraints. In such cases, the common approach is to minimize a multi-objective cost function defined with a given norm, subject to local actuator constraints. ℓ_2- and ℓ_∞-based solutions are more popular since they tend to distribute the control effort over a larger number of actuators [26]. A very common approach is using the ℓ_2 norm to formulate the control allocation problem as a multi-objective constrained optimization problem, solved as a quadratic program:

$$\begin{gathered} \min_{\mathbf{u}} \; \mathcal{J} = W_{\mathbf{d}} \left|\left|G\mathbf{u} - \mathbf{d}_c\right|\right|_2^2 + \epsilon \; W_{\mathbf{u}} \left|\left|\mathbf{u} - \mathbf{u}_p\right|\right|_2^2 \\ \text{subject to} \quad \underline{\mathbf{u}} \leq \mathbf{u} \leq \overline{\mathbf{u}} \end{gathered} \tag{51}$$

where ϵ is a scalar, selected sufficiently small to prioritize the minimization of the allocation error over the secondary objective, and $W_{\mathbf{d}}$ and $W_{\mathbf{u}}$ are nonsingular weighting matrices.

Many numerical algorithms are available to solve the QP problem in real time. In [52], the authors concluded that the active set algorithm converges exactly to the optimal solution in a finite number of steps and is computationally efficient for control allocation problems of small and medium size. In this paper, the QP problem is implemented with the active set algorithm described in [53].

C. Preference Vector in Incremental Form

The INCA scheme requires a reformulation of the preference vector used in the control allocation algorithms, since $\Delta\boldsymbol{\delta}_p$ refers to a preferred actuator position increment. Setting $\Delta\boldsymbol{\delta}_p = 0$ results in complementary actuators diverging to asymmetric nonzero deflections while still producing a resultant moment of zero. In order to bring the actuators to their preferred absolute positions whenever it is possible, the incremental preference vector $\Delta\boldsymbol{\delta}_p$ is computed at each time step as

$$\Delta\boldsymbol{\delta}_p = \min\left(\left|\boldsymbol{\delta}_p - \boldsymbol{\delta}_0\right|, \; \left|\overline{\Delta\boldsymbol{\delta}}\right|, \; \left|\underline{\Delta\boldsymbol{\delta}}\right|\right) \cdot \operatorname{sign}\left(\boldsymbol{\delta}_p - \boldsymbol{\delta}_0\right) \tag{52}$$

VII. Saturation Handling: Pseudo-Control Hedging

Actuator saturation represents a problem when control commands exceed the capabilities of the actuators under rate and position constraints. When physically unachievable control commands are given, the system can run into command windup problems, which compromises the overall performance and stability of the system. To overcome this problem, pseudo-control hedging (PCH) was proposed in [47] and developed in [48, 49] as an adaptation system to hedge the pseudo-control input of the control system to accommodate the commands to the limitations of the actuators set, thus avoiding physically unachievable commands. PCH has been successfully used as a partial form of flight envelope protection and anti-windup system in [29, 50].

PCH was implemented in the designed FCSs to shape the virtual control command $\boldsymbol{\nu}_\omega(\mathbf{x})$ by substracting the difference between the commanded $\boldsymbol{\nu}_\omega(\mathbf{x})$ and the actual virtual control achieved, estimated with measured actuator positions $\boldsymbol{\delta}_0$ as $\hat{\boldsymbol{\nu}}_\omega(\mathbf{x}) = \mathbf{f}(\mathbf{x}_0, \boldsymbol{\delta}_0)$, where $\mathbf{f}(\mathbf{x}, \boldsymbol{\delta})$ is the virtual control law. The pseudo-control hedge is computed as

$$\boldsymbol{\nu}_h(\mathbf{x}) = \boldsymbol{\nu}_\omega(\mathbf{x}) - \hat{\boldsymbol{\nu}}_\omega(\mathbf{x}) \tag{53}$$

The hedge $\boldsymbol{\nu}_h(\mathbf{x})$ is fed back into a first-order reference model (RM) as a compensation signal. The reference model $\boldsymbol{\nu}_{\mathrm{rm}}(\mathbf{x})$ is given by

$$\boldsymbol{\nu}_{\mathrm{rm}}(\mathbf{x}) = K_{\mathrm{rm}}(\boldsymbol{\omega}_c - \boldsymbol{\omega}_{\mathrm{rm}}) \tag{54}$$

with K_{rm} a diagonal matrix. The hedged reference signal fed as a control input into the attitude control system is the state vector of the reference model

$$\boldsymbol{\omega}_{\mathrm{rm}} = \frac{1}{s}\left(\boldsymbol{\nu}_{\mathrm{rm}}(\mathbf{x}) - \boldsymbol{\nu}_h(\mathbf{x})\right) \tag{55}$$

When no saturation occurs, $\boldsymbol{\nu}_h(\mathbf{x}) = 0$ and the reference model behaves as a low-pass filter of bandwidth K_{rm_i} for the i-th component of $\boldsymbol{\omega}_{\mathrm{rm}}$. Under actuator saturation, the hedge $\boldsymbol{\nu}_h(\mathbf{x})$ corresponds to the difference between the commanded virtual control input and the estimated virtual control achieved, based on the actual positions of the control effectors. The hedge signal $\boldsymbol{\nu}_h(\mathbf{x})$ is used to reshape the reference and avoid unfeasible commands. The reference model $\boldsymbol{\nu}_{\mathrm{rm}}(\mathbf{x})$ corresponds to the first-order derivatives of the commanded variables, which can be used as a feedforward term added to $\boldsymbol{\nu}_\omega(\mathbf{x})$ to improve tracking performance [29].

In the LCA-based FCS the virtual control input is given by the control law

$$\boldsymbol{\nu}_\omega(\mathbf{x}) = \frac{1}{2}\rho V^2 S I^{-1} B(\mathbf{x})\boldsymbol{\delta} + I^{-1}(\boldsymbol{\tau}_a - \boldsymbol{\omega} \times I\boldsymbol{\omega}) \tag{56}$$

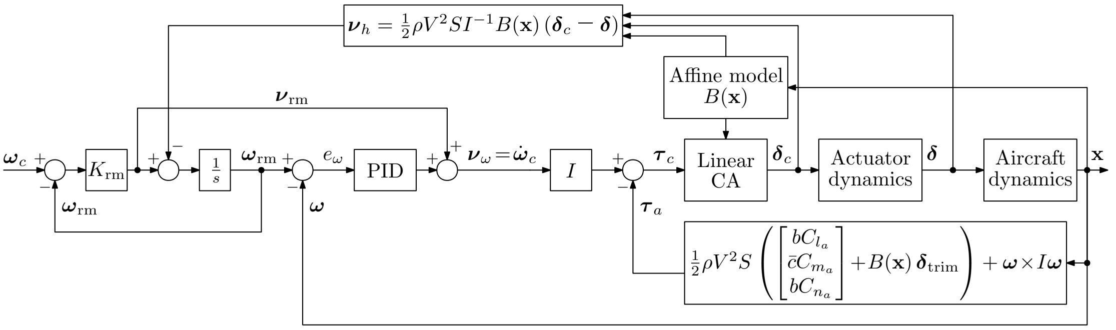

Fig. 7 Schematic of the LCA-based angular rate control system with PCH.

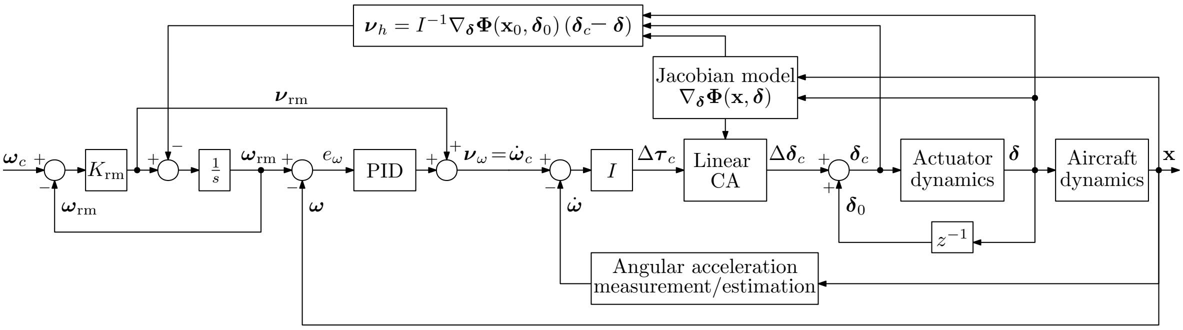

Fig. 8 Schematic of the INCA-based angular rate control system with PCH.

and therefore the pseudo-control hedge is given by

$$\boldsymbol{\nu}_{h_{\mathrm{LCA}}}(\mathbf{x}) = \left[\frac{1}{2}\rho V^2 S I^{-1} B(\mathbf{x})\,\boldsymbol{\delta}_c + I^{-1}(\boldsymbol{\tau}_a - \boldsymbol{\omega}\times I\boldsymbol{\omega})\right] - \left[\frac{1}{2}\rho V^2 S I^{-1} B(\mathbf{x})\,\boldsymbol{\delta} + I^{-1}(\boldsymbol{\tau}_a - \boldsymbol{\omega}\times I\boldsymbol{\omega})\right] \tag{57}$$

$$\boldsymbol{\nu}_{h_{\mathrm{LCA}}}(\mathbf{x}) = \frac{1}{2}\rho V^2 S I^{-1} B(\mathbf{x})\,(\boldsymbol{\delta}_c - \boldsymbol{\delta}) \tag{58}$$

In the INCA-based FCS the virtual control input is given by the control law

$$\boldsymbol{\nu}_\omega(\mathbf{x}) = \dot{\boldsymbol{\omega}}_0 + I^{-1}\nabla_{\boldsymbol{\delta}}\boldsymbol{\Phi}(\mathbf{x}_0, \boldsymbol{\delta}_0)\,(\boldsymbol{\delta} - \boldsymbol{\delta}_0) \tag{59}$$

and therefore the pseudo-control hedge is given by

$$\boldsymbol{\nu}_{h_{\mathrm{INCA}}}(\mathbf{x}) = \left[\dot{\boldsymbol{\omega}}_0 + I^{-1}\nabla_{\boldsymbol{\delta}}\boldsymbol{\Phi}(\mathbf{x}_0, \boldsymbol{\delta}_0)\,(\boldsymbol{\delta}_c - \boldsymbol{\delta}_0)\right] - \left[\dot{\boldsymbol{\omega}}_0 + I^{-1}\nabla_{\boldsymbol{\delta}}\boldsymbol{\Phi}(\mathbf{x}_0, \boldsymbol{\delta}_0)\,(\boldsymbol{\delta} - \boldsymbol{\delta}_0)\right] \tag{60}$$

$$\boldsymbol{\nu}_{h_{\mathrm{INCA}}}(\mathbf{x}) = I^{-1}\nabla_{\boldsymbol{\delta}}\boldsymbol{\Phi}(\mathbf{x}_0, \boldsymbol{\delta}_0)\,(\boldsymbol{\delta}_c - \boldsymbol{\delta}) \tag{61}$$

The internal structures of the LCA-based and the INCA-based body rate control systems, including PCH, are given in Figures 7 and 8 respectively.

VIII. Outer Control Loops

The reference maneuvers used to assess the performance of the LCA-based and the INCA-based controllers were coded as predefined reference signals. In order to fly these maneuvers, a series of outer loops were designed to track each kind of reference. Three different outer loops were designed to fly different types of reference trajectories: a sideslip compensation loop, an aerodynamic inversion loop and an Euler angle inversion loop with flight path guidance. In order to make a fair comparison, the same outer loops were used with both the LCA-based and the INCA-based controllers. The design and implementation of these outer loops is discussed in this section. Additionally, an auto-throttle (A/T) linear control loop was implemented for speed control using throttle as control input.

A. Sideslip Inversion Outer Loop

The sideslip dynamic inversion loop compensates the sideslip angle to perform coordinated turns whereas leaving roll and pitch rates as direct controlled variables. For this, a dynamic inversion of the sideslip angle was performed. The sideslip angle β can be computed as

$$\beta = \arcsin \frac{v}{V} \tag{62}$$

The first derivative of Eq. (62) is

$$\dot{\beta} = \frac{\dot{v}V - v\dot{V}}{V\sqrt{u^2+w^2}} = \frac{\dot{v}}{\sqrt{u^2+w^2}} - \frac{v\left(u\dot{u}+v\dot{v}+w\dot{w}\right)}{\left(u^2+v^2+w^2\right)\sqrt{u^2+w^2}} \tag{63}$$

The accelerations in aerodynamic frame are given by

$$\begin{aligned}
\dot{u} =& A_x - g\sin\theta + rv - qw \\
\dot{v} =& A_y + g\sin\phi\cos\theta - ru + pw \\
\dot{w} =& A_z + g\cos\theta\cos\phi + qu - pv
\end{aligned} \tag{64}$$

Substituting Eqs. (64) into Eq. (63) gives

$$\dot{\beta} = \left(\frac{1}{\sqrt{u^2+w^2}}\right)\left(F_x + F_y + F_z\right) + \begin{bmatrix} \frac{w}{\sqrt{u^2+w^2}} & 0 & \frac{-u}{\sqrt{u^2+w^2}} \end{bmatrix} \begin{bmatrix} p \\ q \\ r \end{bmatrix} \tag{65}$$

with

$$\begin{aligned} F_x &= -\frac{uv}{V^2}\left(A_x - g\sin\theta\right) \\ F_y &= \left(1 - \frac{v}{V^2}\right)\left(A_y + g\sin\phi\cos\theta\right) \\ F_z &= -\frac{vw}{V^2}\left(A_z + g\cos\phi\cos\theta\right) \end{aligned} \tag{66}$$

Introducing the virtual control input $\nu_\beta\left(\mathbf{x}\right) = \dot{\beta}$ and solving for the input r the sideslip dynamic inversion law is obtained:

$$\begin{aligned} r_c = \underbrace{\left(\frac{-u}{\sqrt{u^2+w^2}}\right)}_{a_\beta(\mathbf{x})}^{-1} \left[\nu_\beta\left(\mathbf{x}\right) - \underbrace{\frac{1}{\sqrt{u^2+w^2}}\left(F_x + F_y + F_z + wp_c\right)}_{b_\beta(\mathbf{x})}\right] \\ = a_\beta\left(\mathbf{x}\right)^{-1}\left[\nu_\beta\left(\mathbf{x}\right) - b_\beta\left(\mathbf{x}\right)\right] \end{aligned} \tag{67}$$

B. Aerodynamic Inversion Loop

Similarly, a dynamic inversion loop can be used to control the aerodynamic angles ϕ, α and β. The dynamics of the bank angle are given by

$$\dot{\phi} = \begin{bmatrix} 1 & \sin\phi\tan\theta & \cos\phi\tan\theta \end{bmatrix} \begin{bmatrix} p \\ q \\ r \end{bmatrix} \tag{68}$$

Introducing the virtual control input $\nu_\phi\left(\mathbf{x}\right) = \dot{\phi}$ and solving for the body rates as control inputs, the bank angle dynamic inversion law is obtained:

$$\begin{bmatrix} p_c \\ q_c \\ r_c \end{bmatrix} = \underbrace{\begin{bmatrix} 1 & \sin\phi\tan\theta & \cos\phi\tan\theta \end{bmatrix}}_{a_\phi(\mathbf{x})}^{-1} \nu_\phi\left(\mathbf{x}\right) = a_\phi\left(\mathbf{x}\right)^{-1}\nu_\phi\left(\mathbf{x}\right) \tag{69}$$

The dynamics of the angle of attack α are given by

$$\dot{\alpha} = \arcsin\frac{w}{V} = \frac{u\dot{w} - w\dot{u}}{u^2 + w^2} \tag{70}$$

Substituting Eqs. (64) into Eq. (70) gives

$$\dot{\alpha} = \left(\frac{1}{u^2+w^2}\right)\left(u\left(A_z + g\cos\theta\cos\phi\right) - w\left(A_x - g\sin\theta\right)\right) + \begin{bmatrix} \frac{-uv}{u^2+w^2} & 1 & \frac{-vw}{u^2+w^2} \end{bmatrix} \begin{bmatrix} p \\ q \\ r \end{bmatrix} \tag{71}$$

Introducing the virtual control input $\nu_\alpha(\mathbf{x}) = \dot{\alpha}$ and solving for the body rates as control inputs, the angle of attack dynamic inversion law is obtained:

$$\begin{bmatrix} p_c \\ q_c \\ r_c \end{bmatrix} = \underbrace{\begin{bmatrix} \frac{-uv}{u^2+w^2} & 1 & \frac{-vw}{u^2+w^2} \end{bmatrix}}_{a_\alpha(\mathbf{x})}^{-1} - \underbrace{\left(\frac{1}{u^2+w^2}\right)\left(u\left(A_z + g\cos\theta\cos\phi\right) - w\left(A_x - g\sin\theta\right)\right)}_{b_\alpha(\mathbf{x})}$$

$$= a_\alpha(\mathbf{x})^{-1}\left[\nu_\alpha(\mathbf{x}) - b_\alpha(\mathbf{x})\right] \tag{72}$$

The sideslip angle dynamic inversion law for the aerodynamic inversion loop can be obtained by re-arranging Eq. (65) with the three body rates as control inputs:

$$\begin{bmatrix} p_c \\ q_c \\ r_c \end{bmatrix} = \underbrace{\begin{bmatrix} \frac{w}{u^2+w^2} & 0 & \frac{-u}{u^2+w^2} \end{bmatrix}}_{a_\beta(\mathbf{x})}^{-1} - \underbrace{\left(\frac{1}{\sqrt{u^2+w^2}}\right)\left(F_x + F_y + F_z\right)}_{b_\beta(\mathbf{x})}$$

$$= a_\beta(\mathbf{x})^{-1}\left[\nu_\beta(\mathbf{x}) - b_\beta(\mathbf{x})\right] \tag{73}$$

Combining the three control channels, the aerodynamic inversion control law is

$$\begin{bmatrix} p_c \\ q_c \\ r_c \end{bmatrix} = \begin{bmatrix} a_\phi(\mathbf{x}) \\ a_\alpha(\mathbf{x}) \\ a_\beta(\mathbf{x}) \end{bmatrix}^{-1} \left(\begin{bmatrix} \nu_\phi(\mathbf{x}) \\ \nu_\alpha(\mathbf{x}) \\ \nu_\beta(\mathbf{x}) \end{bmatrix} - \begin{bmatrix} 0 \\ b_\alpha(\mathbf{x}) \\ b_\beta(\mathbf{x}) \end{bmatrix} \right) \tag{74}$$

C. Flight Path Guidance Loop with Euler Angle Inversion

A guidance loop was designed in order to use flight path angle γ and bank angle ϕ as control inputs from a reference trajectory and a sideslip compensator in the directional channel to coordinate turns. For this, first an Euler angle dynamic inversion loop was set up, whose pseudo-control inputs were provided by an outer linear loop controlling ϕ, γ and β.

The relationship between body angular rates and Euler angular rates in the lateral and longitudinal channels is

$$\begin{bmatrix} \dot{\phi} \\ \dot{\theta} \end{bmatrix} = \begin{bmatrix} 1 & \sin\phi\tan\theta & \cos\phi\tan\theta \\ 0 & \cos\theta & -\sin\phi \end{bmatrix} \begin{bmatrix} p \\ q \end{bmatrix} \tag{75}$$

setting the virtual control inputs $\nu_\phi(\mathbf{x}) = \dot{\phi}$ and $\nu_\theta(\mathbf{x}) = \dot{\theta}$ and solving for the body rates as control inputs, the Euler dynamic inversion law is obtained:

$$\begin{bmatrix} p_c \\ q_c \end{bmatrix} = \underbrace{\begin{bmatrix} 1 & \sin\phi\tan\theta & \cos\phi\tan\theta \\ 0 & \cos\theta & -\sin\phi \end{bmatrix}}_{[a_\phi(\mathbf{x}) \;\; a_\theta(\mathbf{x})]^T}{}^{-1} \begin{bmatrix} \nu_\phi(\mathbf{x}) \\ \nu_\theta(\mathbf{x}) \end{bmatrix} \tag{76}$$

Including the sideslip inversion law in Eq. (73), the Euler angle inversion law is

$$\begin{bmatrix} p_c \\ q_c \\ r_c \end{bmatrix} = \begin{bmatrix} a_\phi(\mathbf{x}) \\ a_\theta(\mathbf{x}) \\ a_\beta(\mathbf{x}) \end{bmatrix}^{-1} \left(\begin{bmatrix} \nu_\phi(\mathbf{x}) \\ \nu_\theta(\mathbf{x}) \\ \nu_\beta(\mathbf{x}) \end{bmatrix} - \begin{bmatrix} 0 \\ 0 \\ b_\beta(\mathbf{x}) \end{bmatrix} \right) \tag{77}$$

The references for the pseudo-control input $\boldsymbol{\nu}_{\text{guid}}(\mathbf{x}) = \begin{bmatrix} \dot{\phi}_c & \dot{\theta}_c & \dot{\beta}_c \end{bmatrix}$ are provided by a linear outer loop with ϕ_c, γ_c and β_c as references:

$$\begin{bmatrix} \dot{\phi}_c \\ \dot{\theta}_c \\ \dot{\beta}_c \end{bmatrix} = \mathbf{K}_{\text{guid}_P} \begin{bmatrix} (\phi - \phi_c) \\ (\gamma - \gamma_c) \\ (\beta - \beta_c) \end{bmatrix} + \mathbf{K}_{\text{guid}_I} \begin{bmatrix} \int (\phi - \phi_c)\, dt \\ \int (\gamma - \gamma_c)\, dt \\ \int (\beta - \beta_c)\, dt \end{bmatrix} + \mathbf{K}_{\text{guid}_D} \begin{bmatrix} (\dot{\phi} - \dot{\phi}_c) \\ (\dot{\gamma} - \dot{\gamma}_c) \\ (\dot{\beta} - \dot{\beta}_c) \end{bmatrix} \tag{78}$$

IX. Simulations and Results

Real-time flight simulations were performed to assess the performance of the INCA-based FCS with respect to the baseline LCA-based system. First, a simple maneuver with direct body rate input was performed to obtain straightforward insight on the overall behaviour of both systems. Second, this manoeuvre was used to perform a sensitivity analysis of the INCA system to Jacobian model mismatch. Finally, four reference maneuvers with different degrees of aggressiveness were flown to assess the systems when pushed towards the limits of the flight envelope.

The flight simulations were set up in a Matlab/Simulink framework. The simulations were run in real time with a 4th-order Runge-Kutta solver with a fixed sampling rate of 100Hz. The simulations were performed in a 64-bit computer with four Intel(R) Core(TM) i7-4702MQ CPU @ 2.20GHz processors and 16.0 Gb RAM. The simulations were initialized in trim conditions at an altitude of 20000 ft and $M = 0.85$. The initial true airspeed of 880 ft/sec was set as a constant reference to the A/T controller. In all the simulations, the linear gains of the innermost body rate control loop were set to $K_{P_p} = K_{P_q} = 6.5$, $K_{P_r} = 5.8$, $K_{I_p} = K_{I_q} = K_{I_r} = 0$ and $K_{D_p} = K_{D_q} = K_{D_r} = 0.5$. The reference model gains K_{rm} were all set to 10. The penalization gains in $W_{\boldsymbol{\delta}}$ were set to 1 for all control effectors except for the AMTs, which were set to 0.5, and for the SSDs, which were set as a function of α as given by Eq. (46). The penalization gains in $W_{\boldsymbol{\tau}}$ were all set to 1. The control preference vector $\boldsymbol{\delta}_p$ was 0 for all control effectors in all cases.

X. 3211 maneuver with Sideslip Compensation

The first simulation was set up with the sideslip inversion loop, using roll and pitch body rates and sideslip angle as control input commands. These simulations are intended to provide general insight on the behaviour of the two FCS solved with both RWPI and QP. The control inputs were simultaneous 3211 signals with amplitudes of 10 deg/sec for the roll and pitch channels and 3 deg for the sideslip channel. 3211 inputs consist of two consecutive pulse doublets, the pulses of which have durations of 3, 2, 1 and 1 seconds. These inputs are known to excite a significant frequency range of the aircraft operational bandwidth [54]. The gains used for the sideslip loop were $K_{\beta_P} = 1.60$, $K_{\beta_I} = 0.30$ and $K_{\beta_D} = 0.00$.

The time histories of the controlled variables along the 3211 maneuver are given in Figures 9 and 10 with the FCS using the RWPI and QP solvers respectively. Important deficiencies can be observed with the LCA-based controller, which exhibits large excursions from the commanded values, including overshoots and oscillations. This behaviour is consistent with the fact that many nonlinear aerodynamic effects and interactions between control effectors are neglected in the linear model used in the LCA-based controller, which need to be compensated with other actuators resulting in a substantial degradation of the tracking performance. On the other hand, it can be observed that INCA presents a remarkably superior tracking performance in both cases. It is worth noting that the tracking performance is considerably better with the QP solver in both systems. Consequently, for the sake of conciseness, only results with the QP solver will be shown in the remainder.

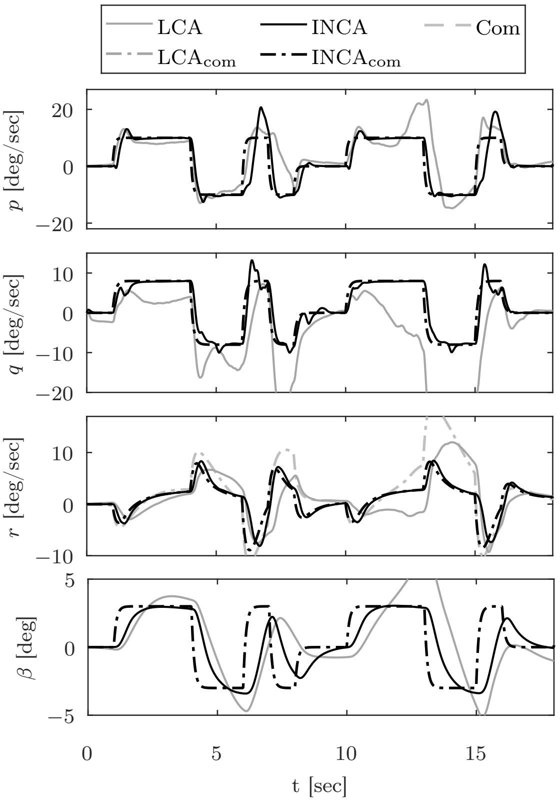

Fig. 9 Controlled variables for the 3211 maneuver using the RWPI solver.

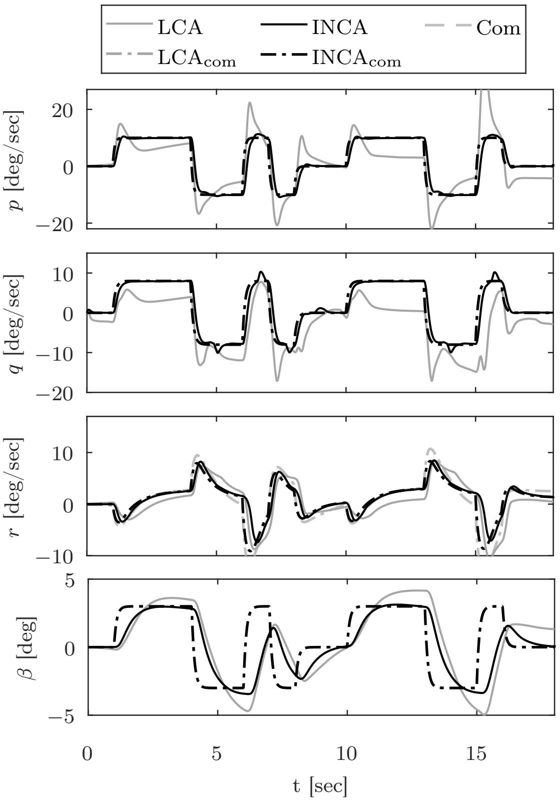

Fig. 10 Controlled variables of the 3211 maneuver using the QP solver.

A key performance metric for CA systems is allocation performance, which refers to the capability of the control allocator to attain the control moments required by the high-level FCS, i.e. minimizing the allocation error $\boldsymbol{\tau} - \boldsymbol{\tau}_c$. The time histories of the commanded and attained control-induced moments for the 3211 maneuver with LCA and INCA solved with QP are given in Figure 11. Large excursions are observed with LCA in the three channels. On the other hand, the control allocation performance is remarkably superior with INCA. Note, in addition, that due to the better allocation performance, INCA requires considerably smaller control-induced moments to track the reference commands. Finally, the time histories of the 13 control effector positions along the 3211 maneuver are given in Figure 12.

A. Robustness Analysis to Jacobian Model Mismatch

The sensitivity of the performance of INCA to errors in the control effectiveness Jacobian model $\nabla_{\boldsymbol{\delta}} \Phi \left(\boldsymbol{x}, \boldsymbol{\delta}\right)$ is a relevant subject of study. As deduced in the theoretical development of the method,

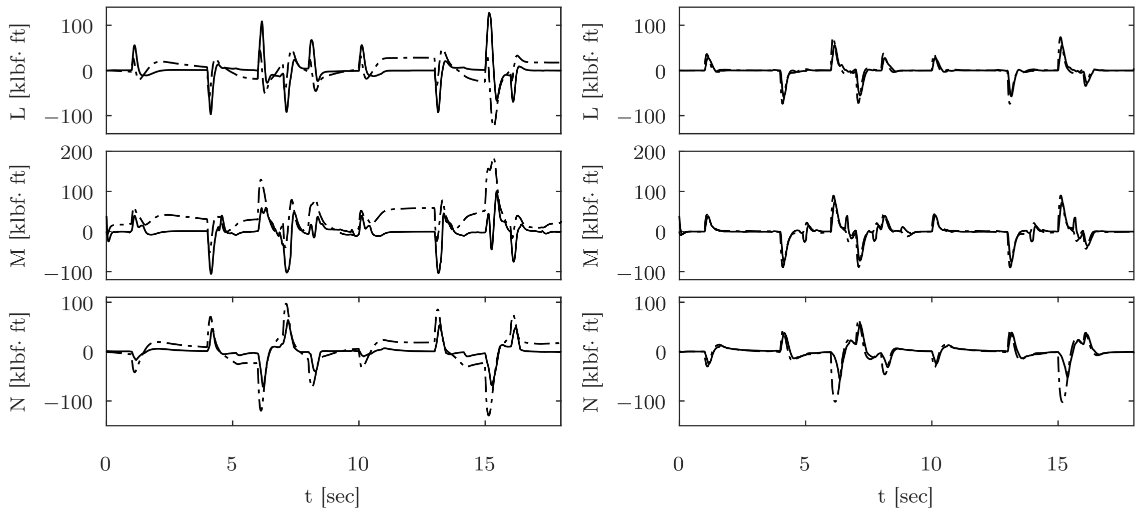

Fig. 11 Commanded (dot-dashed line) and attained (solid line) control-induced moments of the 3211 maneuver with the LCA (left) and INCA (right) control allocators with the QP solver.

it is expected that the angular acceleration feedback provides considerable robustness against model mismatch. The sensitivity analysis presented here was intended to support this hypothesis.

There are three ways in which the accuracy of the Jacobian model can be altered. First, by changing the order of continuity between the simplices of the original spline model $\Phi\left(\boldsymbol{x},\boldsymbol{\delta}\right)$. Abrupt discontinuities in the control effectiveness model cause undesirable peaks in the Jacobian function. The spline model used in this paper has 0th-order continuity between simplices, and therefore represents the worst case scenario in terms of continuity. The two other possible alterations to the model are the introduction of a scaling factor and offset in the Jacobian terms. To analyze model sensitivity, offset and scaling were introduced in the Jacobian model as follows:

$$\nabla_{\boldsymbol{\delta}}\Phi'\left(\boldsymbol{x},\boldsymbol{\delta}\right) = m_{\Phi}\nabla_{\boldsymbol{\delta}}\Phi_{\max} + n_{\Phi}\nabla_{\boldsymbol{\delta}}\Phi\left(\boldsymbol{x},\boldsymbol{\delta}\right) \tag{79}$$

where $\nabla_{\boldsymbol{\delta}}\Phi_{\max}$ is a matrix containing the maximum values of the Jacobian terms obtained along the 3211 reference trajectory, m_{Φ} represents the fraction of the maximum Jacobian values introduced as offset and n_{Φ} represents the scaling factor of the original Jacobian function.

The sensitivity analysis consisted on simulating the 3211 maneuver described in Section X with INCA/QP by varying the model offset and scaling between simulations. The scale factor n_{Φ} was varied from 0.6 to 1.4 in steps of 0.01 taking a total of 81 values, and the offset m_{Φ} was varied

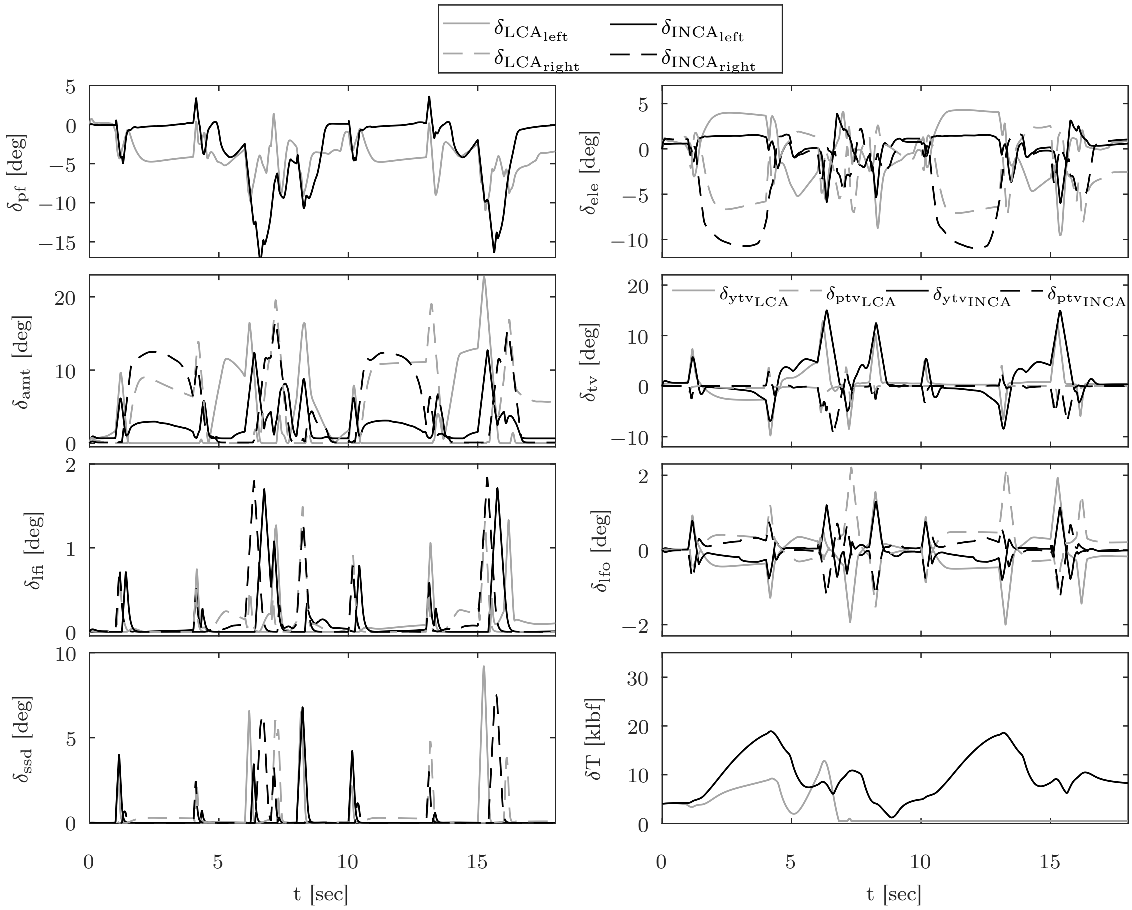

Fig. 12 Control effector positions of the 3211 maneuver with the QP solver.

between -0.35 and 0.35 in steps of 0.01 taking a total of 101 values. This led to a total amount of 8181 simulations. The allocation error RMS $(\boldsymbol{\tau} - \boldsymbol{\tau}_c)$ and the control effort RMS $(\boldsymbol{\delta} - \boldsymbol{\delta}_p)$ along the trajectory were recorded for each simulation. The maps of control allocation error and control effort obtained for the range of tested conditions are given in Figures 13 and 14 respectively.

For the baseline condition with no model alteration, the allocation error was 11.2 klbf·ft and the control effort was 3.4 deg. For the whole region of study, the maximum increases of allocation error and control effort were of 25% and 17% respectively, which demonstrates considerable robustness against Jacobian model mismatch. It is worth noting that the allocation performance improves considerably for decreasing scaling factors. The best allocation performance, with an error reduction of more than 13%, was achieved with the minimum scaling factor tested, close to the 0% offset region. This reveals that INCA benefits from underestimation of the magnitude of the Jacobian terms.

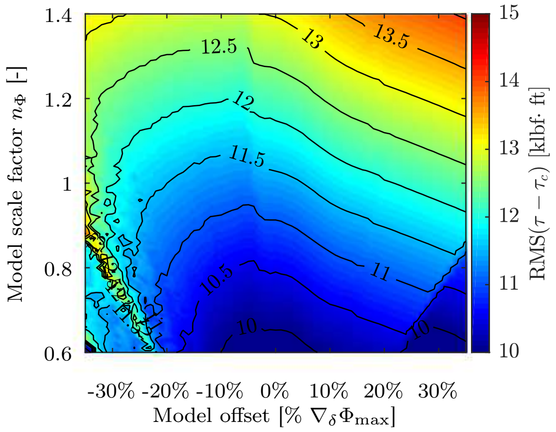

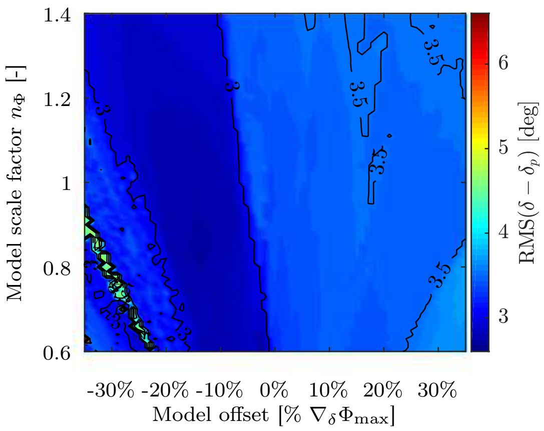

Fig. 13 Sensitivity of the control allocation error to Jacobian model mismatch.

Fig. 14 Sensitivity of the control effort to Jacobian model mismatch.

B. Aggressive Flight Maneuvers

The ICE aircraft is a highly maneuverable fighter designed for air combat, and therefore its design, including flight control and stability systems, must demonstrate high maneuverability and stability in extreme regions of its flight envelope. In order to assess the performance of the INCA-based FCS when the aircraft is pushed towards the limits of its operational range, four tests were designed with aggressive air combat aerobatic maneuvers:

1. Maneuver A: high-bank climbing spiral using the guidance outer loop with Euler angle inversion with bank angle ϕ, glide path angle γ and sideslip β as control inputs. The reference trajectory consists of a constant bank angle reference of 80 deg with a constant flight path angle of 15 deg and zero sideslip.

2. Maneuver B: barrel roll using the sideslip compensation loop with direct roll and pitch body rate control inputs. The reference trajectory consists of constant pitch and roll rate inputs, synchronized to complete two barrel rolls and exit the maneuver with the initial heading and zero flight path angle (straight-and-level flight).

3. Maneuver C: highly demanding sequence of aerobatic maneuvers using the sideslip compensation loop with direct roll and pitch body rate control inputs. The sequence of maneuvers is: aileron roll, asymmetric looping with nonzero sideslip, half 8-point hesitation roll and Immelmann turn. The aileron roll consists on an agressive roll input of 180 deg/sec with two full

turns about the x-axis in 4 seconds. The asymmetric looping consists on a constant pitch rate input of 18 deg/sec for 20 sec. During the first 10 seconds of the looping, a 5 deg sideslip input is given, which returns to 0 deg for the last 10 seconds of the looping maneuver. This results in some lateral displacement during the looping. The half 8-point hesitation roll consists on four quick roll rate step inputs of 90 deg/sec with a duration of 0.5 sec each and with a separation of 1 sec after each step, finishing the maneuver with a roll angle of 180 deg. At this position, a downward half-looping follows, completing an Immelmann turn and ending the trajectory in straight-and-level flight.

4. Maneuver D: high-AoA and high-sidselip commands using the aerodynamic inversion loop with the aerodynamic angles α and β and the bank angle ϕ as control inputs. This maneuver is designed to test the behaviour of the flight control system at high AoA, where the nonlinearities and interactions between control effectors become most significant. The reference trajectory consists on a doublet α input of ± 40 deg followed by a doublet β input with ± 25 deg, while keeping the bank angle reference at 0 deg.

All four maneuvers were flown with the LCA- and INCA-based FCS using the RWPI and QP solvers to compare performance. The simulation of maneuver D with LCA/QP resulted in unstable flight. This was also the case for the highly demanding maneuver C, which resulted in unstable flight with LCA/QP and INCA/RWPI. The spatial trajectories obtained from the aggressive maneuvers with LCA and INCA with the QP solver are shown in Figure 15. Note that, since LCA/QP was unstable for maneuver C, LCA/RWPI is shown for this maneuver instead.

As an example, the results of maneuver B (barrel roll) with LCA and INCA solved with QP are shown below. Figure 16 shows the controlled variables for this maneuver. Very large excursions from the commanded values can be observed with LCA, especially in the longitudinal and directional channels. INCA, however, tracks all the body rate references with excellent performance, with no major excursions, oscillations or peaks. Figure 17 shows the commanded and attained moments by both control allocators. Large control allocation errors are observed with LCA in contrast to INCA, which produces the commanded moments quickly and accurately. This results in smaller moments required to track the reference commands.

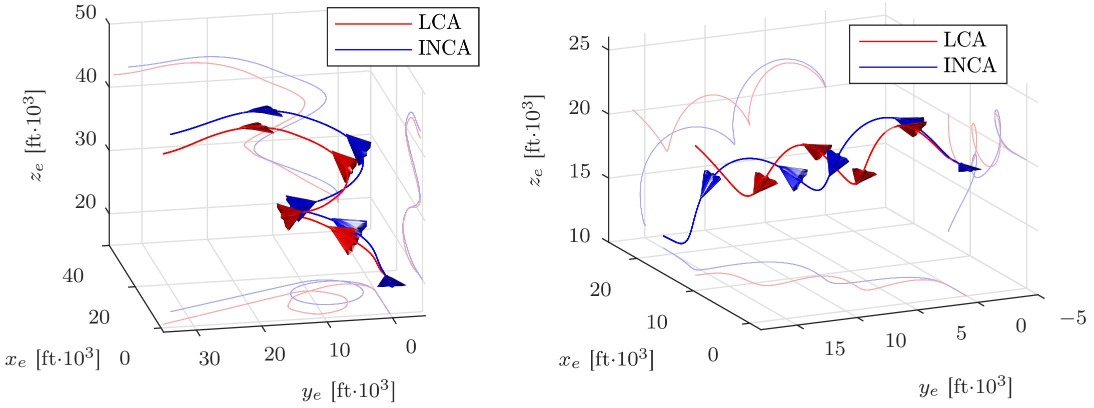

(a)Maneuver A with LCA/QP and INCA/QP.

(b)Maneuver B with LCA/QP and INCA/QP.

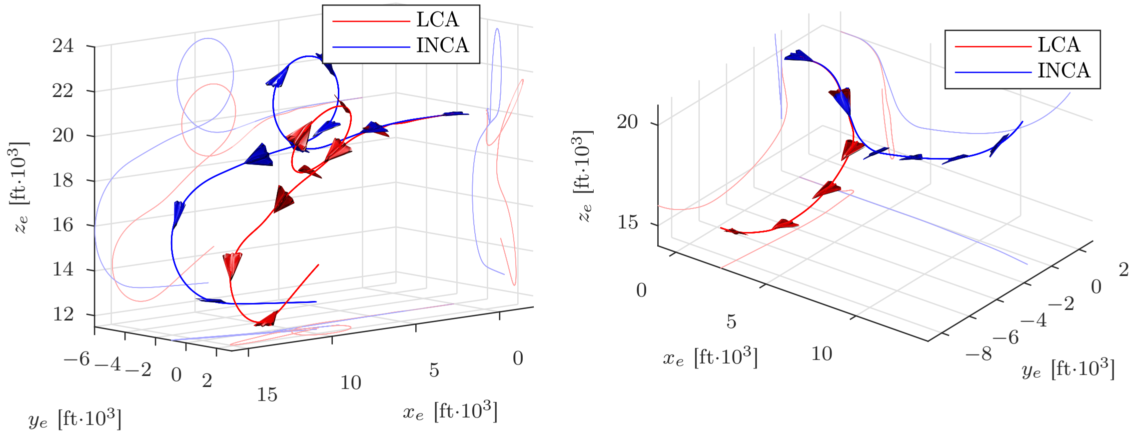

(c)Maneuver C with LCA/RWPI and INCA/QP.

(d)Maneuver D with LCA/QP and INCA/QP.

Fig. 15 Spatial trajectories of the aggressive maneuvers.

Finally, the control effector positions along the barrel roll maneuver are given in Figure 18. Some remarkable effects can be observed. INCA makes more extensive use of the pitch flap for longitudinal control, whereas LCA allocates more control load on the elevons. Since the on-board model of INCA captures parabolic yawing moments, it makes sense that it prioritizes the use of uncoupled control effectors for pitch control to minimize undesired secondary-axis yawing contributions. On the other hand, since LCA lacks information about the interaction effects of the SSDs on trailing-edge actuators at low AoA, this system opens the SSDs causing the couplings that can be observed between SSDs and elevons. Finally, it is worth noting that, since the parabolic yawing moments of the outboard LEFs had to be removed from the linear control effector model, LCA barely uses these effectors for lateral-directional control.

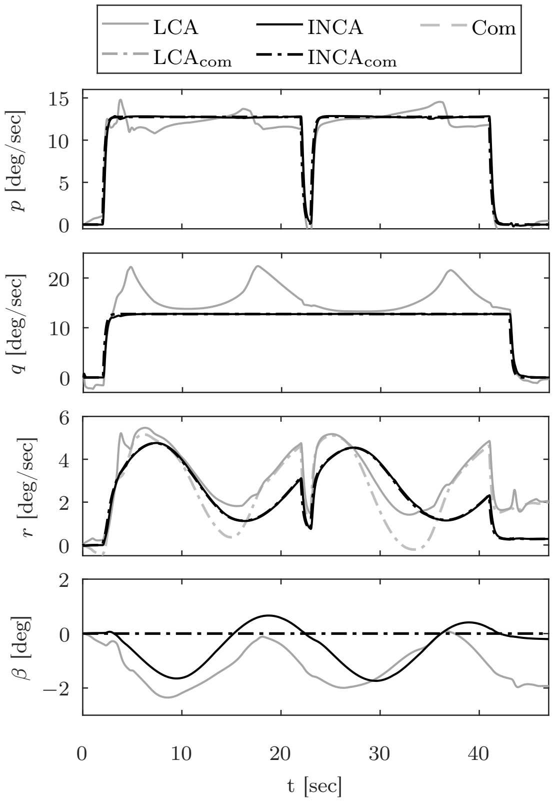

Fig. 16 Controlled variables for the barrel roll maneuver using the QP solver.

C. Overall Performance Assessment

The overall performance of the systems was evaluated with four performance metrics. First, the tracking error RMS $(\mathbf{u} - \mathbf{u}_c)$, with $\mathbf{u}$ the vector of control input variables, evaluates the overall ability of the FCS to track reference input commands. Second, the allocation error RMS $(\boldsymbol{\tau} - \boldsymbol{\tau}_c)$ evaluates the ability of the control allocator to attain the control-induced moments required by the high-level FCS. Third, the control effort RMS $(\boldsymbol{\delta} - \boldsymbol{\delta}_p)$ evaluates the amount of deflection of the control effectors required to satisfy the control commands. Since the INCA algorithm is intended to run in real time on FCS, the number of iterations carried out by the CA algorithm per time step n_i was used to assess the added computational load of INCA with respect to typical LCA methods. The overall performance metrics were computed for the combined data from the flight simulations performed with LCA/RWPI, LCA/QP, INCA/RWPI and INCA/QP. Since maneuvers C and D resulted in unstable flight for some of the tested systems, only maneuvers 3211, A and B

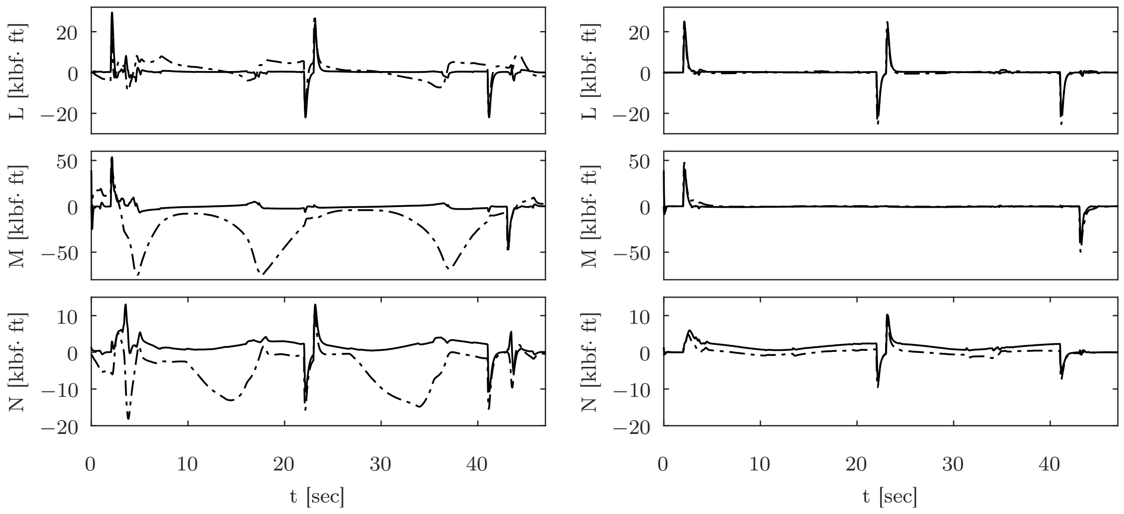

Fig. 17 Commanded (dot-dashed line) and attained (solid line) control-induced moments of the barrel roll maneuver with the LCA (left) and INCA (right) control allocators with the QP solver.

Table 2 Overall tracking error combining maneuvers 3211, A and B.

	RMS $(\mathbf{u}-\mathbf{u}_c)$			
Solver	RWPI		QP	
CA Method	LCA	INCA	LCA	INCA
p [deg/sec]	2.13	1.46	2.07	0.97
q [deg/sec]	3.98	0.73	3.19	0.67
r [deg/sec]	1.55	0.60	1.07	0.60
Total	2.76	1.01	2.28	0.76

were considered in the overall analysis to ensure a fair comparison.

The overall tracking errors for the four tested systems are listed in Table 2. As observed in previous results, the overall tracking performance is better with QP for both LCA and INCA. In both cases, INCA outperforms LCA in terms of tracking performance by a factor of 2.5 with RWPI and of 3.0 with QP. Furthermore, LCA performs worst in the longitudinal channel, in which INCA implies an improvement by a factor of 4.7 with the QP solver.

Table 3 provides the overall allocation errors. It can be observed that the improvement of INCA with respect to LCA is remarkably high in terms of allocation performance. INCA outperforms

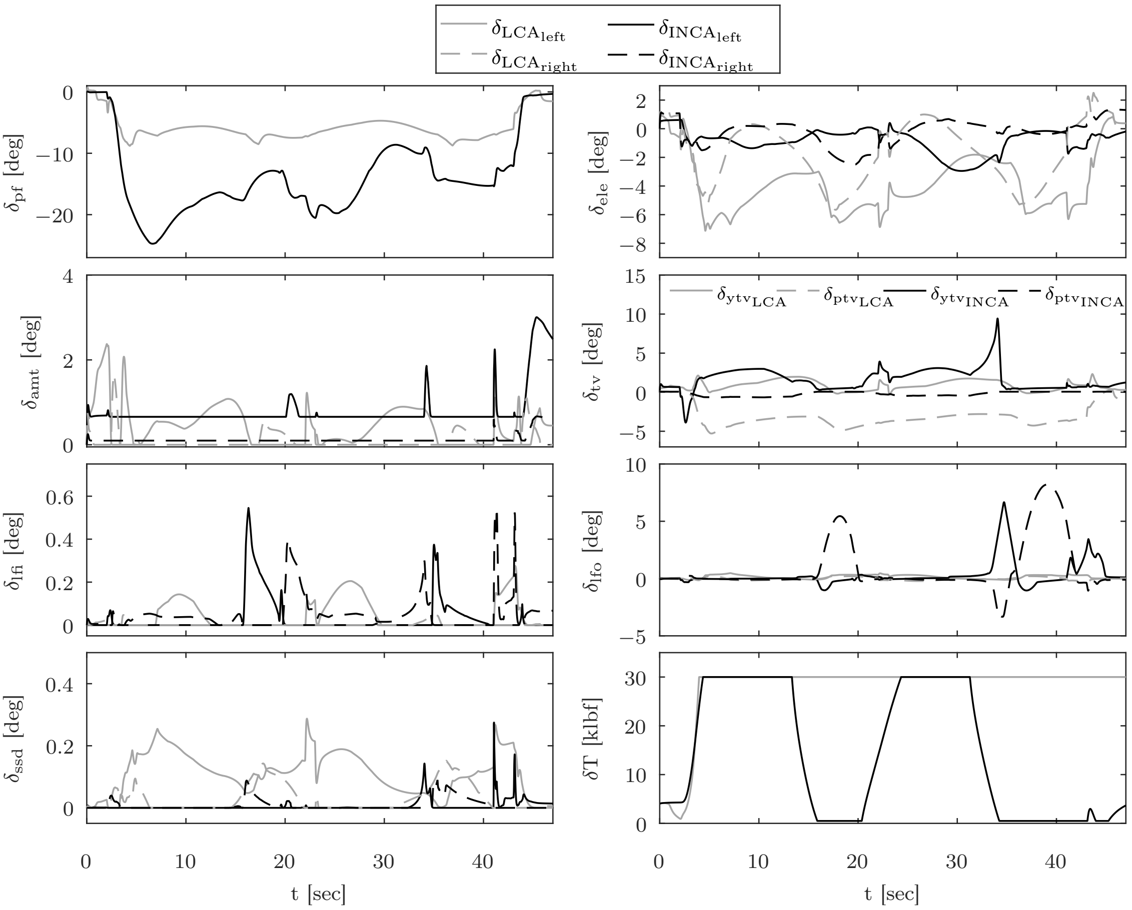

Fig. 18 Control effector positions of the barrel roll maneuver with the QP solver.

Table 3 Overall allocation error combining maneuvers 3211, A and B.

	RMS(RMS $(\boldsymbol{\tau} - \boldsymbol{\tau}_c)$)			
Solver	RWPI		QP	
CA Method	LCA	INCA	LCA	INCA
L [klbf·ft]	8.85	5.93	10.9	2.52
M [klbf·ft]	30.8	5.67	24.7	3.69
N [klbf·ft]	12.9	4.81	8.52	4.92
Total	19.9	5.49	16.3	3.84

LCA by a factor of 3.6 with RWPI and of 4.5 with QP. As in the case of tracking performance, LCA performs worst in the longitudinal channel, where INCA shows an improvement in allocation performance by a factor of 5.34 with RWPI and of 6.7 with QP.

Table 4 **Overall control effort combining maneuvers 3211, A and B.**

	RMS $(\boldsymbol{\delta} - \boldsymbol{\delta}_p)$													
Actuator	Total	δ_{lfi}	δ_{lfo}	δ_{la}	δ_{le}	δ_{ls}	δ_{pf}	δ_{rfi}	δ_{rfo}	δ_{ra}	δ_{re}	δ_{rs}	δ_{ptv}	δ_{ytv}
LCA/RWPI	2.0	0.1	0.2	1.5	2.9	0.2	4.4	0.1	0.2	2.3	2.3	0.3	2.6	1.3
INCA/RWPI	3.7	0.2	0.6	1.5	1.3	0.2	13	0.1	1.4	1.0	1.1	0.5	0.6	2.4
LCA/QP	2.0	0.1	0.2	2.2	2.9	0.4	4.5	0.1	0.2	2.4	2.5	0.3	2.7	1.3
INCA/QP	3.7	0.1	0.6	1.4	1.2	0.3	13	0.1	1.3	2.4	2.0	0.4	0.7	1.9

The overall control efforts per control effector and in total are listed in Table 4. It can be observed that the overall control effort is higher for INCA than for LCA by a factor of 1.8. However the differences in the control effort allocated to each individual control effector reveal interesting trends. First, note that the elevons are more extensively used with LCA than with INCA. Since the parabolic yawing moments of the elevons were removed from the linear model used in LCA but are taken into account by INCA, it is reasonable that INCA allocates lateral-longitudinal control effort on uncoupled control effectors to avoid undesired secondary-axis yawing moments. Also, note that the outboard LEF is underexploited by LCA, despite being an excellent source of lateral-directional control power at high AoA. This is due to the fact that yawing contributions of the outboard LEF were removed from the linear model and their contributions on other axes are weak.

The computational complexities of the RWPI and active set-based QP algorithms were evaluated in [9, 53]. Both studies concluded that these solvers are well-suited for real-time control allocation in FCS. Thus, further analysis of the computational complexity of the algorithms is not required here. However, in order to evaluate whether INCA is suitable or not for real-time implementation, it is necessary to demonstrate that INCA does not increase the computational load on these algorithms in comparison with traditional LCA schemes. Since each iteration implies the same number of operations for both LCA and INCA, it suffices to demonstrate that the number of iterations required per time step is statistically comparable for both CA methods.

Figure 19 shows the distributions of the number of iterations per time step for each trajectory with the RWPI and QP solvers. It can be noted that the number of iterations per time step are very similar in every case. The fact that n_i it is higher for LCA in some cases is due to the large excursions

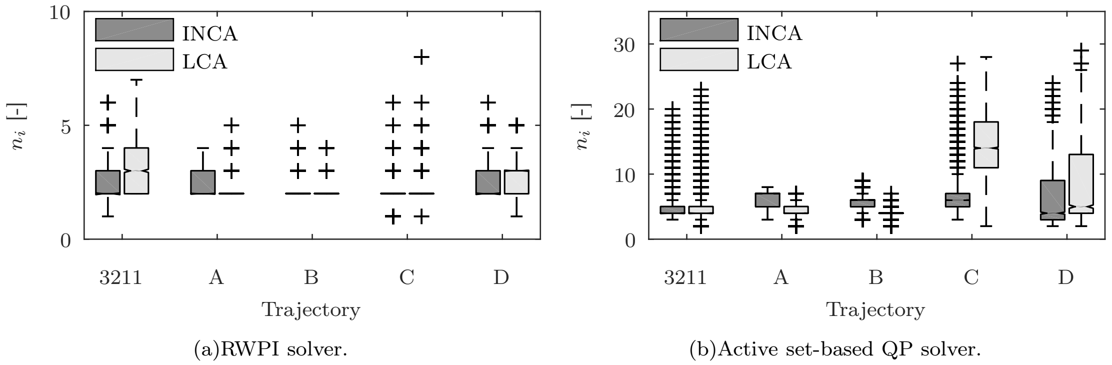

(a)RWPI solver.

(b)Active set-based QP solver.

Fig. 19 Distributions of the number of iterations per time step per trajectory.

and instabilities observed in some trajectories. The maximum number of iterations possible with RWPI is 14, although the maximum iteration count reached was 7. On the other hand, the iteration limit set for the active set algorithm was 100, although the maximum iteration count reached was 23. This proves that INCA has a computational load on the RWPI and active set-based QP algorithms similar to traditional LCA, and therefore the INCA method is well-suited for real-time applications.

XI. Conclusions and Final Remarks

Conventional linear control allocation (LCA) methods are unable to provide satisfactory performance in advanced and unconventional control effector configurations due to the impossibility of linear effector models to capture nonlinearities and interactions between control effectors. In this paper, a novel incremental nonlinear control allocation (INCA) approach is presented to overcome these issues. The INCA method operates in an incremental scheme based on a Jacobian model of the control effectiveness of the actuators. This way of operation enables the consideration of nonlinear control moment curves such as secondary-axis yawing moments and nonlinear interactions between control effectors. The incremental reformulation of the problem enables the use of simple and computationally efficient linear control allocation solvers, enabling the use of INCA in real-time flight control systems. In addition, INCA dynamically drives the actuators towards their optimal positions and is based on real-time actuator position measurements, mitigating coupling effects between the control allocator and actuator dynamics. Moreover, it uses angular acceleration measurements to reduce its model dependency, improving robustness against aerodynamic uncertainties.

The results presented in this thesis have shown very significant improvements of INCA with respect to typical linear control allocation (LCA) methods in terms of tracking performance, allocation performance and control effort. A robustness analysis of INCA against Jacobian model mismatch showed that for model offsets of ±30% and scaling factors between 0.6 and 1.4, the allocation error and control effort over a reference maneuver increase up to 25% and 17% respectively, which demonstrates considerable robustness against Jacobian model mismatch. Also, it was observed that INCA performs better when the magnitude of the Jacobian terms is underestimated. The INCA-based flight control system was tested in real-time simulations against aggressive maneuvers, showing substantially superior performance than the LCA-based control system. It was also proven that the computational load of INCA is similar to that of LCA-based schemes for the redistributed weighted pseudo-inverse (RWPI) and active set-based quadratic programming (QP) control allocation methods. Since these methods are known to be well-suited for real-time implementation, it was demonstrated that INCA is well-suited for real-time implementation in flight control systems.

INCA is expected to be strongly beneficial in fault-tolerant flight control systems. Future work will focus on upgrading the current flight control system into and adaptive flight control system with on-line system identification to investigate benefits in terms of recoverability in faulty conditions. Additionally, the INCA system will be tested with larger suites of control effectors, using innovative actuators such as flow control devices.

References

[1] Oppenheimer, M. W., Doman, D. B., and Bolender, M. A., "Control Allocation for Over-Actuated Systems," *2006 14th Mediterranean Conference of Control and Automation*, IEEE, 2006.

[2] Buffington, J.M. and Enns, D. F., "Lyapunov stability analysis of daisy chain control allocation," *Journal of Guidance, Control, and Dynamics*, Vol. 19, No. 6, 1996, pp. 1226-1230.

[3] Durham, W. C., "Constrained Control Allocation," *Journal of Guidance, Control, and Dynamics*, Vol. 16, No. 4, 1993, pp. 717-725.

[4] Durham, W. C., "Constrained Control Allocation: Three Moment Problem", *Journal of Guidance, Control, and Dynamics*, Vol. 17, No. 2, 1994, pp. 330-336.

[5] Durham, W. C., "Attainable Moments for the Constrained Control Allocation Problem," *Journal of Guidance, Control, and Dynamics*, Vol. 17, No. 6, 1994, pp. 1371-1373.

[6] Bordignon, K., *Constrained Control Allocation for Systems with Redundant Control Effectors*, PhD Thesis, Virginia Polytechnic Institute and State University, 1996.

[7] Durham, W. C., "Efficient, Near-Optimal Control Allocation," *Journal of Guidance, Control, and Dynamics*, Vol. 22, No. 2, 1999, pp. 369-372.

[8] Durham, W. C., "Computationally Efficient Control Allocation," *Journal of Guidance, Control, and Dynamics*, Vol. 24, No. 3, 2001, pp. 519-524.

[9] Bodson, M., "Evaluation of Optimization Methods for Control Allocation," *Journal of Guidance, Control, and Dynamics*, Vol. 25, No. 4, 2002, pp. 703-711.

[10] Paradiso, J., "A Highly Adaptable Method of Managing Jets and Aerosurfaces for Control of Aerospace Vehicles," *Proceedings of the Guidance, Navigation and Control Conference*, 1989, pp. 35-44.

[11] Paradiso, J., "Adaptable Method of Managing Jets and Aerosurfaces for Aerospace Vehicle Control," *Journal of Guidance Control and Dynamics*, Vol. 14, No. 1, 1991, pp. 44-50.

[12] Enns, D., "Control allocation approaches," *Guidance, Navigation, and Control Conference and Exhibit*, 1998, pp. 98-108.

[13] "Buffngton, J. M., "Modular Control Law Design for the Innovative Control Aircraft Effectors (ICE) Tailless Fighter Configuration," Tech. rep., 1999.

[14] Oppenheimer, M. W. and Doman, D. B., "A Method for Including Control Effector Interactions in the Control Allocation Problem," *Proceedings of the AIAA Guidance, Navigation, and Control Conference and Exhibit*, 2007.

[15] Doman, D. B. and Sparks, A. G., "Concepts for Constrained Control Allocation of Mixed Quadratic and Linear Effectors," *Proceedings of the American Control Conference*, 2002, pp. 3729-3734.

[16] Bolender, M. A. and Doman, D. B., "Nonlinear Control Allocation Using Piecewise Linear Functions," *Journal of Guidance, Control, and Dynamics*, Vol. 27, No. 6, 2004, pp. 1017-1027.

[17] Bolender, M. A. and Doman, D. B., "Method for Determination of Nonlinear Attainable Moment Sets," *Journal of Guidance, Control, and Dynamics*, Vol. 27, No. 5, 2004, pp. 907-914.

[18] Doman, D. B. and Oppenheimer, M., "Improving Control Allocation Accuracy for Nonlinear Aircraft Dynamics," *AIAA Guidance, Navigation, and Control Conference and Exhibit*, 2002.

[19] Poonamallee, V. L., Yurkovich, S., Serrani, A., Doman, D. B., and Oppenheimer, M. W., "A Nonlinear Programming Approach for Control Allocation," *American Control Conference*, Boston, Massachusetts, 2004, pp. 1689-1694.

[20] Harkegard, O., "Dynamic Control Allocation Using Constrained Quadratic Programming," *Journal of Guidance Control and Dynamics*, Vol. 27, No. 6, 2004, pp. 1028-1034.

[21] Luo, Y., Serrani, A., Yurkovich, S., Doman, D. B., and Oppenheimer, M. W., “Model Predictive Dynamic Control Allocation with Actuator Dynamics,” *American Control Conference*, 2004, pp. 1695-1700.

[22] Luo, Y., Serrani, A., Yurkovich, S., Oppenheimer, M. W., and Doman, D. B., “Model-Predictive Dynamic Control Allocation Scheme for Reentry Vehicles,” *Journal of Guidance, Control, and Dynamics*, Vol. 30, No. 1, 2007, pp. 100-113.

[23] Hanger, M. B., *Model Predictive Control Allocation*, PhD. Thesis, Norwegian University of Science and Technology, 2011.

[24] Johansen, T. A., “Optimizing Nonlinear Control Allocation,” *43rd IEEE Conference on Decision and Control*, 2004, pp. 3435-3440.

[25] Niestroy, M. A., Dorsett, K. M., and Markstein, K., “A Tailless Fighter Aircraft Model for Control-Related Research and Development,” *AIAA Modeling and Simulation Technologies Conference*, 2017.

[26] Johansen, T. A., “Optimizing Nonlinear Control Allocation,” *43rd IEEE Conference on Decision and Control*, 2004, pp. 3435-3440.

[27] Ostroff, A. J. and Bacon, B. J., “Enhanced NDI Strategies for Reconfigurable Flight Control,” *American Control Conference*, 2002, pp. 3631-3636.

[28] Sieberling, S., Chu, Q. P., and Mulder, J. a., “Robust Flight Control Using Incremental Nonlinear Dynamic Inversion and Angular Acceleration Prediction,” *Journal of Guidance, Control, and Dynamics*, Vol. 33, No. 6, 2010, pp. 1732-1742.

[29] Simplício, P., Pavel, M. D., van Kampen, E., and Chu, Q. P., “An Acceleration Measurements-Based Approach for Helicopter Nonlinear Flight Control Using Incremental Nonlinear Dynamic Inversion,” *Control Engineering Practice*, Vol. 21, No. 8, 2013, pp. 1065-1077.

[30] Smeur, E. J. J., Chu, Q. P., and de Croon, G. C. H. E., “Adaptive Incremental Nonlinear Dynamic Inversion for Attitude Control of Micro Aerial Vehicles,” *Journal of Guidance, Control, and Dynamics*, Vol. 39, No. 3, 2016, pp. 450-461.

[31] Doman, D. B. and Ngo, A. D., “Dynamic Inversion-Based Adaptive/Reconfigurable Control of the X-33 on Ascent,” *Journal of Guidance, Control, and Dynamics*, Vol. 25, No. 2, 2002, pp. 275-284.

[32] da Costa, R. R., Chu, Q. P., and Mulder, J. a., “Reentry Flight Controller Design Using Nonlinear Dynamic Inversion,” *Journal of Spacecraft and Rockets*, Vol. 40, No. 1, 2003, pp. 64-71.

[33] Tol, H. J., de Visser, C. C., Sun, L. G., van Kampen, E., and Chu, Q. P., “Multivariate Spline-Based Adaptive Control of High-Performance Aircraft with Aerodynamic Uncertainties,” *Journal of Guidance, Control, and Dynamics*, Vol. 39, No. 4, 2016, pp. 781-800.

[34] Oppenheimer, M. W. and Doman, D. B., “Methods for Compensating for Control Allocator and Actuator Interactions,” *Journal of Guidance, Control, and Dynamics*, Vol. 27, No. 5, 2004, pp. 922-927.

[35] Tol, H.J., de Visser, C.C., Sun, L.G, van Kampen, E., Chu, Q.P., “Nonlinear Multivariate Spline-Based Control Allocation for High-Performance Aircraft”, *Journal of Guidance, Control, and Dynamics*, Vol. 37, No. 6, 2014, pp. 1840-1862.

[36] Bowlus, J., Multhopp, D., Banda, S., “Challenges and Opportunities in Tailless Aircraft Stability and Control,” *Guidance, Navigation, and Control Conference*, 1997, pp. 1713-1718.

[37] Dorsett, K. M. and Mehl, D. R., “Innovative Control Effectors (ICE) Phase I,” Tech. rep., Lockheed Martin Tactical Aircraft Systems, 1996.

[38] Dorsett, K. M., Fears, S. P., and Houlden, H. P., “Innovative Control Effectors (ICE) Phase II,” Tech. rep., 1997.

[39] Buffington,, J. M., “Tailless aircraft control allocation,” *AIAA Guidance, Navigation, and Control Conference*, 1997, pp. 737-747.

[40] Ngo, A. D., Reigelsperger, W., Banda, S., and Bessolo, J., “Multivariable Control Law Design for a Tailless Airplane,” *AIAA Guidance, Navigation and Control Conference*, 1996.

[41] Gillard, W. J. and Dorsett, K. M., “Directional Control for Tailless Aircraft Using All Moving Wing Tips,” *22nd Atmospheric Flight Mechanics Conference*, 1997m pp. 51-58.

[42] Eberhardt, R. and Ward, D., “Indirect Adaptive Fight Control of a Tailless Fighter Aircraft,” *Guidance, Navigation, and Control Conference and Exhibit*, 1999, pp. 466-476.

[43] Shtessel, Y., Buffington, J., and Banda, S., “Tailless Aircraft Flight Control Using Multiple Time Scale Reconfigurable Sliding Modes,” *IEEE Transactions on Control Systems Technology*, Vol. 10, No. 2, 2002, pp. 288-296.

[44] van der Peijl, I., de Visser, C., and Niestroy, M. A., “Physical Splines for Aerodynamic Modelling of Innovative Control Effectors,” *MSc Thesis*, Delft University of Technology, Delft, 2017 (unpublished).

[45] de Visser, C. C., Chu, Q. P., and Mulder, J. A., “A New Approach to Linear Regression with Multivariate Splines,” *Automatica*, Vol. 45, No. 12, 2009, pp. 2903-2909.

[46] Tol, H. J., de Visser, C. C., and Kotsonis, M., “Model Reduction of Parabolic PDEs Using Multivariate Splines,” *International Journal of Control*, 2016.

[47] Johnson, E. N. and Calise, A. J., “Pseudo-Control Hedging: a New Method for Adaptive Control,” *Advances in Navigation Guidance and Control Technology Workshop*, 2000.

[48] Johnson, E. N. and Kannan, S. K., “Adaptive Trajectory Control for Autonomous Helicopters,” *Journal of Guidance, Control, and Dynamics*, Vol. 28, No. 3, 2005, pp. 524-538.

[49] Lam, Q. and Barkana, I., “Direct Adaptive Control Treatment to Flight Control Input Saturation,” *AIAA Guidance, Navigation, and Control Conference and Exhibit*, 2005.

[50] Lombaerts, T., Looye, G., Chu, Q., and Mulder, J., “Pseudo Control Hedging and its Application for Safe Fight Envelope Protection,” *AIAA Guidance, Navigation, and Control Conference*, 2010.

[51] Lewis, F. L. and Syrmos, V. L., *Optimal Control*, John Wiley & Sons, Inc., New York, NY, 1995.

[52] Petersen, J. A. M. and Bodson, M., “Constrained Quadratic Programming Techniques for Control Allocation,” *IEEE Transactions on Control Systems Technology*, Vol. 14, No. 1, 2006, pp. 91-98.

[53] Harkegard, O., “Efficient Active Set Algorithms for Solving Constrained Least Squares Problems in Aircraft Control Allocation,” *IEEE Conference on Decision and Control*, 2002, pp. 1295-1300.

[54] Mulder, J. A., “Design and evaluation of dynamic fight test manoeuvres”, Technical Report, 1986.

Appendix C

Aggressive Flight Maneuvers: Additional Results

C.1 Maneuver A: High-Bank Climbing Spiral (RWPI)

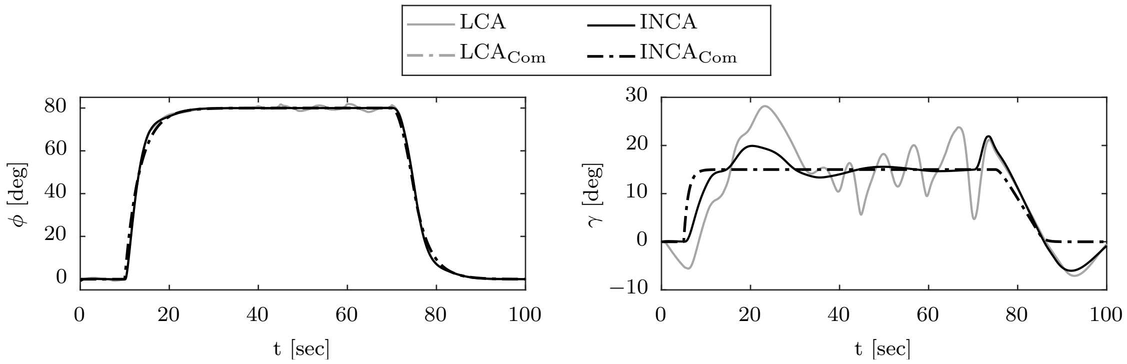

Figure C.1: Outer loop control variables of maneuver A with LCA and INCA solved with RWPI.

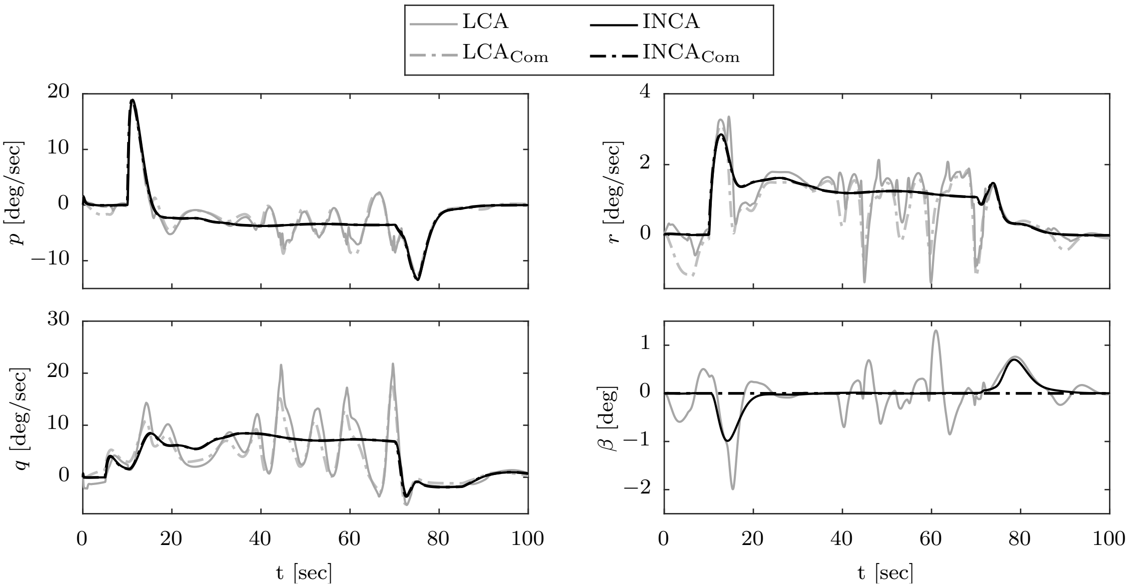

Figure C.2: Inner loop and sideslip control variables of maneuver A with LCA and INCA solved with RWPI.

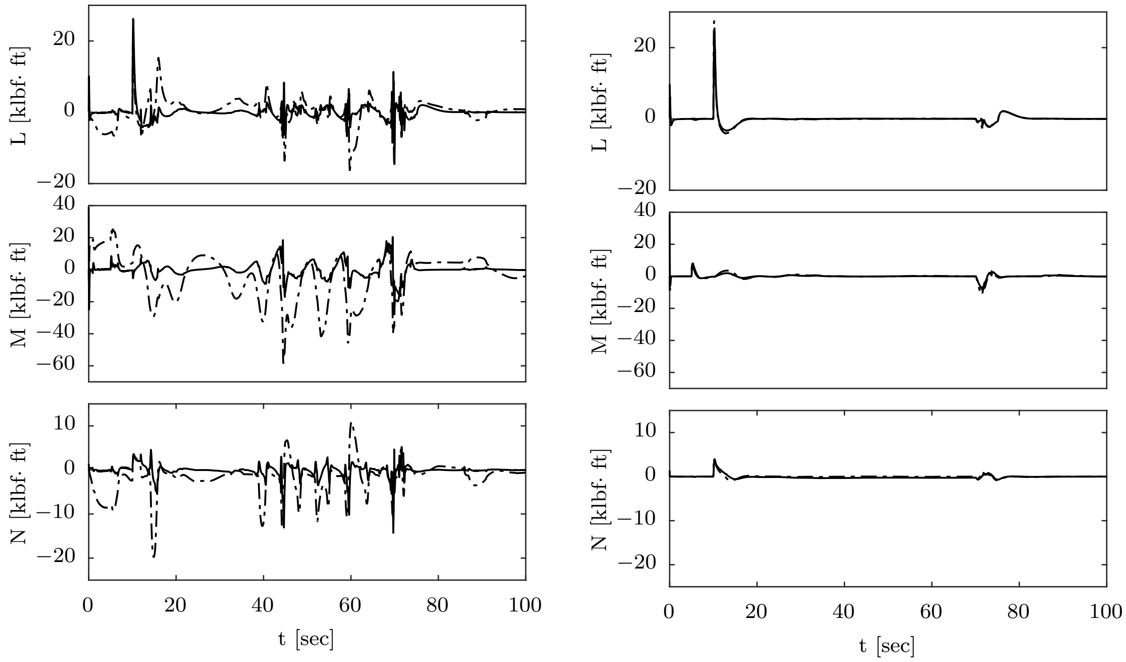

Figure C.3: Commanded (dot-dashed line) and attained (solid line) control-induced moments of maneuver A with LCA and INCA solved with RWPI.

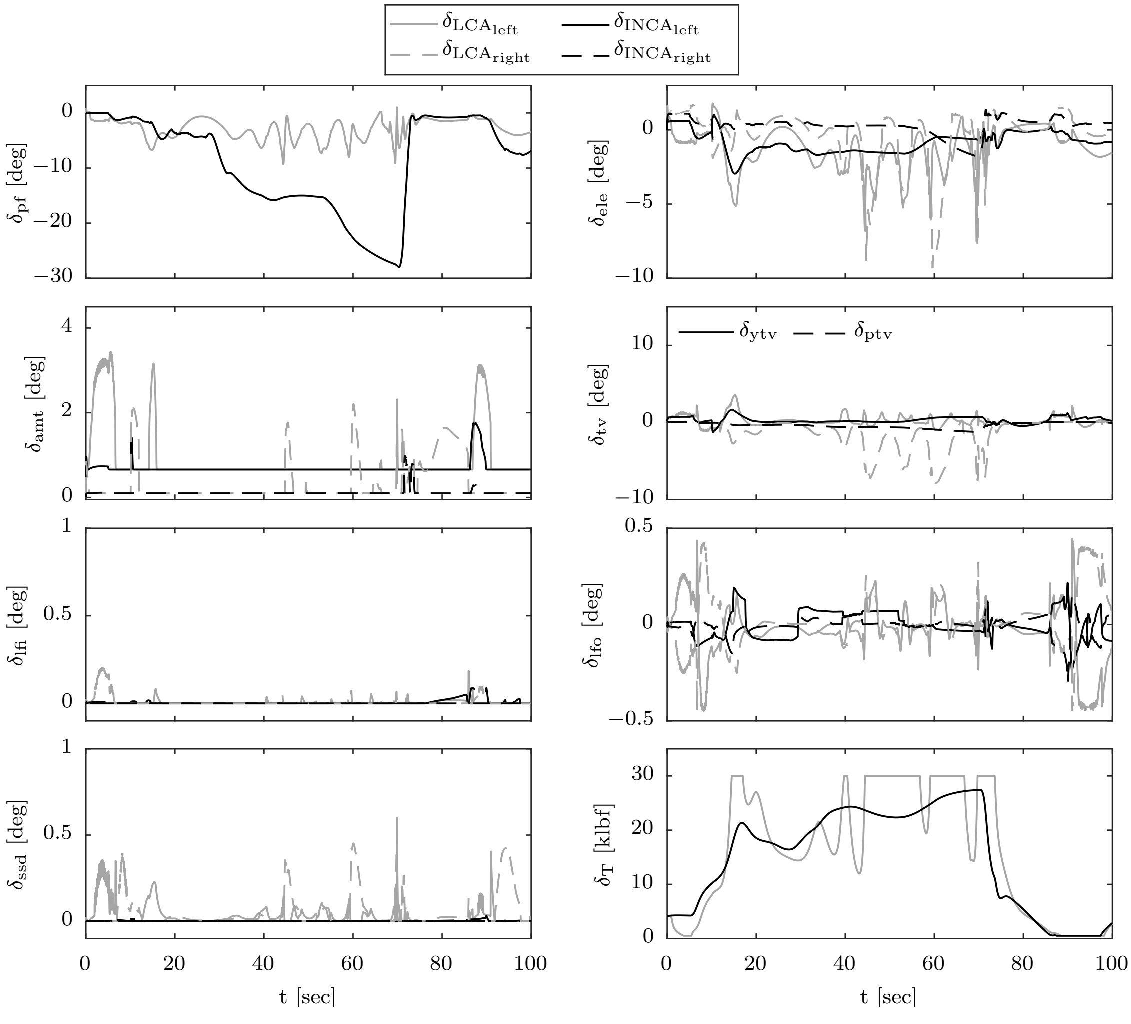

Figure C.4: Control effector positions of maneuver A with LCA and INCA solved with RWPI.

C.2 Maneuver B: Barrel Roll (RWPI)

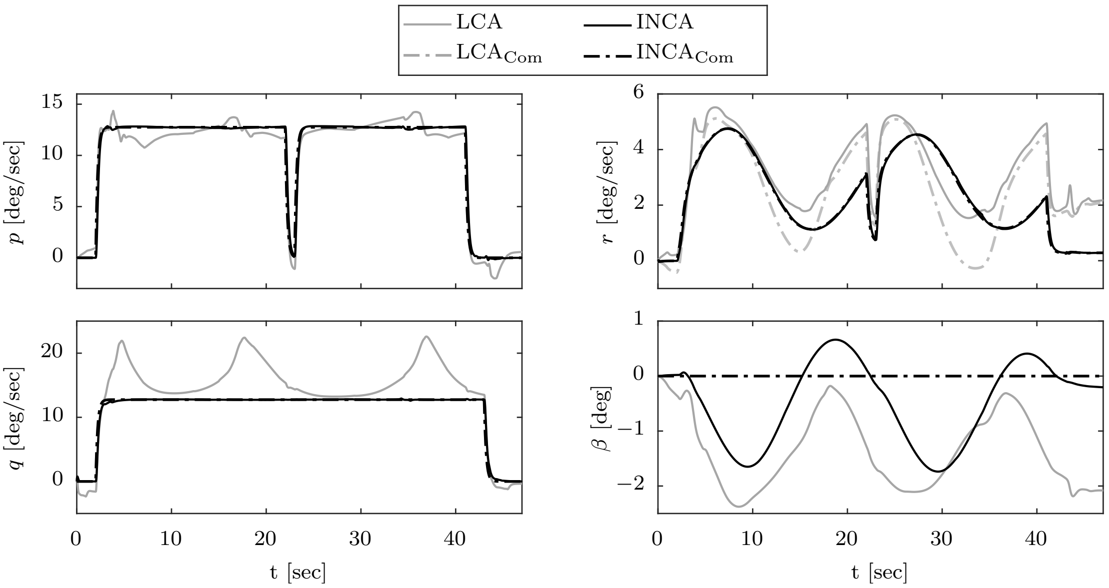

Figure C.5: Control variables of maneuver B with LCA and INCA solved with RWPI.

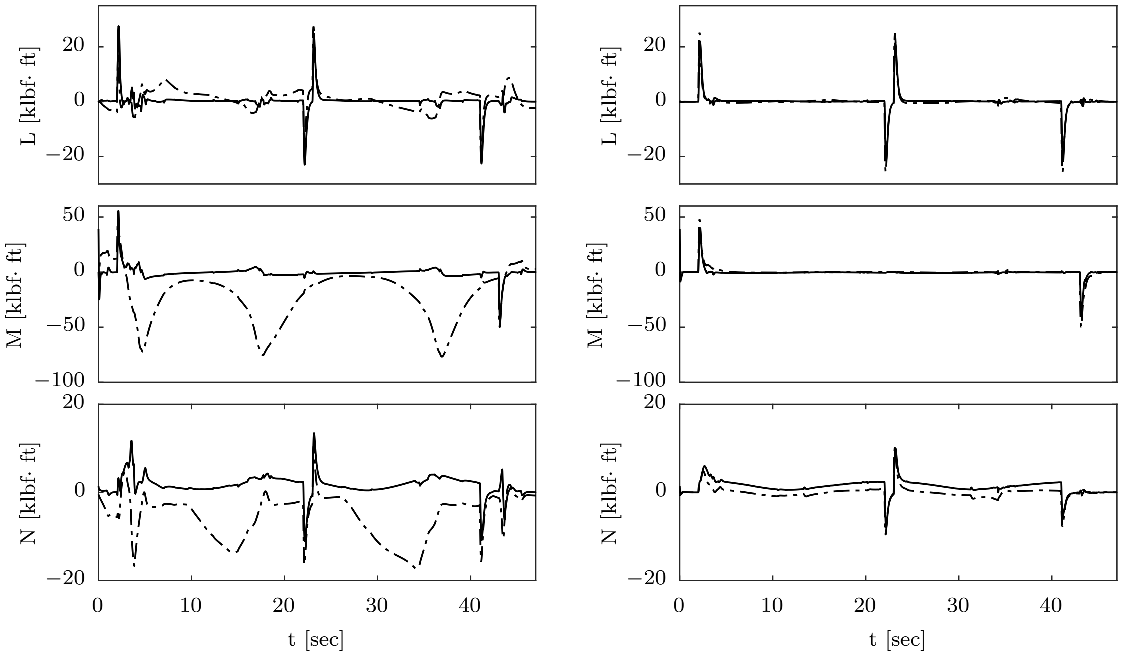

Figure C.6: Commanded (dot-dashed line) and attained (solid line) control-induced moments of maneuver B with LCA and INCA solved with RWPI.

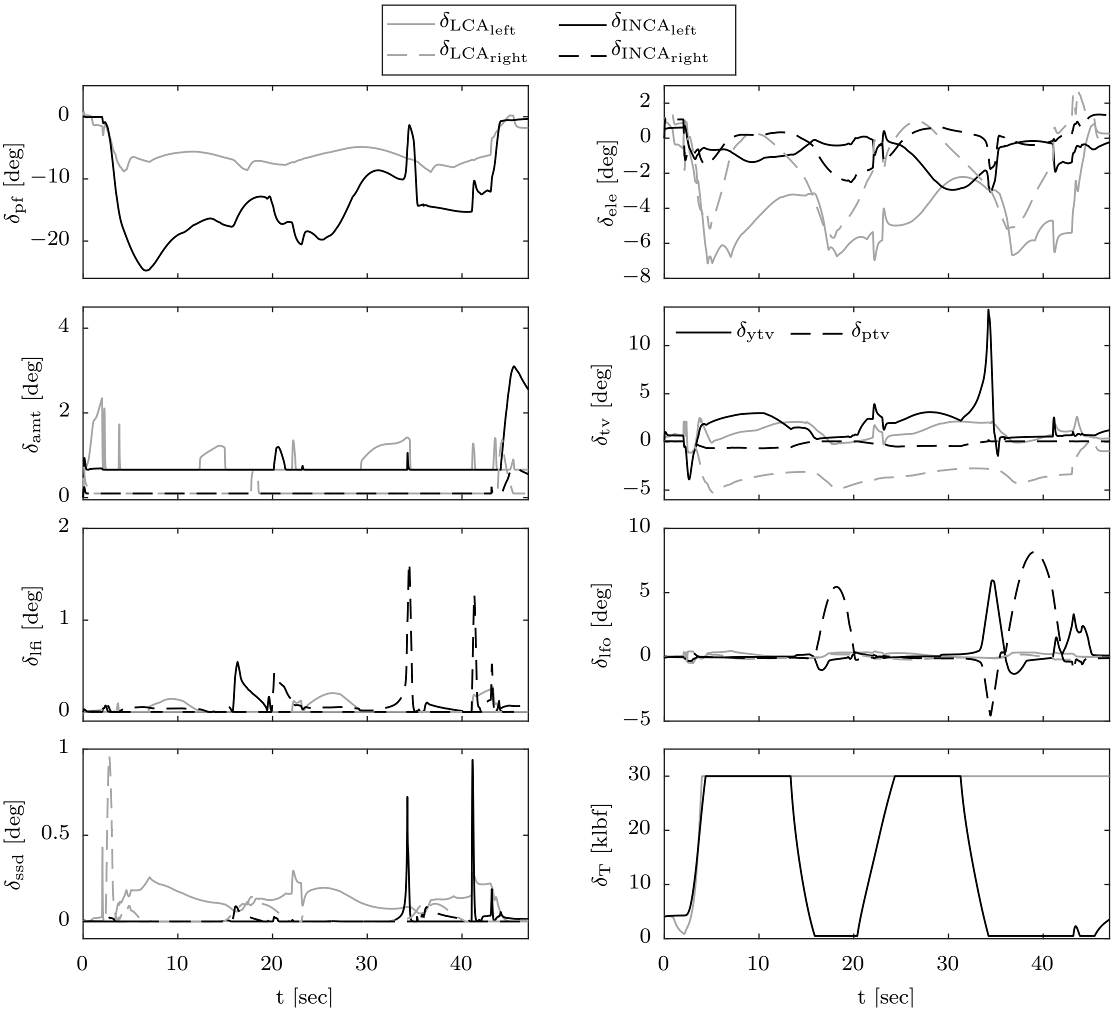

Figure C.7: Control effector positions of maneuver B with LCA and INCA solved with RWPI.

C.3 Maneuver C: High AoA and High Sideslip Commands (QP)

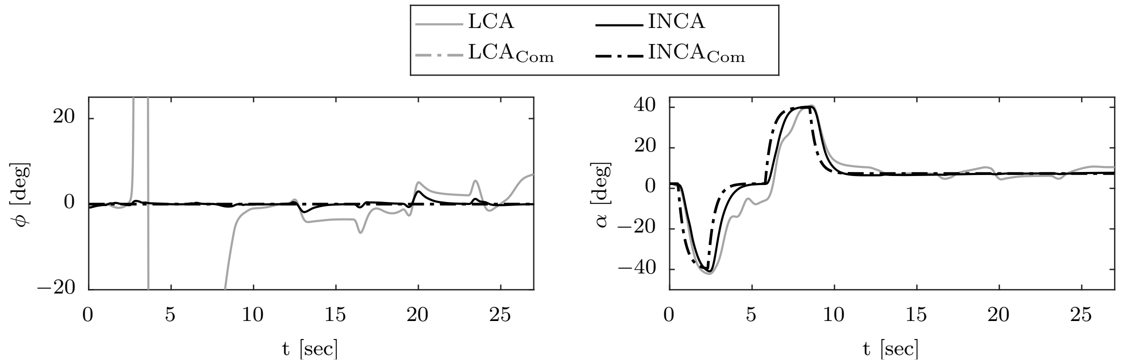

Figure C.8: Outer loop control variables of maneuver C with LCA and INCA with QP.

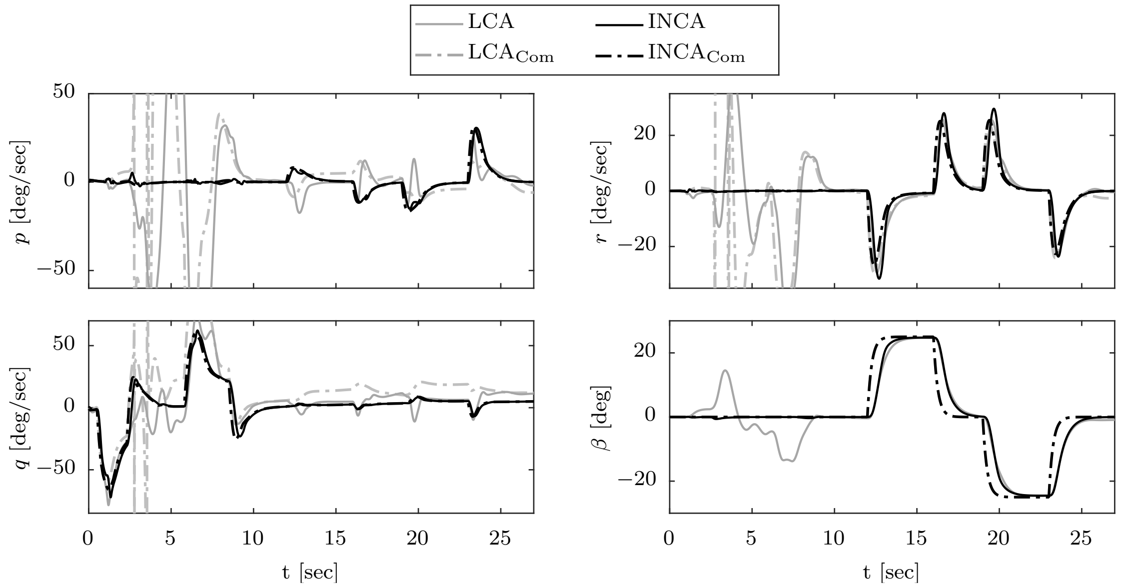

Figure C.9: Inner loop control variables of maneuver C with LCA and INCA with QP.

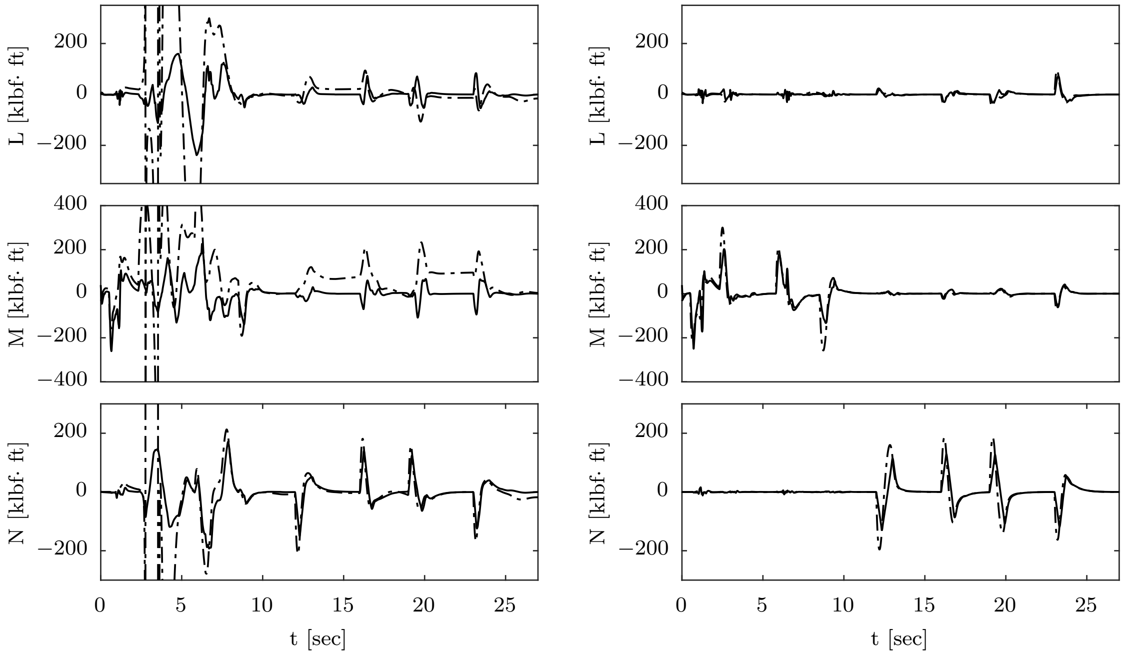

Figure C.10: Commanded (dot-dashed line) and attained (solid line) control-induced moments of maneuver C with LCA and INCA with QP.

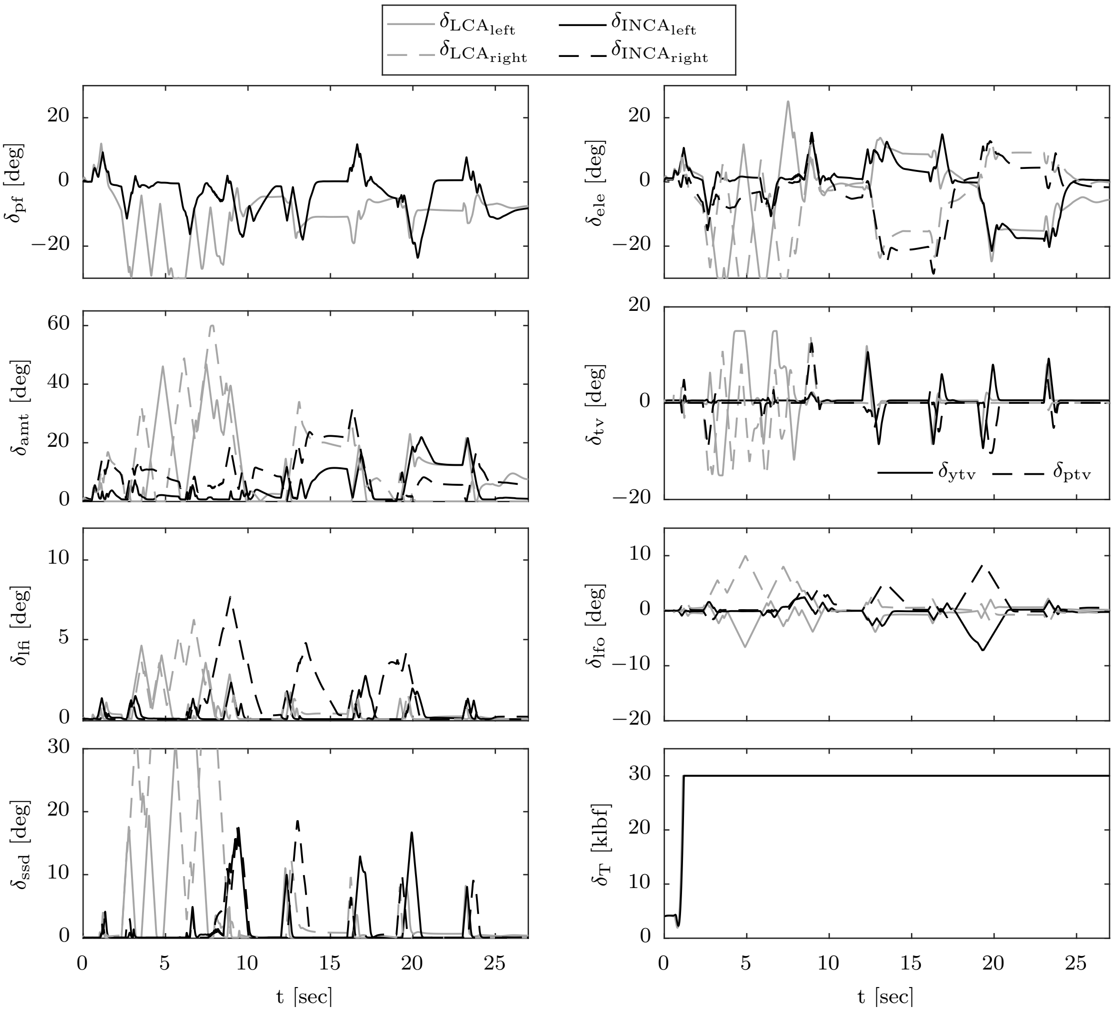

Figure C.11: Control effector positions of maneuver C with LCA and INCA with QP.

C.4 Maneuver D: Aerobatics Sequence (Unstable Trajectories)

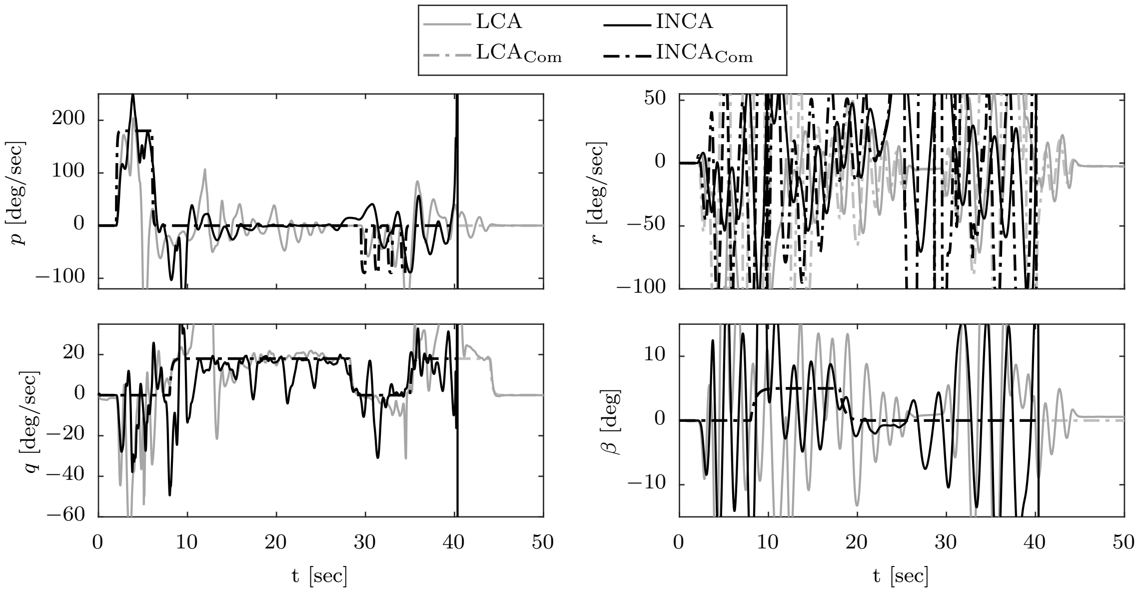

Figure C.12: Control variables of maneuver B with LCA/QP and INCA/RWPI.

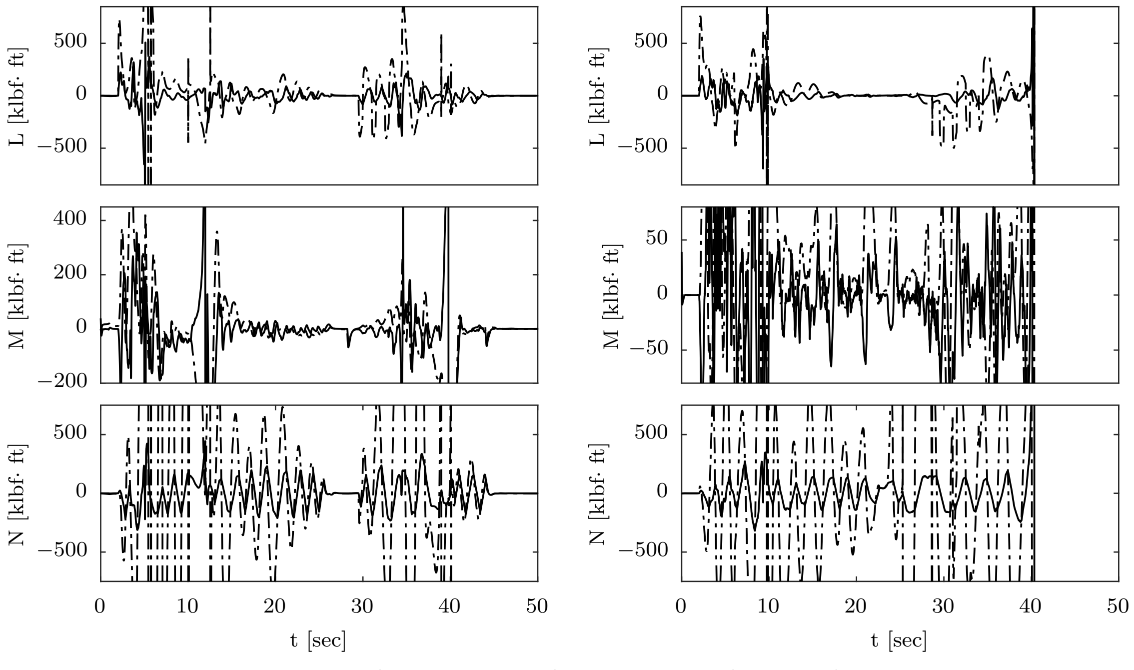

Figure C.13: Commanded (dot-dashed line) and attained (solid line) control-induced moments of maneuver D with LCA/QP and INCA/RWPI.

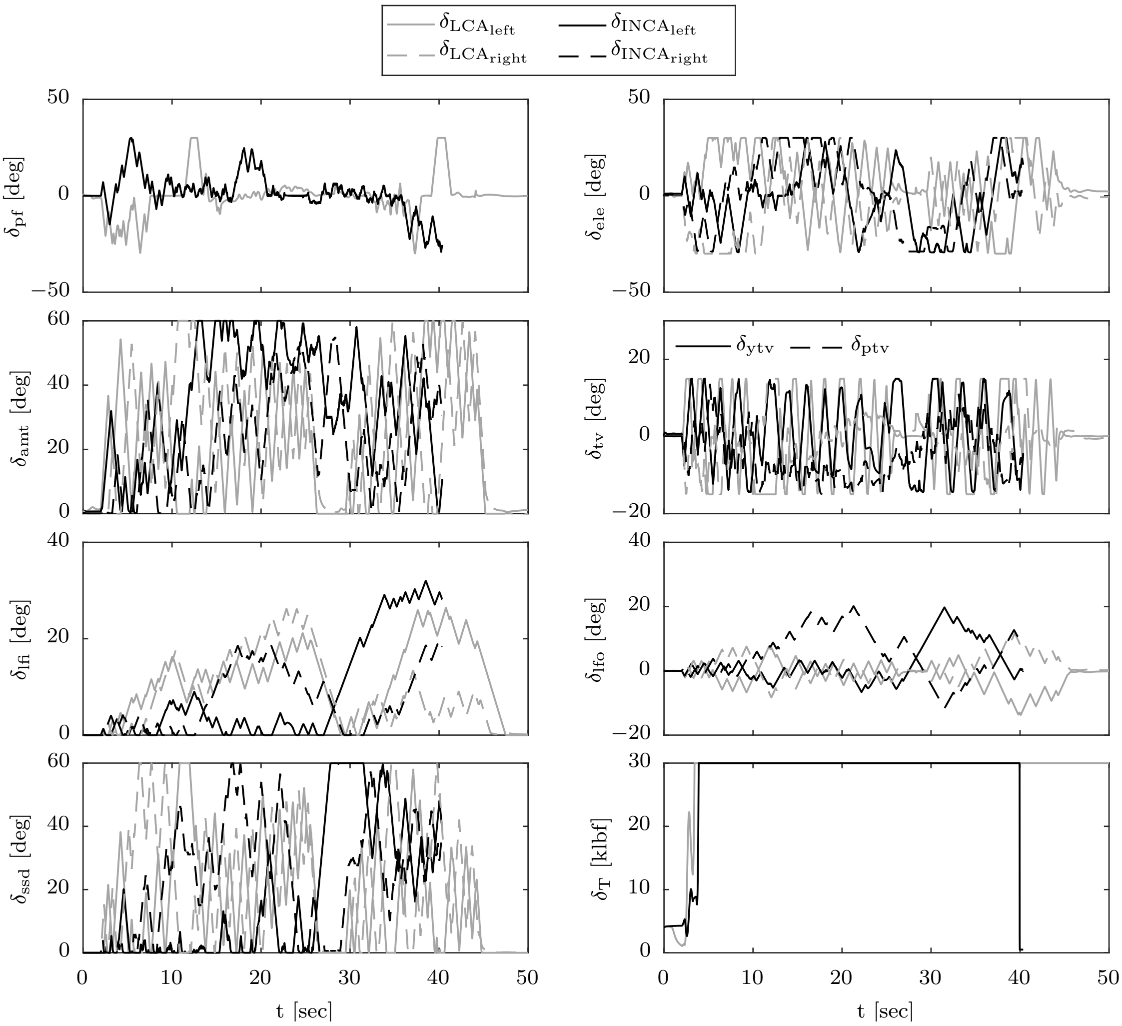

Figure C.14: Control effector positions of maneuver D with LCA/QP and INCA/RWPI.